Flow characteristics and power extraction from bluff bodies in vortex-induced vibration

A thesis submitted
in partial fulfillment of the requirements
for the degree of

Doctor of Philosophy

by

Abhijit Pal

Department of Mechanical Engineering
Indian Institute of Technology Guwahati

May 2026

Dedicated to
My Parents

CERTIFICATE

It is certified that the work contained in the thesis entitled "**Flow characteristics and power extraction from bluff bodies in vortex-induced vibration**", submitted by **Abhijit Pal** (Reg no. 196103101), a research scholar in the *Department of Mechanical Engineering, Indian Institute of Technology Guwahati*, for the award of the degree of **Doctor of Philosophy** is a record of an original work carried out by him under my supervision and guidance. The results embodied in this thesis has not been submitted to any other University or Institute for the award of any other degree or diploma.

(Dr. Atul K. Soti)
Assistant Professor
Department of Mechanical Engineering
Indian Institute of Technology Guwahati

January 2026

Acknowledgements

This thesis represents the outcome of several years of learning and growth at the Indian Institute of Technology Guwahati. I have been fortunate to receive support from many individuals, to whom I express my heartfelt appreciation.

I am deeply grateful to my supervisor, Dr. Atul K. Soti, for his unwavering guidance, encouragement, and insightful discussions, which have greatly shaped my academic and professional development. I also thank my doctoral committee members—Prof. Amaresh Dalal, Dr. Tapan K. Mankodi, and Prof. Suresh A. Kartha—for their valuable feedback and support.

I acknowledge the Computer and Communication Center, IIT Guwahati, for providing access to PARAM Kamrupa and PARAM Ishan supercomputing facilities, which were essential for my simulations. I also thank the Technology Innovation Hub, IIT Guwahati, and the Science & Engineering Research Board (SERB), India, for the research grant that supported this work.

I am grateful to Deepak, Dhanjita, and Suman for their genuine friendship and steady support. My special thanks to Debajit, Shahrukh, and Bipul, whose understanding and kindness helped me through challenging phases of my Ph.D.

I extend my sincere thanks to Kanak, Sumit, Pijush, Pranab, and Rahul for bringing joy and energy to daily life, and to my seniors—Dr. Tanuj, Dr. Nitesh, Dr. Ashok, Dr. Santanu, Dr. Chandan, Dr. Neeraj, Dr. Kaustabh, Dr. Dheeraj, Dr. Rohit, and Brijesh—for their guidance and camaraderie. I am also thankful to all my friends in the Mechanical Engineering department and beyond for adding warmth and balance to my journey.

Finally, I offer my deepest gratitude to my family, whose unconditional love, sacrifices, and unwavering belief in me made this journey possible and continue to inspire me every day.

Abhijit Pal
January 2026

Abstract

Vortex-induced vibration (VIV) is extensively studied as a design constraint for high-rise buildings, slender marine risers, heat exchanger pipe arrays, bridges, chimneys, power-carrying cables, and aircraft parts. Though VIV is seen as a design challenge, it can also be used to extract energy from the free stream flow of rivers and oceans. VIV of rigidly coupled multiple circular cylinders is numerically studied to observe the flow characteristics and power extraction capabilities at various arrangements (tandem and staggered). The cylinders are only free to move in the cross-flow direction. The study is extended to non-circular geometry (ellipse) to explore the difference in flow features with respect to the circular cylinder. Different aspect ratios are employed to investigate the effect of geometry on flow characteristics and power harvesting. A two-degree-of-freedom (2-DOF) VIV system, with passively controlled transverse oscillation and rotation, exhibits different flow behavior compared to a single-degree-of-freedom (1-DOF) system. The 2-DOF system of elliptical cylinder is also compared with that of the 1-DOF system to study the differences in power extraction. The numerical studies are performed in an open-source finite-volume-based solver, OpenFOAM.

The flow characteristics of two rigidly coupled staggered and tandem circular cylinders undergoing vortex-induced vibration (VIV) are investigated numerically at a fixed Reynolds number (Re $= 150$). In these studies, the center-to-center distance between cylinders is varied in both the streamwise (L) and transverse (T) directions from 2.0 to 4.0. The tandem cases exhibit a greater maximum vibration amplitude and a broader region of significant amplitude than their corresponding staggered cases, except at $L = 2.0$. In comparison to tandem cases, staggered cases display a broader synchronization region. The downstream cylinder primarily influences the wake characteristics, which significantly affect overall lift and phase. Three response branches (initial, upper, and lower) are observed for all the arrangements. For the tandem case where $L = 2.0$, three vortex modes are identified: overshoot mode (OS) at transition from initial to lower branch, alternate reattachment (AR) at initial branch, and continuous reattachment (CR) at lower branch. In contrast, at $L = 4.0$, only the

AR mode is found. Both AR and co-shedding (CS) modes are present at $L = 3.0$. The staggered cases exhibit either asymmetric vortices with the downstream cylinder shear layer being more elongated than that of the upstream cylinder, or symmetric in-phase 2S vortex streets.

Power extraction from rigidly coupled tandem cylinders involves the introduction of damping. The power extraction is modeled as the power dissipated by the linear damper. The maximum vibration amplitude and corresponding U^* increase with the increase in L for undamped and damped responses. Average power is observed to be a non-monotonic function of U^*. The maximum average power increases with L, reaches a peak at $L = 5.0$, and then decreases with further increase in L. The optimal damping for maximum power is also found to be a non-monotonic function of L. The peak of non-dimensional extracted power is equal to 0.245 (at $L = 5.0$), which is two times that of a single cylinder. Maximum average power is formulated as an exponential function of mass-damping parameter ($\alpha = m^*\zeta$). Power extraction efficiency, defined as the ratio of average extracted power to the available fluid power, peaks at $L = 5.0$. Power density, the ratio of extracted power to the available flow power in a volume occupied by the cylinders, reaches its maximum at $L = 3.0$. Considering both energy output and structural compactness, $L = 3.0$ offers the most cost-effective configuration.

The rigidly coupled staggered arrangement reveals that vibration amplitude and power output exhibit strong non-monotonic dependence on U^* and ζ, with optimal performance at intermediate damping. Additionally, the maximum vibration amplitude decreases with increasing T. The optimal α for all arrangements, except for the $L = 3.0, T = 2.0$, is recorded at $\alpha = 0.32$. The configuration $L = 2.0, T = 3.0$ yields the maximum average power (0.28) and power density (0.02), nearly twice that of a single cylinder, while $L = 3.0, T = 2.0$ achieves the highest power extraction efficiency (0.075). Overall, the findings demonstrate that appropriate staggered arrangements can significantly enhance power generation efficiency, offering useful design insights for compact VIV-based energy harvesters.

The aspect ratio (ϵ) of the elliptical cylinder is varied from 0.10 to 1.00 (circular cylinder). The vibration amplitude response of the elliptical cylinders is found to be similar to that of the circular cylinder, consisting of initial and lower branches. The maximum vibration amplitude and the width of the synchronization region of the elliptical cylinders are observed to increase with decreasing ϵ. The peak power output ($\bar{P}_{peak}$) is a non-monotonic function of ϵ. The elliptical cylinder with $\epsilon = 0.40$ is found to maximize $\bar{P}_{peak}$. With respect to the circular cylinder ($\epsilon = 1.00$), it attains a 62.37% increase in $\bar{P}_{peak}$ and a 24.40% increase in power extraction efficiency (η). As compared to the circular cylinder, elliptical cylinders are found to produce significantly more power over a wider range of α. Thus, elliptical cylinders are better suited for VIV-based hydrokinetic energy extraction devices.

The power extraction capability of an elliptical cylinder undergoing two-degree-of-freedom (2-DOF) (passive heaving and pitching) motion is explored with the variation of frequency ratio (f_r) between 0.25 and 3.0. Frequency ratio is defined as the ratio between the natural frequency of oscillation of the heaving and pitching. The ζ for heaving and pitching is kept the same. The aspect ratio is fixed at 0.40. Total power is modeled as the algebraic sum of power dissipated from the damper for heaving and pitching motion. The power contribution from pitching motion is an order of magnitude lower than that from heaving motion. At $f_r = 2.0$ and 3.0, the maximum power from heaving motion shows a drop at mass-damping parameters 0.5 and 0.7, respectively. However, the maximum extracted power and efficiency are three times lower than those of a one-degree-of-freedom (translation) elliptical cylinder at Re = 100. It is also more than twice as low as a circular cylinder. Therefore, this 2-DOF arrangement is not viable for power extraction.

Contents

List of Figures

List of Tables

Nomenclature

Roman Symbols

A^* Non-dimensional vibration amplitude

b Semi-minor axis of the cylinder

c Damping coefficient

C_A Added mass coefficient

C_L Lift coefficient

C_P, C_V Potential and vortex force coefficients

$\hat{u}$ Non-dimensional mesh velocity

D Characteristic dimension

F Fluid force

f Oscillating cylinder frequency

$f_{C_{L_1}}$ Vortex-shedding frequency of the upstream cylinder lift

$f^*_{C_{L_1}}$ Normalized upstream cylinder lift frequency, $f_{C_{L_1}}/f_n$

$f_{C_{L_2}}$ Vortex-shedding frequency of the downstream cylinder lift

$f^*_{C_{L_2}}$ Normalized downstream cylinder lift frequency, $f_{C_{L_2}}/f_n$

$f^*_{C_L}$ Normalized combined lift frequency, f_{C_L}/f_n

f_n Natural frequency of the system

f_r Frequency ratio

f^* Non-dimensional frequency, f/f_n

f_s/f_{C_L} Vortex-shedding frequency of the oscillating cylinder

f_{St} Strouhal frequency / Vortex-shedding frequency of the stationary cylinder

f^*_{St} Normalized downstream cylinder lift frequency, f_{St}/f_n

I Moment of inertia about axis perpendicular to both cross-flow and inline direction

I^* Non-dimensional moment of inertia

k Spring constant

l Span-wise cylinder length / distance from the moving surface

L, T Non-dimensional streamwise and transverse spacing

m Total oscillating mass

m_d Mass of the displaced fluid

$M(t)$ Instantaneous moment

m^* Mass ratio, m/m_d

$\bar{P}$ Average extracted power

p Pressure

$P(t)$ Instantaneous power

Re Reynolds number

t Non-dimensional time

T_e Time period of single oscillation of cylinder

U Freestream velocity

U^* Reduced velocity, U/f_nD

u, v Non-dimensional fluid velocity in x and y direction

y Cylinder displacement in cross flow direction

Greek Symbols

α Mass-damping parameter

χ Power density

δ Kronecker delta

ϵ Aspect ratio

Γ Diffusivity coefficient

γ Mesh deformation coefficient

η Power extraction efficiency

μ Dynamic viscosity

ν Kinematic viscosity

ω Angular velocity

ϕ Phase difference between force and displacement / flow variable

ρ Density of fluid

σ Standard deviation/ root-mean-square of the lift fluctuation

τ Viscous stress

θ Instantaneous rational angle

ζ Damping ratio

Superscripts

n Current time step

Subscripts

1 Upstream cylinder

2 Downstream cylinder

c Critical damping coefficient

d	Downstream distance
f	Skin friction coefficient
g	Gap flow velocity
m	Maximum
n	Natural frequency
p	Pressure coefficient
s/C_L	Vortex-shedding frequency of the oscillating cylinder
St	Strouhal frequency / Vortex-shedding frequency of the stationary cylinder
u	Upstream distance
y	Cross-flow / transverse component

Acronyms / Abbreviations

ALE	Arbitrary Lagrangian-Eulerian
AR	Alternate reattachment
CS	Co-shedding
CR	Continuous reattachment
DOF	Degree of freedom
FIV	Flow-induced vibration
OS	Overshoot
PTC	Passive turbulence control
VIVACE	Vortex induced vibration aquatic clean energy
VIVEC	Vortex induced vibration energy converter
VIV	Vortex-induced vibration
WIV	Wake induced vibration

Chapter 1

Introduction

The discovery of electricity in 1752 marked the beginning of a new era, and the invention of alternating current in 1884 revolutionized its transmission, paving the way for the modern age in which human civilization is powered by electricity. Despite all the technological advancements, we still rely on fossil fuels for a significant part of the global electricity generation. Although we take small steps towards popularizing renewable energy sources, they are still not used as a mainstream electricity generation option. Nuclear energy has promise in the future, but as long as there is no proper, environmentally friendly solution for disposing of nuclear waste, it is far from being the answer to clean energy harvesting. Coal and oil together account for approximately 60.1% of the global primary energy mix in 2019, based on BP Statistical Review data (Looney, 2020), and around 65% of mortality from pollution accounts for fossil fuels (Lelieveld et al., 2019). However, renewable energy contributes only about 5% of total primary energy, although it accounted for nearly 41% of the growth in energy demand, making it the fastest growing energy source. Additionally, air pollution related to fossil fuels has resulted in approximately 100 million deaths over the past 50 years (Sovacool et al., 2016).

Among the renewable energy sources, hydro power contributes 6.4% (Looney, 2020). Traditional turbines and windmills generate steady lift, like airplane wings, and produce high efficiency. However, there are also disadvantages of traditional turbines and wind mills, like high water head, construction cost, safety issues regarding the dam, and environmental hazards such as death of birds due to rotating blades and sound pollution due to high blade speed near the speed of sound (Peng and Zhu, 2009). The number of reported accidents ranged from hundreds to thousands of deaths between 1950 and 2014, with wind power having the highest accident/risk frequency 0.0917 (risk per TWh) (Sovacool et al., 2016). Moreover, traditional hydraulic energy sources require a high water column and can only operate at specific velocities within a narrow range of frequencies. Searching for efficient and clean energy sources leads to Marine Hydro-kinetic Energy (MHK), which is abundant in oceans and rivers. The possibilities and potential of MHK are still unexplored. As the name suggests, it involves extracting energy from waves of the ocean and river currents. A part of this MHK system focuses on extracting energy from bluff bodies. In this context, periodical vortical structures (region of rotating concentric shear layers) influence body motion, allowing its kinetic energy to be harnessed for power generation. Due to the oscillating nature of vortices, pressure around the bluff body changes periodically, creating an oscillating force on the body. This phenomenon is called flow-induced vibration (FIV).

This chapter first introduces types of FIV and their general outline (§ 1.1.1). We then describe FIV of single and multiple circular cylinders (§ 1.1.2). The following section discusses (§ 1.1.3) power extraction from both single and multiple circular geometries, as well as different cross-section bodies undergoing FIV. The literature gaps are then highlighted, and the thesis objectives are summarized (§ 1.3). The chapter concludes with an outline of the remainder of the dissertation (§ 1.4).

1.1 Literature review

1.1.1 Types of FIV

FIV can be categorized into three groups based on the sources of excitation for the body (Naudascher, 2017). They are as follows extraneously-induced excitation (EIE), instability-induced excitation (IIE), and movement-induced excitation (MIE). Both IIE and MIE are self-excited oscillation phenomena; however, MIE represents an instability, whereas IIE does not. Instability, like MIE, should be avoided for power extraction due to unbounded growth of instability with the flow velocity. Large amplitude oscillations due to growing instability is desirable for power extraction; however this occurs at the cost of shorter life of the power-harnessing setup and low power extraction efficiency. Galloping and flutter are examples of MIE. IIE can also exhibits large amplitude oscillations within a narrow frequency band, but these oscillations do not increase with flow velocity (Khalak and Williamson, 1999). However, according to types of motion and their relation with excitation (Rostami and Armandei, 2017), the FIV was

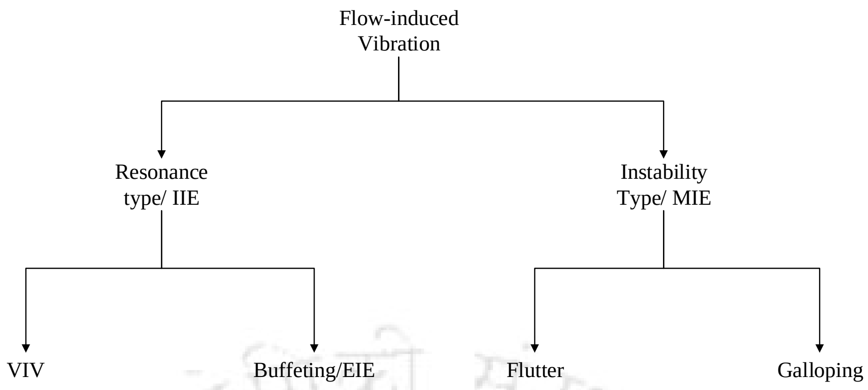

Fig. 1.1 Classification of FIV according to Naudascher (2017) and Rostami and Armandei (2017)

classified into two groups: resonance and instability (Figure 1.1). The resonance type is subdivided into vortex-induced vibration (VIV) and buffeting.

Galloping is a form of flow-induced instability where large oscillation of the body is accompanied by low frequency. It is also a velocity dependent phenomenon and is intrinsic to the structure and primarily observed with non-circular and asymmetric geometry. The fluid force experienced by the body is dependent on angle of attack. If the force increases the vibration, it becomes galloping instability (Blevins, 1977). Also, the galloping would still occur even if the flow is steady. If the body is free to rotate rather than translate, autorotation occurs, i.e., the body would continue to rotate on its own without external actuation (Lugt, 1983). Galloping can be broadly classified into two classes, transverse galloping and torsional galloping (Parkinson, 1971), both of which represent one-degree-of-freedom (1-DOF). On the contrary, flutter is also a type of instability involving coupled transverse and torsional instability. Therefore, flutter is 2-DOF in nature. Flutter is a type of galloping; only in aerospace and civil engineering are the terms "flutter" and "galloping" coined. Flutter is often observed in deformable bodies, whereas galloping typically occurs in rigid bodies, although exceptions exist in systems with coupled degrees of freedom. A classic example of transverse galloping occurs due to icing on electrical transmission lines and on bridge decks. One of the most well-known cases associated with galloping is the failure of the Tacoma Narrows Bridge, which occurred due to large-amplitude torsional oscillations (Scruton, 1970). At the same time, some researchers pointed out that the cause of the collapse is due to aeroelastic flutter (Scanlan and Tomko, 1971). Other example of flutter includes airplane wing flutter (Hodges and Pierce, 2011), turbine blade flutter (Dowell, 2021), and car-hood flutter (Blevins, 1977).

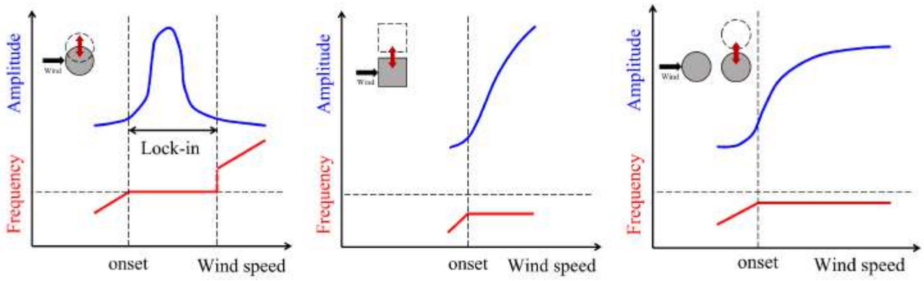

Fig. 1.2 The variation of vibration amplitude and oscillation frequency with fluid velocity for different types of FIV: (from left to right) VIV, galloping and flutter, buffeting (Wu et al., 2022)

Buffeting comes under the resonance type of FIV, as the source of resonance is upstream turbulence or fluctuation in flow velocity or pressure; hence, the vibration is sustained by an extraneous energy source. Upstream turbulence can arise due to meteorological conditions and, when observed in the bridge, produce transverse and torsional vibrations even at low speed (Su et al., 2022). The fluctuation of flow due to upstream bodies can induce buffeting, called wake buffeting (Rostami and Armandei, 2017). The vibration amplitude due to buffeting is typically smaller than that of VIV, but the frequency range is greater than that of VIV (Païdoussis et al., 2010). VIV is also a resonance type of FIV, where the body oscillates due to the fluctuating fluid force. The fluctuating fluid force arises from the fluctuating pressure distribution due to periodic detachment of shear layers on both sides of the body, which creates vortices. The body motion is coupled with the fluctuating fluid force, as the oscillation frequency modulates the vortex-shedding frequency (Sarpkaya, 2004). When the vortex-shedding frequency matches the natural frequency of the body, resonance occurs, a phenomenon known as ‘lock-in’ or ‘synchronization’ (Gabbai and Benaroya, 2005). Lock-in occurs over very constricted range of flow velocity. The vibration amplitude plummets after lock-in. Therefore, VIV represents a self-excited, self-limiting, and highly non-linear phenomenon (Khalak and Williamson, 1999). The comparative figure of oscillation amplitude and vibration frequency variation is shown for different FIV phenomena in Figure 1.2.

1.1.2 FIV of single and multiple cylinders

VIV of single cylinder

At very low Reynolds numbers (Re $<$ 5), the fluid remains attached to the surface of the bluff body, and no flow separation occurs. When the Reynolds number increases to $5 \leq \mathrm{Re} \leq 45$, periodic vortex shedding develops in the wake (Blevins, 1977). With further increase in Re, the boundary layer grows which in turn increases adverse pressure gradient. Beyond a critical Re, the flow cannot overcome the adverse pressure gradient and flow reversal occurs with flow separation. At Re $>$ 100, periodic wakes of vortices with opposite sign are shed behind the body. These staggered vortices create an asymmetric pressure distribution around the body (Techet et al., 2002), which generates periodic forces that induce body motion. The periodic vortices have their own frequency, known as the vortex-shedding frequency (f_s), expressed as StU/D, where St is a non-dimensional parameter, referred to as the Strouhal number and U and D represent the freestream velocity and the characteristic dimension, respectively. The equation of motion of a spring-supported, damped, rigid cylinder constrained to move in the transverse direction is given by,

$$m\ddot{y} + c\dot{y} + ky = F(t) \tag{1.1}$$

where m is the structural mass, c is the damping coefficient, k is the spring constant, and $F(t)$ is the transient fluid force on the cylinder in the cross-flow direction. The damping coefficient can be expressed as $2\zeta\sqrt{km}$, and the damping ratio, $\zeta = c/c_c$; c_c = critical damping coefficient defined as $c_c = 4\pi m f_n$. Here, f_n is the natural frequency of the oscillating system in a vacuum. The non-dimensional oscillation amplitude of the cylinder is denoted by A^* ($A^* = A/D$, where A is the dimensional oscillation amplitude). As VIV works in a feedback system, the vortex-shedding frequency of the oscillating cylinder (f_s) is modulated by the cylinder oscillation frequency (f). In the synchronization regime, f_s synchronizes with f_n. When f matches f_n and consequently f_s, the structure locks in on the frequency, and the oscillation becomes large. This phenomenon is called lock-in. However, synchronization and lock-in are used interchangeably (Sarpkaya, 2004). The maximum amplitude of oscillation (A^*_{max}) of a single circular cylinder in the lock-in regime is a function of the transverse coefficient in-phase with the cylinder velocity ($C_L \sin\phi$), where C_L is the transverse force coefficient, i.e., lift coefficient, ϕ is the phase difference between fluid force and cylinder displacement (Khalak and Williamson, 1999). At high mass ratio ($m^* \gg 1$)

in the lock-in regime, f approaches the vortex-shedding frequency of a stationary cylinder, i.e., $f \approx f_{\mathrm{St}} \approx f_n$, where f_{St} is the vortex-shedding frequency of a stationary cylinder (Bearman, 1984). The reduced velocity, U^* is defined by $U^* = U/f_n D$, also affects the vibration amplitude. In the lock-in regime, the non-dimensional frequency $f^* = f/f_n$ is close to unity. Moreover, at resonance, $U^*/f^* \approx U/fD \approx U/f_{\mathrm{St}}D \approx 1/\mathrm{St}$. Therefore, U^*/f^* and f^* are constant at lock-in. Khalak and Williamson (1999) showed that as the Strouhal number is constant, A^* can be represented as a function of U^*/f^*. For a constant $(m^* + C_A)\zeta$, A^* is unique for a given U^*/f^*. Hence, A^*_{max} at lock-in can be expressed as,

$$A^*_{\mathrm{max}} \propto \frac{C_L \sin\phi}{(m^* + C_A)\,\zeta} \tag{1.2}$$

where C_A is the added mass coefficient (Khalak and Williamson, 1999). Vibration amplitude also depends on f^*. Therefore, all amplitude data should collapse with U^*/f^* even if m^* varies. However, according to the relationship in Equation 1.2, $C_L \sin\phi$ depends on A^*, and Khalak and Williamson (1999) showed f^* is a function of A^* and m^*. Hence, A^* should be a function of m^*. Therefore, A^* does not collapse with U^*/f^* as m^* varies. Sarpkaya (1978) found that m^* and ζ independently influence the dynamic response at low mass-damping, rather than combined mass-damping parameter, $m^*\zeta$. However, Griffin and Ramberg (1982) demonstrated that for $m^* \sim O(1)$, approximately the same value of $m^*\zeta$ for different m^* (34 and 3.8) leads to almost the same A^*_{max}. Contrary to the previous observation, even with constant $m^*\zeta$, low m^* shows a higher amplitude at a wide range of U^* than higher m^* (Khalak and Williamson, 1996). The maximum amplitude also increases with decreasing m^*. Bearman (1984) stated in his study that for small m^*, if $m^*\zeta$ is kept constant, the frequency of oscillation is still affected independently by m^*.

At subcritical mass ratios ($m^* < 1$), Govardhan and Williamson (2002) identified a phenomenon termed Vortex-Induced Vibration Forever (VIVF), where for circular cylinders a critical mass ratio of 0.54 exists, below which large-amplitude vibrations persist even at infinitely high reduced velocity. This occurs because the effective added-mass force generated by the wake dynamics is sufficient to balance the structural inertia over an increasingly wide range of reduced velocities. Han et al. (2023) further showed that damping exerts limited influence on VIVF, with large-amplitude vibrations persisting even under relatively high structural damping.

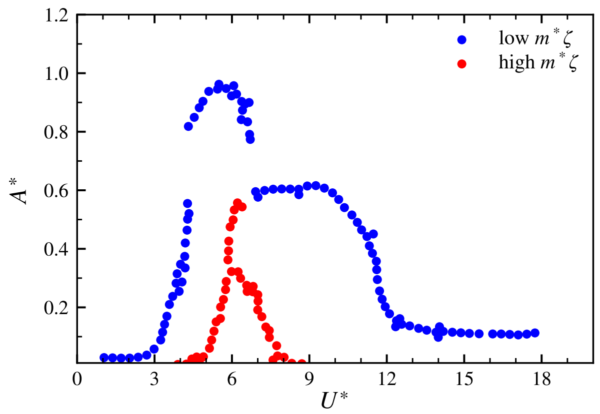

Fig. 1.3 Variation of vibration amplitude with U^* for low $m^*\zeta = 0.013$ (Khalak and Williamson, 1999) and high $m^*\zeta$ (Feng, 1968). Three response branches (initial, upper and lower) are observed at low $m^*\zeta$, while at high $m^*\zeta$, two (initial and lower) are reported.

In Figure 1.3, the high mass ratio data $m^* = 248$ were taken from Feng (1968), while the low mass ratio data $m^* = 10.1$, with $m^*\zeta = 0.013$, were obtained from Khalak and Williamson (1999). At high $m^*\zeta$, as in low-density air, only the initial and lower branches occur (Figure 1.3). However, for low $m^*\zeta$, three response branches appear (additional upper branch). The upper branch is characterized by high A^*. The range of U^* for the upper branch is visible in the range of $U^* = 4.0 - 7.0$. Beyond that, the amplitude drastically reduces in the lower branch. For $U^* > 12$, the body loses synchronization, and the oscillation stops. The maximum oscillation amplitude is approximately equal to the diameter of the cylinder. The lock-in range for high $m^*\zeta$ is much narrower than that for low $m^*\zeta$, which is why most VIV research has been done on water. From the VIV studies in water (Anagnostopoulos and Bearman, 1992; Blackburn and Karniadakis, 1993; Dean et al., 1977; Gharib, 1999; Hover et al., 1998; King, 1975; Moe and Wu, 1990; Newman and Karniadakis, 1996; Pesce and Fujarra, 2000; Sarpkaya, 1995; Shiels et al., 2001; Vickery and Watkins, 1964), they found that at $\mathrm{Re} = 5 \times 10^4 - 1 \times 10^5$, A^*_{max} of a elastically mounted rigid circular cylinder achieve $A^*_{\mathrm{max}} = 1.13$, which is higher than the A^*_{max} reported earlier for a single circular cylinder at low Re. There is also a disparity between experimental and numerical studies. It may be due to the effect of Re on the vibration amplitude. Therefore, not only $m^*\zeta$ but also Re significantly affect the amplitude. There is hysteresis between the two modes (initial and lower) at a high mass ratio. For low mass-damping, there

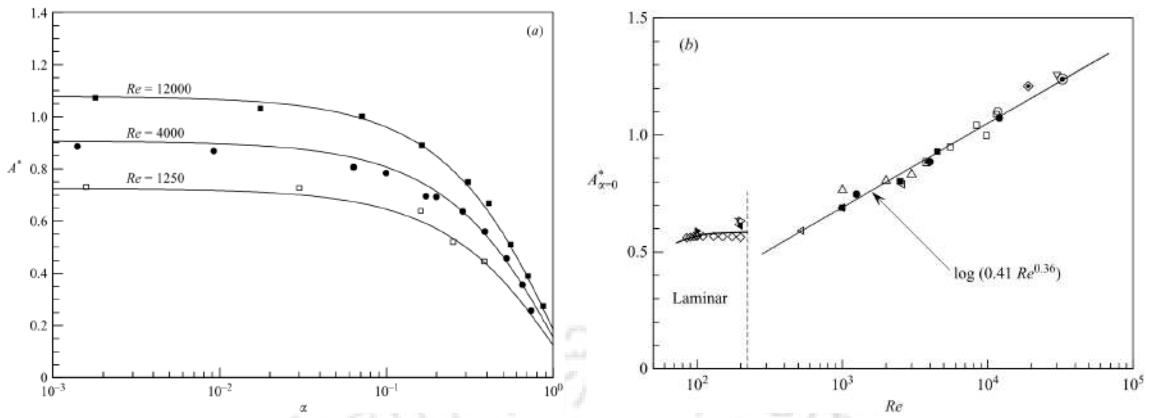

(a) (b)

Fig. 1.4 (a) Variation of $A^*_{\alpha=0}$ with $(m^* + C_A)\zeta$ (b) Variation of $A^*_{\alpha=0}$ with Re. Figure (b) shows a linear relationship with logarithmic Re (Govardhan and Williamson, 2006)

is intermittency and hysteresis between the three modes (initial, upper, and lower). Khalak and Williamson (1999) and Klamo et al. (2006) pointed out the extra response to the fact that at low Re ($90 < \mathrm{Re} < 150$), the upper branch is not observed and is only observed at high Re and low mass-damping. Govardhan and Williamson (2006) stated that this mode shift is due to the change in vortex mode, from 2S (two single opposite sign vortices shed per oscillation cycle) mode at high mass damping, to 2P (two pairs of vortices shed per oscillation cycle) mode at low mass-damping. Lower m^* is achieved by reducing the cylinder diameter and increasing the Reynolds number. For $\mathrm{Re} > 1000$, a trend of increasing amplitude at zero damping is observed as Re increases. In Figure 1.4, the results of A^* with $\alpha = (m^* + C_A)\zeta$ are plotted for Re = 1250, 4000, and 12000 at a constant $m^* = 10$. As damping is increased, the amplitude reduces drastically. Govardhan and Williamson (2006) also tried to devise a relationship between A^* and Re. They kept m^* constant and changed Re. They observed an almost linear relationship of A^* with $\log_{10}\mathrm{Re}$. A wide range of Re data is investigated for experimental and numerical studies. They also found the same linear relationship. For zero mass-damping, the relationship of A^* with Re is formulated as:

$$A^*_{\alpha=0} = \log_{10}(0.41\mathrm{Re}^{0.36}) \tag{1.3}$$

where $\alpha = (m^* + C_A)\zeta$. This relationship holds well for Re = 500–33000. For the laminar region slightly above Re = 200, A^* is quite independent of Re and maintains a range of 0.5–0.6. Vibration amplitude is a function of both α and Re. So, they combined both of the data and defined a new relation as $A^* = f(\mathrm{Re}, \alpha)$.

$$A^* = (1 - 0.96\alpha)\log_{10}\left(0.41\mathrm{Re}^{0.36}\right) \tag{1.4}$$

This relation perfectly exhibits a linear relationship without loss in accuracy and holds good for $\alpha < 0.75$. Soti et al. (2018) define another functional relation that can predict A^* with greater accuracy and expressed as:

$$A^* = \log_{10}(0.402\mathrm{Re}^{0.366})\exp\left(-0.940\alpha - 0.935\alpha^2\right) \tag{1.5}$$

The rise in vibration amplitude when transitioning from initial to upper branch associated with the change in periodic lift force. Moreover, the energy transfer between the fluid and the structure strongly dependent on the phase between the lift force and the structural displacement. Williamson and Roshko (1988) stated that a abrupt change in timing and characteristics of vortex formation is necessary for the change in lift force. The force on the body can be decomposed into two force components: the potential force and the vortex force. This vortex force is generated by the impulse that arises from the rate of change of shed vorticity.

$$F_{vortex}(t) = F_{total}(t) - F_{potential}(t) \tag{1.6}$$

$$F_{potential}(t) = -C_A m_d \ddot{y}(t) \tag{1.7}$$

where, displaced fluid mass $m_d = \pi/4\rho D^2 l$, and C_A is the added mass coefficient, and its value is 1 for a circular cylinder. The equation of vortex force is written as,

$$(m + m_A)\ddot{y} + c\dot{y} + ky = F_{vortex}\sin(\omega t + \phi_{vortex}) \tag{1.8}$$

where, ϕ_{vortex} is the phase between vortex force and displacement. The change in potential part is linked with the oscillation period and the oscillation period is a function of shed vorticity dynamics. Therefore, the lift force is a function of vortex force also. The synchronization characteristics are described in the (λ, A) plane by Williamson and Roshko (1988) in Figure 1.5. The wavelength $\lambda = UT_e$, where T_e is the time period of cylinder oscillation. Therefore, the wavelength ratio, λ/D, essentially represents the reduced velocity. Figure 1.5 shows three vortex patterns, 2S, 2P, and P+S, in the synchronization region. The 2S and 2P modes are symmetric vortex patterns, while the P + S mode is an asymmetric vortex pattern where a single vortex is shed with a pair of vortices at each oscillation cycle. The P+S mode is observed at higher Re (Re = 300–1000), while at low Re, 2P dominates. In Figure 1.5, Curves I and II highlight an abrupt change in the body force corresponding to a shift in the vortex-formation regime, specifically from the 2S to the 2P mode. Below the critical curve, 2S mode is predominant, and beyond the critical curve, the 2P mode emerges. The initial-to-upper branch transition coincides with a shift in the vortex-formation regime from 2S to 2P, accompanied by an abrupt change in vortex phase (Bishop et al., 1964). This transition also exhibits hysteresis and a modification of the vortex-shedding timing.

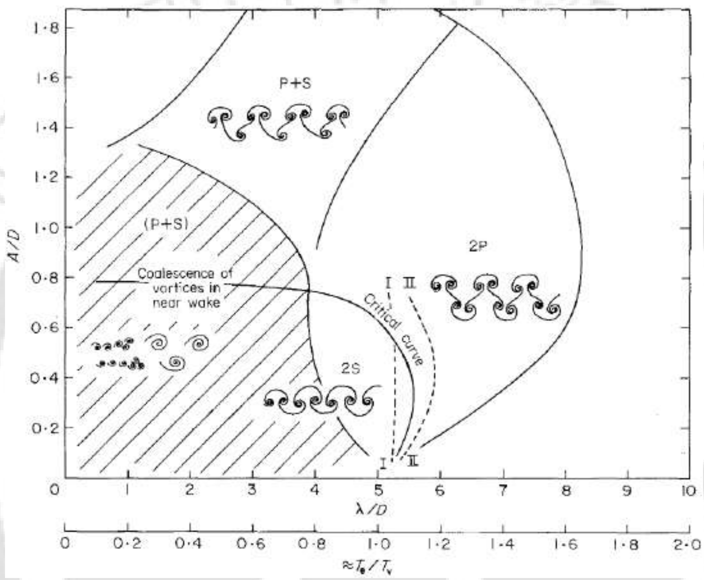

Fig. 1.5 Map of vortex modes in the vicinity of fundamental lock-in (Williamson and Roshko, 1988)[1]. Here A/D is same as A^*

In the lock-in region, the frequency ratio $f^* = f/f_n$ remains close to unity as noticed in Figure 1.6, for moderate m^*=10–20. This relation only applies to high m^*, as at low m^*, f^* is not precisely equal to unity (Khalak and Williamson, 1999). The "added mass" coefficient significantly affects the oscillation frequency, as at large oscillation amplitudes, frequency deviates from unity (Sarpkaya, 1978). From Equation 1.9, it is clear that f^* is a function of "effective added mass" coefficient C_{EA} and C_A. The role of these coefficients strengthens as m^* is reduced.

$$f^* = \sqrt{\frac{m^* + C_A}{m^* + C_{EA}}} \tag{1.9}$$

[1]"Reprinted from Journal of Fluids and Structures, Vol. 2, No. 4, Williamson, C. H. and Roshko, A. (1988), Vortex formation in the wake of an oscillating cylinder, pp. 355–381, Copyright © 1988, with permission from Elsevier."

C_{EA} includes an apparent effect due to the total transverse fluid force in-phase with the body acceleration ($C_y \cos\phi$):

$$C_{EA} = \frac{1}{2\pi^3}\frac{C_y \cos\phi}{A^*}\left(\frac{U^*}{f^*}\right)^2 \tag{1.10}$$

As discussed earlier, at constant $m^*\zeta$, f^* also varies with independent variation of

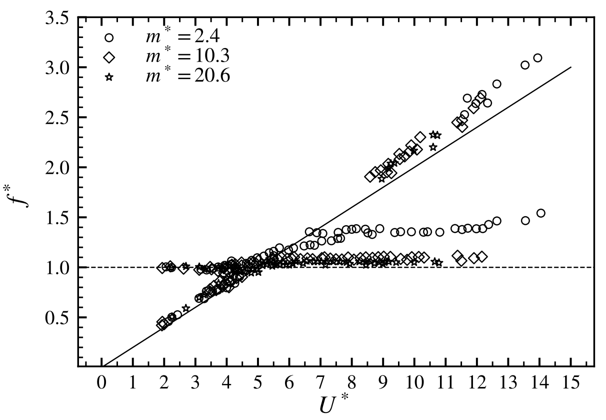

Fig. 1.6 Variation of non-dimensionalized $f^* = f/f_n$ with U^* for different m^* values (Khalak and Williamson, 1999). The dotted line represents $f^* = 1.0$. The solid line indicates the vortex-shedding frequency of a stationary cylinder, when $f = f_{\mathrm{St}}$.

m^*. Therefore, lock-in or synchronization can not be defined as $f_s \approx f_{n_{medium}}$. It also cannot be assumed that $f_s \approx f$ implies synchronization, as the wake mode may involve multiple vortices per oscillation cycle. However, synchronization can be defined as matching the vortex shedding frequency with the body's oscillation frequency. As shown in in Figure 1.8a the transition from the upper to the lower branch is marked by a sudden change in the phase angle, ϕ. The phase is in-phase ($\phi \approx 0°$) in upper branch and out-of-phase ($\phi \approx 180°$) in lower branch. Interestingly, even when the dynamics shift from the initial to upper branch, the phase angle ϕ remains just above $0°$. The initial branch has two sub-branches: periodic and quasi-periodic. Hysteresis occurs during the initial to upper branch transition within the range of $U^* = 4.5 - 4.7$. The oscillation frequency shows discontinuity at initial to upper branch transition (Figure 1.7a) for $m^* = 10.1$, where f crosses $f_{n_{medium}}$. At the quasi-periodic regime, the transient behavior of vibration amplitude is quasi-periodic in nature, and there is intermittent switching of transient ϕ from $0°$ to $360°$; but the average ϕ remains $0°$. In this transition, $\phi = \phi_{vortex}$ as seen from Figure 1.8b. Also, in this regime, $f \approx f_{\mathrm{St}}$. In

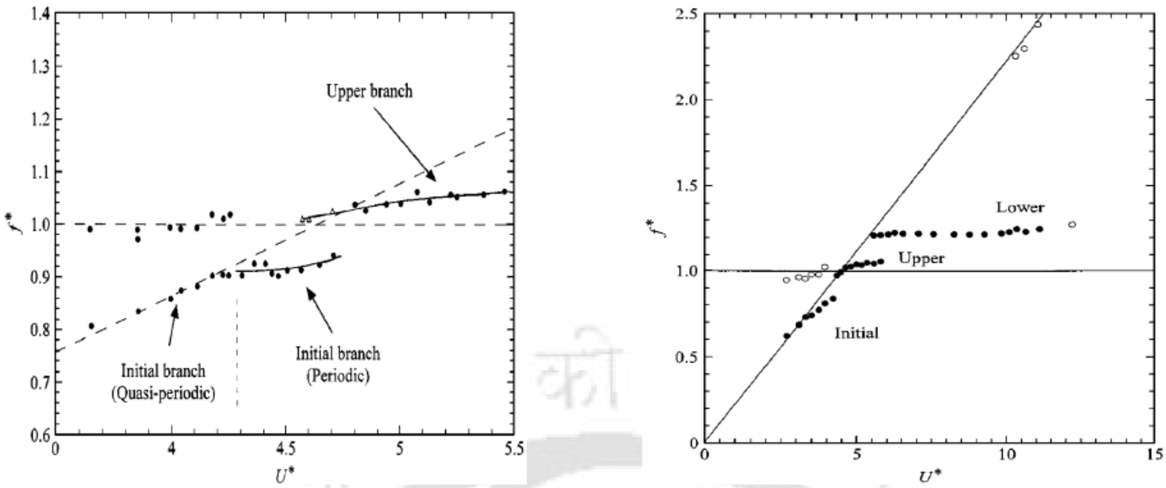

(a) (b)

Fig. 1.7 Initial to upper branch jump shows hysteresis in frequency response. (a) $m^* = 10.1$; $\zeta = 0.0013$ and (b) $m^* = 3.3$, $\zeta = 0.0026$ (Khalak and Williamson, 1999). The diagonal dotted line demonstrates $f = f_{\mathrm{St}}$ while the horizontal line denotes $f^* = 1.0$.

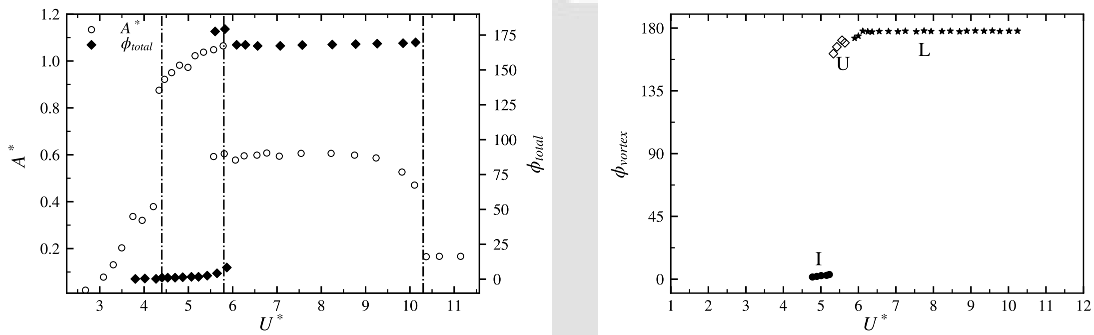

(a) (b)

Fig. 1.8 (a) Variation of A^* and ϕ_{total} with U^* for $m^* = 3.3$ and $\zeta = 0.0013$ (Khalak and Williamson, 1999); (b) variation of ϕ_{vortex} with U^* for $m^* = 8.63$ and $\zeta = 0.00151$ (Govardhan and Williamson, 2000). Here 'I', 'U' and 'L' denotes initial, upper and lower branch, respectively.

the periodic initial branch, f strays away from f_{St} and ϕ remains $0°$. When the upper branch jumps to the lower branch, intermittent switching between the two branches is associated with $\phi = \phi_{total}$ and $f \approx f_n$. There is no change in vortex-shedding timing within this transition.

The three-dimensionality of VIV starts at a different Re than that of a stationary cylinder. For a stationary cylinder, the range is $100 < \mathrm{Re} < 160$. However, for

VIV, three-dimensionality is delayed. As stated by Leontini et al. (2006), the flow is three-dimensional for VIV for Re > 300. Therefore, VIV is purely two-dimensional at Re = 200. At high mass-damping values, the numerically simulated oscillation amplitudes tend to exceed experimental measurements. Blackburn and Karniadakis (1993) attributed this to three-dimensional wake effects in experiments at low amplitudes, which reduce spanwise correlation and overall lift on a finite-length cylinder—an effect absent in two-dimensional (2D) simulations. This observation is supported by Zhao et al. (2014), who conducted numerical simulations over Re = 150–1000. At Re = 1000, stream-wise vortices dominate the wake in the lock-in regime, and three response branches are observed, consistent with experiments. The amplitude and frequency trends match well with experimental data, with the highest amplitude occurring in the upper branch. Among the three branches, three-dimensionality is strongest in the upper branch and weakest in the initial branch. The wake remains two-dimensional at Re = 250, but becomes weakly three-dimensional (3D) at Re = 300 and 350.

Wake-induced vibration

When more than one cylinder is in the picture, like an array of marine risers, the hydrodynamic interference effect of one cylinder in the wake of another cylinder results in a different amplitude response than in the case of a single cylinder. Several researchers have tried different arrangements (i.e., tandem, side-by-side, staggered) of cylinders to use the vortical energy efficiently, either to reduce drag or enhance lift. Zdravkovich (1988) stated that the amplitude response of multiple cylinders, due to interference, mainly depends upon $L = L^*/D$ and $T = T^*/D$, where L and T are non-dimensionalized stream-wise and transverse spacing. The interference also depends upon U^*, Re, and the diameter ratio of the two cylinders. Wake-induced vibration (WIV) differs from single cylinder VIV and the two-stationary-cylinder flow interference phenomenon, as the upstream cylinder is stationary and the downstream cylinder is free to oscillate. King and Johns (1976) experimented with two flexible cylinders with $0.25 < L < 6.0$ and $10^3 < \mathrm{Re} < 2 \times 10^4$. At $L = 0.55$, they found that the upstream cylinder exhibits a VIV response similar to that of a single cylinder, with $A^*_{\max} \approx 0.45$. However, the downstream cylinder's amplitude response increases beyond the synchronization regime, resembling galloping. Zdravkovich and Medeiros (1991) reported in their 2-DOF wind tunnel test that a significantly high value of $m^*\zeta$ is needed to induce WIV for the downstream cylinder. They got $A^*_{\max} = 1.7$ at around $U^* = 80$. Bokaian and Geoola (1984) reported a significant monotonous increase in amplitude response with reduced velocity. Later, Hover and Triantafyllou (2001) and Assi et al. (2006) also experimented with rigid cylinders and observed WIV as shown in Figure 1.9b. They also found a similar amplitude response with reduced velocity at constant Re. However, they reported their results against the reduced velocity measured in vacuum, whereas Bokaian and Geoola (1984) plotted against water, as shown in Figure 1.9a. Sumner et al. (2000) identified nine flow patterns when they varied center-to-center distance P/D from 1.0 to 5.0 and the angle of incidence from 0° to 90°. They observed that the vortex-shedding frequency of the upstream stationary cylinder is higher than that of the downstream moving cylinder at low P/D ratios and incidence angles. It leads to different frequency gap vortices and alignment with individual shear layers. The two shear layers are shed at various times with different frequencies, a key factor in designing staggered cylinder arrangements in FIV. The researchers also found that when the cylinders are farther apart, the downstream cylinder has a negligible effect on the upstream cylinder, which then behaves as a single cylinder in VIV. The hydrodynamic interference is not visible beyond cylinder spacing $2.5D$–$3D$. The effect of the diameter ratio is also an important factor in the WIV response of cylinders in tandem. Lam and To (2003) conducted an experiment on two cylinders in tandem, where the upstream cylinder is fixed and has a diameter twice that of the downstream cylinder, and the downstream cylinder is flexibly mounted. They have observed that for a side-by-side arrangement, the downstream cylinder amplitude is significantly suppressed. For a tandem and near-tandem arrangement, the downstream cylinder is totally or partially shadowed by the upstream cylinder. However, for staggered arrangements, they observed large amplitudes spanning a wide range of reduced velocity. Moreover, for larger tandem spacing, the two cylinders do not act like a single entity; rather, continuous gap flow is observed. A similar type of experiment was carried out by Huera-Huarte and Jiménez-González (2019). Qin et al. (2017) experimented on a different arrangement than Lam and To (2003), as the smaller one is in the upstream, and the diameter ratio is varied between 0.2 and 1.0. The spacing also varies between 1.0 and 5.5. The flow regime is divided into six according to the diameter ratio and L. The response in regime I (diameter ratio 0.9–0.2 and spacing 1.0–5.5) is the most violent. The shear layer reattaches from one side of the upstream cylinder to the other side of the downstream cylinder, causing this violent vibration. In other regimes, little to no vibration is observed.

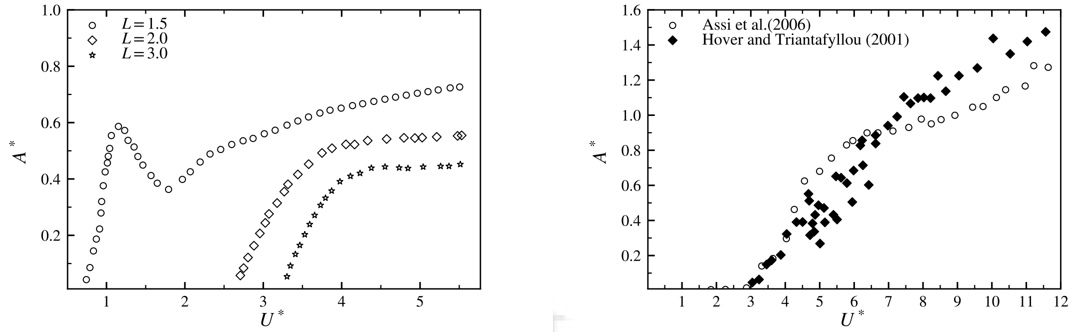

(a) (b)

Fig. 1.9 WIV response: (a) at varying L at $m^* = 8.4$, $\zeta = 0.013$, Re = 700–2000 (Bokaian and Geoola, 1984) (b) at $L = 4.75$, $m^* = 3.0$, $\zeta = 0.04$, Re = 3×10^4 (Hover and Triantafyllou, 2001)[2]; and at $L = 4.0$, $m^* = 1.9$, $\zeta = 0.007$, Re=3000–13000 (Assi et al., 2006)[3]

FIV of multiple cylinders in different arrangement

Different arrangements of multiple cylinders significantly influence interference characteristics, wake structures, vortex dynamics, and vibration amplitude response. Two arrangements have been widely studied: the tandem and the side-by-side arrangements. There is also a staggered arrangement. FIV of tandem arrangement is an extension of WIV, where wake interference not only affects the downstream cylinder but also changes the response of the upstream cylinder. For small L, galloping instability occurs, while at large L, the tandem arrangement exhibits VIV. When spacing increases beyond 2-cylinder diameter, VIV occurs. During galloping instability, the vibration amplitude grows rapidly with flow velocity and then saturates at a critical velocity. Kim et al. (2009) experimented with a flexibly mounted cylinder in a tandem arrangement. They divide the flow characteristics based on cylinder spacing with flow velocity into five regimes (Re = 4365 –74200). In regimes I ($0.1 \leqslant L < 0.2$) and IV ($2.0 \leqslant L < 2.7$), the vibration is suppressed. In regime III ($0.6 \leqslant L < 2.0$) and V ($L \geqslant 2.7$), proximity-wake interference is observed. This regime is characterized by the alternate reattachment

[2]"Reprinted from Journal of Fluids and Structures, Vol. 15, No. 3, Hover, F. and Triantafyllou, M., "Galloping response of a cylinder with upstream wake interference", pp. 503–512, Copyright © 2001, with permission from Elsevier."

[3]"Reprinted from Journal of Fluids and Structures, Vol. 22, Nos. 6–7, Assi, G. R., Meneghini, J. R., Aranha, J. A., Bearman, P. W., and Casaprima, E., "Experimental investigation of flow-induced vibration interference between two circular cylinders", pp. 819–827, Copyright © 2006, with permission from Elsevier."

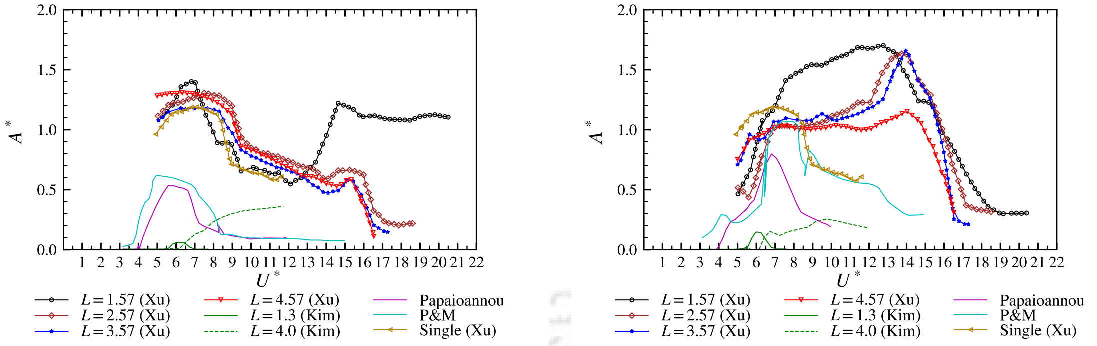

(a) (b)

Fig. 1.10 Variation of A^* with U^* for tandem arrangement for (a) upstream cylinder and (b) downstream cylinder Xu et al. (2019)[4], Kim et al. (2009), Papaioannou et al. (2008), Prasanth and Mittal (2009a) (P&M)

of shear layers shed from the upstream cylinder onto the downstream cylinder and large vibration amplitude for both cylinders. However, in Regime II ($0.2 \leqslant L < 0.6$), divergent vibration of the upstream cylinder is observed as one of the shear layers from the upstream cylinder reattaches, and the other bifurcates into two. It causes unsteady lift in the cylinder. However, Xu et al. (2019) observed galloping response at $L = 1.57$ as the Re ($2.86 \times 10^4 < \text{Re} < 1.14 \times 10^5$, $m^*\zeta = 0.0269$) is higher than that of Kim et al. (2009) (Figure 1.10). VIV exhibits a wider synchronization region for larger gaping ($L > 1.57$), and the response becomes narrower for the upstream cylinder with increasing gaping. However, at larger gap ($L = 2.57$), the upstream cylinder amplitude is identical to that of a single cylinder. In addition, Prasanth and Mittal (2009a); Xu et al. (2019) also showed the higher vibration response of the downstream cylinder compared to that of the upstream and a single cylinder (Figure 1.10). However, the synchronization region for the upstream cylinder starts at a lower U^* than for the single cylinder. Prasanth and Mittal (2009b) demonstrated that not only in tandem but also the staggered arrangements, the flow characteristics of the upstream and downstream cylinders differ. At $L = 1.57$, the results of the upstream cylinder from Xu et al. (2019) (shown in Figure 1.10) fall within the regime II of Kim et al. (2009). For the downstream cylinder, Xu et al. (2019) observed lower amplitude at $L = 4.57$ compared to $L = 1.57$, 2.57, and 3.57, which is consistent with the results of Papaioannou et al. (2008), where a similar reduction was reported at $L = 5.0$ compared to $L = 2.5$ and 3.5. Zhao (2013) observed that at $\text{Re} = 150$, the oscillation amplitude of rigidly coupled cylinders in tandem arrangements increases as the gap between them increases. In side-by-side arrangements, the A^*_{max} is of the same order as that of a single cylinder. However, at Re = 100, in the case of three uncoupled cylinders arranged in a tandem configuration, increasing the spacing up to $L = 5.0$ results in the A^*_{max} of the upstream cylinder becoming comparable to that of an isolated cylinder (Chen et al., 2018). Compared to the upstream cylinder, the downstream cylinders exhibit substantially higher vibration amplitudes. Additionally, T+S wake patterns are observed instead of 2S patterns in the case of rigidly coupled cylinders (Zhao, 2013). Chen et al. (2018) also observed wake-induced galloping at $L = 1.2$. When the spacing is greater than $1.5D$, wake-induced galloping disappears, and VIV appears. Borazjani and Sotiropoulos (2009) numerically investigated the VIV response of two elastically mounted cylinders in tandem at a Re = 200. They found that tandem cylinders exhibit a larger vibration amplitude and a wider range of increased amplitude than an isolated cylinder. At low U^*, the upstream cylinder exhibits higher vibration amplitude than that of the downstream cylinder. However, beyond a threshold U^*, the gap flow excites the downstream cylinder, causing the amplitude to increase several-fold compared to the upstream cylinder. The lift coefficient is also higher in the U^* range, and the lock-in region is wider than a single cylinder. At high Re, Zhao et al. (2016) showed a decrease in vibration amplitude and synchronization region with an increase in side-by-side gaping, whereas the synchronization region gets wider with tandem gaping. Sharma and Bhardwaj (2023) pointed out the lock-in mechanism behind uncoupled and elastically coupled cylinders in tandem. For the uncoupled cylinders, the lock-in in the upper branch is driven by flow coupling with the upstream cylinder, while the gap flow dominates the lower branch lock-in. Meanwhile, the gap flow dominates upper and lower branch lock-in for the coupled cylinder. The coupling between the cylinders balances the energy, the downstream cylinder dissipates to the flow due to the early reattachment of shear layers. Other researchers (Ji et al., 2018), (Zhu et al., 2024), and (Zhu et al., 2025) also confirmed that the oscillation amplitude of downstream cylinders increases with an increase in tandem gaping, and the amplitude of the downstream cylinders is higher than that of the upstream cylinder. FIV can be enhanced by tripping the flow into galloping using a roughness patch, i.e., passive turbulence control (PTC) (Chang et al., 2011). Chang et al. (2011) observed that using PTC on a cylinder increases the synchronization range and decreases the idle

[4]"Reprinted from Ocean Engineering, Vol. 173, Xu, W., Ji, C., Sun, H., Ding, W., and Bernitsas, M. M., "Flow-induced vibration of two elastically mounted tandem cylinders in cross-flow at subcritical Reynolds numbers", pp. 375–387, Copyright © 2019, with permission from Elsevier."

time between VIV and galloping. At high Re ($3 \times 10^4 < \mathrm{Re} < 1.2 \times 10^5$), using PTC, they obtained three times the amplitude in galloping than in VIV. This method is used to enhance the FIV response of multiple cylinders by several researchers (Ding et al., 2013, 2015a; Kim et al., 2013; Sun et al., 2019). Kim et al. (2013) showed enhancement in the amplitude response as PTC trips the flow into galloping. While increasing L, the upstream cylinder amplitude is hardly affected, whereas the downstream cylinder response exhibits a slight dip at $L = 2.5$ and 3.0, followed by an increase beyond $L = 3.5$. With varying T, the upstream cylinder remains unaffected. However, the downstream cylinder response increases with decreasing T in the VIV regime and increases in the galloping regime with increasing T. For three and four cylinders, the downstream cylinder is hardly affected by the upstream cylinder after $L > 2.5$. The amplitude response of the first cylinder is not affected by the other cylinders for any L values. The jump in amplitude smoothens out for the second cylinder as L increases. At higher Re, the response is predominantly galloping for all L. The fourth cylinder's amplitude response curve is similar to the third cylinder's. However, the maximum amplitude is lower than that of the other cylinders. A separate numerical study revealed deviations from experimental results for PTC cylinders (Ding et al., 2013), as the turbulent simulations are assumed to be two-dimensional, and a one-equation model is employed. With the increasing spring stiffness and damping, the amplitude of both cylinders is reduced (Sun et al., 2019). However, with a rising gap, the vibration amplitudes of both cylinders increase, and their amplitudes are higher than that of a single cylinder.

Another arrangement of cylinders is a side-by-side arrangement where cylinders are arranged in cross-flow direction (90° to the flow direction). In tandem arrangements, the flow interference is felt up to $20D$, whereas in side-by-side arrangements, the flow interference region is narrower. For rigid side-by-side cylinders, the flow interference region is only $3D$–$4D$ whereas for flexible cylinders, it is up to $6D$. After that, the response is almost similar to that of a single cylinder. Huera-Huarte and Gharib (2011) reported flow-induced vibration of two cylinders in the side-by-side arrangement, and they found that, irrespective of cylinder gaping, the oscillation amplitude of the upper cylinder is more than that of the lower cylinder. Kim and Alam (2015) investigated the suppression of the vibration in two rigidly coupled cylinders arranged in a side-by-side arrangement. They identified four distinct flow regimes. The U^* varies from 1.5 to 26, and T varies from 0.1 to 3.2. In regime I ($0.1 \leqslant T < 0.2$), the cylinders oscillate as a single body, and the maximum amplitude occurs at much higher U^*. Due to a thin gap flow, one cylinder has a slightly higher amplitude. The gap flow suppresses the oscillation amplitude in regime II ($0.2 \leqslant T \leqslant 0.9$). In regime III ($0.9 < T < 2.1$), the maximum amplitude occurs at a lower U^* for the narrow-wake cylinder and a higher U^* for the wide-wake cylinder. In regime IV ($2.1 \leqslant T \leqslant 3.2$), both cylinders act as isolated cylinders, and their maximum amplitude is the same as that of an isolated cylinder. Munir et al. (2019) numerically simulated the side-by-side arrangement of two cylinders at different T and U^*. They found that the maximum amplitude at $T = 0.5$ is twice that of a single cylinder and has a wider range of vibration. The vibration amplitude is divided into two parts: the lock-in and the sub-harmonic region. They observed that the sub-harmonic component of vibration frequency is in-phase with displacement, much like in Kim and Alam (2015). The vibration amplitude reduces at $T = 1.0$; at $T = 3.0$, the amplitude is similar to that of the isolated cylinder. Chen et al. (2019) also presented similar work. They observed various wake patterns at different T values and identified eight distinct patterns. In their later work, Chen et al. (2020) demonstrated substantial interference between cylinders for $T < 2.3$ accompanied by large vibration amplitudes and lift forces. Beyond $T > 2.3$, the response of both cylinders resembles that of an isolated cylinder. Works on flexible cylinders have been conducted by Xu et al. (2018a), Sanaati and Kato (2014), and Bao et al. (2013). Sanaati and Kato (2014) demonstrated similar vibration amplitude behavior with varying transverse distance, as observed in rigid cylinder cases. They found a different frequency response in the upper cylinder at small separations, distinct from that of the lower cylinder and a single cylinder. Unlike the lower and isolated cylinders, the upper cylinder does not exhibit an upper branch at a smaller transverse separation.

Zhu et al. (2024) numerically investigated three independently moving tandem cylinders at $\mathrm{Re} = 150$ with varying L, and they found a similar response to that of Chen et al. (2018). At small L, due to the shielding effect of the upstream cylinder, the downstream cylinders experience negative drag while the upstream cylinder behaves like an isolated cylinder. However, at high U^*, the downstream cylinder shows higher lift and oscillation amplitude than an isolated cylinder. Moreover, the response amplitude at high U^* decreases with L for the middle cylinder, whereas for the third cylinder, the amplitude decreases up to $L = 3.0$ and then increases again. With the two-degree-of-freedom (2-DOF) study of rigidly coupled tandem cylinders, Zhu et al. (2025) showed that cross-flow (CF) amplitude increases with L, where the peak inline (IL) amplitude is almost constant after $L = 2.5$. The middle and the third cylinders exhibit higher amplitude than the upstream cylinder in a 2-DOF three-cylinder tandem arrangement (Gao et al., 2020). The change in L has little effect on CF amplitudes for middle and third cylinders, while the CF amplitude decreases with an increase in L for the upstream cylinder. Moreover, the 2-DOF CF amplitudes are higher than those of 1-DOF amplitudes irrespective of L. Xu et al. (2020) investigated the effect of the angular position of cylinders of different diameters at a constant center-to-center distance. The smaller cylinder amplifies the large cylinder's amplitude at angular positions of 15° and 30°, irrespective of the upstream–downstream placement. The CF and IL responses of the smaller cylinder also increase when it is placed downstream of the larger cylinder. Gao et al. (2019) showed that four cylinders undergoing 2-DOF FIV in a square arrangement can exhibit higher CF vibration than a single cylinder, especially in the downstream position. Three rigidly coupled cylinders in an equilateral triangular arrangement show that flow incidence angles and U^* have a significant impact on the CF oscillation (Han et al., 2018). For incidence angles 45° to 60°, the synchronization region shrinks, and at 30°, the VIV is suppressed. Although at 0°, galloping is observed for $U^* > 12$. Cylinders arranged in staggered formation but undergoing 2-DOF motion show increased cross-flow oscillation amplitude with increased side-by-side gaping when in proximity-wake interference region (Wang et al., 2025). However, in the wake-interference region, the cross-flow oscillation amplitude remains unchanged with side-by-side gaping and stays close to that of a single cylinder (Gao et al., 2022). Zhang et al. (2023) used an isosceles triangle arrangement to simulate 2-DOF FIV. They found that the CF and IL vibration amplitudes peaked at a lower vertex angle between the cylinders, and the downstream cylinder amplitude was always higher than that of the upstream cylinder. The amplitudes also increase with Re. Chen et al. (2024, 2025) also used three rigidly coupled cylinders in an equilateral triangle arrangement at low Re with 2-DOF. They have varied orientations and gaps between them. At lower gaping, the synchronization regime increases. The CF amplitude still depends on orientation, as some orientations enhance it for all gaps compared to a single cylinder, while others show no influence. The frequency ratio, f_r (ratio between the inline natural frequency and the cross-flow natural frequency) of the 2-DOF arrangement also affects the vibration amplitude. Bao et al. (2012) showed that for a single circular cylinder, with an increase in f_r, peak CF and IL amplitude increase, while the region of significant amplitude remains unchanged. The maximum C_L increases with f_r, peaks, and then decreases. However, for two tandem cylinders in 2-DOF, the upstream cylinder response remains unaffected by a change in f_r, whereas the downstream cylinder is significantly affected by f_r. Moreover, the maximum 2-DOF oscillation amplitudes (CF and IL) are higher than those of a 1-DOF (CF) system. Kang and Jia (2013) showed similar results as those of Bao et al. (2012). However, as $f_r < 1$ throughout their study, the peak IL amplitude decreases with increasing f_r for a cross-flow oscillation frequency of 1.465 Hz. However, for cross-flow oscillation of 1.785 Hz, they observe no change in peak CF amplitude with f_r. The peak oscillation amplitudes of both CF frequencies are lower than the 1-DOF CF amplitude of a single cylinder as $f_r < 1$. Nepali et al. (2020) reported similar observation similar to that of Bao et al. (2012) for two tandem 2-DOF square cylinders with varying f_r. Han et al. (2016) used different definition of frequency ratio as $f_r = f_{n_{medium}}$ and they found significant CF amplitude in the range of $f_r = 0.6 - 1.1$. However, the enhancement is too little. The peak IL amplitude decreases with f_r, while the force coefficients remain the same as those of a single cylinder.

Researchers have also investigated the FIV characteristics of different geometries and found response characteristics, such as amplitude and frequency response, that differ from those of circular cylinders. An asymmetric D-section body shows both galloping and VIV phenomena when the flat section of the D-section is oriented upstream. In contrast, there is no effect in the reversed D-section because of the lack of after-body, which cannot develop oscillating pressure and thus lift on the body (Brooks, 1960). In later years, Zhao et al. (2018) showed in their experimental study that the after-body is not essential for VIV at low mass-damping parameters. The maximum amplitude response associated with D-section is only 6% less than that of a circular cylinder at the same parameters. Thus, there is no need for an after-body for VIV and galloping. A square cylinder undergoing free vibration (cross-flow and inflow direction) can experience both VIV and galloping at low Reynolds number ($60 \leq \mathrm{Re} \leq 250$) and mass ratio of 10 (Sen and Mittal, 2011). Their findings revealed that the maximum amplitude response in the VIV regime was approximately 50% of that of a circular cylinder, and the lock-in exhibited a significantly steeper behavior than that of a circular cylinder. The transition from VIV to galloping is also noticeable for square, trapezoidal, and triangular cylinders. The transition is characterized by low oscillation frequency and high vibration amplitude with increasing flow velocity at high Re. Kumar et al. (2009) studied the influence of the corner radius of the square cylinder and found that the near-wake flow structure is highly dependent on the corner radius. At a higher corner radius, the near wake is found to be uniform. Apart from the square cylinder, a study on a rectangular cylinders of $2 \leqslant 1/\epsilon \leqslant 5$ (where ϵ is defined as the minor axis length to the major axis length) has been done by Zhao et al.

(2019), where the longer side is kept normal to the direction of flow. As ϵ decreases, there is a corresponding increase in the amplitude response within the lock-in regime. Furthermore, both VIV and galloping phenomena occur in this study. In the case of an ellipse, the amplitude response is the main focus in most of the studies. Elliptical cylinders encompass a broad spectrum of geometries, from circular cylinders to flat plates. The elliptic cylinders do not have any sharp edges that can trip the flow into galloping. An elliptic cylinder at free vibration exhibits seven flow regimes (Navrose et al., 2014) at low $60 \leqslant \mathrm{Re} \leqslant 140$ based on time histories of the oscillating elliptical cylinder, force coefficient, and vortex shedding patterns. The initial and lower branches can be further classified into periodic and quasi-periodic. Not all branches may be visible in all aspect ratios (ϵ). When the elliptic cylinder is constrained to move only in the cross-flow direction at Re = 100, Vijay et al. (2020) noticed only two branches, initial and lower. The vortex shedding pattern is 2S throughout all ϵ. The amplitude response is approximately twice at $\epsilon = 0.1$ compared to a circular cylinder with an earlier onset to the initial branch. Kim and Park (2006) studied the effect of angle of attack, ϵ, and Reynolds number on lift and drag forces. They found that the average lift force increases with larger angles of attack (AOA) or reduced cylinder thickness. With the increase in Re, the average drag force decreases, whereas with little effect on the lift force. The variation in lift coefficient is also noticed for the elliptic cylinder when the rotational frequency is varied from St/4 (St, Strouhal number) to 4×St (Alawadhi, 2015). They simulated for $\epsilon = 0.50$ in the range of Re = 50 to 150 at varying angles of attack (AOA) from 10° to 60°. In their study, the lift coefficient initially decreases at a frequency of St = 1, then increases to St = 2, and subsequently decreases at St = 4. However, with an increase in AOA, the lift coefficient increases. The experimental study conducted by Zhao et al. (2019) demonstrated that the lock-in region depends on aspect ratio (ϵ = 0.67–1.5) in the range of $860 \leqslant \mathrm{Re} \leqslant 8050$. At lower ϵ, lock-in spans two amplitude regimes at a range of $4.0 \leqslant U^* \leqslant 12.0$. In contrast, at higher Re, the lock-in spans along three response regimes with increasing amplitude. Therefore, when the major axis of the ellipse is oriented perpendicular to the flow direction, we get an increased amplitude of around 1.05 and 1.56 at ϵ = 1.25 and 1.50. Leontini et al. (2018) showed different flow regimes at $\epsilon = 1.5$ with varying AOA from 0 to $\pi/2$. Four different flow regimes have been observed at different U^* and AOA. The initial branch appeared with negligible amplitude in the narrow region of low U^* with changes in AOA. The 2S mode appears over the entire range of U^*. However, with increasing AOA at higher U^*, the 2S band decreases. They got a P+S type pattern with stronger vortices from the top side. This regime is above 2S with a high AOA. They also obtained a period double regime inside the desynchronized mode, where the primary period of oscillation is twice the natural frequency. Therefore, two cycles of vortex shedding in a single cycle of body oscillation. The time history reveals only a positive lift coefficient and displacement, i.e., the body oscillates only in the positive direction, not about the mean position. This asymmetric oscillation and lift is also seen in the 2S regime when the AOA is high. At AOA = 90°, the P+S mode arises from growing instabilities, with a large vortex on one side and a smaller top vortex that pairs with a counter-rotating lower vortex. Moreover, at this AOA, there is an infinite range of U^*, where a large amplitude occurs. The flow characteristics of a 2-DOF ellipse with transverse and rotational motion (Wang et al., 2019) are different from those of a 2-DOF system with transverse and longitudinal vibration (Sourav et al., 2020). Flow regimes are not significantly different at $\epsilon = 0.40$, 0.50, and 0.66 from the circular cylinder (Wang et al., 2019). They have also found that with the increase in ϵ, the amplitude decreases for 1-DOF transverse vibration. Rotational amplitude for a 2-DOF system also increases with ϵ. In the case of a 2-DOF ellipse with transverse and longitudinal vibrations (Sourav et al., 2020), at a low mass ratio ($m^* = 1$) and zero damping, four additional branches are observed: the extended initial branch, the extended lower branch, the terminal branch, and the quasi-periodic desynchronization branch.

1.1.3 Power extraction from single and multiple cylinders on FIV

Power extraction from VIV has long been a lucrative area of research in harnessing clean energy, as it has a self-limiting amplitude response and a broad synchronization region. Bernitsas et al. (2008) made pioneering contributions to this field. They invented a novel energy converter named VIVACE (Vortex Induced Vibration Aquatic Clean Energy). It extracts energy from the ocean current through the circular cylinder's oscillatory transverse motion and generates electricity through a rotary generator. While traditional water turbines require a high water head and dams, wind energy harvesters require wind velocities greater than 2 m/s. In contrast, the present system can extract energy over a broad range of flow velocities, from 0.257 to 2.57 m/s. This energy converter introduces damping into the system, and optimizing the total damping ratio (ζ_{total}) and structural stiffness (k) maximizes the electrical power output. If the fluid force and cylinder oscillation are modeled in sinusoidal form, the power from VIVACE is expressed as:

$$P_{VIVACE-fluid} = \frac{1}{2}\rho\pi C_L U^2 f A^* D l \sin\phi \tag{1.11}$$

where, ρ is the density of the fluid and l is the length of the cylinder. The mechanical power can be described as the power dissipated by the damper. The mechanical power can be computed by multiplying Equation 1.1 by cylinder velocity ($\dot{y}$) and integrating over an oscillation cycle:

$$P_{VIVACE-mech} = 8\pi^3 (m + m_A)\, \zeta_{total}\, (A^* f)^2\, f_n \tag{1.12}$$

where m_A is the added mass. The mechanical power given by Equation 1.12 represents the total power dissipated through damping, which includes both useful energy extraction and parasitic losses. To distinguish the useful component, the total damping is decomposed into harvesting and loss contributions. The harnessed (useful) power, $P_{VIVACE-harn}$, is associated with the damping component representing the energy conversion mechanism, while the remaining components account for structural, transmission, and generator losses. In this context, ζ_{total} comprises the actual damping ratio (ζ) associated with energy harvesting and the sum of the damping ratios of the structure, transmission, and generator, $\zeta_{total} = \zeta_{har} + \zeta_{sys} + \zeta_{tra} + \zeta_{gen}$. Therefore, the harnessed power is given by the power dissipated through the harvesting-related damping, whereas the remaining damping contributions represent losses. Consequently, the efficiency of this converter is defined as:

$$\eta_{VIVACE} = \frac{P_{VIVACE-harn}}{\frac{1}{2}\rho U^3 D l} \tag{1.13}$$

Bernitsas et al. (2008) got η_{VIVACE} of 0.22 at $U = 0.84$ m/s. They stated that the power extraction device is modular and scalable, as one can obtain enhanced power output by increasing the number of cylinders or size. They proposed several methods to increase power, including changing the diameter of the cylinder to manipulate the Re, introducing roughness to the cylinders to trip the flow into galloping, or introducing upstream turbulence (like buffeting). Besides these, m^* and ζ are key parameters in increasing power and efficiency as C_L and amplitude of oscillation decrease with increasing ζ and increase with lower m^* at high Re. From the discussion of the functional relationship of A^* with Re and α in Equations 1.3, 1.4, and 1.5, we can

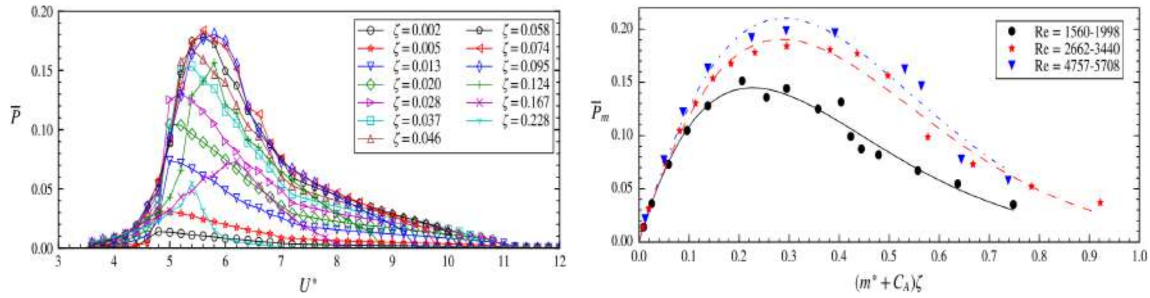

(a) (b)

Fig. 1.11 (a) The average extracted power versus reduced velocity for various values of damping ratios (Soti et al., 2018); (b) The maximum average extracted power versus damping ratio for three Reynolds number ranges (Soti et al., 2018)[5]

extend this relationship to power extraction also. Soti et al. (2018) defined a similar functional relationship with peak average power with peak average amplitude as: $\bar{P}_m = C\alpha {\bar{A}^*}^2$, where C is a constant. In Figure 1.11a, $\bar{P}$ is plotted against U^* at different ζ, and it is observed that an optimal U^* exists for any ζ where $\bar{P}$ is maximum. A similar non-monotonic variation of $\bar{P}$ with varying Re is observed in Figure 1.11b. With an increase in Re as the maximum amplitude increases, maximum power also increases. From the above relationship, at zero mass-damping, the power is zero, and there is negligible cylinder oscillation at high damping. Therefore, $\bar{P}$ attains its maximum for a given mass-damping, corresponding to the optimal damping. Assuming peak amplitude at zero damping follows a logarithmic relation, as Govardhan and Williamson (2006), Soti et al. (2018) defined $\bar{P}_m$ as a function of Re and α:

$$\bar{P}_m = \log_{10}(0.252\mathrm{Re}^{0.538})^2 \alpha \exp\left(-0.2882\alpha - 1.779\alpha^2\right) \tag{1.14}$$

Soti and De (2020) also defined a new relationship based on U^* and α value at which the power is maximum.

$$\bar{P}_m = \frac{4\pi^4}{e} \frac{\left[\log\left(0.41\mathrm{Re}^{0.36}\right)\right]^2}{{U^*_{c0}}^3} \alpha_c \tag{1.15}$$

where, U^*_{c0} is the value of U^* where the amplitude is maximum at zero damping. It is approximated that the value at which power is maximum and amplitude is maximum

[5]"Reprinted from Journal of Fluids and Structures, Vol. 81, Soti, A. K., Zhao, J., Thompson, M. C., Sheridan, J., and Bhardwaj, R., "Damping effects on vortex-induced vibration of a circular cylinder and implications for power extraction", pp. 289–308, Copyright © 2018, with permission from Elsevier."

for U^* is nearly the same. The optimal mass-damping parameter, α_c, corresponds to the value at which the average power reaches its maximum. This result generates a maximum power of 0.44 at Re = 33000, which is very close to the value 0.457 at Re = 60000 obtained by Ding et al. (2015a). Soti and De (2020) demonstrated that with the logarithmic relation between A^* and Re, a linear relation between $\bar{P}$ and η with Re can be possible, as shown in Figure 1.12. Soti et al. (2017) considered both

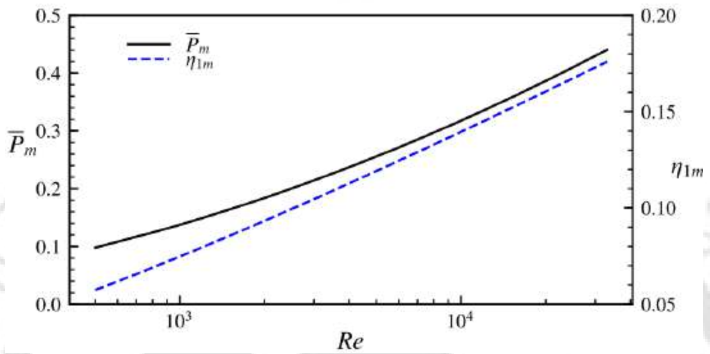

Fig. 1.12 Estimate of the maximum extracted power and efficiency with Re (Soti and De, 2020)[6]

constant damping and non-constant electromagnetic damping cases and found that the maximum average power is independent of the damper used. A maximum of 10%, 13%, and 14% of the flowing fluid power can be extracted at Re = 100, 150, and 200, respectively. Lee and Bernitsas (2011) employed a virtual spring and damper that can simulate a real spring-damper system using a feedback loop. They observed that VIV strongly depends on Re and within the upper branch, the amplitude increases with an increase in Re up to a specific value of Re, then decreases. In their experiment, the stiffness varies from 400 to 1800 N/m and ζ_{har} varies from 0.04 to 0.16. The increased damping decreases the maximum A^*, and the synchronization range becomes narrower as stiffness increases. With increasing stiffness, the power output rises to a specific stiffness. For A^*, the optimum stiffness is 1200 N/m, but it is 1000 N/m for average power. Moreover, the maximum A^* is observed at no damping, while the optimal ζ_{har} for power is observed to be 0.12. Figure 1.13 shows the average power at optimal ζ_{har}. Narendran et al. (2016) developed a new type of VIV energy converter (VIVEC) in the towing tank facility in IIT Madras. The test cylinder has a mass ratio of $m^* = 1.01$ and $m^*\zeta = 0.097$. They have a mean mechanical efficiency of about

[6] "Reprinted from Soti, A. K. and De, A. (2020). Vortex-induced vibrations of a confined circular cylinder for efficient flow power extraction. Physics of Fluids, 32(3). Copyright © (2020), with the permission of AIP Publishing."

25% at a resistance of 80Ω, while the peak mechanical efficiency is around 4 times the mean efficiency. However, they have not figured out how to address the problem of lower electrical and overall efficiency of the linear generator as the load increases. They got 26% of electrical and only 8% of overall efficiency in comparison to 95% and 90% efficiencies in wind and solar power, respectively. The power density ratio of VIVEC is almost equal to that of VIVACE, indicating that they produce high energy with less volume occupied. One way to enhance power extraction from bluff bodies is to trip the flow into galloping. Introducing surface roughness via selective roughness patches influences passive turbulence control (PTC). PTC can induce galloping, and the oscillation amplitude increases. The high amplitude increases the operating region for power extraction at the expense of an instability (Ding et al., 2016). The numerical result of Ding et al. (2016) also shows a discrepancy with the experimental results, as the numerical study uses a simplified linear viscous damper model instead of the complex damping mechanism in the experiment. While the peak power from the experiment is 23.54 W, the peak power from the numerical study is 20.96 W. The efficiency also does not match, which can be attributed to the 2D simulation instead of the 3D simulation. Gu et al. (2020) experimented on the effect of submerged depth on VIV response and found that the impact of submerged depth on power extraction is negligible, as at all depths, the power curve is almost the same. The peak power efficiency is observed at a depth of 0.5 m, as at low depth, the surface undulation decreases the lift force, resulting in a loss of available energy of fluid.

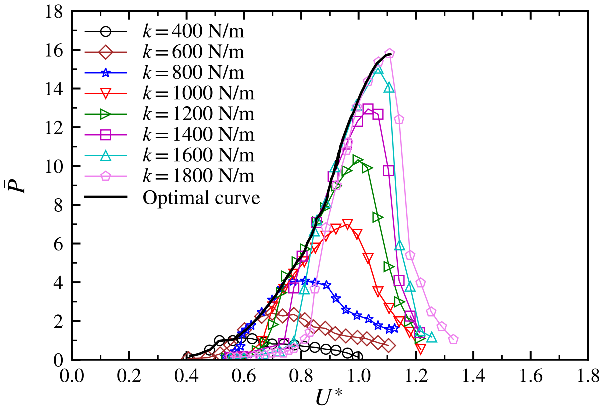

Fig. 1.13 Power signature from converter for single cylinder at $\zeta_{harn} = 0.12$ (Lee and Bernitsas, 2011)[7]

Apart from surface roughness, the shape of the body also affects the power generation. The effect of geometry on FIV characteristics has already been discussed in the earlier section. Ding et al. (2015b) showed the impact of different geometries and PTC on power harvesting. They used a circular with PTC, a square, a quasi-trapezoid, and a triangular cylinder. Quasi-trapezoid has two arrangements: long edge faced to the flow (Q-trapezoid I) and short edge faced to the flow (Q-trapezoid II). In the VIV and galloping regime, Q-trapezoid I attains maximum amplitude at lower Re, while Q-trapezoid II does not vibrate. From the aspect of power conversion, the PTC cylinder and Q-trapezoid I are far better than the square geometry, while the square geometry can not attain high power. However, the efficiency is better in Q-trapezoid I than in the PTC cylinder. Sun et al. (2016) showed the effect of PTC on power conversion for a single circular cylinder at different mass ratios ($1.007 < m^* < 1.685$) and reduced velocity ($2.92 < U^* < 17.73$). Increasing mass ratio enhances power harvesting, resulting in a 69% increase in harvested power at $m^* = 1.685$ compared to $m^* = 1.007$. However, increasing spring stiffness is detrimental for the transition between VIV and galloping. Damping ratio, ζ, is also a important parameter that has significant effect on power harvesting efficiency, and at $\zeta = 0.24$, maximum power harvesting efficiency (42%) is observed at Re $= 5 \times 10^4$. Therefore, without PTC, different geometries can perform better in power extraction. Zhang et al. (2018a) demonstrate that in the VIV regime, optimum damping is $\zeta = 0.8$, while in galloping optimal $\zeta = 0.6$. The optimal ζ for efficiency varies from 0.4 to 0.8 in the VIV, transition, and galloping regions. Moreover, with an increase in m^* for a constant ζ, power output increases (Barrero-Gil et al., 2012). However, the region of significant power output decreases with an increase in m^*. They also noticed that with an increase in ζ at a constant m^*, power output increases to an optimal damping, then decreases. In addition to cylinders with sharp corners and rough surfaces, smooth corners with symmetric shapes, such as ellipses, can also enhance power extraction. Bhattacharya and Shahajhan (2016) numerically simulated flow past an elliptic cylinder at Re = 100 and 200 attached to a torsional spring with $\epsilon = 0.5$. Power extraction is then modeled as the power dissipated by the torsional spring only. They have attached the spring such that the ellipse is making a $\pi/4$ angle with the incoming flow to generate a high unsteady rotational moment. They have varied density ratios from 0.1 to 25.0, which are similar to m^*, and found that power output increases up to a certain density ratio and then decreases for a particular

[7]"Reprinted from Ocean Engineering, Vol. 38, No. 16, Lee, J. H. and Bernitsas, M. M., "High-damping, high-Reynolds VIV tests for energy harnessing using the VIVACE converter", pp. 1697–1712, Copyright © 2011, with permission from Elsevier."

damping coefficient. At Re = 100, power output is highest for a damping coefficient = 400, and decreases for a higher damping coefficient. While at Re = 200, the power output increases with increasing damping coefficient. Pal and Soti (2025) numerically investigated the effect of ϵ and damping ratio (ζ) on power extraction of an elliptical cylinder oscillating in the transverse direction (1-DOF). At Re = 100, a maximum of 16.4% efficiency is reported at $\epsilon = 0.40$. Without using PTC or different-shaped geometry, Wang et al. (2020) used two small rod attachments on a circular cylinder. They noticed that at a 55° position of rods, the power is maximized in the VIV region, and in the transition and galloping regimes, the positions are 60° and 65°, respectively.

Increasing the number of cylinders and changing the spacing between them also changes the power conversion characteristics. Zhang et al. (2017) numerically simulated bluff bodies in tandem arrangement at cylinder spacing from $2D$ to $50D$ and for different cross-sections (Triangular prism, Square prism, Pentagon prism, Circular prism, Cir-Tria prism). For the upstream cylinder, the amplitude response increases with the increase in L; after $L = 5.0$, the amplitude becomes nearly constant (Figure 1.14). Up to $35D$, the effect of the upstream cylinder on the downstream cylinder is not pronounced, and after $35D$, the amplitude of the downstream cylinder tends to that of the upstream cylinder. The power from the upstream cylinder is higher than that of the downstream cylinder, and after $10D$, the power from the upstream cylinder is constant. The power from the downstream cylinder is very low at a small spacing, as the upstream cylinder's wake shadows the downstream cylinder. Beyond $25D$, the power from the downstream cylinder monotonically increases with L. Kim and Bernitsas (2016) experimented with multiple cylinders having PTC, and they obtained a synergistic effect on amplitude response on two, three, and four cylinders. The spacing between cylinders varies in the longitudinal direction from $2D$ to $5D$ and the transverse direction from $0.5D$ to $1.5D$. The Re varies from 28,000 to 120,000, and $m^*\zeta$ from 0.0283 to 0.0346. All experiments were conducted in a low turbulence free surface water (LTFSW) channel. They have studied the synergy of the multiple cylinders on power conversion and power-to-volume ratio. They have calculated the synergy scale by introducing E_{VIVACE_N}, which is the energy converted from the flow by the converter by N number of cylinders. So, the synergy scale, $S_{synergy}$ is defined by,

$$S_{synergy} = \frac{E_{VIVACE_N}}{N \times E_{VIVACE_1}} \tag{1.16}$$

where E_{VIVACE_1} is the converted energy by the single cylinder in isolation. The

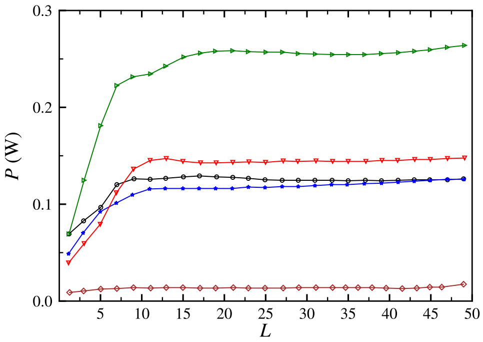

(a)

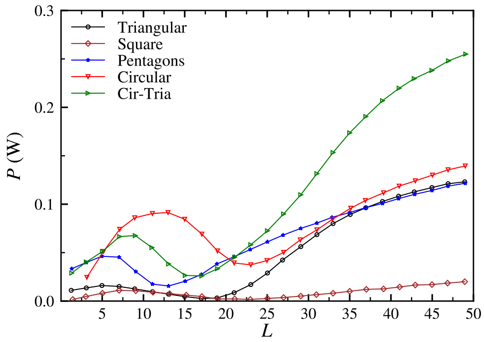

(b)

Fig. 1.14 Variation of converted power P (W) for different cross-section of bluff bodies for (a) Upstream cylinder and (b) Downstream cylinder with the variation of L (Zhang et al., 2017)[8]

experiments are carried out for four cylinders in tandem, with the flow speed varying from 0.51 to 1.30 m/s. It is clear from Figure 1.15 that the converted energy increases with the increasing number of cylinders. For $U < 1.08$ m/s, the converted energy does not depend on the cylinder spacing. Moreover, from Figure 1.15, it is evident that 2, 3, and 4 cylinders have a greater synergy scale than a single cylinder in the range of 0.79 m/s $< U <$ 1.12 m/s. At $U = 1.08$ m/s, the synergy for 3 and 4 cylinders is 1.95 and 1.91, respectively. Therefore, it means that the converted energy from each cylinder for the three and four-cylinder arrangements is almost twice that of the single cylinder in isolation. For the four-cylinder case, the synergy is 1.65 at $2.5D$. Therefore, the cylinders exhibit greater synergy when placed in proximity than when spaced apart. They also reported that the power-to-volume ratio for the four cylinders increases as the spacing decreases. Han et al. (2020) numerically simulated three rigidly coupled cylinders arranged in an equilateral-triangular pattern in VIV at different damping ratios, $\zeta = 0.013$–0.7. They also found similar results to those of Zhang et al. (2017) as the power output and amplitude response are higher when the cylinders are close-spaced. The fully developed galloping response is observed at higher flow velocity for gaping of 0.01 and 0.2. At a gap of 0.5, they found a new branch in

[8]"Reprinted from Energy, Vol. 133, Zhang, B., Song, B., Mao, Z., Tian, W., and Li, B., Numerical investigation on VIV energy harvesting of bluff bodies with different cross sections in tandem arrangement, pp. 723–736, Copyright © 2017, with permission from Elsevier."

[9]"Reprinted from Applied Energy, Vol. 170, Kim, E. S. and Bernitsas, M. M., Performance prediction of horizontal hydrokinetic energy converter using multiple-cylinder synergy in flow induced motion, pp. 92–100, Copyright © 2016, with permission from Elsevier."

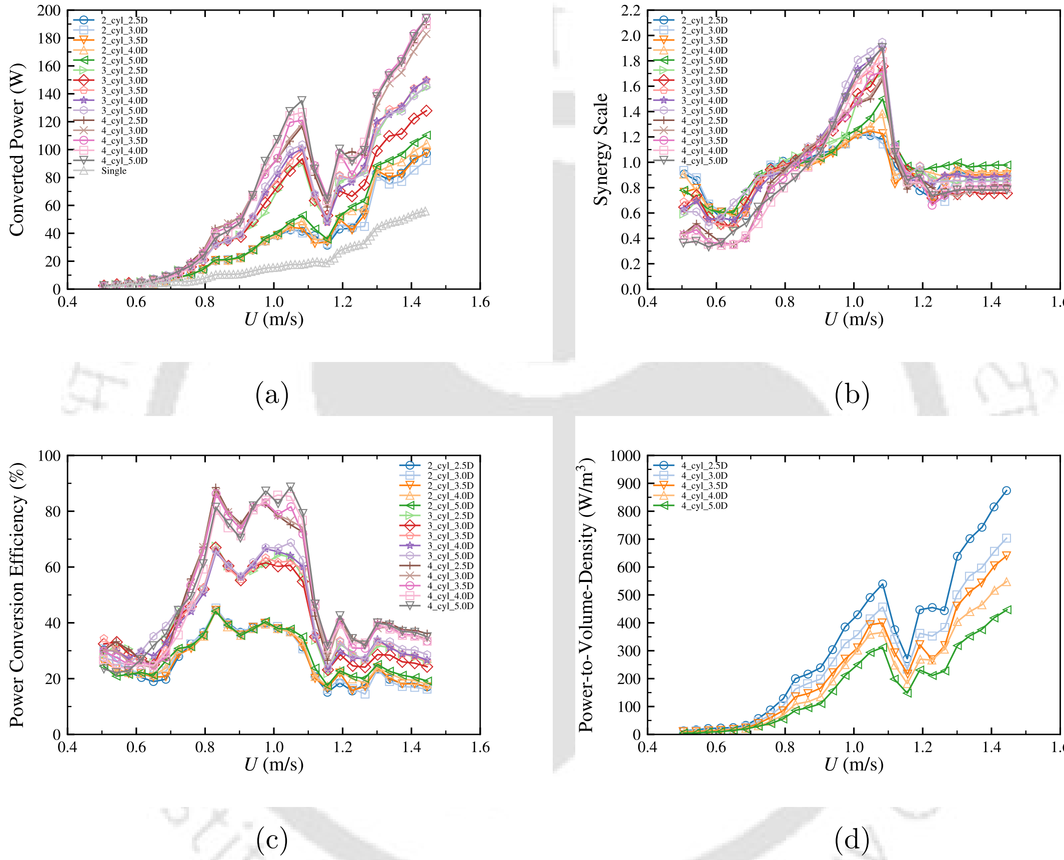

Fig. 1.15 VIV attributes of multiple cylinders: (a) Converted power (W) vs flow velocity, (b) Synergy scale vs flow velocity, (c) Power conversion efficiency (%) vs flow velocity, (d) Converted Power-to-Volume Density (W/m^3) vs flow velocity (Kim and Bernitsas, 2016)[9]

which VIV and galloping can coexist with an amplitude higher than the upper branch response. The power curve shows VIV response at the highest gaping, while at a lower gaping, the power monotonically increases with flow velocity. However, the efficiency is the highest at the highest gaping, with a decreasing trend as the gaping decreases. Sun et al. (2017) observed increased synergy with two rough cylinders (more than two times), and optimal harnessed power decreases as L increases. Moreover, with increasing stiffness, harnessed power increases for both cylinders in VIV and galloping regimes. When the number of cylinders is increased to three, the power converted by the three cylinders exceeds that of two or a single cylinder; however, the efficiency of all cylinders tends to converge at high flow velocities (Ding et al., 2018). In a closed diamond configuration of four cylinders, the power increases as T increases at smaller L values (Zhang et al., 2018b). However, with increasing L, the power curve collapses for all T for all cylinders. Synchronized frequency and phase at small L ($L < 2.0$) leads to synchronized movement of the cylinders, increasing power. At a higher L ($L > 4.0$), the interactions between the cylinders reduce, and the power tends to be that of an isolated cylinder. Xu et al. (2018b) reported more than two times the harvested energy of a single cylinder in VIV and galloping regimes with two cylinders in a staggered formation. They also found an increasing trend of power with the damping ratio. Sun et al. (2020) employed adaptive non-linear damping for tandem cylinders and reported a 46% increase in power output during the transition from VIV to galloping, as well as 35% increase in fully developed galloping region. Additionally, Kim et al. (2021) observed maximum power outputs of 15.85 W and 49.8 W for smooth and PTC cylinders, respectively. Kim and Bernitsas (2016) found that as the number of cylinders and their spacing increase, the synergy also improves, with three cylinders being the optimal configuration for power extraction. However, Li et al. (2021) found that synergy decreases with flow velocity. Li et al. (2024) and Liu et al. (2025) showed that three cylinders in tandem can produce more power than an isolated cylinder. Furthermore, as the gap between the cylinders increases, the efficiency for all uncoupled cylinders in the galloping region also increases (Liu et al., 2025). However, at the lowest gap ($L = 2.0$), the upstream cylinder extracts the most energy, while the second and third cylinders achieve their maximum power output at $L = 4.0$ and $L = 3.0$, respectively.

While modifications in bluff body geometry, implementation of passive turbulence control techniques, and interactions in multiple-cylinder configurations can enhance power extraction, another significant approach lies in actively imposing kinematics on the foil. The study of pitching- and heaving-induced motion—whether prescribed, semi-active, or passively excited by the flow—provides a fundamental understanding of flapping-body dynamics and forms the foundation for energy harvesting using oscillatory motion. Liao et al. (2003) showed how a fish can swim with minimum muscle activity with the help of vortices from an upstream bluff body. They demonstrated that the fish can entrap energy from upcoming vortices from a D-section cylinder. The energy captured by the fish is so impressive that it can outgrow the drag on itself even after a much greater distance from the upstream cylinder (Beal et al., 2006). This oscillatory motion can also entrap energy from uniform flow as reported by Zhu et al. (2002). Oscillatory heaving and pitching motions can be controlled actively, passively, or by combining both approaches. The power extraction from a passively controlled heaving and pitching airfoil is thoroughly investigated by Peng and Zhu (2009). They showed an optimal region of the pivoting point on the airfoil, where they achieved a 20% efficiency. This type of oscillating foil is robust due to the absence of rotating parts and can achieve 50% efficiency (Simpson et al., 2008). Zhu (2012) also demonstrated that in a shear flow, an airfoil with all the mass distributed at the tip of the foil can achieve as much as 30% efficiency. Young et al. (2013) simulated a passively heaving and pitching airfoil at high Re ($Re = 1 \times 10^6$). They modeled power extraction as the angular damper attached to a flywheel that acts as a load. Without control over the angle of attack, they achieved 29.6% efficiency by maintaining a constant pitch angle of 65° during part of the heave. However, with a controlled angle of attack of 40°, a whopping 41.4% efficiency can be achieved. Wang et al. (2017) achieved 32% efficiency at $Re = 400$ with a fully passive flapping foil. They found that the pivot location can affect the amplitude of vibration of heave and pitch. It can also enhance the energy extraction. The pivot location (location of pivot point from the leading edge) of 0.37 gives the highest amplitude for both heave and pitch. At a higher Re ($Re = 1 \times 10^5$), Mumtaz Qadri et al. (2020) reported the same 32% efficiency for a fully passive flapping foil. They observed the effect of pivot location, pitching amplitude, and flow speed on power generation. They used heaving and pitching limiters to achieve a seamless flapping mechanism. They observed an increased power coefficient with increasing pivot location, pitching amplitude, and flow speed. By optimizing the distance between heaving limiters and stream-wise distance between the heaving limiters and the sweep plane of the pivot axis, Zhao et al. (2021) got 47% efficiency. In addition to passive approaches, active heaving and pitching have also garnered significant research interest for their potential in energy extraction. Pioneering work was done by Dumas and

Kinsey (2006), as well as Kinsey and Dumas (2008, 2012), achieving a 40% power extraction efficiency. Subsequently, Dumas's research team focused on semi-passive pitching of an airfoil (Boudreau et al., 2019), where pitching motion is passive while the heaving motion is actively controlled in a sinusoidal manner. Boudreau et al. (2019) varied the static moment—i.e., the location of the pitch axis—from 0 to 0.8, and prescribed the heaving frequency in the range of 0.1 to 0.3, while maintaining a constant Re = 3.9×10^6. The phase lag between heaving and pitching ranges from 90° to 105°, with a maximum efficiency of 45.4% achieved. Active pitching and passive heaving have been numerically investigated by Griffith et al. (2016) at Re = 200 using an elliptical cylinder. They varied the aspect ratio of the cylinder from 0.167 to 1.0 at a fixed pitch amplitude of $\pi/2$. They modeled the power extraction as the energy dissipated by heave motion and achieved a maximum of 20% efficiency at an aspect ratio of 6.0. They also showed an increase in efficiency as ϵ decreases.

1.2 Motivation

Experiments and numerical studies demonstrate that increasing the number of bluff bodies and the shape of the bodies enhances the flow characteristics (vibration amplitude and lift coefficient) and power extraction. Apart from that, many key parameters influence the power generation, i.e., Re, damping ratio, roughness on the body, and multiple degrees of motion. Most of the works are focused primarily on uncoupled cylinders. Despite extensive studies on uncoupled cylinders, the influence of rigid coupling on flow-induced vibration characteristics and power extraction remains insufficiently understood. A rigidly coupled system can suppress the phase mismatch between the cylinders, while uncoupled arrangements are susceptible to out-of-phase oscillations. Moreover, a rigidly coupled arrangement eliminates the need for independent supports and control mechanisms for each cylinder, reducing system complexity while enabling effective VIV response. Therefore, the need to study the flow characteristics of tandem and staggered arrangements undergoing VIV is evident when exploring power harvesting capabilities. This study examines the flow characteristics and power extraction of multiple smooth cylinders undergoing VIV at low Re. Furthermore, the effects of geometric modification and multiple degrees of motion on the altered geometry are also explored. The studies are concentrated at low Re; as discussed earlier, the low Re results can be translated to high Re using oscillation amplitude-Re and power extraction-Re relations. To avoid galloping instability, this research does not include rough cylinders.

1.3 Objectives

The understanding of flow characteristics and power harvesting capabilities from rigidly coupled cylinders in different arrangements undergoing VIV is still lacking. Apart from that, power extraction from any other curvilinear geometry except circular, undergoing VIV, is unexplored. We require a detailed discussion on the flow characteristics and power extraction of rigidly coupled cylinders arranged in tandem and staggered. Also, there are unexplored chapters on power extraction from curvilinear geometry undergoing 1-DOF and 2-DOF motions.

1. To understand the flow characteristics of rigidly coupled cylinders in staggered arrangements at low Re and compare them to the tandem arrangements.
2. To investigate the effect of gap and damping ratio on power extraction from rigidly coupled tandem cylinders at low Re.
3. To investigate the power extraction from rigidly coupled staggered cylinders at low Re with varying gap and damping ratios.
4. To extend the VIV-based power extraction framework developed for circular cylinders to non-axisymmetric bodies by investigating the effect of aspect ratio on a 1-DOF elliptical cylinder.
5. To further examine how the ratio of translational to rotational natural frequencies affects the vibration response and power extraction of a 2-DOF elliptical cylinder undergoing VIV.

1.4 Outline of thesis

This chapter (Chapter 1) offers a comprehensive literature review, highlighting key findings and developments pertinent to the present study. The research gaps have been identified from the review, and the objectives of the thesis are clearly outlined and articulated. This thesis solely deals with numerical investigations to understand the flow characteristics and power extraction from rigidly coupled cylinders in various arrangements, as well as power extraction from 1-DOF and 2-DOF elliptical cylinders. Chapter 2 describes the numerical methodology utilized for the studies. Chapter 3 examines how the gap affects on the flow characteristics of rigidly coupled cylinders arranged in a staggered that undergo VIV at a Re of 150. The findings are compared with the tandem arrangement studies at the same Re. The vibration amplitude, frequency response, and lift characteristics are investigated. Different flow regimes are cataloged for both arrangements at various gaps. Chapters 4 and 5 explore the power harvesting capabilities of previously discussed tandem and staggered arrangements at Re = 150, respectively. The effect of gap and damping ratios on power harvesting is also explored. Optimal dampings for power generation and power extraction efficiency are reported. Moreover, relations between extracted power and mass-damping parameter are established for the respective arrangements. Chapter 6 elucidates the effect of aspect ratio on power extraction from an elliptical cylinder in VIV at low Re. An optimal aspect ratio and damping ratio for power extraction are found. Chapter 7 demonstrates the effect of frequency ratio on power extraction from a 2-DOF (translation and rotation) elliptical cylinder. The optimum frequency ratio is highlighted. The viability of the aforementioned 2-DOF setup, compared to a 1-DOF setup for power extraction, is also investigated. Finally, Chapter 8 concludes the thesis by summarizing key contributions and delineating the scope for future research.

Chapter 2

Formulation and numerical modeling

In the previous chapter, the type of flow-induced vibration (FIV) is discussed with particular attention to vortex-induced vibration (VIV). The effect of various parameters on flow characteristics is discussed with special attention to number of cylinder, their relative arrangements, and geometry of the bluff bodies. The power extraction capabilities from single and multiple cylinder VIV are cataloged along with the effect of various parameters. The effect of the parameters on flow characteristics and power harvesting can be studied using experimental investigation, analytical techniques, numerical simulations or any combination of those previous methods. The analytical procedure needs some parameter values that can be found using experimentation. At low Reynolds numbers (Re), VIV experiments are difficult due to the challenges in generating stable low-Re flows and accurately measuring the small forces and vibration amplitudes involved. These constraints increase uncertainty and experimental complexity. Numerical simulations, however, can reliably impose low-Re conditions and capture the flow–structure dynamics with high resolution. This is the reason numerical simulations are preferred over experimental investigation at low Re.

The VIV phenomenon is governed by fluid-structure interaction (FSI) coupling. FSI coupling has two main approaches:

- Monolithic approach (Ryzhakov et al., 2010) where fluid and solid structure equation are solved in a single and unified systems of equations. The one solver treats both domains as a single domain. It can handle strong coupling and large deformation with greater numerical stability and accuracy. However, the implementation of this approach is rather complex. It also involves high

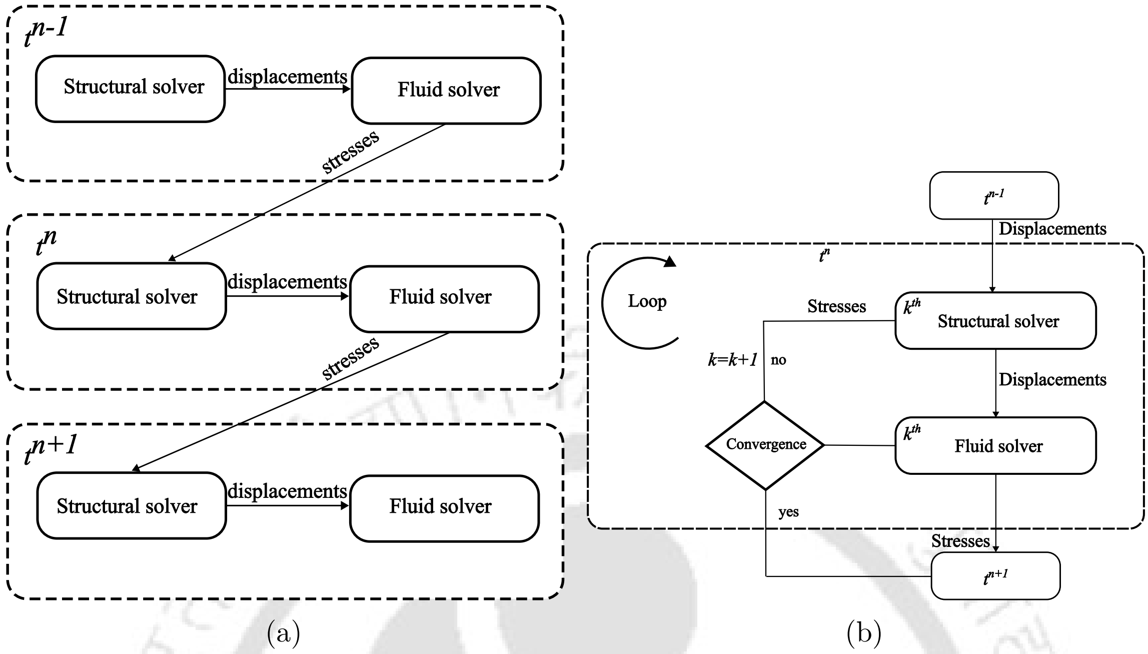

Fig. 2.1 Flowchart of (a) weak and (b) strong coupling

computational cost and has low flexibility to implement in a already available solvers.

- Partitioned or staggered approach (Piperno et al., 1995), where fluid and structure solvers are decoupled. Fluid solver computes flow field to derive pressure and viscous stress on the structure, where structure computes deformation and sends updated geometry and motion of the body to the fluid solver. This process repeats until convergence. It is highly flexible and easier to implement in existing solvers. There partitioned approach has two schemes: a) Explicit partitioned or weak coupling, and b) Implicit partitioned or strong coupling.
  - In weak coupling the solvers exchange data once per time step with no inner iteration to exchange data within the time step. This approach is faster but may suffer instability for large deformation.
  - In strong coupling the solver iterate multiple times within each time step to reach desired interface convergence. Therefore it is more stable and accurate albeit computationally expensive.

The flowchart of a weak and strong coupling are shown in Figure 2.1. The partitioned FSI problems have mainly two parts: Fluid part and Structural part. The fluid part of the problem is solved using unsteady incompressible continuity and Navier-Stokes (NS) for Newtonian fluid flow. The incompressible form is adopted since the flow velocities correspond to low Mach numbers (Ma $\ll 1$), for which density variations are negligible, while the flow regime is characterized by low Re. The equations for continuity and momentum conservation can be expressed as

$$\frac{\partial u_i^*}{\partial x_i^*} = 0 \tag{2.1}$$

$$\frac{\partial(\rho u_i^*)}{\partial t^*} + \frac{\partial}{\partial x_j^*}(\rho u_i^* u_j^*) = -\frac{\partial p^*}{\partial x_i^*} + \frac{\partial}{\partial x_j^*}\left(\tau_{ij}^*\right) \tag{2.2}$$

The velocity (u^*, v^*), time t^*, length (x^*, y^*) and pressure p^* is non-dimensionalized as $(u, v) = (u^*, v^*)/U, t = t^*U/D, (x, y) = (x^*, y^*)/D$ and $p = p^*/\rho U^2$, where * denotes the dimensional parameters, ρ is the fluid density and ν is the kinematic viscosity. Here, $i, j = 1, 2$, and i and j denote the parameters in stream-wise and cross-flow directions, respectively. Hence, $u_1 = u$, $u_2 = v$ and $x_1 = x$, $x_2 = y$. The dimensional viscous stress tensor, τ_{ij}^*, can be written as follows,

$$\tau_{ij}^* = 2\mu S_{ij}^* + \lambda\frac{\partial u_k^*}{\partial x_k^*} = 2\mu S_{ij} - \left(\frac{2\mu}{3}\right)\frac{\partial u_k^*}{\partial x_k^*}\delta_{ij} \tag{2.3}$$

where δ_{ij} is the Kronecker's delta

$$\delta_{ij} = \begin{cases} 0, & i \neq j \\ 1, & i = j \end{cases}$$

From Stokes's hypothesis we implemented second viscosity $\lambda = \frac{2\mu}{3}$ and for incompressible flow the term $\frac{\partial u_k^*}{\partial x_k^*}$ becomes zero from the continuity. S_{ij}^* is the strain-rate tensor, which can be expressed as,

$$S_{ij}^* = \frac{1}{2}\left(\frac{\partial u_i^*}{\partial x_j^*} + \frac{\partial u_j^*}{\partial x_i^*}\right) \tag{2.4}$$

Then the τ_{ij}^* can be written as,

$$\tau_{ij}^* = \mu\left(\frac{\partial u_i^*}{\partial x_j^*} + \frac{\partial u_j^*}{\partial x_i^*}\right) \tag{2.5}$$

The moving boundary is described by ALE (Arbitrary Lagrangian-Eulerian) scheme in which the mesh can move along with the moving body and can track large deformation precisely. In the ALE method, there is the velocity of mesh movement $\hat{u}_j$, which is different from particle velocity u and is greater than zero. So in the NS equation, the convective velocity is modified by $(u_j - \hat{u}_j)$, where $\hat{u}_j$ is the mesh movement velocity in the j-th direction. The non-dimensional ALE formulation of continuity and momentum conservation equation as follows,

$$\frac{\partial u_i}{\partial x_i} = 0 \tag{2.6}$$

$$\frac{\partial u_i}{\partial t} + (u_j - \hat{u}_j)\frac{\partial u_i}{\partial x_j} = -\frac{1}{\rho}\frac{\partial p}{\partial x_i} + \frac{1}{\mathrm{Re}}\frac{\partial}{\partial x_j}\left(\frac{\partial u_i}{\partial x_j} + \frac{\partial u_j}{\partial x_i}\right) \tag{2.7}$$

Where Re is Reynolds number UD/ν. The initial and boundary conditions for velocity, U and pressure, p is given by the following Table 2.1 and 2.2.

Table 2.1 Boundary and Initial conditions of velocity

Domain/Boundaries		Equation
	Boundary Condition	
Top/Bottom	symmetry	$(\partial u/\partial n) = 0$ and $v = 0$
Inlet	fixedValue	$u = u_\infty$
Outlet	zeroGradient	$(\mathbf{n} \cdot \nabla u) = 0$
		$u = 0$
Cylinder	movingWallVelocity	$u = u_{cylinder}$
	Initial Condition	
Inner doamin and Inlet		$u_\infty = (U, 0, 0)$

Table 2.2 Boundary and Initial conditions of pressure

Domain/Boundaries		Equation
	Boundary Condition	
Top/Bottom	zeroGradient	$(\mathbf{n} \cdot \nabla p) = 0$
Inlet	zeroGradient	$(\mathbf{n} \cdot \nabla p) = 0$
Outlet	fixedValue	$p = p_0$
Cylinder	zeroGradient	$(\mathbf{n} \cdot \nabla p) = 0$
	Initial Condition	
Inner doamin and Inlet		$p = p_0$

At the cylinder surface, a zero-gradient boundary condition is imposed for pressure. Although, in principle, the normal pressure gradient at a moving boundary can be expressed as $\mathbf{n} \cdot \nabla p = -\rho \frac{Du_{cylinder}}{Dt}$, where $u_{cylinder}$ is the velocity of the cylinder surface. In the present incompressible formulation, the pressure field is obtained from the solution of the pressure Poisson equation, which is coupled with the momentum equations. The moving wall velocity is prescribed through the velocity boundary condition, and the corresponding pressure field adjusts consistently to satisfy the governing equations. Therefore, the use of a zero-gradient pressure boundary condition at the cylinder surface is appropriate and widely adopted in similar VIV simulations. The simulations are carried out in an open-source CFD tool, OpenFOAM, based on the C++ library. Governing equations are discretized using different schemes, and OpenFOAM reads it through the fvSchemes system directory. For discretization of time derivative Euler scheme is used, which is implicit and first-order accurate can be expressed as,

$$\left.\frac{\partial \phi}{\partial t}\right|_{n} = \frac{\phi^{n} - \phi^{n-1}}{\Delta t} \tag{2.8}$$

where ϕ is the flow variable and Δt represents timestep and n denotes the current timestep. Although higher-order schemes can improve temporal accuracy, the first-order scheme is sufficient for the present study as demonstrated by the temporal independence results (Appendix B). The gradient (∇) and divergence ($\nabla\cdot$) operators are discretized by the Gauss method using linear interpolation. The Laplacian (∇^2) operator is discretized in the same manner using the Gauss method with linear interpolation but with a mixture of corrected (unbounded, second-order, and conservative) and uncorrected (bounded, first-order, and non-conservative) schemes. The gradient (∇) and divergence ($\nabla\cdot$) schemes are second order discretization scheme. The discretized equations are integrated over the volume of the cell but we are replacing the volume integral to surface integral. The surface integral at each face of the element is computed through Gauss quadrature (Moukalled et al., 2016). Here we are using midpoint rule which is second order accurate.

$$\int_{f} \phi \cdot d\mathbf{S} = \int_{f} (\phi \cdot \mathbf{n}) dS = \sum_{ip(f)} (\phi \cdot \mathbf{n}) \omega_{ip} S_f \tag{2.9}$$

where ϕ is the flow variable, $\mathbf{n}$ is the unit normal to the faces and S denotes the area of the surface. For the integration we are using one integration point in each faces which is called the midpoint rule. Thus, $\omega_{ip} = 1$, ip represents number of integration points along the surface f. The convective term can be represented as follows,

$$\int_{V} \nabla \cdot (\rho \mathbf{u} \phi) dV = \int_{S} d\mathbf{S} \cdot (\rho \mathbf{u} \phi) = \sum_{f} \mathbf{S}_f (\rho \mathbf{u} \phi) \tag{2.10}$$

Diffusion term can be represented as

$$\int_V \nabla \cdot (\rho\Gamma_\phi\phi)dV = \int_S d\mathbf{S} \cdot (\rho\Gamma_\phi\phi) = \sum_f \mathbf{S}_f(\rho\Gamma_\phi\phi) \tag{2.11}$$

where Γ_ϕ is the diffusivity coefficient and in the NS equation it represents μ.

The gradient terms are coined by the below expression at the cell-centre P with volume of the cell V_P (Figure 2.2)

$$(\nabla\phi)_P = \frac{1}{V_P}\sum_f \mathbf{S}_f\phi_P \tag{2.12}$$

There is no explicit equation for pressure in incompressible flow that tells us the

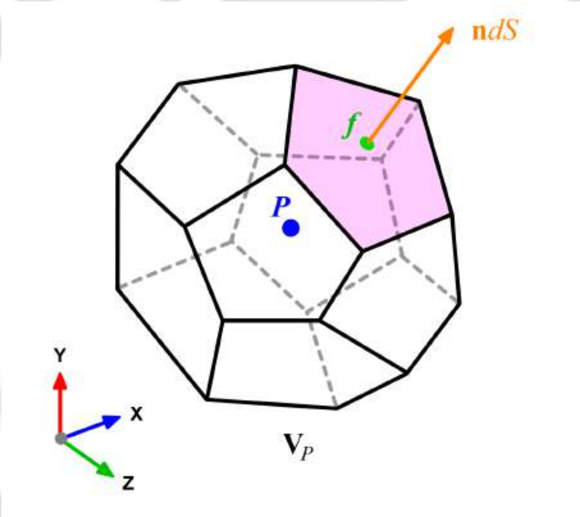

Fig. 2.2 Schematic of a control volume V_P with centroid P and $\mathbf{n}dS$ represents the normal on the face center f of the surface area S. The volume of the finite volume is also denoted as V_P[1]

evolution of pressure over time. Hence, numerical methods for incompressible flow must find a way to couple velocity and pressure while satisfying continuity. In OpenFOAM, several pressure-velocity coupling methods are available. The PIMPLE algorithm is employed in our studies to couple pressure and velocity, as it provides a robust and accurate solution, particularly with the use of a large time step. PIMPLE algorithm is a combination of the PISO (Pressure Implicit with Splitting of Operators) and the

[1]"Adapted from Wolf Dynamics, "OpenFOAM® Introductory Training – 2020 Edition", licensed under Creative Commons Attribution–ShareAlike 4.0 International (CC BY-SA 4.0), available at http://creativecommons.org/licenses/by-sa/4.0/."

SIMPLE (Semi-Implicit Method for Pressure Linked Equations) algorithms. However, unlike PISO, PIMPLE allows us to keep the Courant number (Co) greater than 1. PIMPLE algorithm comprises SIMPLE loops (nOuterCorrectors) and PISO loops (nCorrectors). The PIMPLE algorithm works as shown: At each time step:

1. Set $p^{(0)} = p^n$. Here p^n is the pressure value of previous iteration.

2. For $k = 0$ to (nOuterCorrectors - 1):

2.1. Solve momentum equation or momentum predictor to get provisional velocity $\mathbf{u}^*$ using $p^{(k)}$.

2.2. For $j = 1$ to nCorrectors:

- Solve the pressure correction equation:

$$\nabla^2 p' = \frac{\rho}{\Delta t} \nabla \cdot \mathbf{u}^*.$$

- Update pressure:

$$p^{(k)} \leftarrow p^{(k)} + p'.$$

- Correct velocity:

$$\mathbf{u}^* \leftarrow \mathbf{u}^* - \frac{\Delta t}{\rho} \nabla p'.$$

2.3. Check outer convergence; if converged, break.

3. Set final values:

$$p^{n+1} = p^{(k)}, \qquad \mathbf{u}^{n+1} = \mathbf{u}^*.$$

The algorithmic version of the PIMPLE in OpenFOAM looks like below:

Step 1. Initialization:

- Read and initialize fields: velocity $\mathbf{U}^n$, pressure p^n.
- Set fluid properties (ρ, ν) and time step Δt.
- Specify iterations for:
  - Outer (SIMPLE) loop: nOuterCorrectors
  - Inner (PISO) loop: nCorrectors

Step 2. At each time step ($t^n \rightarrow t^{n+1}$):

- Set initial guesses:

$$p^{(0)} = p^n, \qquad \mathbf{U}^{(0)} = \mathbf{U}^n$$

Step 3. Outer loop: for $k = 1$ to nOuterCorrectors

- **Momentum predictor:** assemble and solve

$$M\mathbf{U}^* = -\nabla p^{(k-1)}$$

- compute $H(\mathbf{U})$ matrix

$$H(\mathbf{U}) = A\mathbf{U} - M\mathbf{U}$$

  where:
  - A is the diagonal coefficient matrix (self-contribution).
  - $H(\mathbf{U})$ contains neighbour and source terms.

  This gives provisional velocity:

$$\mathbf{U}^* = A^{-1}[H(\mathbf{U}) - \nabla p^{(k-1)}]$$

- **Inner loop:** for $j = 1$ to nCorrectors
  - Solve the pressure correction equation:

$$\nabla \cdot (A^{-1}\nabla p') = \frac{\rho}{\Delta t}\nabla \cdot \mathbf{U}^*$$

  - Update pressure:

$$p^{(k)} \leftarrow p^{(k-1)} + p'$$

  - Correct velocity:

$$\mathbf{U}^* \leftarrow \mathbf{U}^* - \frac{\Delta t}{\rho}A^{-1}\nabla p'$$

- Check convergence (pressure and velocity residuals). If converged, exit the outer loop.

Step 4. Update final fields:

$$p^{n+1} = p^{(k)}, \qquad \mathbf{U}^{n+1} = \mathbf{U}^*$$

These fluid-structure interaction problems deal with large deformation of mesh surrounding the moving body. There are two techniques to tackle large deformation in continuum mechanics, namely, mesh deformation and topological change. Topological changes are actually remeshing method which is computationally expensive as in every iteration a mesh-generator need to be called to introduce new connectivity points, faces, and cells. It also attracts the chances of projection and discretization errors (Johnson and Tezduyar, 1994). The mesh deformation is simply movement of mesh points. During motion of the body mesh must remains geometrically valid (preservation of cell and face concavity and non-orthogonality). The finite volume must satisfy space conservation law (SCL) which is a relationship between the rate of change in finite volume V and the boundary surface velocity $\hat{u}$ of surface S.

$$\frac{\partial}{\partial t}\int_V \partial V - \oint_S \mathbf{n}\cdot\hat{\mathbf{u}}\partial S = 0 \tag{2.13}$$

ALE or Arbitrary Lagrangian-Eulerian method is one of the mesh rezoning method to track large deformation. It reduces discretization error similar to a static mesh technique. In Lagrangian approach, the mesh points track the material points, where in Eulerian manner the computational mesh will be fixed and the material points will move. ALE can combine both of the approach where the mesh nodes can move arbitrarily between Lagrangian and Eulerian approach where the mesh nodes neither totally moves with the material point nor is fixed in space. In the ALE method the mesh distortion or velocity can be computed by three methods: i) analytical functions, ii) smoothing of co-ordinates, and iii) smoothing of mesh velocities (Löhner and Yang, 1996). The mesh velocity should satisfy two condition: velocity at the moving surface should be equal to mesh velocity and at a distance away from the body the velocity should be zero. The analytic distance based function should be such that it assumes a value of 1 at the moving surface and decays to 0 as distance from the body increases. The complexity of implementation is the main drawback. Smoothing of co-ordinate involves attaching spring to the mesh nodes, where the forces exerted by the springs are a function of its length and acts along its direction. It suffers drawbacks with initial smoothing and generation of negative element. Moreover, co-ordinate smoothing does not ensure mesh displacements in other co-ordinate direction even if the body is constraint to move in a single direction. In the velocity smoothing method, Laplacian smoothing is used in present study, where gradient of mesh velocity will be larger for smaller elements and it will distort faster than the larger elements. However, this needs for remeshing of small elements close to the moving boundary. Hence, a diffusion coefficient should be introduced that can enforce higher distortion to the larger elements. Our objective is that the smaller elements close to the moving boundaries should translate together with the moving interfaces with the least amount of distortion, and the larger elements in the far field should absorb most of this distortion. To achieve this in OpenFOAM, we solve a Laplacian equation for the mesh displacement (Alletto, 2022). The Laplacian is expressed as $\nabla \cdot (\gamma \nabla d_i) = 0$. d_i is the displacement of the mesh nodes in the i-th direction and γ is a coefficient which constraints the mesh deformation. OpenFOAM uses several types of diffusion coefficient i.e., inversDistance: $\gamma = 1/r$, where r is the distance from the moving surface. Other diffusion coefficients are inverseQuadraticDistance: $\gamma = 1/r^2$, inverseVolume: $\gamma = 1/A_r$, where A_r is the area of an element. For the body motion, the classical mass-damper-spring oscillator model is used. The body is constrained to move in the transverse direction with respect to the incoming flow.

$$m\ddot{y^*} + c\dot{y^*} + ky^* = F(t) \tag{2.14}$$

m is the mass of the structure, c is the damping coefficient of the body, k is structural stiffness, and $F(t)$ denotes unsteady fluid force on the body in the transverse direction of the fluid flow. The above equation can be non-dimensional by non-dimensional parameters as follows:

$$\ddot{y} + \frac{4\pi\zeta}{U^*}\dot{y} + \frac{4\pi^2}{U^{*2}}y = \frac{2}{\pi}\frac{C_L}{m^*} \tag{2.15}$$

where, m^* denotes the non-dimensional mass-ratio as the ratio between the total oscillating mass of the structure (m) and the mass of the displaced fluid (m_d), and ζ is the damping ratio which is defined by the ratio of the damping coefficient and critical damping coefficient. Following the non-dimensionalization mass ratio, $m^* = m/m_d$, and damping ratio, $\zeta = c/c_c$, where $c_c = 4\pi m f_n$ and spring coefficient, $k = 4\pi^2 f_n^2 m$. Lift coefficient, C_L, is defined by $2F(t)/\rho U^2 D$, with ρ denoting the fluid density. The damping ratio can also be given as $\zeta = c/(2\sqrt{km})$. The reduced velocity (U^*) is defined as the ratio between freestream flow velocity and characteristic speed of the structure, defined as the product of natural frequency, f_n in vacuum, and cylinder diameter D, $U^* = U/f_n D$. We move the body with some initial guess of displacement and velocity in a single iteration. We solve the incompressible NS equation with this initial guess to get the pressure and viscous forces. Then the fluid forces are fed into the oscillator model to find the new position and velocities of the body. If the relative error between the new and previous position and velocity of all the cells is less than

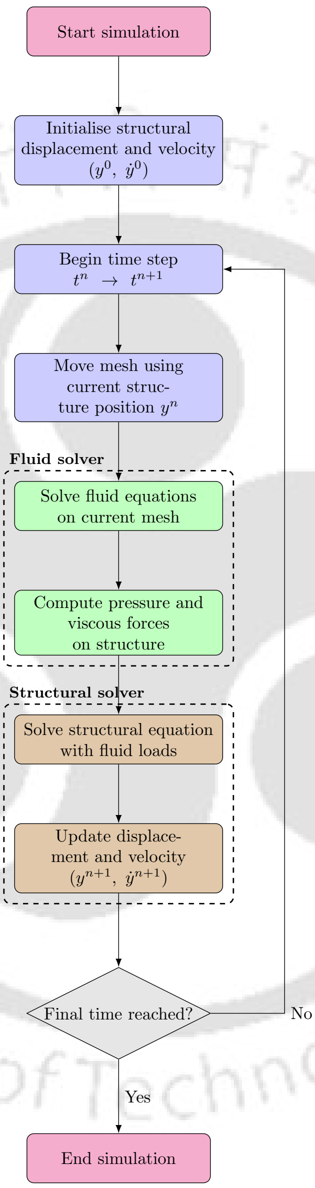

Fig. 2.3 Flowchart of the fluid-structure interaction solver in OpenFOAM

the convergence criteria, then the solver moves to the next timestep. The flowchart of the fluid-structure interaction solver is provided in the Figure 2.3. The Newmark-β method is used for temporal integration of structural response (Bathe, 2014). It uses an extended mean-value theorem for interpolation. According to this method, the velocity at the current time-step is written as

$$\dot{y}^{n+1} = \dot{y}^{n} + \Delta t \ddot{y}^{\alpha} \tag{2.16}$$

Where $\ddot{y}^{\alpha}$ can be written as

$$\ddot{y}^{\alpha} = (1-\alpha)\ddot{y}^{n} + \alpha \ddot{y}^{n+1} \tag{2.17}$$

Combining above two equation we get,

$$\dot{y}^{n+1} = \dot{y}^{n} + (1-\alpha)\Delta t \ddot{y}^{n} + \alpha \Delta t \ddot{y}^{n+1} \tag{2.18}$$

Using the same interpolation for displacement we get,

$$y^{n+1} = y^{n} + \Delta t \dot{y}^{n} + \frac{1}{2}\Delta t^{2} \ddot{y}^{\beta} \tag{2.19}$$

Where

$$\ddot{y}^{\beta} = (1-2\beta)\ddot{y}^{n} + 2\beta \ddot{y}^{n+1} \tag{2.20}$$

Combining above two equation becomes

$$y^{n+1} = y^{n} + \Delta t \dot{y}^{n} + \Delta t^{2}[(1/2-\beta)\ddot{y}^{n} + \beta \ddot{y}^{n}] \tag{2.21}$$

Combining equation for velocity and displacement, the final form will be

$$\ddot{y}^{n+1} = \frac{1}{\beta \Delta t^{2}}\left(y^{n+1} - y^{n} - \Delta t \dot{y}^{n}\right) - \frac{\left(\frac{1}{2}-\beta\right)}{\beta}\ddot{y}^{n} \tag{2.22}$$

$$\dot{y}^{n+1} = \dot{y}^{n} + \Delta t\left(1 - \frac{\alpha}{2\beta}\right)\ddot{y}^{n} + \frac{\alpha}{\beta \Delta t}\left(y^{n+1} - y^{n} - \Delta t \dot{y}^{n}\right) \tag{2.23}$$

The motion of the body at time $n+1$ can be expressed as,

$$m\ddot{y}^{n+1} + c\dot{y}^{n+1} + ky^{n+1} = F(t)^{n+1} \tag{2.24}$$

Unknown $\ddot{y}^{n+1}$ and $\dot{y}^{n+1}$ is solved using known quantities such as $\ddot{y}^n$, $\dot{y}^n$ and y^n. We write the above equation

$$[K] \cdot u^{n+1} = [F] \tag{2.25}$$

Where $[K] = k + \frac{1}{\beta \Delta t^2} m + \frac{\alpha}{\beta \Delta t} c$ and $[F] = F(t)^{n+1} + [\frac{1}{\beta \Delta t^2} y^n + \frac{1}{\beta \Delta t} \dot{y}^n + (\frac{1}{2\beta} - 1)\ddot{y}^n]m + [\frac{\alpha}{\beta \Delta t} y^n + (\frac{\alpha}{\beta} - 1)\dot{y}^n + (\frac{\alpha}{2\beta} - 1)\Delta t \ddot{y}^n]c$. In our case, the Newmark-β scheme is used with default parameters ($\alpha = 0.5$, $\beta = 0.25$), which is equivalent to the Crank–Nicolson scheme with default off-centering coefficients in OpenFOAM. Therefore, no difference is expected between these two schemes under the default parameter choices (Bathe, 2014; Hughes J R, 1987). The symplectic scheme, being an explicit energy-conserving method (Hairer, 2006), is primarily suited for conservative systems, whereas the present problem involves dissipative fluid–structure interaction. Furthermore, the temporal independence study (Appendix B) ensures adequate resolution of the dynamics. Hence, the solution is not expected to be significantly sensitive to the choice of time integration scheme. Moreover, Newmark-β scheme is successfully implemented in oscillatory system in several studies (Han et al., 2018; Teixeira and Awruch, 2005; Zhang et al., 2017).

Chapter 3

Vortex-induced vibration of two rigidly coupled cylinders in staggered arrangement at low Re

Flow characteristics of vortex-induced vibration (VIV) of rigidly coupled cylinder is different than the uncoupled cylinders. The mechanical linkage between the cylinders govern the phase between the cylinders not by the fluid forcing only. The distance between the cylinders and their relative arrangement have profound impact on the flow characteristics. The chapter begins by a short literature review on the effect of number of cylinder and their spacing between them on the flow characteristics followed by the motivation of this study (§ 3.1). Next, the numerical setup used for this study is described (§ 3.2). The mesh independence study and the numerical validation is outlined in the following section (§ 3.3). The mesh independent and validated framework is used to study the flow characteristics of rigidly coupled cylinders in staggered arrangement (§ 3.4). The staggered results of vibration amplitude, frequency response, lift coefficient, phase difference and wake characteristics are compared to that of the tandem results. The chapter then concludes with a summary of the results and identify the parameters influencing vibration amplitude and lift coefficient (§ 3.5).

3.1 Introduction

The flow-induced vibration of multiple bluff bodies is strongly influenced by their relative arrangement and spacing. Previous studies have shown that tandem and staggered configurations can significantly modify wake interactions and vibration response (Borazjani and Sotiropoulos, 2009; Chen et al., 2018; Zhao et al., 2016). However, most of these investigations have focused on uncoupled cylinders. Only a limited number of studies have addressed rigidly coupled configurations, particularly in tandem and staggered arrangements (Zhao, 2013).

Motivated by this gap, this study aims to compare the flow characteristics of rigidly coupled undamped staggered cylinders with those of coupled tandem cylinders. In the staggered configurations, the spacing in the tandem direction varies from $L =$ 2.0 to 4.0, while the spacing in the side-by-side direction ranges from $T = 2.0$ to 4.0. The cylinders can only move in the transverse direction to the flow, resulting in a one-degree-of-freedom (1-DOF) system. The reduced velocity (U^*) is varied in the range of 3.0–15.0 at Re = 150. The mass ratio, $m^* = 2.0$, is kept constant for all cases.

3.2 Formulation

3.2.1 Numerical setup

This fluid-structure interaction problem is solved using unsteady incompressible Navier-Stokes (NS) for fluid flow coupled with the mass-damper-spring equation for body motion. The details of the numerical formulation is described in Chapter 2. The mass ratio is defined as $m^* = m/m_d$, where m is the structural mass per unit span and $m_d = 2 \times \frac{\pi}{4}\rho D^2$ is the mass of the displaced fluid per unit span.

3.2.2 Problem definition

Figures 3.1 and 3.2 show the schematic of the rectangular numerical domain of the tandem and staggered arrangement, respectively. The present 1-DOF VIV arrangement includes two rigidly coupled cylinders with diameter D with mass m, a spring with stiffness k, and a damper with a damping coefficient c. For tandem arrangement, the upstream boundary is situated at $20D$ from the midpoint of the line joining the two cylinder centers, while the downstream boundary is at $30D$ away from the midpoint. The lateral width of the domain is $40D$. The computational domain is $50D$ in the flow direction and $50D$ in the cross-flow direction for staggered arrangement. In this study, the maximum blockage effect due to side boundaries is 10%, which is within the permissible range (Zhao et al., 2012). The domain boundaries should be located far enough from the bluff body so that its impact on the flow condition at the domain boundaries is negligible. In the present work, the length of the computational domain

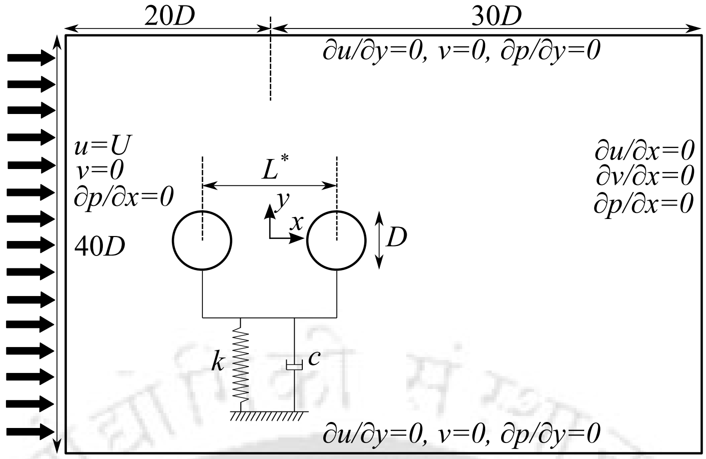

Fig. 3.1 Schematic of computational domain of the vortex-induced vibration of the tandem arrangement of the cylinders.

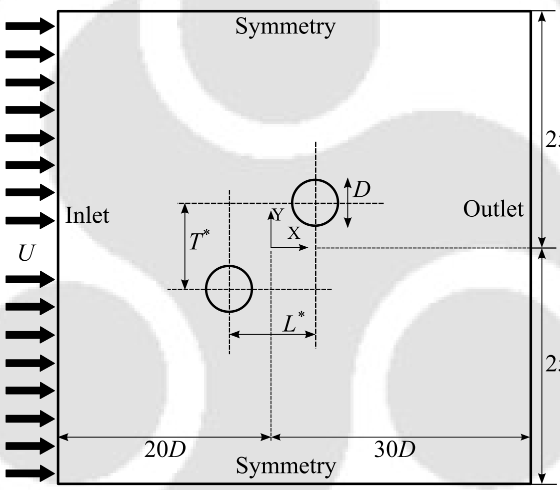

Fig. 3.2 Schematic of computational domain of the vortex-induced vibration of staggered arrangement of the cylinders.

is based the domain size independence study. The domain independence study was performed by systematically varying the upstream (L_u/D) and downstream (L_d/D) distances from the inlet and outlet boundaries, respectively. These distances are measured from the midpoint of the line joining the centers of the two cylinders. The corresponding results of tandem arrangement are summarized in Tables 3.1 and 3.2, where the vibration amplitude (A^*) at $U^* = 7.5$ under zero damping was selected as the reference metric. It can be concluded from the data that values of $L_u/D > 20$ and $L_d/D > 30$ exert no significant influence on the vibration amplitude. Hence, $L_u/D = 20$ and $L_d/D = 30$ are adopted for all subsequent simulations in the tandem cases. The corresponding results of staggered arrangement are summarized in Tables

Table 3.1 Domain independence study of tandem arrangement at $U^* = 7.5$ for $L = 6.0$ under zero damping condition. Effect of the upstream distance from the inlet on the vibration amplitude.

L_u/D	Vibration amplitude (A^*)
20	0.8172
25	0.8207
30	0.8174

Table 3.2 Domain independence study of tandem arrangement at $U^* = 7.5$ for $L = 6.0$ under zero damping condition. Effect of the downstream distance from the outlet on the vibration amplitude.

L_d/D	Vibration amplitude (A^*)
20	0.8165
30	0.8172
40	0.8175

3.3 and 3.4, where the vibration amplitude (A^*) at $U^* = 4.0$ for $L = 2.0, T = 3.0$ under zero damping is selected as the reference metric. It can be concluded from the data that values of $L_u/D > 20$ and $L_d/D > 30$ exert no significant influence on the vibration amplitude. Hence, $L_u/D = 20$ and $L_d/D = 30$ are adopted for all subsequent simulations in the present study for the staggered cases. The mass ratio is kept constant at 2.0. The reduced velocity varies between 3.0 and 15.0 while Re is fixed at 150.

Five boundaries are shown in Figure 3.1. The domain is initialized with uniform velocity U. At the inlet, a uniform fluid velocity of $u = U$, and $v = 0$ is implemented. Symmetry conditions ($\frac{\partial u}{\partial y} = 0$ and $v = 0$) are applied at the top and bottom boundaries. At the outlet, Neumann boundary condition is applied: $\frac{\partial u}{\partial x} = 0$ and $\frac{\partial v}{\partial x} = 0$. The no-slip boundary condition is used at the cylinder wall, i.e., $u = u_{wall}$.

A constant m^* is used, since Govardhan and Williamson (2006) showed that, for a given Reynolds number, the peak vibration amplitude for a circular cylinder is

Table 3.3 Domain independence study at $U^* = 4.0$ for $L = 2.0, T = 3.0$ under zero damping condition. Effect of the upstream distance from the inlet on the vibration amplitude.

L_u/D	Vibration amplitude (A^*)
20	0.572363
25	0.574779
30	0.578755

Table 3.4 Domain independence study at $U^* = 4.0$ for $L = 2.0, T = 3.0$ under zero damping condition. Effect of the downstream distance from the outlet on the vibration amplitude.

L_d/D	Vibration amplitude (A^*)
20	0.571614
30	0.572363
40	0.573568

Table 3.5 Mesh independence study at $U^* = 7.5$ for $L = 6.0$ under zero damping condition

No. of mesh elements (N)	$\Delta x_{\min}$	**Vibration amplitude (A^*)**	**Error in $A^*(\%)$**	**CPU Time (s)**
16726	0.06	0.671	19.916	204
27403	0.04	0.797	4.905	303
76769	**0.02**	**0.817**	**3.667**	**1071**
124969	0.015	0.821	2.016	2214
289139	0.01	0.838	0	6698

independent of m^* when the combined mass–damping parameter $\alpha = (m^* + C_A)\zeta$ is held constant (for mass ratios down to $m^* = 1$). Therefore, m^* and ζ need not be considered independently, and α alone is sufficient to characterize the peak response. All simulations are two-dimensional and are carried out at Re = 150, as three-dimensional instabilities in the cylinder wake do not develop until Re $\approx$ 190 (Mode A instability), as established by Carmo et al. (2008); Leontini et al. (2007). Govardhan and Williamson (2006) also showed that the Re dependency of the amplitude collapses onto an exponential fit. This fit extends from laminar to high Re regime and follows a linear relationship with $\log_{10}$ Re. It was further confirmed by Soti et al. (2018). Therefore, the trend of parameters in low Re simulation is also applicable to high Re simulation.

3.3 Validation

3.3.1 Mesh Independence and Validation

The mesh for the computational domain is generated using a combination of structured and unstructured grids. The mesh independence study was performed by refining the mesh near the cylinder in the radial direction. The minimum mesh size $\Delta x_{\min}$, is varied

Table 3.6 Mesh independence data at $U^* = 4.0$ for $L = 2.0, T = 3.0$ under zero damping condition

No. of mesh elements (N)	$\boldsymbol{\Delta x_{\min}}$	**Vibration amplitude ($\boldsymbol{A^*}$)**	**Error in** $A^*(\%)$
22053	0.03	0.572455	1.054
38220	**0.02**	**0.572363**	**1.038**
60531	0.015	0.565765	0.126
123947	0.010	0.566479	0

with values of 0.06, 0.04, 0.02, 0.015, and 0.01 for the tandem cases. The amplitude data corresponding to $L = 6.0$, $U^* = 7.5$, and $\zeta = 0$ is used as the reference for the mesh independence study shown in Table 3.5. The variation of amplitude from $\Delta x_{\min} = 0.04$ to 0.02 is 1.28% and from $\Delta x_{\min} = 0.02$ to 0.015 is 1.68%. As the change in A^* remains below 2%, the mesh with $\Delta x_{\min} = 0.02$ is deemed adequate for numerical calculations. The minimum mesh size $\Delta x_{\min}$ for the staggered cases is varied as 0.03, 0.02, 0.015, and 0.010 as shown in Table 3.6. The non-dimensional oscillation amplitude (A^*) at $U^* = 4.0$ and $\zeta = 0$ is taken as test data. The number of elements (N) for those $\Delta x_{\min}$ are 22053, 38220, 60531, and 123947, respectively. The amplitude varies by 0.003% when the minimum mesh size ($\Delta x_{\min}$) changes from 0.03 to 0.02, and by 0.394% when it reduces from 0.02 to 0.015. With a variation in A^* around 1%, the mesh resolution $\Delta x_{\min} = 0.02$ is sufficient to ensure mesh independence. To provide a more rigorous assessment of mesh convergence, Richardson extrapolation (RE) was applied using the two finest mesh resolutions. For the tandem case (Table 3.5), the extrapolated peak amplitude is $A^*_{RE} = 0.852$, yielding a Grid Convergence Index (GCI) of approximately 3.2% for the selected mesh ($\Delta x_{\min} = 0.02$) (Celik et al., 2008). For the staggered case (Table 3.6), the extrapolated value is $A^*_{RE} = 0.567$, with the selected mesh deviating by less than 1% from this value. These results confirm that the chosen mesh resolution provides adequate accuracy for the present simulations. The close-up view of the computational mesh around the cylinder for a representative tandem and staggered case are shown in Appendix A. The present numerical framework was validated by comparing the amplitude response of a single-degree-of-freedom cylinder with the results reported by Zhao (2013). Figure 3.3 shows the variation of the non-dimensional vibration amplitude (A^*) with reduced velocity (U^*) for several spacing ratios ($L = 2.0$, 4.0, and 6.0) at $\zeta = 0$. The present results closely follow the numerical data of Zhao (2013), accurately capturing both the lock-in region and the maximum response, which occurs around $U^* \approx 5.0$. The amplitude decays beyond the synchronization range in good agreement with the reference data, indicating that the present numerical methodology can reliably reproduce the dynamic response of the cylinder under VIV. The temporal independence study for tandem and staggered arrangement is represented in Appendix B. From the temporal independence study, time step size of $\Delta t = 0.002$ and $\Delta t = 0.008$ is adopted for tandem and staggered cases, respectively.

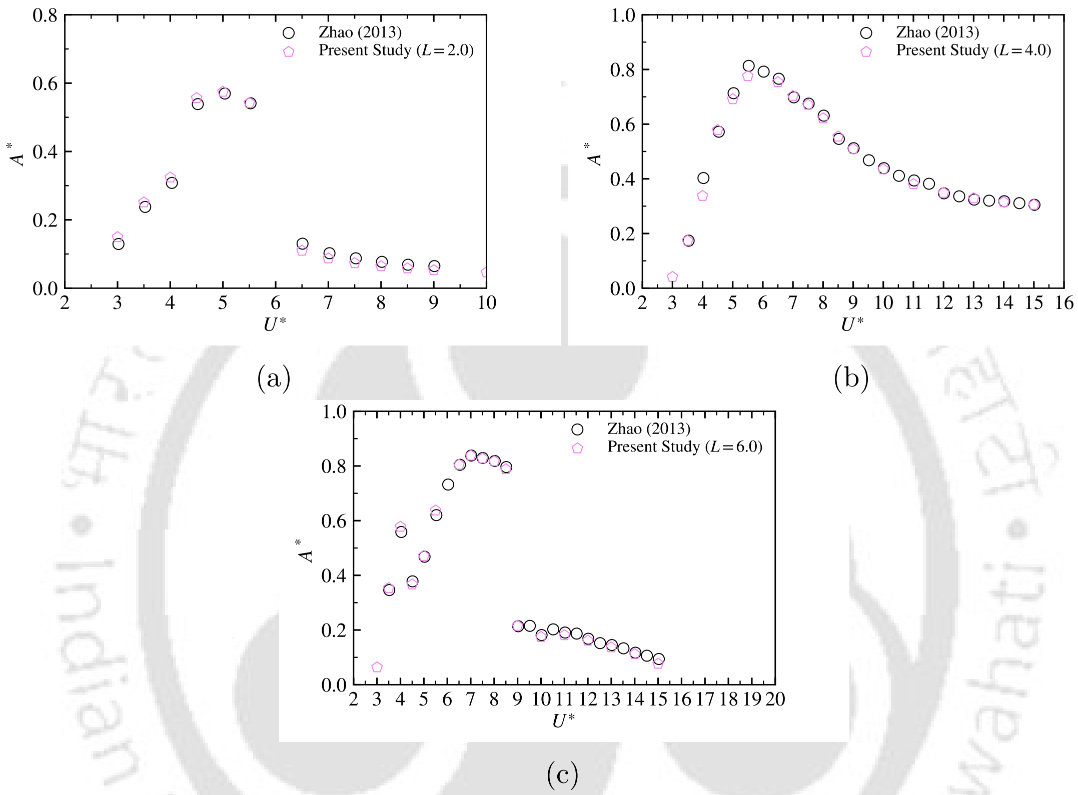

Fig. 3.3 Numerical validation of amplitude data with Zhao (2013) at (a) $L = 2.0$, (b) $L = 4.0$, and $L = 6.0$ at $\zeta = 0$

3.4 Results and discussion

The flow characteristics of nine arrangements of staggered cylinders compared to their respective tandem arrangement (when $T = 0$) are discussed. The results for $T = 0$ at $L = 2.0$ and 4.0 are taken from Zhao (2013). The tandem results for $L = 3.0$ are simulated to highlight the variation in flow parameters at varying T.

3.4.1 Effect of L and T on vibration amplitude

Figure 3.4 represents the variation of non-dimensional amplitude (A^*) with U^* for three L. For each L, the effect of variation of T on A^* is also shown. The error bars represent the variation in transient amplitude, quantified as the standard deviation of the response envelope obtained via a Hilbert transform (Khalak and Williamson, 1999). The vibration amplitude A^* is defined as:

$$A^* = \frac{1}{2}(y_{\max} - y_{\min}) \tag{3.1}$$

where $y_{\max}$ and $y_{\min}$ are the maximum and minimum cylinder displacements evaluated after the system reaches a dynamic steady state, once the initial transients have decayed and the motion is nearly periodic. For the staggered configurations, the asymmetric flow may produce a non-zero mean transverse displacement. Inspection of representative cases confirms that the mean displacement $\bar{y} = (y_{\max} + y_{\min})/2$ remains negligibly small ($< 0.01D$) across all configurations tested, and therefore A^* as defined above accurately represents the oscillatory amplitude.

At $L = 2.0$, the maximum A^* for $T = 0$, 3.0, and 4.0 are comparable, while the maximum A^* at $T = 2.0$ is lower. A jump in amplitude is observed at $U^* = 4.0$ for $T = 0$ and $U^* = 3.5$ for other T values. The initial branch of amplitude response thus extends to $U^* = 4.0$ for $T = 0$ and $U^* = 3.5$ for $T = 2.0$, 3.0, and 4.0 (Soti et al., 2018). The jump in vibration amplitude is associated with the onset of the upper branch. Within the range $4.5 \leqslant U^* \leqslant 5.5$ at $T = 0$, the response is characterized by significant vibration amplitude and maximum transient fluctuation. While at $T = 2.0$, the same vibration response is found within a significantly wider U^* range ($3.5 \leqslant U^* \leqslant 9.0$). With the increase in T, the range of U^*, where significant amplitude is observed, decreases ($3.5 \leqslant U^* \leqslant 7.0$). The amplitude fluctuations also decrease with an increase in T. The range of the upper branch and the start and end of the lower branch can only be found from the discussion of the phase difference of the lift force and displacement.

At $L = 3.0$, the maximum vibration amplitude, the U^* range of significant A^* and cycle-to-cycle amplitude fluctuations is the highest at $T = 0$ and decreases as T increases. The jump in vibration amplitude at $U^* = 3.5$ is due to initial to upper branch transition for $T = 2.0$ and 3.0. In the range $6.0 \leqslant U^* \leqslant 10.0$, high cycle-to-cycle fluctuation of vibration amplitude is observed for $T = 0$. At $U^* > 10.0$, the transient amplitude fluctuation decreases as T increases, pointing towards stabilization of wake characteristics. However, the amplitude fluctuation is the least at a higher U^* for

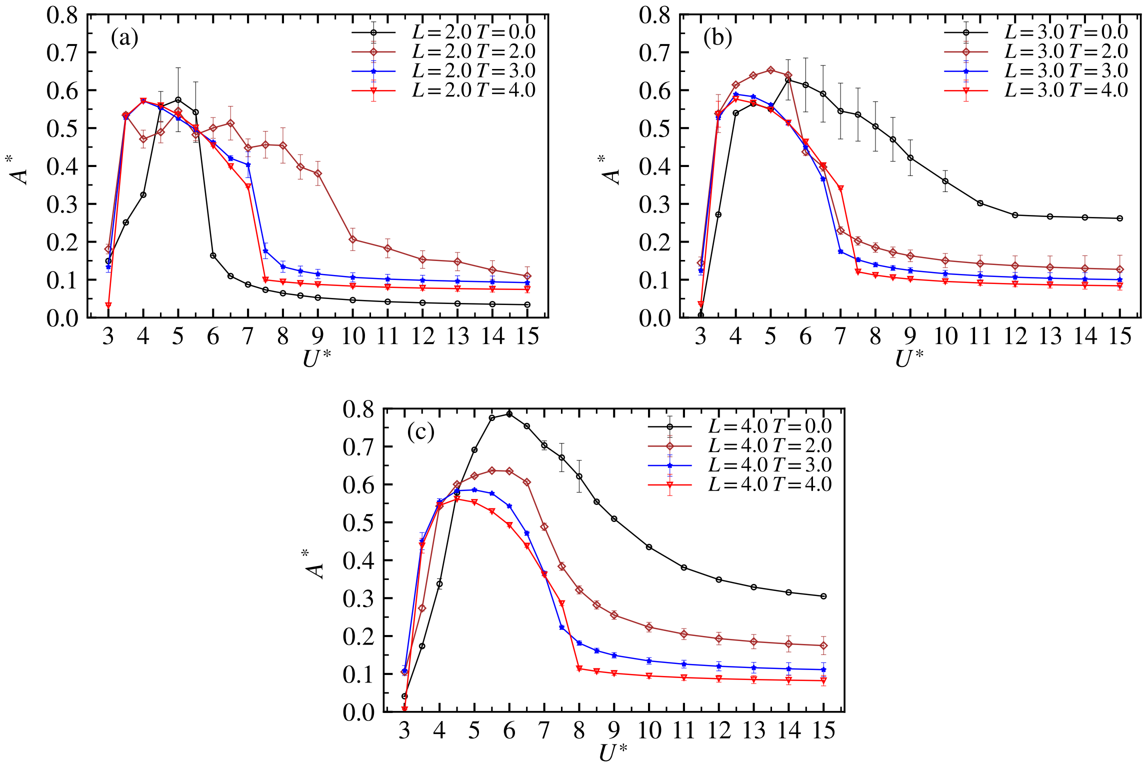

Fig. 3.4 Variation of A^* with U^* for $L =$ (a) 2.0, (b) 3.0, and (c) 4.0 with varying T from 0 to 4.0.

$T = 0$. It means that the wake characteristics for tandem and staggered are different. The initial branch for $L = 3.0$ extends only up to $U^* = 3.5 - 4.0$, and after that, the upper branch starts.

Significant transient amplitude fluctuation is noticed between $7.0 \leqslant U^* \leqslant 8.0$ at $L = 4.0$ and $T = 0$. However, the transient fluctuation regime shifts to lower U^* as T increases. The maximum amplitude and significant amplitude region diminish with T. The amplitude fluctuations increase at high U^* ($U^* > 10.0$) across all T except at $T = 0$. For all the tandem cases, there is no jump in amplitude at low U^* ($U^* \leq 4.0$), while a clear jump is observed for all staggered cases. Moreover, the maximum A^* and the U^* range of significant A^* increase with L. The span of the initial branch and the onset of the upper branch for $L = 4.0$ are the same as those of $L = 3.0$.

3.4.2 Effect of L and T on frequency response

The frequency ratio, f^*, defined as the ratio of oscillation frequency f to the system's natural frequency f_n in vacuum, is shown as a function of U^* in Figure 3.5. When f^*

is close to 1.0, large amplitude vibration is observed in the case of a single cylinder Khalak and Williamson (1999); Williamson and Govardhan (2004). Moreover, at low mass-damping ($m^*\zeta$), the deviation of f^* from unity in the lock-in region is more Khalak and Williamson (1999). The range of lock-in covers the upper and lower branches Govardhan and Williamson (2000); Khalak and Williamson (1999). In the tandem case of $L = 2.0$, the frequency of oscillation matches the natural frequency of the system in the range of $U^* = 5.0$–7.0. The matching criterion for synchronization is defined based on the relative frequency deviation, where synchronization is identified when $\Delta f_{\%} = |max(f_{ref}, f)/min(f_{ref}, f) - 1| \times 100\%$ is less than 15%, where $f_{ref} = f_n$ in this case. However, significant vibration amplitude is noticed between U^* of 4.5 and 5.5. The oscillation frequency becomes desynchronized beyond $U^* = 7.5$ as $\Delta f_{\%}$ is beyond 15%. The region of $f \approx f_n$ for $T = 2.0$ is wider ($5.0 \leqslant U^* \leqslant 10.0$) than the tandem case. But again, the region of significant amplitude is wider than the $f \approx f_n$ region. The same scenario is observed at $T = 3.0$ and 4.0. Moreover, $f \approx f_n$ region decreases as T increases ($4.0 \leqslant U^* \leqslant 7.0$ for $L = 2.0$,$T = 3.0$ and $T = 4.0$). At $T = 3.0$ and 4.0, the U^* range of significant amplitude is approximately similar to the $f \approx f_n$ range. Therefore, $f \approx f_n$ ensures a large oscillation amplitude, but a large oscillation amplitude does not correspond to $f \approx f_n$. The onset of the desynchronization region varies with T: for $T = 0$, it begins at $U^* = 7.5$; for $T = 2.0$, from $U^* = 10.0$; while for $T = 3.0$ and $T = 4.0$, desynchronization commences from $U^* = 8.5$. For the tandem case of $L = 3.0$, desynchronization region starts at $U^* = 8.5$. While for other T, the desynchronization region starts from $U^* = 7.5$ onward. At $L = 4.0$, the onset of the desynchronization region for the staggered case shifts to $U^* = 8.0$ as T increases and $U^* = 8.5$ for the tandem case.

The frequencies presented in Figures 3.5 and 3.6 are obtained via Fast Fourier Transform (FFT) of the respective time signals, and represent the dominant (peak) frequency in each spectrum. The complete amplitude spectral density (ASD) of all normalized frequency components for each arrangement is presented in Appendix C. The vortex-shedding frequency, f_s, can be depicted as the frequency of combined root-mean-square (RMS) lift and is denoted as f_{C_L}. The upstream and downstream cylinder parameters are marked as 1 and 2, respectively. The variation of lift frequencies with U^* is shown in Figure 3.6. In Appendix C, $f^*_{C_L} = f_{C_L}/f_n$, $f^*_{C_{L_1}} = f_{C_{L_1}}/f_n$ and $f^*_{C_{L_2}} = f_{C_{L_2}}/f_n$ are the lift frequencies of the combined, upstream, and downstream cylinders normalized by the natural frequency f_n, respectively. Also, $f^*_{\mathrm{St}} = f_{\mathrm{St}}/f_n$ denotes normalized Strouhal/vortex-shedding frequency of the stationary cylinders.

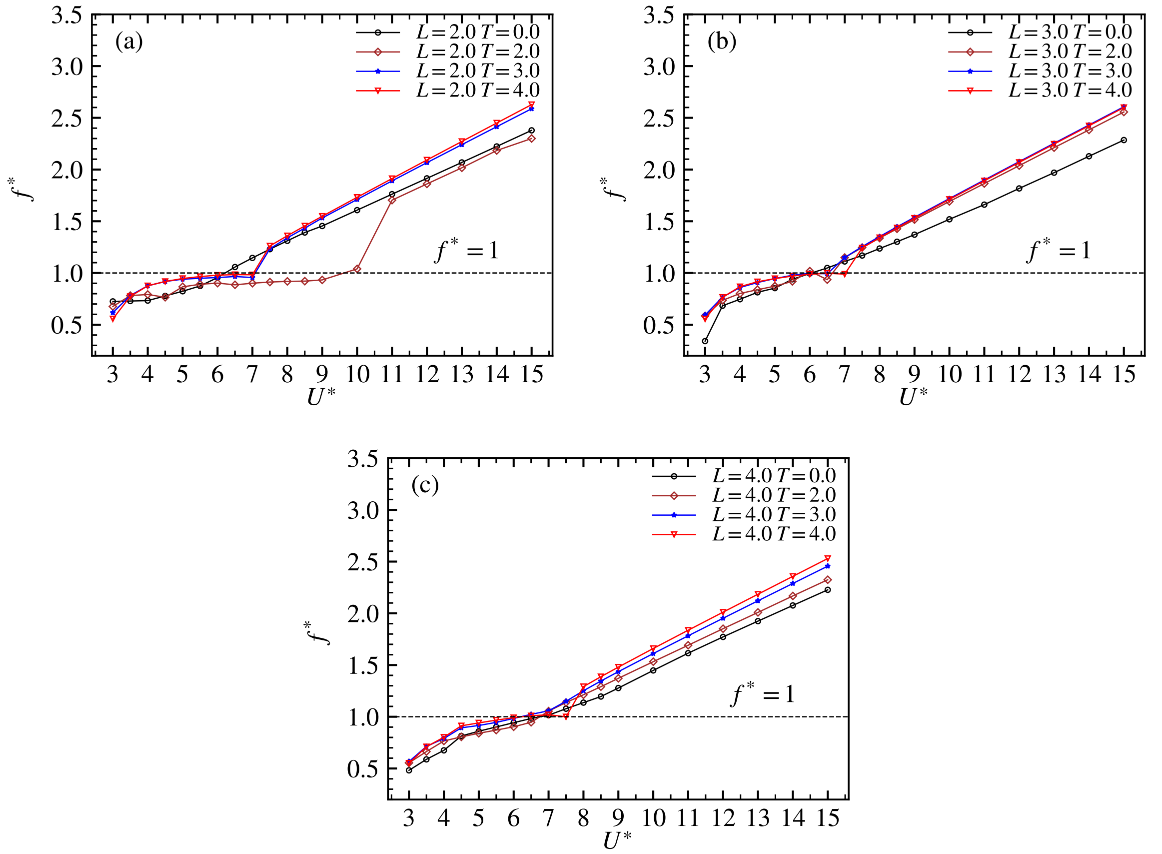

Fig. 3.5 Variation of $f^* = f/f_n$ with U^* at L = (a) 2.0, (b) 3.0, and (c) 4.0 with varying T from 0 to 4.0.

The classical theory of synchronization suggests that when f_{C_L} matches f_n, it is referred to as the synchronization or lock-in region. At $L = 2.0$, $T = 2.0$, the frequency response in the synchronization region ($U^* = 5.0$–10.0) shows deviations from classical synchronization. For example, at $U^* = 5.5$, 7.0, and 9.0, only one cylinder synchronizes with f_n, while the other remains desynchronized. At $U^* = 6.0$, $f_{C_{L_1}}$ and $f_{C_{L_2}}$ do not follow f_n while f_{C_L} does. The dominant frequency of $f_{C_{L_1}}$ and $f_{C_{L_2}}$ match each other (~ 0.23), and f_{C_L} and f match each other (~ 0.15), but they are different. Surprisingly, the frequency of both cylinders synchronized with each other at $U^* = 8.0$, but f_{C_L} does not synchronize with either of $f_{C_{L_1}}$ and $f_{C_{L_2}}$, or f_n and f. At $U^* = 8.5$, lift frequencies $f_{C_{L_1}}$ and $f_{C_{L_2}}$ synchronize (i.e., $f_{C_L} = f_{C_{L_1}} = f_{C_{L_2}}$), while the oscillation frequency f deviates from both f_{C_L} and f_n, indicating partial desynchronization. However, at a certain U^* ($U^* = 5.0$ and 6.5), all the frequencies of lift, natural frequency, and oscillation frequency match with each other. Figure 3.6(ai–aiii) shows that at $U^* \geqslant 8.0$, the frequency of oscillation remains close to f_n, but the individual frequency components

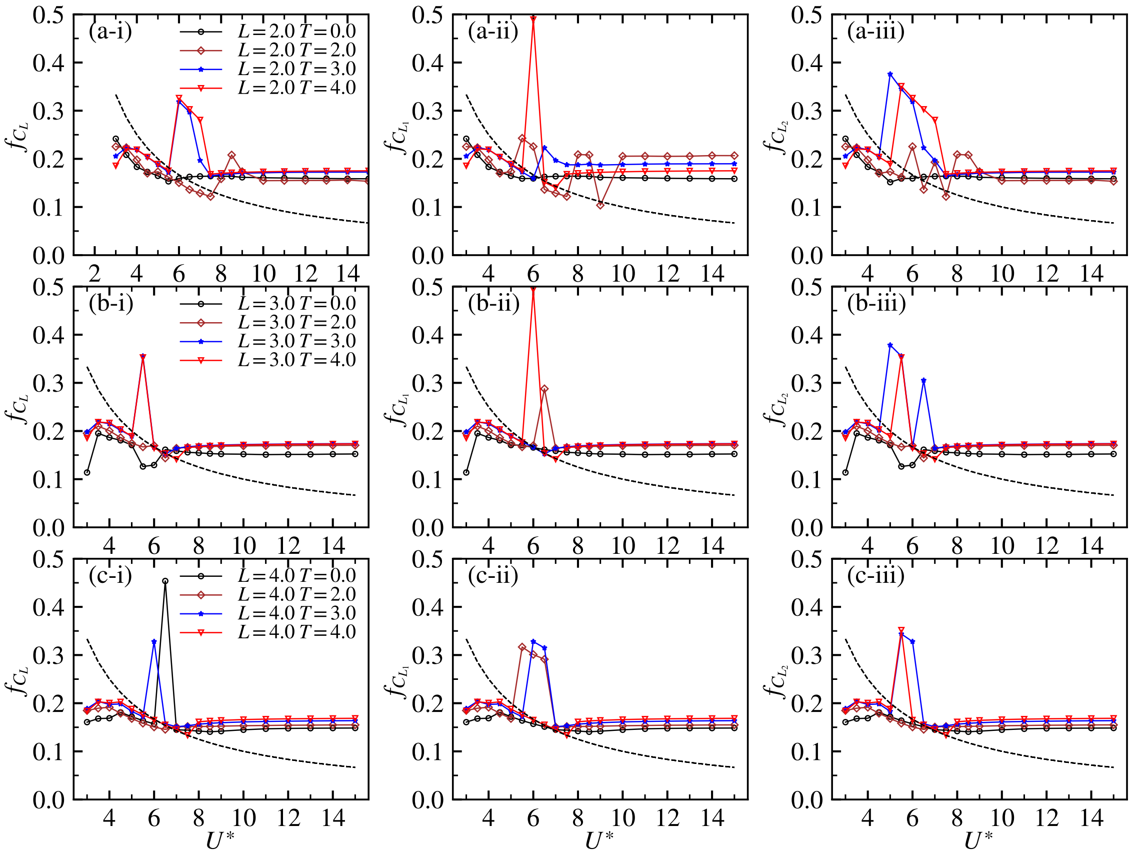

Fig. 3.6 Variation of f_{C_L}, $f_{C_{L_1}}$, and $f_{C_{L_2}}$ with reduced velocity U^* at (ai–aiii) $L = 2.0$, (bi–biii) $L = 3.0$, and (ci–ciii) $L = 4.0$, for $T = 0$ to 4.0 (left to right). The black dashed line indicates the natural frequency in vacuum, f_n.

of lift ($f_{C_{L_1}}$, $f_{C_{L_2}}$) diverge, showing partial synchronization. It indicates a complex interaction between the vortex-induced forces and structural response, characterized by intermittent transitions between localized and global lock-in states. Global lock-in is sustained between $U^* = 5.0$ and 6.5, while synchronized sub-harmonics of individual or total lift frequency dominate the response at other U^* values. For the case of $T = 4.0$, the U^* values from 3.5 to 8.0 exhibit synchronization with sub-harmonics, except at $U^* = 6.0$, where the upstream cylinder desynchronizes from the rest of the frequencies. This behaviour arises because, in several cases particularly within the synchronization region, the lift force spectra exhibit multiple spectral peaks rather than a single dominant frequency. The presence of these harmonics and sub-harmonics means that while the dominant frequency of $f_{C_{L_1}}$ and $f_{C_{L_2}}$ may match each other, it need not coincide with the dominant frequency of the combined lift f_{C_L} or the oscillation frequency f. The latter are influenced by the combined effect of all spectral components. This multi-frequency character of the spectra is the underlying reason for the observed discrepancies between $f_{C_{L_1}}$, $f_{C_{L_2}}$, and f, and is consistent with the harmonic-dominated synchronization described above. No such partial lock-in is noticed in the synchronization regime for the tandem case. The f_{C_L} at $T = 3.0$ and 4.0 closely follows $f_{C_{L_2}}$, as f matches the harmonics of both f_{C_L} and $f_{C_{L_2}}$. Therefore, the gap vortex is influenced by vortex-shedding from the downstream cylinder.

In the tandem case with $L = 3.0$, no global lock-in is observed throughout the entire synchronization region. Specifically, within the range of $U^* = 5.5 - 6.0$, the f_n only locks onto $f_{C_{L_1}}$, not f_{C_L}. However, for the staggered cases, the synchronization region exhibits global lock-in characterized by sub-harmonics of the lift frequencies. Even the number of harmonics increases as T increases, which indicates substantial interference between wakes. The peaks and valleys of f_{C_L}, $f_{C_{L_1}}$, and $f_{C_{L_2}}$ represent harmonics, suggesting that the vibration is governed by the sub-harmonics of f_{C_L}, $f_{C_{L_1}}$ and $f_{C_{L_2}}$. This is directly evidenced by the ASD contour maps in Appendix C (Figures C.1–C.12). These contour maps show that tandem cases ($T = 0$) exhibit a single dominant frequency band, while staggered cases display an increasing number of harmonic bands as T increases, directly confirming the harmonic-dominated synchronization described above. A similar phenomenon occurs at $L = 4.0$, where the synchronization region is maintained by harmonics. However, in tandem cases, harmonics are absent within the synchronization region. Consequently, the vibration in all tandem scenarios is not sustained by harmonics. The harmonics appear to dominate the oscillation with the increase in both L and T, particularly T. With increasing gaping (characterized by an increase in L and T), the sustained timing of vortex shedding enhances the likelihood of synchronization between the vortex-shedding harmonics and the oscillation frequency. As the gap increases, vortices are more likely to interact and become trapped within the gap region.

3.4.3 Effect of L and T on lift coefficient

Figure 3.7 shows the variation of the combined $C_{L_{\mathrm{RMS}}}$ of two cylinders with U^*, along with the $C_{L_{\mathrm{RMS}}}$ of the individual cylinders. The combined $C_{L_{RMS}}$ is calculated by combining the transient fluid forces of the cylinders, F_T, and computing the RMS value. For the sake of simple nomenclature, the $C_{L_{\mathrm{RMS}}}$ of individual cylinders are denoted by C_{L_i}, where $i = 1, 2$ is the upstream and downstream cylinder, respectively. Hence, $C_{L_{\mathrm{RMS}}}$ can be calculated as,

$$C_{L_{\text{RMS}}} = \sqrt{\frac{1}{T_{total}} \int_0^{T_{total}} \left(C_{L_1}(t) + C_{L_2}(t)\right)^2 dt} \tag{3.2}$$

where, $C_{L_i}(t)$ are the transient lift coefficients of the cylinders. The RMS is taken over 50 cycles of oscillation. Therefore, $T_{total} = 50 \times T_e$, where T_e is the time period of a single oscillation. The $C_{L_{\text{RMS}}}$, C_{L_1}, and C_{L_2} values of tandem cases register the

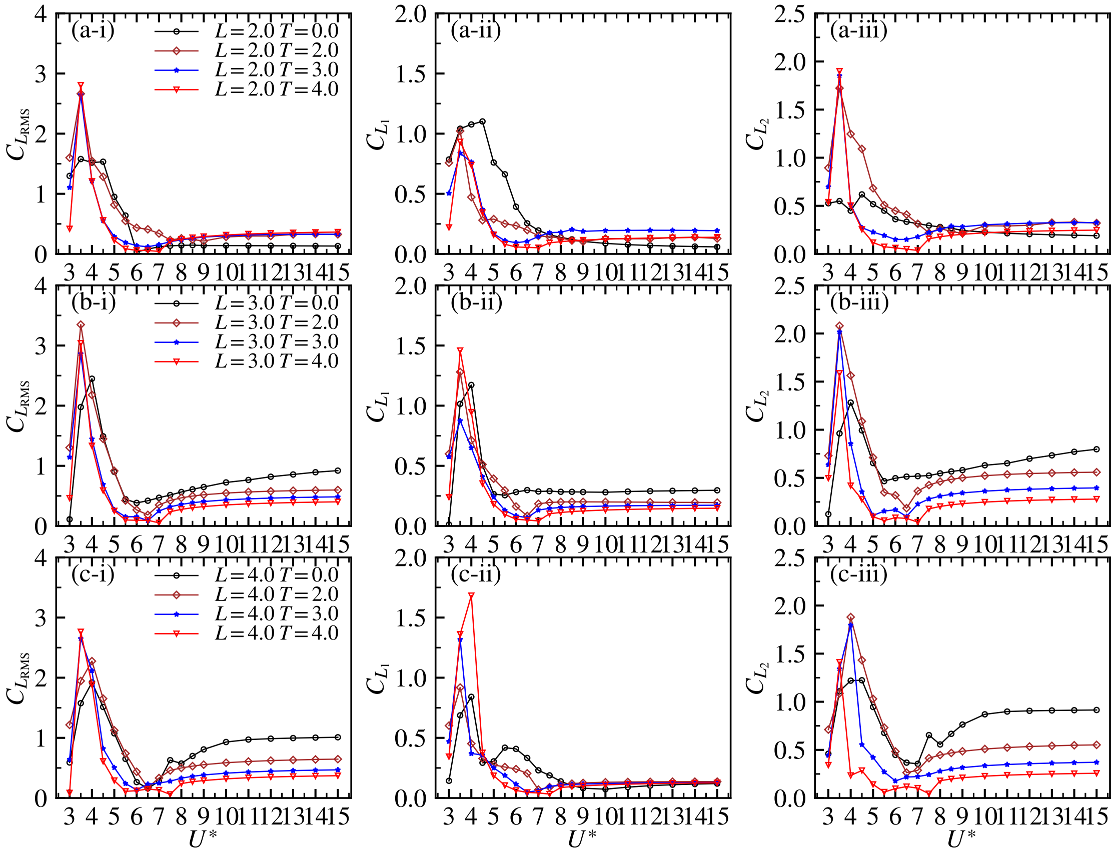

Fig. 3.7 Variation of $C_{L_{\text{RMS}}}$ C_{L_1} and C_{L_2} with U^* for L = (a) 2.0, (b) 3.0, and (c) 4.0 with varying T from 0 to 4.0.

lowest value. Moreover, the peak C_{L_2} is higher than C_{L_1} across all cases except for the tandem case of $L = 2.0$. Consequently, the wake dynamics should be dominated by the downstream cylinder. The trend of maximum C_{L_1} with T for $L = 2.0$ differs from the maximum $C_{L_{\text{RMS}}}$. The small value of C_{L_2} compared to C_{L_1} for the tandem case of $L = 2.0$ is due to the shielding of the downstream cylinder from the shear layer of the upstream cylinder (Zhao, 2013). However, with the increase in T, the shielding effect is diminished. Thus, the peak C_{L_2} increases with T. As L increases to 3.0, the peak C_{L_1} and C_{L_2} both increase compared to the tandem case at $L = 2.0$. The $T = 3.0$ case for $L = 3.0$ shows the lowest C_{L_1} and higher C_{L_2}, similar to that of $L = 2.0$. The C_{L_1} and C_{L_2} values are comparable for $T = 4.0$, as the highest C_{L_1} is recorded at this T. Also, C_{L_2} has a decreasing trend with T. However, in the case of $L = 4.0$, while peak C_{L_1} increases with T, peak C_{L_2} decreases with T. Here, C_{L_2} values are also higher than the C_{L_1} values. The $C_{L_{\mathrm{RMS}}}$ peaks at $L = 3.0$ before dropping at $L = 4.0$. The variation of $C_{L_{\mathrm{RMS}}}$ with T exhibits a monotonic increase for $L = 2.0$ and 4.0, whereas a non-monotonic trend is observed at $L = 3.0$. In the initial branch, the values of C_L ($C_{L_{\mathrm{RMS}}}$, C_{L_1}, and C_{L_2}) peak. In the upper branch, the values exhibit gradually decreasing trend, while in the lower branch, the lift coefficient values attains global minima.

The total fluid force, F_T, can be decomposed into two components: potential force (F_P) associated with the inertial added mass effect of displaced fluid and vortex force (F_V) associated with the shed vortices (Govardhan and Williamson, 2000). Therefore, $F_T = F_P + F_V$, and F_P is given by,

$$F_P = -C_A m_d \ddot{y} \tag{3.3}$$

where C_A is the added mass coefficient, and for a circular cylinder, $C_A = 1.0$. Normalizing all the forces by $1/2\rho U^2 D$ and putting $m_d = 2 \times \pi/4\rho D^2$ and D and U as 1.0, vortex force coefficient (C_V) can be expressed as,

$$C_V = C_L + \pi\ddot{y} \tag{3.4}$$

The variation of the RMS value of C_V, i.e., $C_{V_{\mathrm{RMS}}}$, with U^* at different L and T is

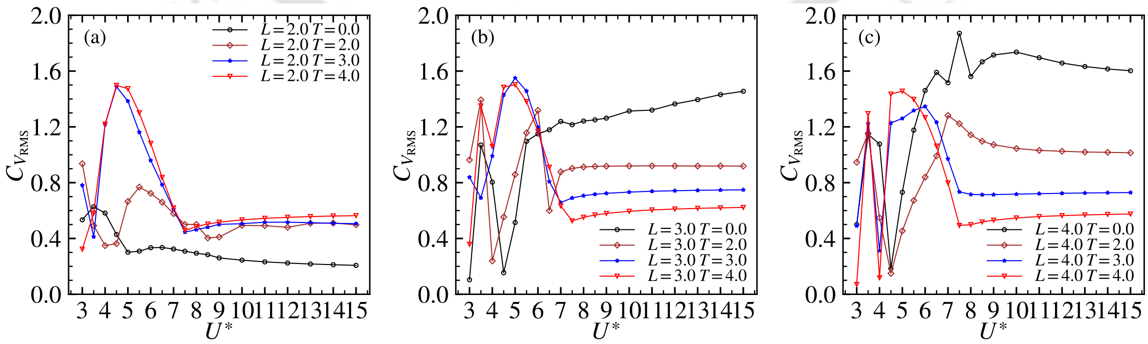

Fig. 3.8 Variation of $C_{V_{\mathrm{RMS}}}$ with U^* for $L =$ (a) 2.0, (b) 3.0, and (c) 4.0 with varying T from 0 to 4.0

shown in Figure 3.8. At the initial branch for $L = 2.0$, $C_{V_{\mathrm{RMS}}}$ is observed to increase for

$T = 2.0$, while for $T = 3.0$ and 4.0, it attains global minima. In the upper and lower branches, $C_{V_{\mathrm{RMS}}}$ increases, reaches a peak, and then decreases with further increase in U^*, except for the tandem case. At higher U^*, $C_{V_{\mathrm{RMS}}}$ remains almost constant. For $L = 3.0$, a local peak is observed at the initial branch except for $T = 3.0$. However, for $T = 3.0$ and 4.0, a global peak is observed, while a global minimum is observed for $T = 0$ and 2.0. After $U^* = 7.5$, $C_{V_{\mathrm{RMS}}}$ does not change with U^*, whereas for the tandem case, an increasing trend is observed with U^*. For $L = 4.0$, a local maxima and a minimum is noticed at the initial branch and in the upper and lower branches, again an increase and a decrease are reported.

3.4.4 Effect of L and T on phase difference

The phase difference ϕ is the difference in phase between the combined lift force and displacement of the cylinders, and ϕ_i $(i = 1, 2)$ denotes the phase difference of the upstream and downstream cylinders, respectively. The phase difference of vortex force and cylinder displacement is referred to as ϕ_V. The ϕ and ϕ_V are calculated from the Hilbert transformation of the lift force and displacement (Khalak and Williamson, 1999). In an undamped case, traditionally ϕ and ϕ_V can only assume the value 0° or 180°. However, Figure 3.9 shows that the value of ϕ is between the two. The combined lift is not entirely in or out of phase with the displacement because of the complex shear layer interactions in the gap. The jump in ϕ_V represents the onset of the upper branch, while the jump in ϕ is observed at the onset of the lower branch (Govardhan and Williamson, 2000; Khalak and Williamson, 1999). For the tandem case of $L = 2.0$, $\phi \sim 0°$ between $U^* = 3.0$ and 6.0 and ϕ_V jumps at $U^* = 4.0$. The region up to $U^* = 4.0$ is referred to as the initial branch (IB), while the region between $U^* = 4.0$ and 6.0, is represented as the upper branch (UB). The IB is characterized by a jump in A^*, whereas in the upper branch, there is a high A^* along with significant fluctuations in transient amplitude. The lower branch (LB) starts at $U^* = 6.0$ and is characterized by decreasing vibration amplitude and smaller transient amplitude fluctuation. When ϕ attains 180° ($U^* > 6.0$), it is the onset of the lower branch. The end of the lock-in region is marked as the end of the LB. In the desynchronization region, ϕ and ϕ_V usually stay at 180° (Khalak and Williamson, 1999). However, except for the tandem cases, ϕ and ϕ_V both are observed to decrease with U^* in the desynchronization region. As T increases to 2.0, the peak ϕ is observed to be 142°, and there is no steep jump observed. The initial branch only spans between $U^* = 3.0$ and 3.5. Beyond $U^* > 10.0$, ϕ decreases, and vibration amplitude drops due to desynchronization. For $T = 3.0$

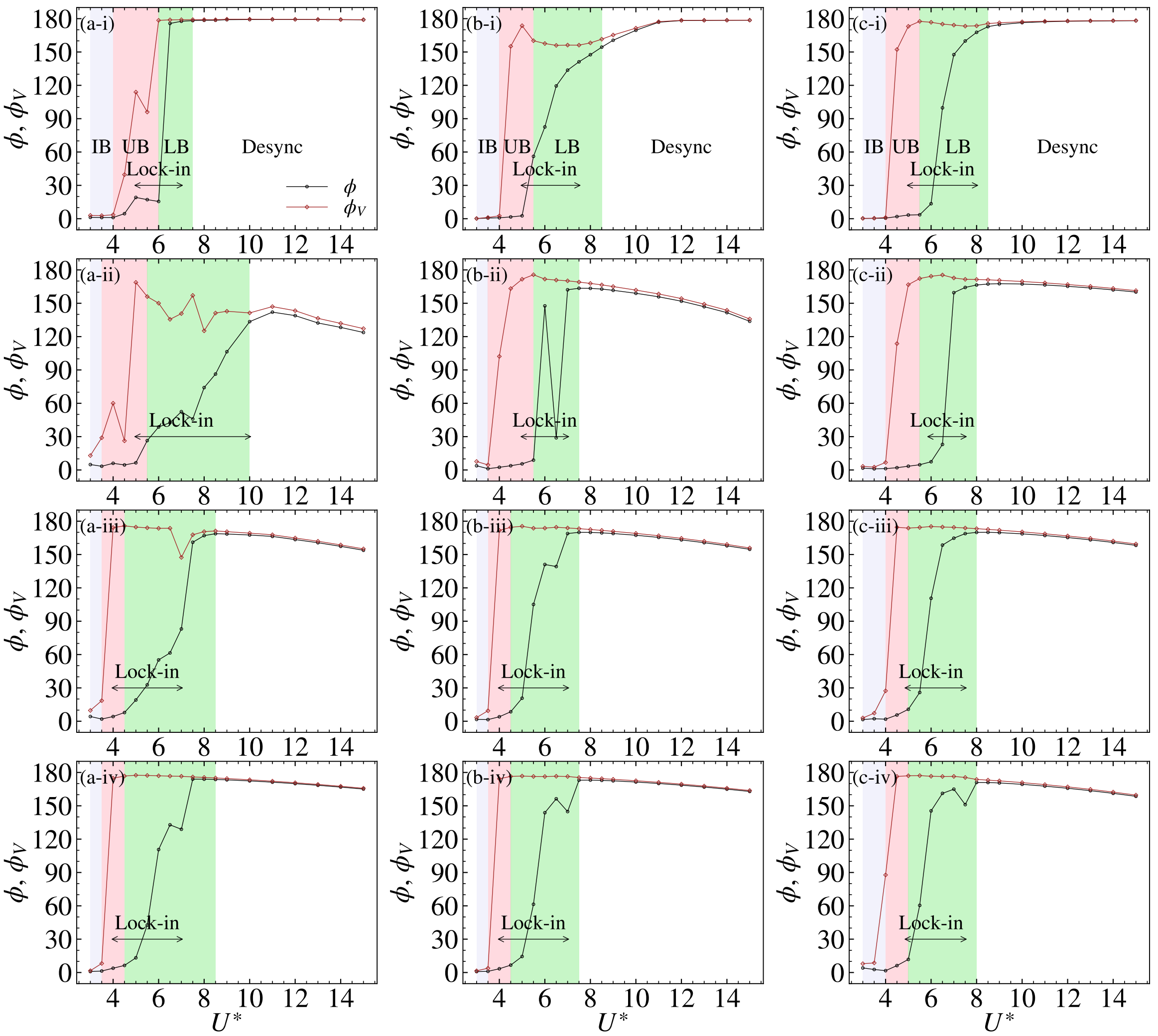

Fig. 3.9 Variation of ϕ and ϕ_V with U^* for L = (a) 2.0, (b) 3.0, and (c) 4.0. Figures (i–iv) show the variation of ϕ and ϕ_V with the variation of T from 0 to 4.0 at a fixed L. The initial branch (IB) is shaded with light-blue, the upper branch (UB) in light-pink and the lower branch (LB) in light-green. The desynchronization region is shown in white.

and $T = 4.0$, the width of the LB and UB both reduced compared to $T = 2.0$. Hence, desynchronization starts early at high T. It suggests a reduced interaction of shear layers in the gap as T increases, resulting in an arrangement more similar to that of an isolated cylinder (Figures 3.11, 3.13, 3.14). In the tandem configurations with $L = 3.0$ and 4.0, while the peak value of ϕ reaches 180°, the transition from UB to LB does not occur abruptly from 0° to 180°; rather, it progresses through intermediate values. For the tandem case with $L = 3.0$, the widths of IB and UB are larger than those of the corresponding staggered cases. However, the LB region gets wider with an increase in T. There is not much change in the IB for $L = 4.0$, but the width of UB decreases with T. The width of the UB and LB remains unchanged for $T = 3.0$ and 4.0 across all L cases. The width of the LB is highest at $L = 2.0$, $T = 2.0$, and lowest at the tandem case of $L = 2.0$. For all configurations, frequency lock-in initiates shortly after the onset of the UB regime and terminates before the completion of the LB regime.

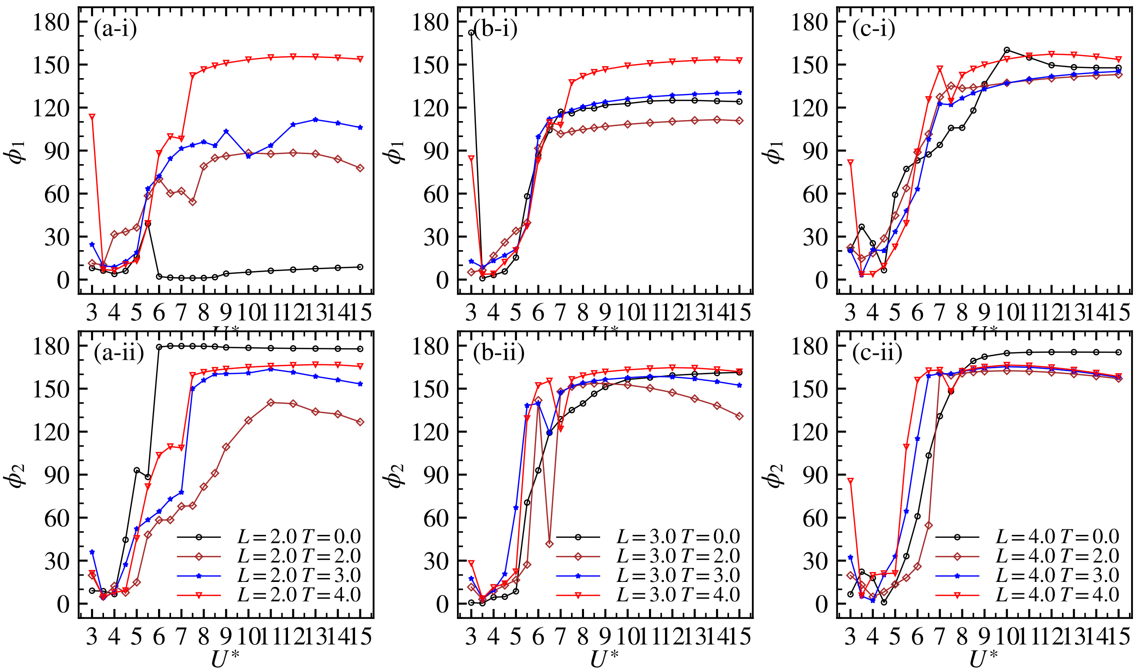

Fig. 3.10 Variation of ϕ_1 and ϕ_2 with U^* for $L =$ (a) 2.0, (b) 3.0 and (c) 4.0 with varying T from 0 to 4.0.

The tandem case of $L = 2.0$ shows that ϕ_1 is always close to 0° except in the lock-in regime. However, ϕ_2 shows a jump to 180°, and the jump and peak of ϕ_2 coincide with the lock-in regime. Comparing ϕ, ϕ_1, and ϕ_2 of $L = 2.0$ from Figures 3.9 and 3.10(ai–aii), it is observed that the trend in ϕ matches with ϕ_2. The findings suggest that the downstream cylinder primarily governs the wake dynamics and vibration characteristics. It applies to other L cases (Figures 3.10bi–cii). Therefore, it can be concluded that the downstream cylinder is likely to generate greater lift, and experiences unsteady gap flow, stronger wake, and shear layer interactions.

3.4.5 Effect of L and T on wake characteristics

The vorticity contours are captured for the initial, upper and and lower branch of oscillation (Figures 3.11, 3.13, 3.14, 3.16, and 3.17). The small black lines represent the maximum displacement position of the center of the cylinder, and the pink line represents the current displacement. The blue arrow illustrates the magnitude and direction of cylinder velocity. The time-averaged skin-friction coefficient ($\bar{C_f}$) and pressure coefficient ($\bar{C_p}$) of individual cylinders are calculated around the surface of the cylinders at varying θ. The angle θ is measured from the front stagnation point in the clockwise direction. The fluctuating components are represented by the filled shaded region within regions of $\bar{C_f} \pm C_f{}'$ and $\bar{C_p} \pm C_p{}'$. The vorticity contours are shown for the for the instantaneous flow fields corresponding to the time instants (a)–(h). The localized gap flow velocity, c_g, is the flow velocity normal to the line joining the cylinder centers, and shown by black arrows (Sharma and Bhardwaj, 2023). The length of the arrow is proportional to the magnitude of c_g.

Figures 3.11(a) to (d) show vorticity contours for $L = 2.0$ with the variation of T from 0 to 4.0 at the initial branch (IB). In the tandem case (a), the shear layer from the upstream cylinder stays attached to the downstream cylinder, and 2S vortices are shed from the cylinder assembly. This wake structure represents the overshoot mode (OS) where the wake from the upstream cylinder overshoots the downstream cylinder without direct impingement (Zhu et al., 2025). The pressure variation around the downstream cylinder is less than that of the upstream cylinder, which renders less lift on the downstream cylinder compared to the upstream one (Figures 3.12(ai) and (bi)). The c_g is distributed evenly and lower in the tandem case. However at $T = 2.0$, the c_g is higher and biased towards the downstream cylinder. The pressure distribution around the cylinders at $T = 2.0$ reveals greater variation, contributing to higher lift in the $L = 2.0$, $T = 2.0$ arrangement than in the tandem case. The shear layer from the upstream cylinder is suppressed by the shear layer of the downstream cylinder. Elongated clockwise shear layer should render low lift (Zeng et al., 2023), but C_{L_1} is lower than C_{L_2}, as depicted in Figure 3.7. Higher C_L on the downstream cylinder due to the higher pressure variation as seen from Figures 3.12 (aii) and (bii). The gap flow velocity at the staggered arrangement increases from the tandem case. There is also a variation of the upper and lower separation points, similar to the tandem case. For the upstream cylinder of the tandem case, there is no clear separation points as weak oscillations in C_{f_1} is seen in the range 100°–240°. The peak suction is located at 85°±8° and 275°±8° followed by a reattachment point at 315°±1°. The downstream

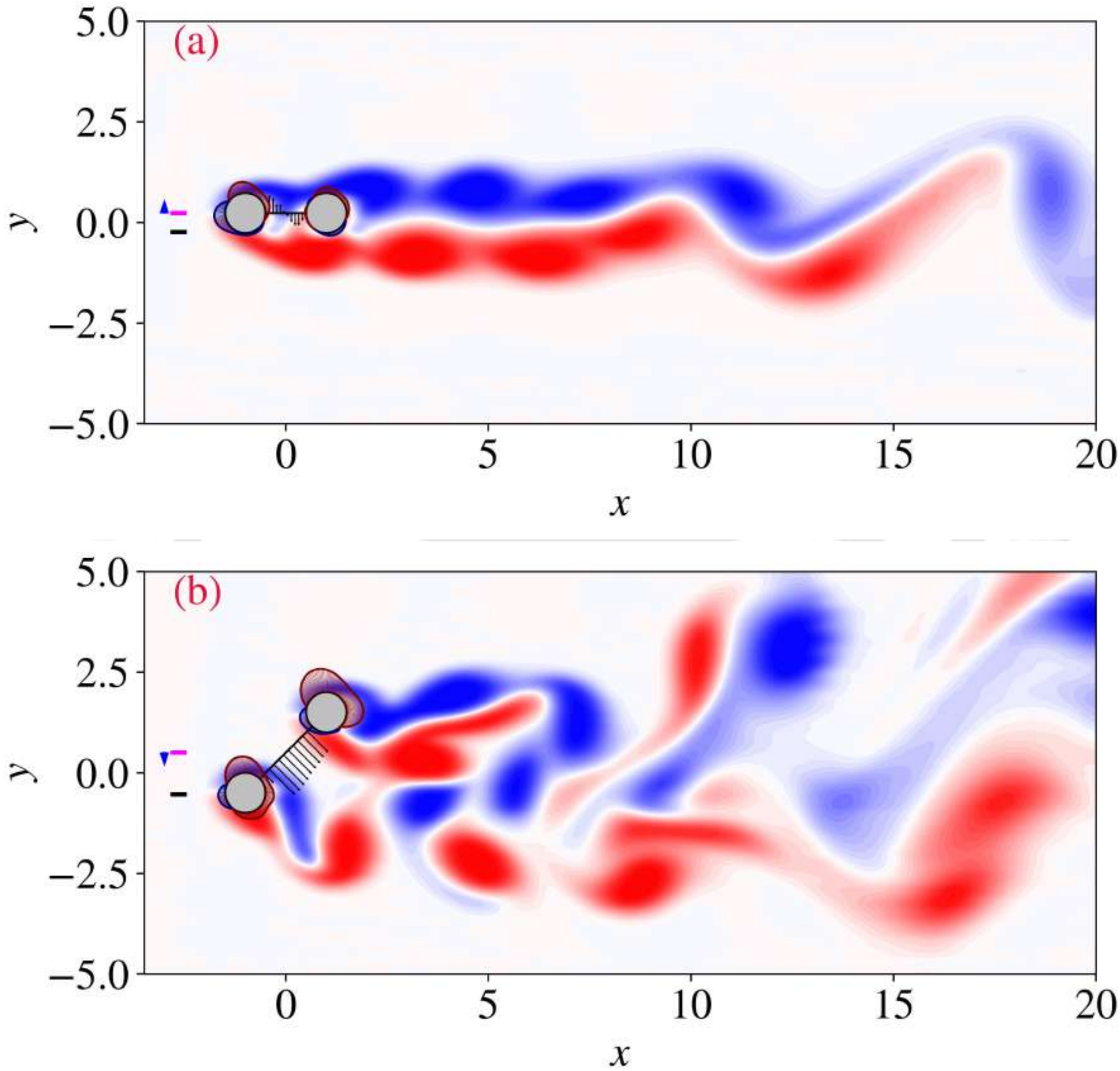
(a)
5.0
2.5
0.0
−2.5
−5.0
y
0
5
10
15
20
x
(b)
5.0
2.5
0.0
−2.5
−5.0
y
0
5
10
15
20
x

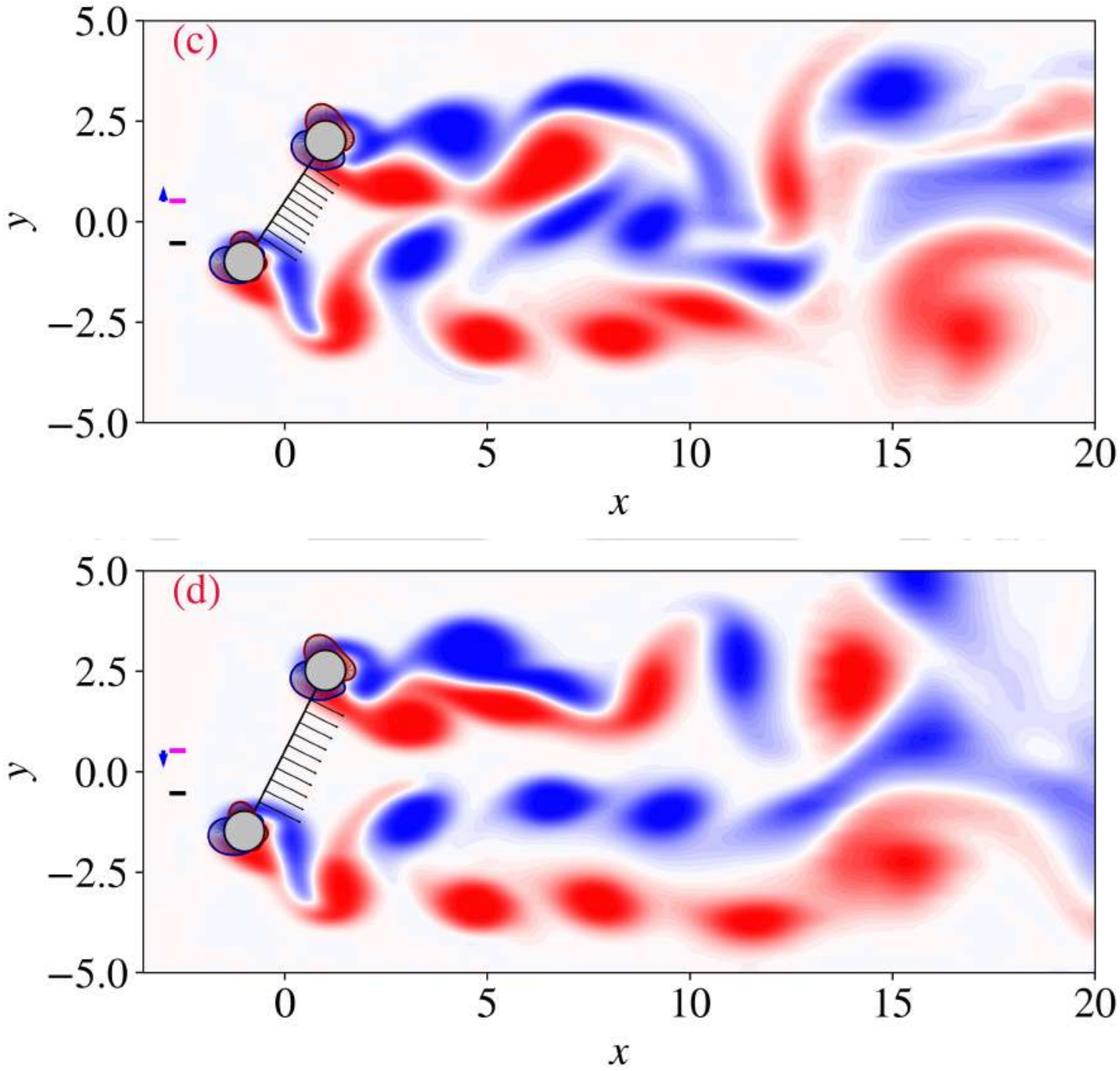

Fig. 3.11 Vorticity contours (scaled between -1 (blue) to 1(red)) and pressure distribution around the cylinders at the initial branch (IB) of oscillation for $L = 2.0$ and $U^* = 3.5$ with the variation of T. From (a) to (d), the T increases from 0 to 4.0; 'navy' and 'maroon' represent negative and positive pressure, respectively. All the contours are captured when the cylinder is at maximum displacement.

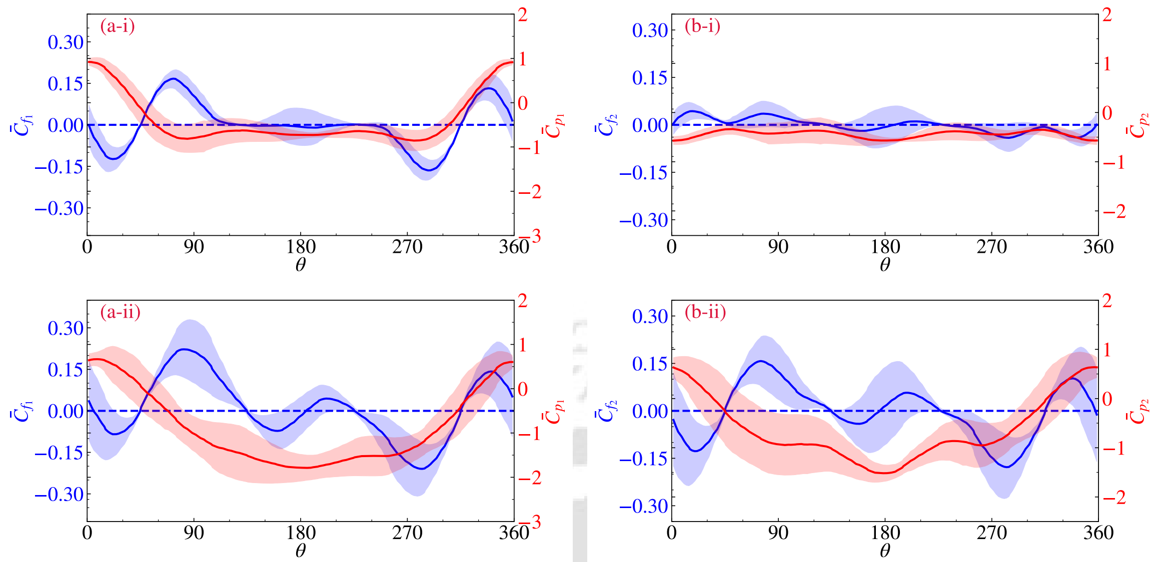

Fig. 3.12 Time-averaged skin friction coefficient ($\bar{C_f}$) and pressure coefficient ($\bar{C_p}$) of upstream cylinder tandem case of $L = 2.0$ (a-i) and staggered case of $L = 2.0$, $T = 2.0$ (a-ii) with the variation of θ at the initial branch (IB). Similar for the downstream cylinder in (b-i) and (b-ii). The shaded region shows the localized transient variation.

cylinder however, does not show any clear separation points. Although it shows peak suction points similar to that of the upstream cylinder. Interestingly, the suction peak of the upstream cylinder for $L = 2.0$, $T = 2.0$ is seen at rear-side of the cylinder (181°±15°), indicating strong influence of downstream cylinder on upstream cylinder. The upper and lower separation is located at 135°±2° and 225°±3°, respectively, while the reattachment point is similar to that of the upstream cylinder of tandem case. The downstream cylinder shows no change in separation and reattachment points. The interaction between the shear layers of the cylinders in the wake decreases as T increases (Figures 3.11(c) and (d)). The upstream cylinder sheds 2S type vortices while the downstream cylinder shear layer elongates to form a complex pattern. The gap flow velocity is again biased towards the downstream cylinder, which can increase lift due to stronger c_g creating more asymmetry in the pressure distribution. The separation points for upstream and downstream cylinders for $L = 2.0$, $T = 3.0$, and $T = 4.0$ are the same as those of $L = 2.0$, $T = 2.0$.

Figure 3.13 shows the vorticity contours at the upper branch (UB) for $L = 2.0$ with the variation of T. A substantial amount of c_g is observed for the tandem case, and stronger vortices are shed from the cylinders (Figure 3.13a). Alternate reattachment (AR) of the upstream shear layer on the downstream cylinder is observed (Zhu et al.,

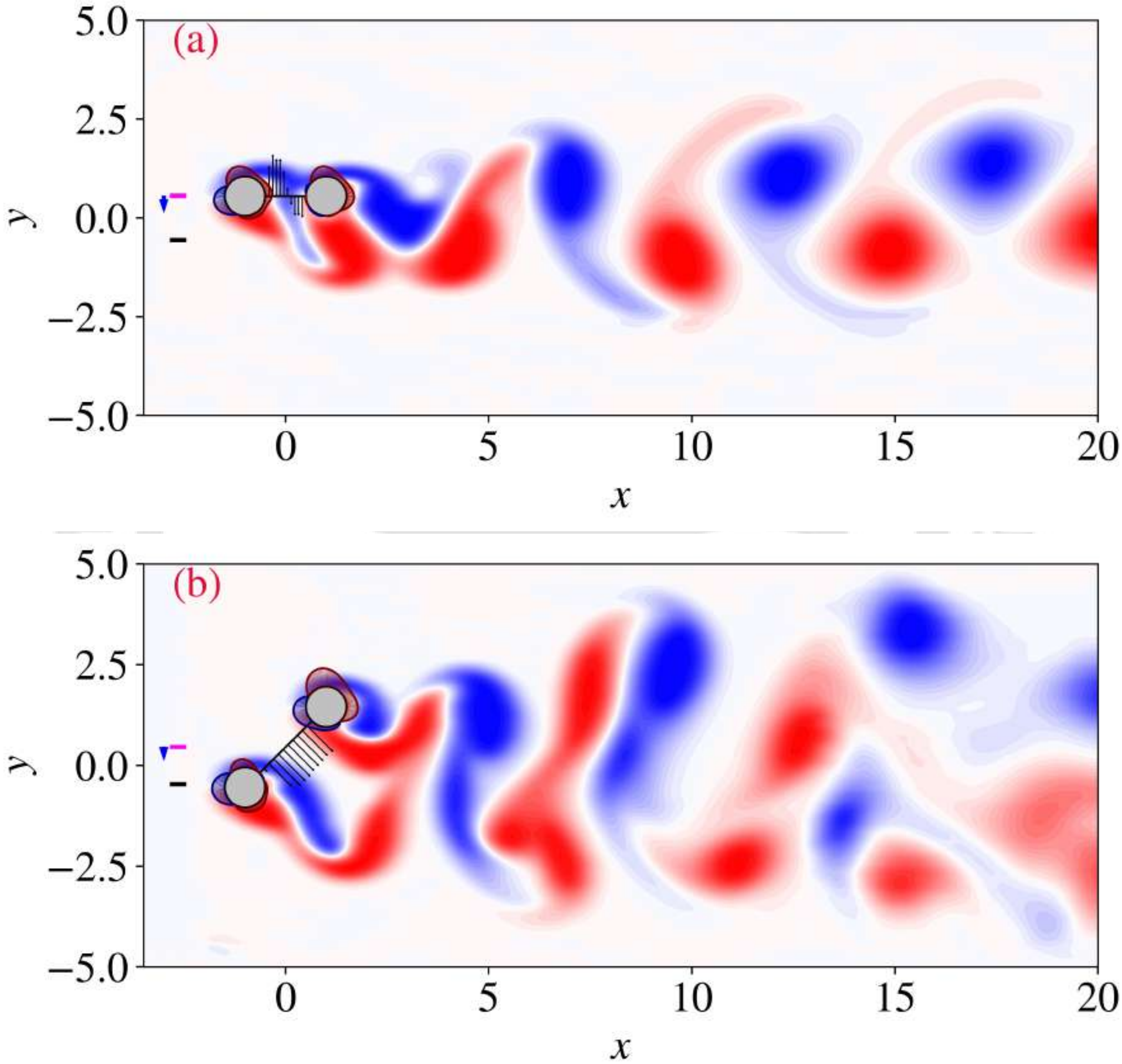

(a)
(b)
5.0
2.5
0.0
−2.5
−5.0
0
5
10
15
20
x
y

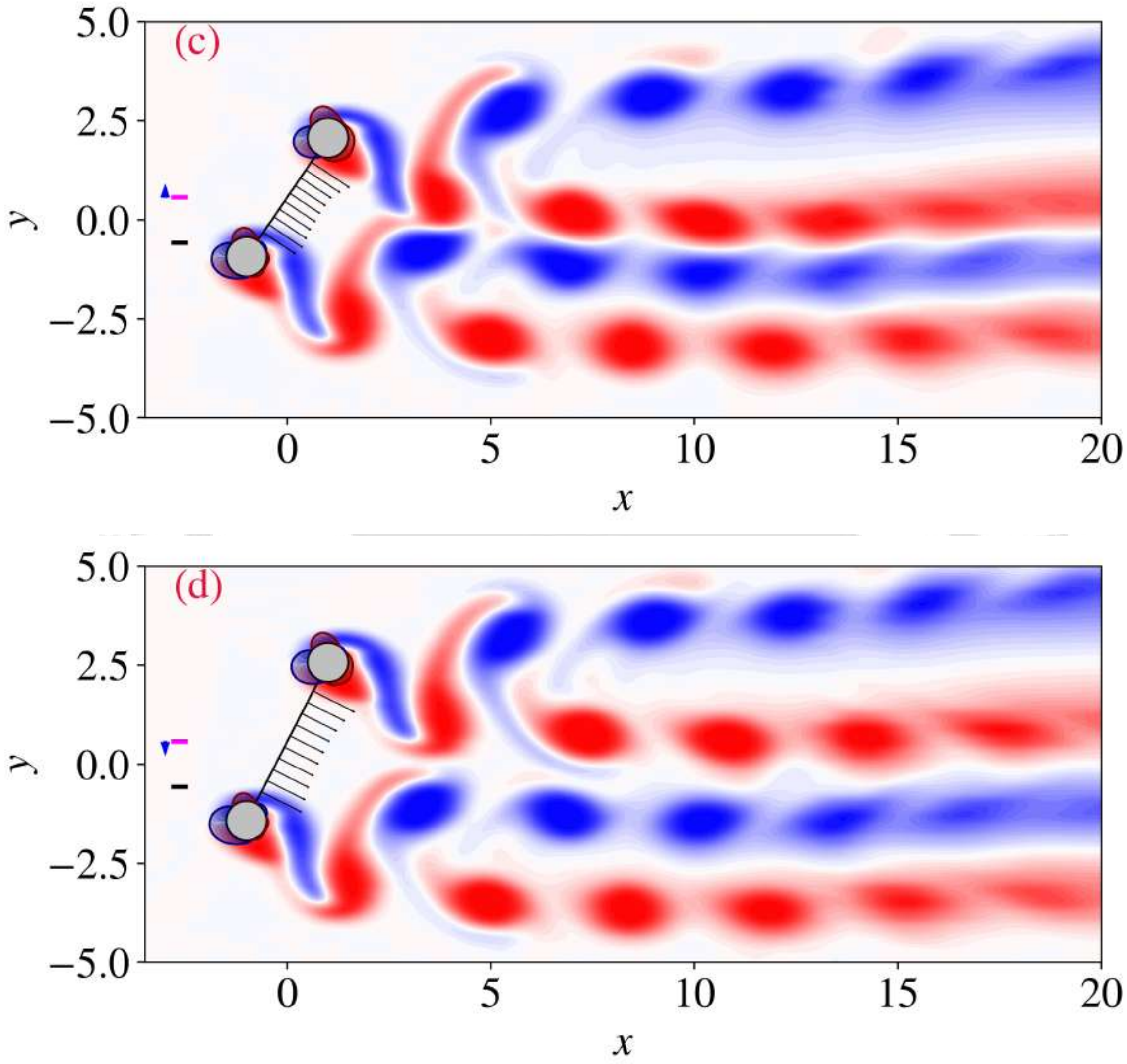

Fig. 3.13 Vorticity contours and pressure distribution around the cylinders at the upper branch (UB) of oscillation for $L = 2.0$ with the variation of T. The reduced velocities are $U^* = 5.0$ for (a), and $U^* = 4.0$ for (b)–(d). From (a) to (d), the T increases from 0 to 4.0. All the contours are captured when the cylinder is at maximum displacement.

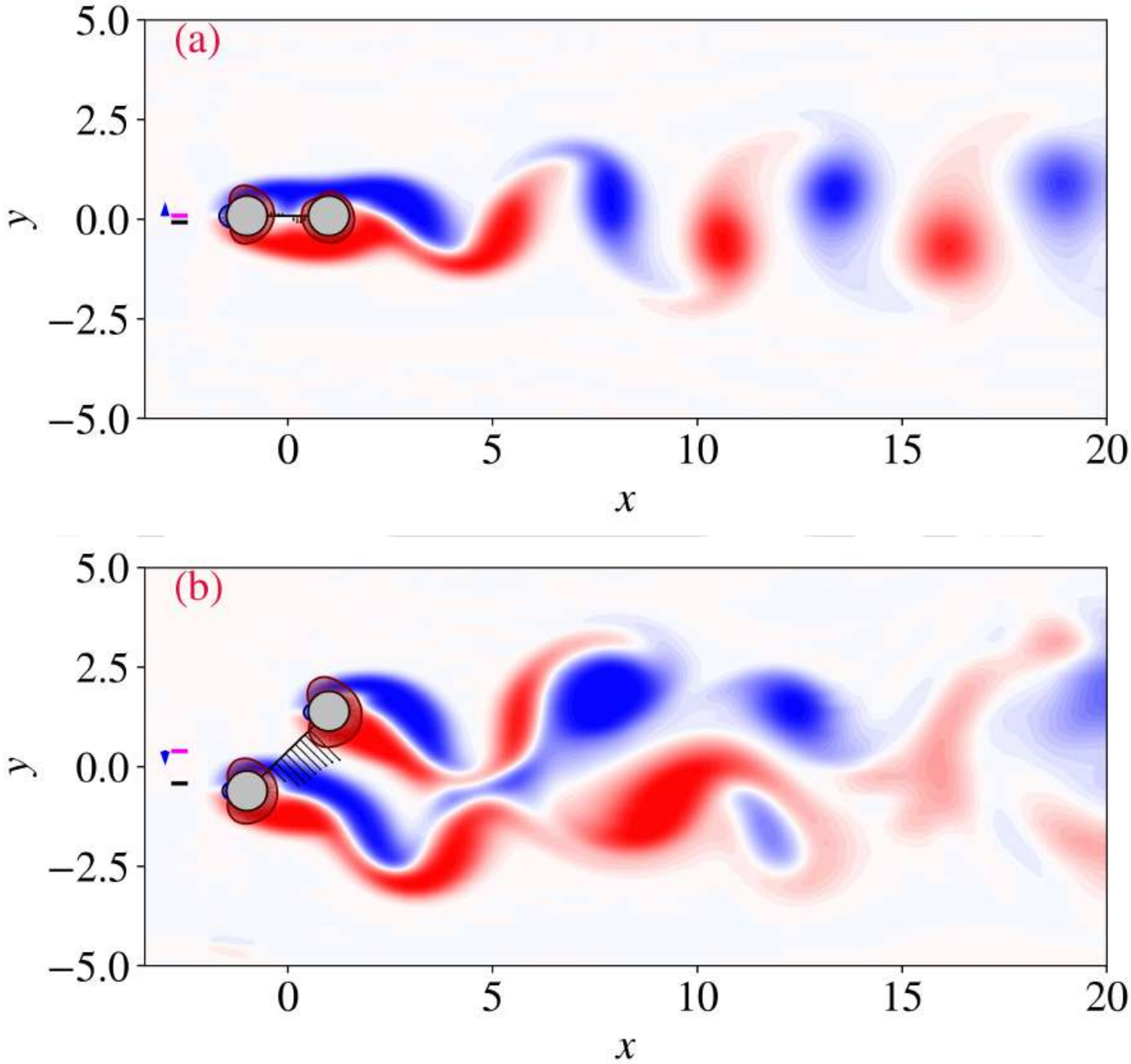

(a)
5.0
2.5
0.0
−2.5
−5.0
y
0
5
10
15
20
x
(b)
5.0
2.5
0.0
−2.5
−5.0
y
0
5
10
15
20
x

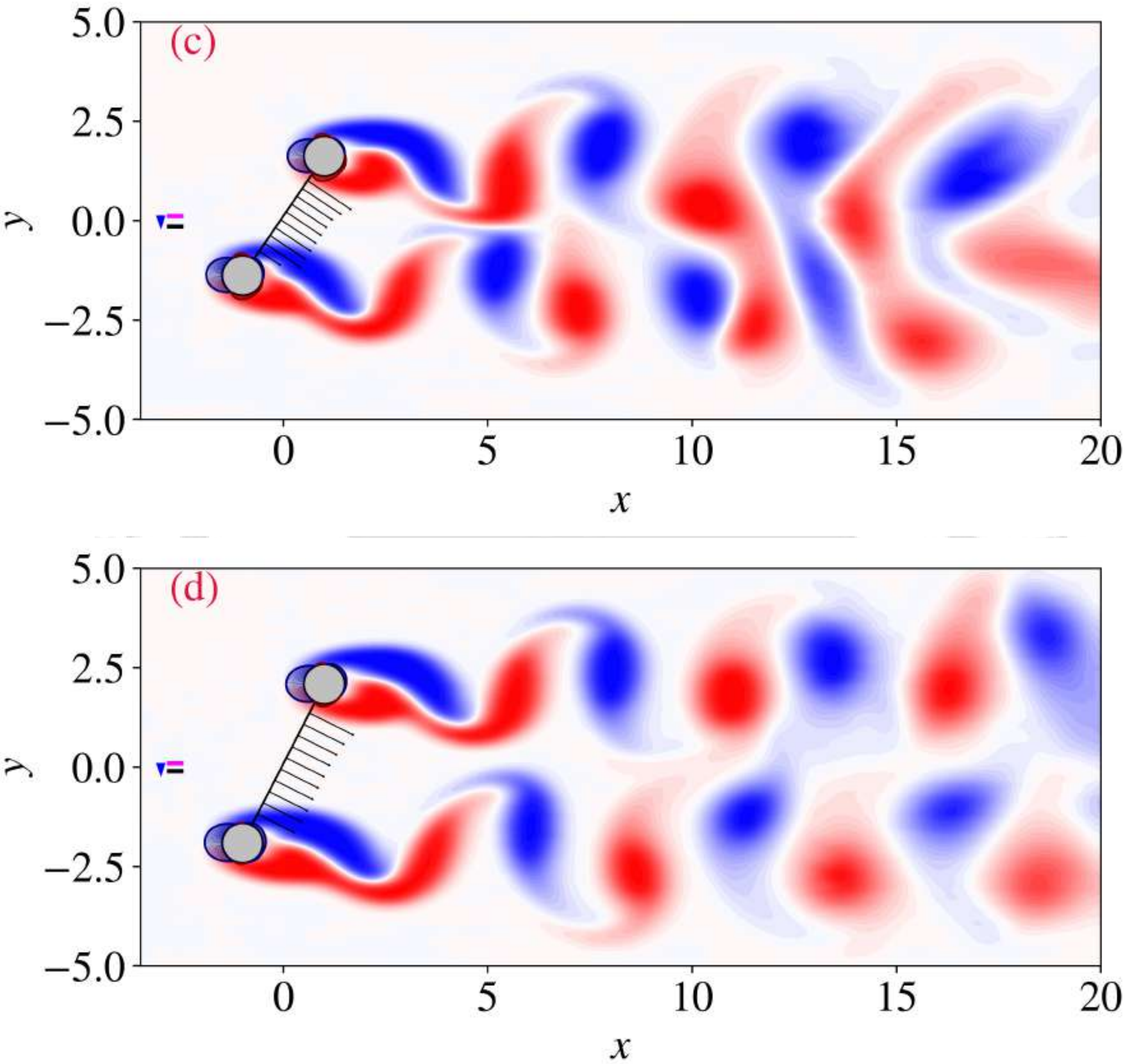

Fig. 3.14 Vorticity contours and pressure distribution around the cylinders at the lower branch (LB) of oscillation for $L = 2.0$ with the variation of T. The reduced velocities are $U^{*} = 7.0$ for (a), and $U^{*} = 8.0$ for (b)–(d). From (a) to (d), the T increases from 0 to 4.0. All the contours are captured when the cylinder is at maximum displacement.

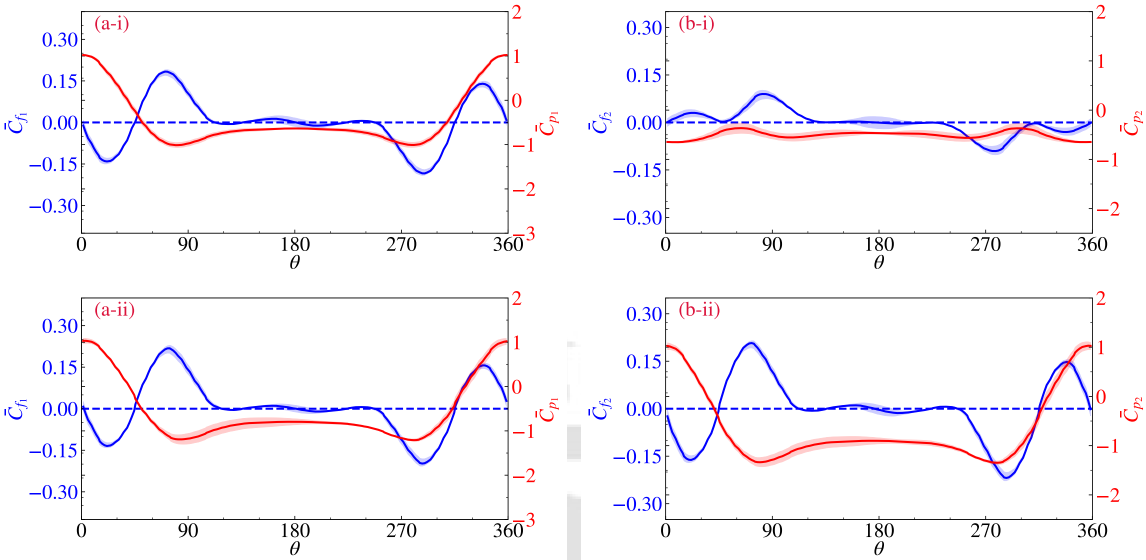

Fig. 3.15 Time-averaged skin friction coefficient ($\bar{C_f}$) and pressure coefficient ($\bar{C_p}$) of upstream cylinder tandem case of $L = 2.0$ (a-i) and staggered case of $L = 2.0$, $T = 4.0$ (a-ii) at the lower branch (LB). Similar for the downstream cylinder in (b-i) and (b-ii). The localized transient variation is shown by the shaded region.

2025). The separation points do not change for the upstream and downstream cylinders; however, they are shifted more towards the leeward side of the cylinders compared to that of the initial branch of the tandem case. At $T = 2.0$, the vortices of the upstream cylinder are suppressed (Figure 3.13b). With a further increase in T, separate 2S vortex-streets are observed, and without any change in separation points (Figures 3.13c and d). When at the lower branch, the tandem case shows a C(2S) type of vortex shedding (Figure 3.14a). The oscillation amplitude diminishes, and the c_g decreases, and continuous reattachment (CR) of the shear layer on the downstream cylinder is noticed. The separation points on the upstream cylinder are observed at 113° and 247°, quite different from that of the initial branch of the tandem case (Figures 3.15(a-i)). The downstream cylinder shows separation from 122° to 177° (Figures 3.15(b-i)). For the staggered case of $L = 2.0$, $T = 2.0$, while the upper separation point of the downstream cylinder shifts to the windward side (115°), the lower separation points of both cylinders stay in the range of 244°–249°. With an increase in T, the lower separation point of both cylinders stabilizes at 247° (Figures 3.15(a-ii) and (b-ii)). The pressure variation across all the arrangements is low, which renders a low lift force on the cylinders.

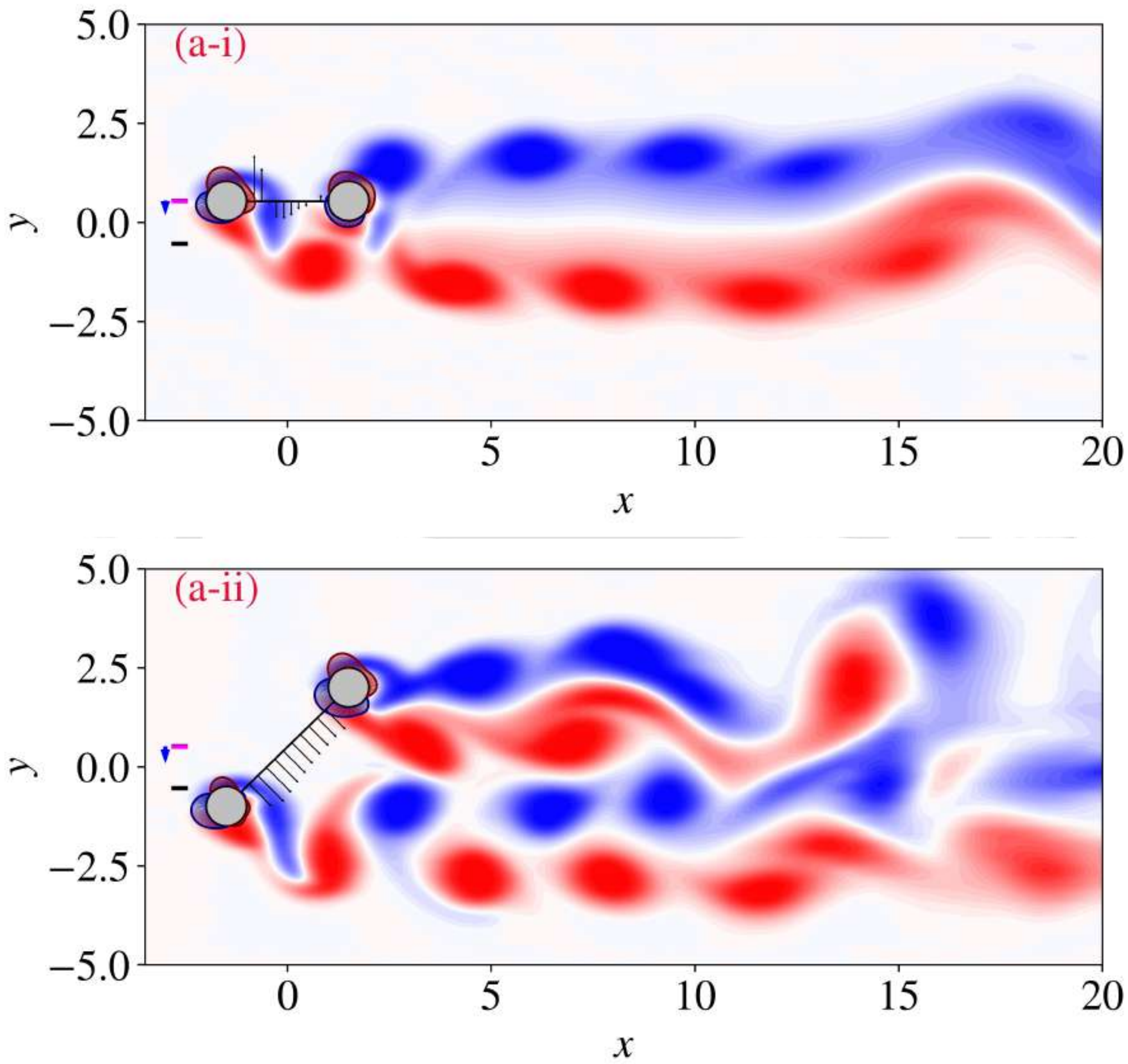
(a-i)
5.0
2.5
0.0
−2.5
−5.0
y
0
5
10
15
20
x
(a-ii)
5.0
2.5
0.0
−2.5
−5.0
y
0
5
10
15
20
x

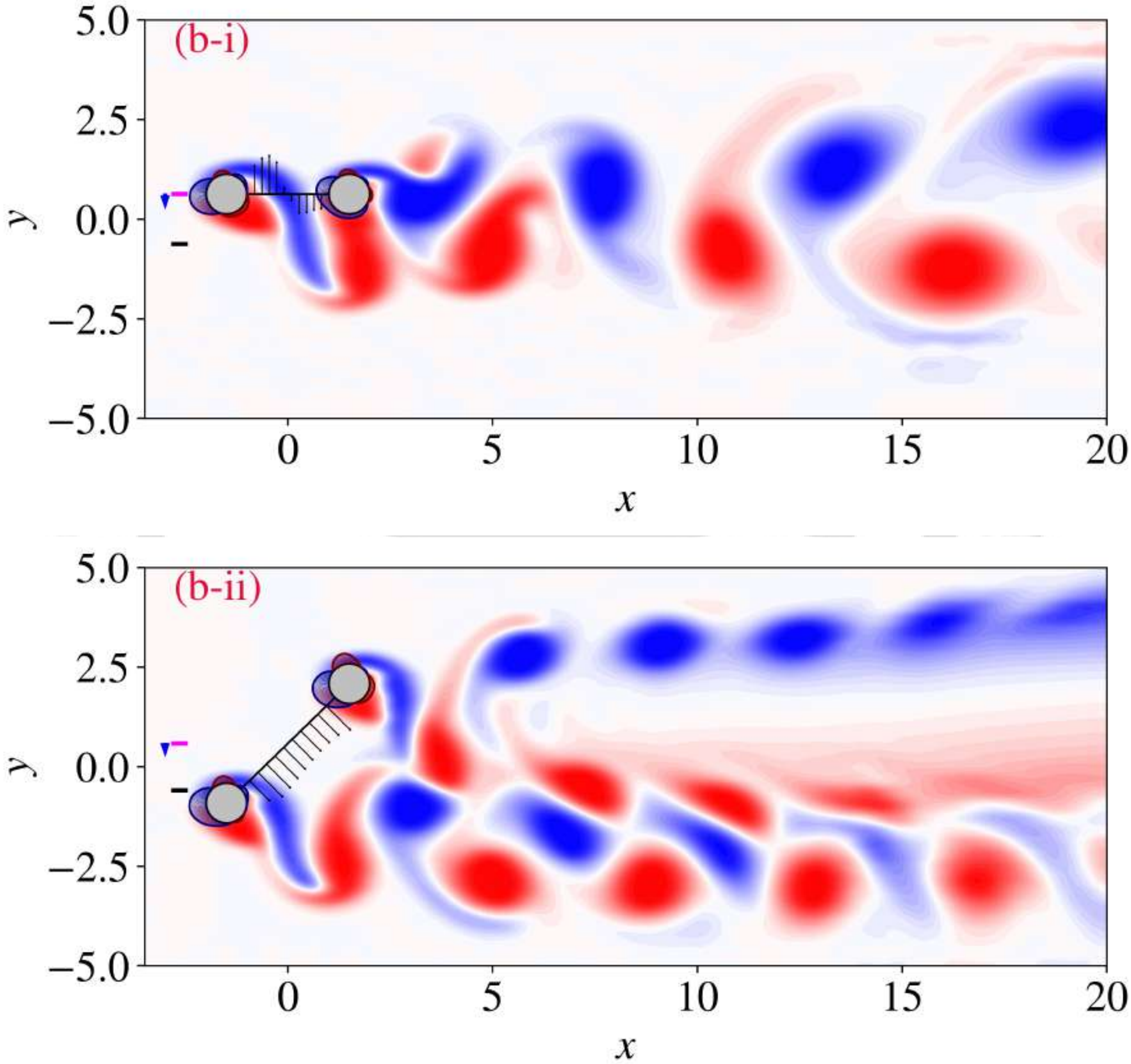
(b-i)
(b-ii)
5.0
2.5
0.0
−2.5
−5.0
y
0
5
10
15
20
x

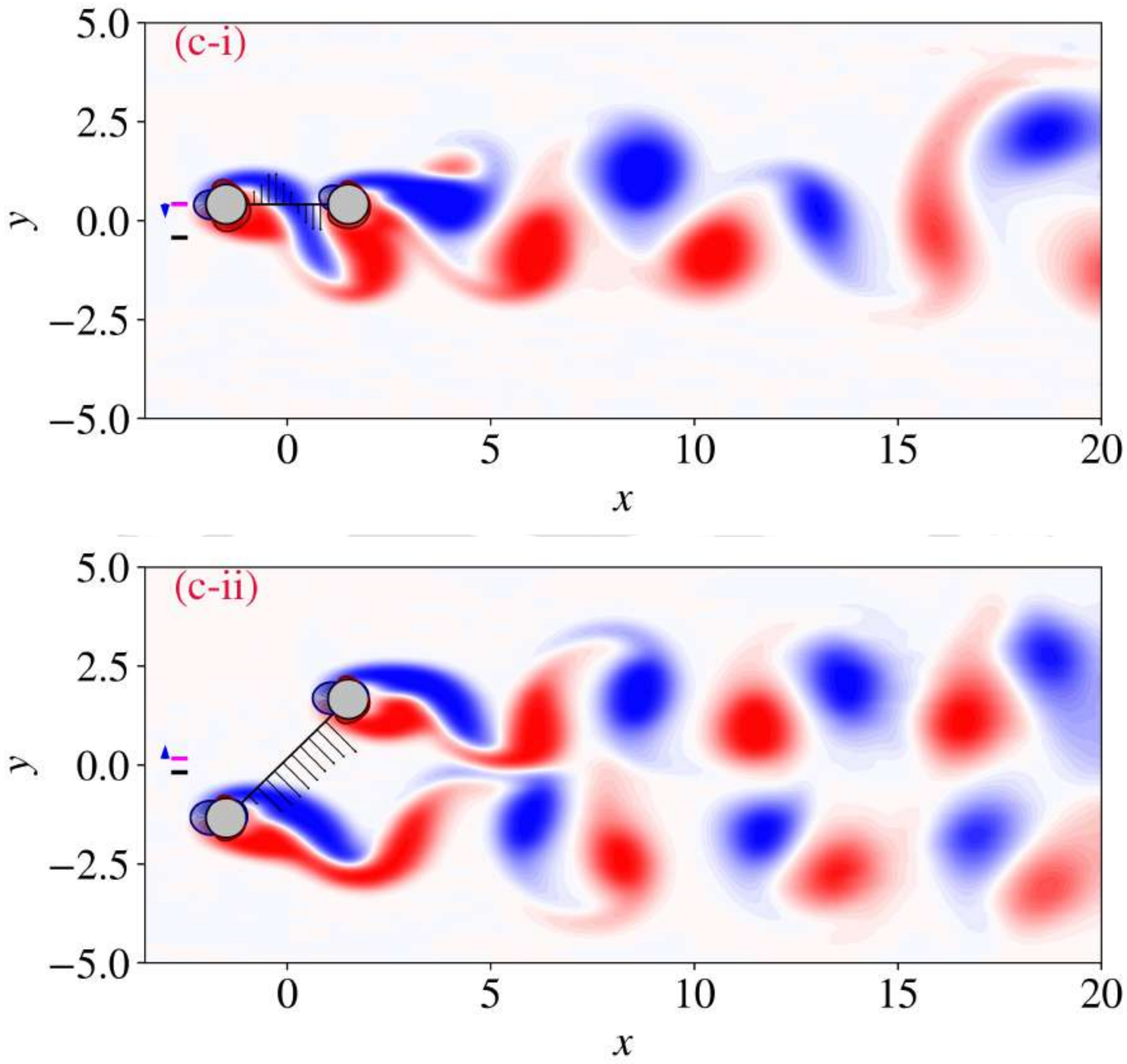

Fig. 3.16 Vorticity contours and pressure distribution around the cylinders for $L = 3.0$ with the variation of T. From (a-i) to (c-i) shows the contours for the tandem case, and from (a-ii) to (c-ii) shows the staggered case of $L = 3.0$, $T = 3.0$. The reduced velocities are $U^* = 4.0$ for (a-i), $U^* = 3.5$ for (a-ii), $U^* = 5.5$ for (b-i), $U^* = 4.0$ for (b-ii), $U^* = 9.0$ for (c-i), and $U^* = 7.0$ for (c-ii). The figures (a) represent the initial, (b) upper, and (c) lower branch of oscillation. All the contours are captured when the cylinder is at maximum displacement.

Figure 3.16 compares the vorticity contours between the tandem case of $L = 3.0$ and $L = 3.0$, $T = 3.0$ at the initial, upper, and lower branch of oscillation. The gap flow is significant for the tandem case of $L = 3.0$ compared to the tandem case of $L = 2.0$. The vorticity contours change from 2S at the initial branch to C(2S) at the upper and lower branch. At the initial branch, though the AR mode is observed, at the upper and lower branch of response, co-shedding (CS) mode emerges where upstream and downstream cylinders shed vortices in phase. As T increases, the gap flow velocity increases. At the initial branch, the shear layer of the downstream cylinder detaches; however, the shear layer also rolls up at the wake. The upstream cylinder exhibits a 2S type of vortex shedding. However, at the upper branch, the elongated shear layer of the downstream cylinder vanishes, and the width of the 2S vortex-street increases while the upstream 2S vortices are suppressed. Two separate C(2S) vortex streets are observed at the lower branch, resulting in a weak interaction between the cylinders. As seen from Figure 3.17, there is no difference in vorticity contours for the tandem cases of $L = 3.0$ and 4.0. The only difference is the increased c_g as L is higher. Therefore, the shear layer is dragged vertically at the upper and lower branch of the vibration response. The AR mode prevails across all U^*. The shear layer stayed attached for a longer streamwise length at the initial branch for $L = 4.0$, $T = 4.0$ (Figure 3.17(aii)). At the upper and lower branch, two individual 2S and C(2S) vortex streets are noticed due to the weak interaction of shear layers between the cylinders. There is no such difference in separation points for the tandem and staggered cases across all U^* for $L = 4.0$.

3.5 Summary

This numerical study examines the effect of transverse spacing on the flow characteristics of rigidly coupled staggered cylinders, and the results are compared with those from tandem configurations at a Reynolds number of $\mathrm{Re} = 150$. The center-to-center distance in streamwise (L) and transverse (T) direction are varied from 2.0 to 4.0 in the U^* range of 3.0–15.0.

The variation in transient amplitudes in the lower branch is smaller than in the upper branch, in contrast to classical single-cylinder VIV. Across all configurations, the transient amplitude and the range of reduced velocity exhibiting significant vibration amplitudes are the largest at $T = 0$ and decrease with increasing T. The maximum vibration amplitude generally decreases with increasing T, except for the tandem case

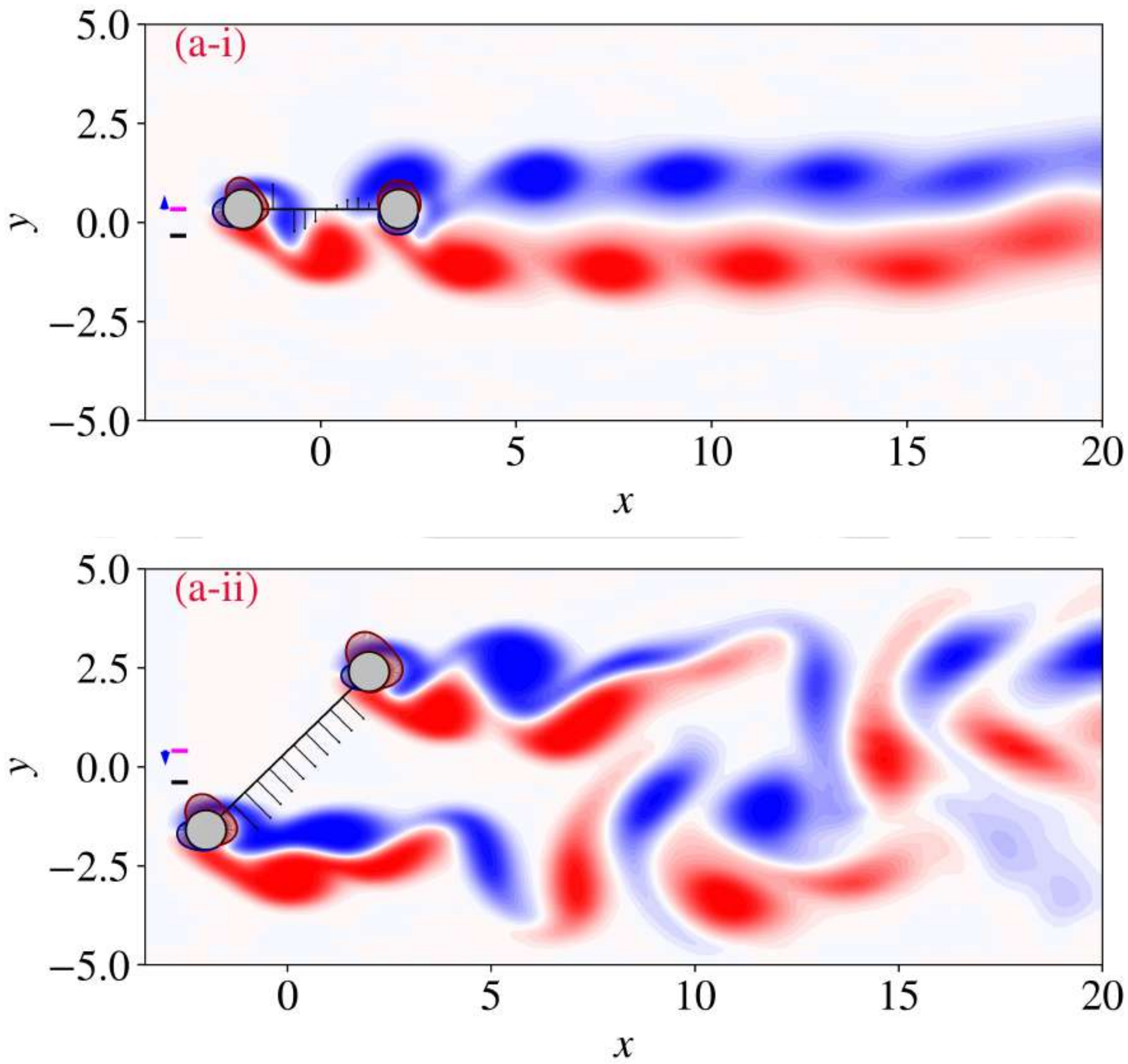
(a-i)
5.0
2.5
0.0
−2.5
−5.0
y
0
5
10
15
20
x
(a-ii)
5.0
2.5
0.0
−2.5
−5.0
y
0
5
10
15
20
x

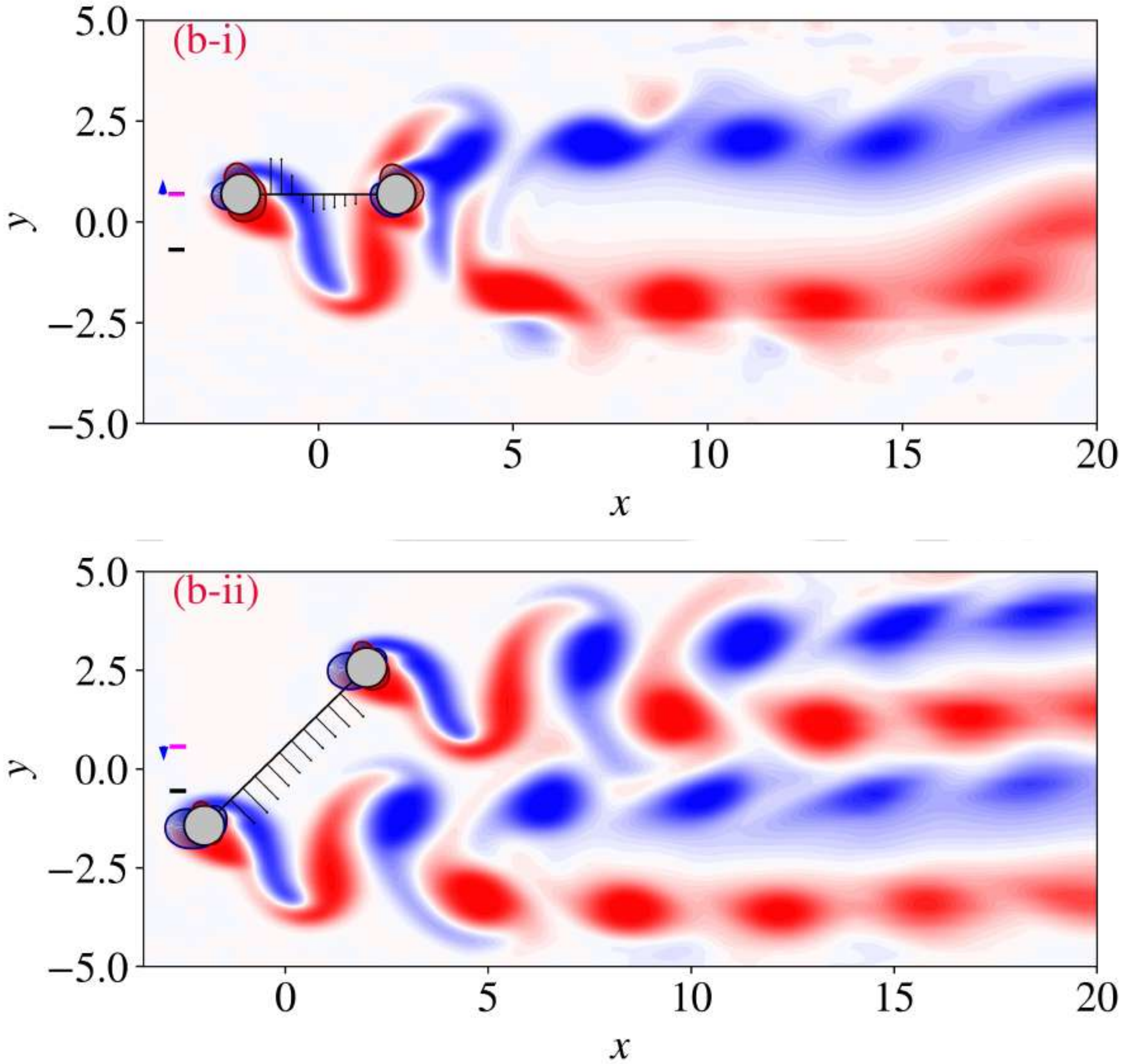

(b-i)
5.0
2.5
0.0
−2.5
−5.0
y
0
5
10
15
20
x
(b-ii)
5.0
2.5
0.0
−2.5
−5.0
y
0
5
10
15
20
x

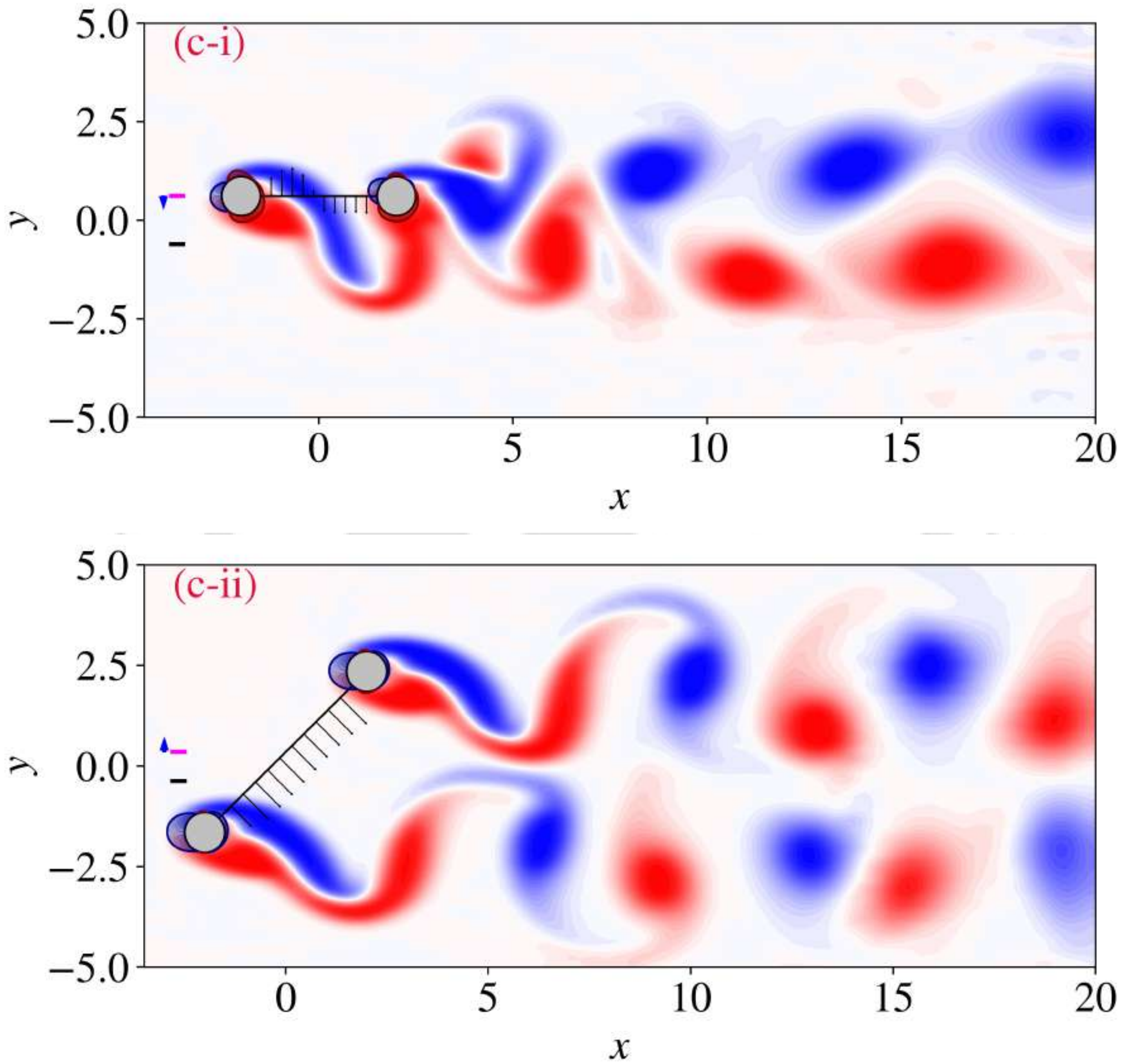

Fig. 3.17 Vorticity contours and pressure distribution around the cylinders for $L = 4.0$ with the variation of T. From (a-i) to (c-i) shows the contours for the tandem case, and from (a-ii) to (c-ii) shows the staggered case of $L = 4.0$, $T = 4.0$. The reduced velocities are $U^* = 4.0$ for (a-i), $U^* = 3.5$ for (a-ii), $U^* = 5.0$ for (b-i), $U^* = 4.5$ for (b-ii), $U^* = 8.0$ for (c-i), and $U^* = 7.0$ for (c-ii). The figures (a) represent the initial, (b) upper, and (c) lower branch of oscillation. All the contours are captured when the cylinder is at maximum displacement.

at $L = 2.0$. Notably, this tandem configuration also exhibits the narrowest band of significant amplitudes. In contrast, the arrangement of $L = 2.0$, $T = 2.0$ exhibits a broad region of both significant amplitudes and considerable transient amplitude variation.

The onset of desynchronization (when $f \approx f_{\mathrm{St}}$) varies non-monotonically with T for $L = 2.0$, but shifts linearly toward lower U^* with increasing T for $L = 4.0$. No global lock-in region is observed for the tandem configuration at $L = 3.0$. Although for staggered cases, the onset consistently occurs near $U^* = 7.5$. From a phase-difference perspective, the lower-branch width at $L = 3.0$ increases with T, which appears contradictory. Despite this, the desynchronization trends inferred from the frequency and phase definitions (i.e. when $\phi \approx 180°$) are broadly consistent.

For $L = 2.0$, the upper- and lower-branch widths reduce as T increases from 2.0 to 4.0, owing to weakened shear-layer interaction. At $L = 3.0$, the tandem configuration exhibits a broader initial and upper branch compared to staggered cases, whereas the lower-branch width increases with T. For $L = 4.0$, the upper-branch width systematically decreases with increasing T.

Classical global synchronization is not observed for the tandem arrangement at ($L = 2.0$, $T = 2.0$). Instead, only partial synchronization occurs. With increasing T, this partial lock-in evolves into a lock-in with sub-harmonics. Even at larger L, global lock-in with sub-harmonics emerges for staggered cases, while tandem cases continue to exhibit partial lock-in.

The downstream cylinder dominates the wake dynamics, as its lift coefficient typically exceeds that of the upstream cylinder, except in the tandem case at $L = 2.0$. Increasing T reduces the shielding effect, though the upstream and downstream lift coefficients vary non-monotonically with T. However, the combined lift increases monotonically with T for $L = 2.0$ and $L = 4.0$ and varies non-monotonically for $L = 3.0$. These lift behaviors are primarily governed by the pressure distribution, which is directly influenced by gap-flow bias and shear-layer interactions: more substantial gap-flow bias and larger pressure variation around a cylinder lead to higher lift. Shear-layer elongation alone does not control the lift characteristics.

For tandem cases, the mean upper and lower separation points on both cylinders shift toward the windward side when transitioning from the initial to the lower branch, explaining the associated reduction in lift. In contrast, staggered cases show little variation in separation location.

Chapter 4

The effects of spacing and damping on vortex-induced vibration of two rigidly coupled circular cylinders in tandem arrangement

Power extraction from multiple bluff bodies undergoing VIV is a newer addition in application VIV. The power generation depends on number of cylinders, their configurations and spacing. A big chunk of past work focuses on power generation from uncoupled multiple cylinders. The power production capabilities of rigidly coupled cylinder in tandem are ventured with varying spacing. The introduction includes various parameters affecting power production of multiple bluff bodies and motivation for this study (§ 4.1). The effects of damping and tandem spacing on different parameters (such as vibration amplitude, phase difference, and lift coefficient) are discussed in § 4.3. Then, the power harvesting of tandem cylinders at different spacing and damping is discussed along with power extraction efficiency and power density. The chapter then concludes with a summary of the findings (§ 4.4).

4.1 Introduction

As discussed in Chapter 3, VIV-based energy harvesting systems have been studied extensively, with damping ratio, cylinder spacing, and configuration identified as the key parameters governing power output. Prior studies on tandem arrangements have focused primarily on uncoupled cylinders: Sun et al. (2017) found that extracted power increases in the galloping region as spacing decreases, Ding et al. (2019) showed that two uncoupled cylinders in tandem outperform a single cylinder, and Kim and Bernitsas (2016) identified three cylinders as the optimal configuration for power synergy, though Li et al. (2021) noted this synergy diminishes at higher flow velocities.

From the above discussion and literature review in Chapter 1, it is evident that increasing the number of cylinders can enhance power generation in the VIV regime, and cylinder spacing plays a key role in overall output. PTC cylinders provide higher power output but are susceptible to galloping-induced instability, which can be catastrophic. Therefore, VIV-based energy harvesting systems remain attractive owing to their higher efficiency and built-in safety due to desynchronization at higher flow speeds. An energy harvesting system consisting of uncoupled cylinders is expected to be costly and susceptible to frequent failures, due to a larger number of moving parts, than a system based on rigidly coupled cylinders mounted on a single linear guide. For these reasons, the application of rigidly coupled cylinders for the large-scale flow energy extraction needs to be explored. While previous studies have examined wake dynamics and vibration response of rigidly coupled cylinders undergoing VIV, their implications for energy harvesting remain unexplored. To fill this gap in the literature, the present study is focused on VIV of rigidly coupled tandem cylinders to assess their power extraction capability across a range of tandem spacings and damping ratios. By numerically analyzing two rigidly coupled cylinders in tandem with spacing ratios $L = 2.0 - 6.0$ and damping ratios $0 - 0.30$, this study provides new insights into how inter-cylinder spacing and structural coupling influence power output, thereby identifying design conditions that can enhance the viability of VIV-based energy harvesters. The tandem spacings considered in this study is consistent with the existing literature on the flow characteristics of rigidly coupled tandem cylinders undergoing vortex-induced vibrations (Zhao, 2013), where increased vibration amplitude and lift coefficient have been reported within this range. The damping ratio is selected in the range 0–0.30, since the optimum damping ratio for a single cylinder undergoing vortex-induced vibrations has been found to lie within this interval (Soti et al., 2017, 2018).

4.2 Formulation

4.2.1 Problem definition

The computational domain for this study is shown in Chapter 3 in Figure 3.1. The domain and temporal independence is mentioned in Chapter 3 and Appendix B. The mass ratio is kept constant at 2.0 while U^* varies from 3.0 to 15.0. The damping ratio varies in the range 0–0.30.

The flow is initialized with a uniform velocity U. At the inlet, uniform velocity boundary conditions are applied: $u = U$ and $v = 0$. The top and bottom boundaries are treated as symmetry planes, enforcing $\frac{\partial u}{\partial y} = 0$ and $v = 0$. At the outlet, a zero-gradient boundary condition is applied: $\frac{\partial u}{\partial x} = 0$ and $\frac{\partial v}{\partial x} = 0$. A no-slip boundary condition is imposed on the cylinder surfaces, $u = u_{wall}$.

All the simulations are carried out in a two-dimensional domain at Re = 150 as the flow remains two-dimensional up to Re = 200 (Leontini et al., 2006). By performing curve fitting on experimental data, Govardhan and Williamson (2006) showed that the maximum vibration amplitude of the circular cylinder increases linearly with $\log_{10}$ Re. This fit extends from laminar to high Reynolds number regimes. Soti et al. (2018) extended the fit to predict the maximum power output from the circular cylinder and found it also to be an increasing function of Re. Their fit requires the knowledge of optimal values of the mass-damping parameter ($\alpha = m^*\zeta$) and reduced velocity (U^*) for the maximum power extraction. By taking the optimal values of α and U^* to be 0.25 and 5.0, respectively, their prediction of the maximum power deviated by 12% for Re = 150 and by 18% for Re = 2222–6661 from the published results. A higher deviation at larger Re could be due to the variation of the optimal α with Re (Soti and De, 2020). The increasing trend of the maximum power with Re has also been demonstrated experimentally (Soti et al., 2018). Therefore, the observations for the power and efficiency from the low-Re studies are expected to extend to higher Re regimes. Also, low-Re simulations can significantly reduce the requirement of computational resources, thereby allowing us to cover the large parameter space of the problem.

The mesh independence and validation are shown in Tables 3.5 and 3.3, respectively. The detailed computational mesh around the cylinders is shown in Appendix A.

4.3 Results and discussion

Vortex-induced vibration of rigidly coupled cylinders depends primarily on five parameters: reduced velocity (U^*), mass ratio (m^*), damping ratio (ζ), Reynolds number (Re) and cylinder gap (L). Two rigidly coupled elastically mounted cylinders in tandem are constrained to move in the cross-flow direction at Re = 150. The U^* varied in the range $3.0 \leqslant U^* \leqslant 15.0$, and the ζ, varies between 0 and 0.30. The effects of damping (ζ) and gap (L) between two cylinders on their VIV characteristics, namely vibration amplitude and the phase difference between lift force and displacement, are presented. Sections 4.3.1, 4.3.2 and 4.3.3 describe the influence of damping and cylinder gaping on oscillation amplitude, phase difference and lift coefficient, respectively. In Section 4.3.4, the influence of damping and tandem gaping on power extraction is discussed, followed by a discussion of efficiency and power density in Section 4.3.5.

4.3.1 The effect of damping and tandem spacing on the vibration response

The effect of U^* and ζ on the vibration response in various tandem arrangements is shown in Figure 4.1. The trend of oscillation amplitude with U^* closely resembles that of a single cylinder at low Re (Leontini et al., 2006). The vibration amplitude, A^*, is calculated using the following expression:

$$A^* = \frac{1}{2}(y_{\max} - y_{\min}) \tag{4.1}$$

where $y_{\max}$ and $y_{\min}$ are the maximum and minimum cylinder displacements after reaching a dynamic steady state, i.e., once the initial transients in the cylinder motion disappears and it settles into a periodic motion with nearly constant amplitude. The maximum undamped and damped amplitude for this L is observed in the range of $U^* = 4.5$ and 5.0. Maximum amplitude at zero damping for $L = 2.0$ is comparable to that of a single cylinder (Zhao, 2013). A sharp jump in amplitude is observed at $U^* = 4.0$, followed by a sudden dip in amplitude at $U^* = 6.0$ (Figure 4.1(a)). However, in the case of $L = 3.0$, the oscillation amplitude falls gradually with U^* at zero damping and becomes constant at $U^* > 11.0$, as observed in Figure 4.1(b). Increasing damping smoothens the jump and fall in amplitude. Another small jump is observed at $U^* = 5.5$ for $L = 3.0$, before a drop in amplitude at $U^* = 5.0$. The drop and jump shift to $U^* = 5.5$ and 6.0 for $\zeta = 0.10$ and 0.15, respectively. Figure

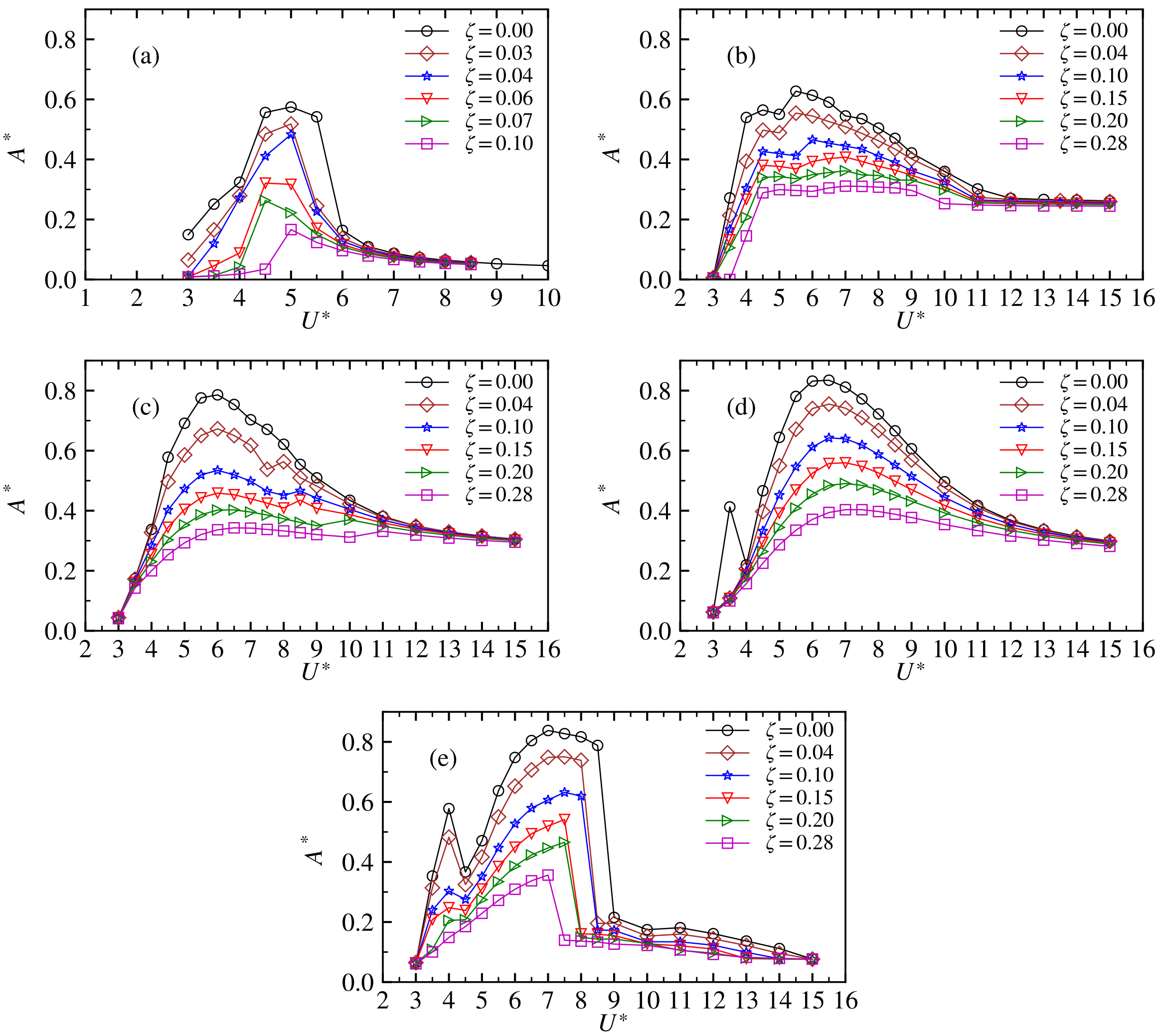

Fig. 4.1 Variation of amplitude response with U^* for (a) $L = 2.0$, (b) $L = 3.0$, (c) $L = 4.0$, (d) $L = 5.0$, and (e) $L = 6.0$ across different ζ.

4.1(c) depicts that for $L = 4.0$, the drop and jump in amplitude are at higher U^* than those of $L = 3.0$. With the increase in ζ, the drop and jump position of the oscillation amplitude shift to a higher U^*. In the case of $L = 5.0$, no sharp or short jump or fall in vibration amplitude is observed except at $U^* = 3.5$ at zero damping (Figure 4.1(d)). The maximum amplitude shifts to higher U^* with an increase in damping at $L = 3.0$, 4.0, and 5.0. But for the case of $L = 6.0$, the maximum amplitude shifts to lower U^* as damping increases. The sharp kink and drop in amplitude are also observed for $L = 6.0$ at $U^* = 4.0$ and 4.5 (Figure 4.1(e)). The sharp fall in amplitude is also observed to shift to lower U^*. The sharp drop in oscillation amplitude at $L = 6.0$ is similar to the drop in amplitude reported at $L = 2.0$. Therefore, the cylinders desynchronize after

$U^* = 6.0$ for $L = 2.0$ and after $U^* = 9.0$ for $L = 6.0$. Irrespective of L, the vibration amplitude values converge across all ζ at low reduced velocity ($U^* = 3.0$) and high reduced velocities ($U^* \geqslant 11.0$) with a few exceptions (Figure 4.1). However, in between the U^* range, the amplitude decreases with increasing ζ. The peak amplitude shifts gradually to a higher U^* with the increase in L, except at $L = 6.0$. The maximum amplitude is also seen increasing with an increase in L. The near-constant oscillation amplitude persisting to high U^* for $L = 3.0$, 4.0, and 5.0 indicates a widening of the synchronization region with increasing spacing, the implications of which for power extraction are discussed in Section 4.3.4.

4.3.2 The effect of damping and tandem spacing on the phase difference

Given the periodic nature of the cylinder motion, both the displacement and lift force can be approximated using their primary harmonic components. In the lower branch, the displacement is largely dominated by a single frequency and can be written as $y = A^* \sin(2\pi ft/U^*)$, while the corresponding lift force takes the form $C_L = C_{L0} \sin(2\pi ft/U^* + \phi)$. Here, C_{L0} represents the amplitude of the lift force, and ϕ denotes the phase difference between the lift force and the cylinder displacement, calculated via the Hilbert transform of the respective signals (see Chapter 3), which is analyzed in the following section. It is also serves as a reliable indicator of different response branches in VIV. When the force and displacement are in phase, the phase angle becomes 0° and the initial branch is observed. Similarly, when both are out of phase, the phase angle becomes 180° and the initial branch switches to the lower branch (Khalak and Williamson, 1999). The Figure 4.2 shows the variation of ϕ with U^* at different ζ for different L. The phase difference ϕ is nearly 0° in the range of $3.0 \leqslant U^* \leqslant 6.0$ at $L = 2.0$, and at $U^* = 6.0$, the phase jumps to 180° at zero damping. It indicates the transition from the initial to the lower branch. Similar observations are recorded in the work of Feng (1968) and Khalak and Williamson (1999). The transition is also visible in the amplitude curve with a dip in vibration amplitude in Figure 4.1. The transition from 0° to 180° is smeared out as ζ increase. Damping slows down the structure's response, and depending on the damping, phase difference takes intermediate values between 0° and 180°. Though in the ideal case for a single cylinder, the highest oscillation amplitude occurs at $\phi = 90°$. However, this does not happen in the case of $L = 2.0$. The relations between ϕ and U^* follows a similar trend at $L = 3.0$

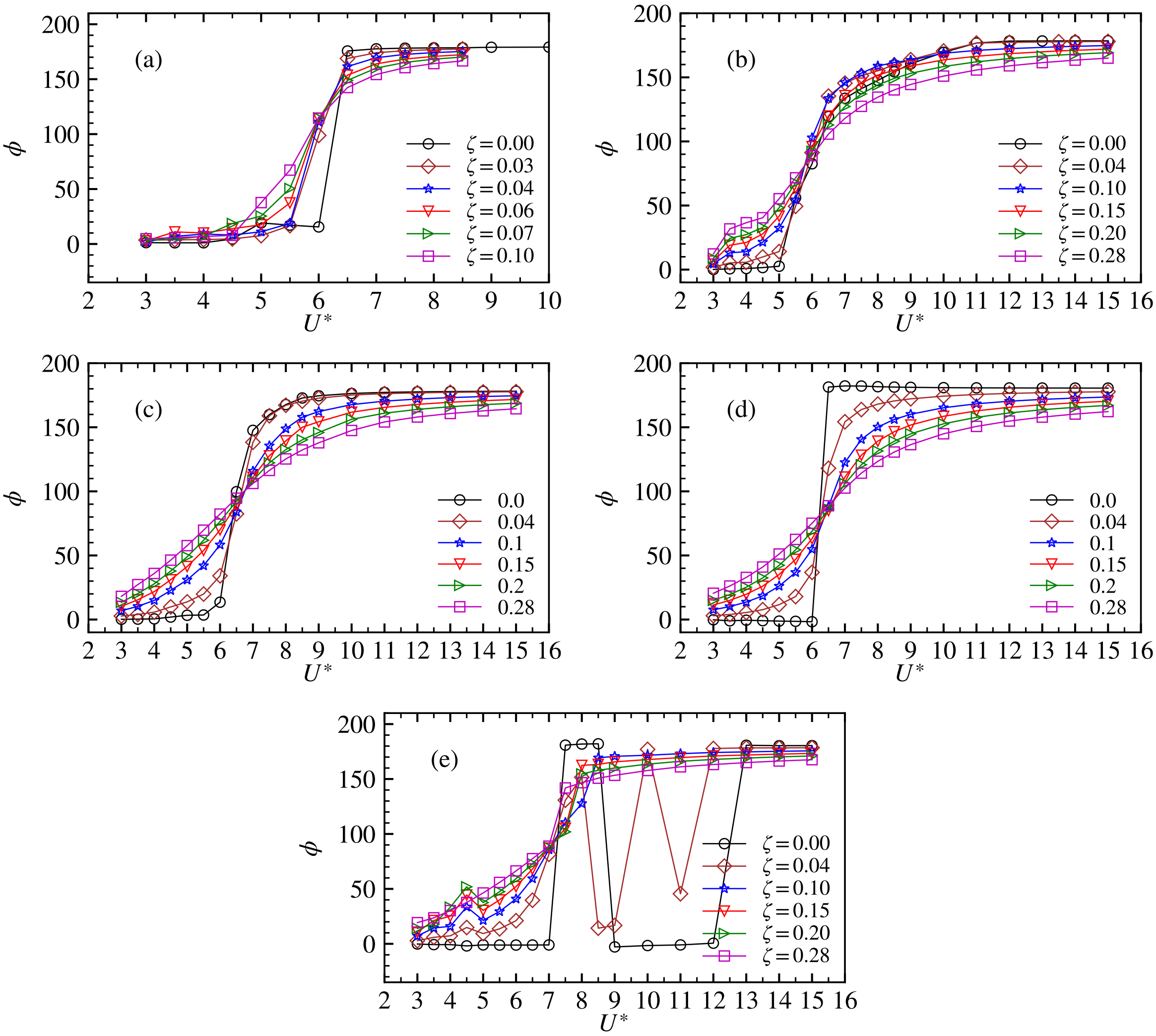

Fig. 4.2 Variation of phase difference with U^* for (a) $L = 2.0$, (b) $L = 3.0$, (c) $L = 4.0$, (d) $L = 5.0$, and (c) $L = 6.0$ across different ζ.

and $L = 2.0$. The only difference is that just before the jump in ϕ, the amplitude starts to diminish at $L = 2.0$. In contrast, at $L = 3.0$, the maximum amplitude occurs just prior to the phase jump. No significant visual variation is noted in the relationship between in ϕ and U^* for $L = 3.0$, 4.0, and 5.0 (Figure 4.2). Hence, only the $L = 3.0$ case is represented. At $L = 6.0$, the drop in phase angle from 180° to 0° is observed at $U^* = 9.0$ with zero damping (Figure 4.2(c)). It can also be inferred from the drop in oscillation amplitude response at $U^* = 9.0$. Following this, ϕ jumps back to 180° at $U^* = 13.0$. The drop in ϕ for $\zeta = 0.04$ occurs only in the range of $8.5 \leqslant U^* \leqslant 9.0$. At $U^* = 10.0$, ϕ again jumps to almost 180°, followed by further fall and jump at $U^* = 11.0$ and 12.0, respectively. A similar phase difference behavior has also been reported for undamped rigidly coupled tandem cylinders by Zhao (2013). However, the physical mechanism behind this phenomenon remains unclear and would require a dedicated hysteresis analysis; as the present study focuses on power extraction across spacing and damping parameters, this is left for future investigation.

4.3.3 The effect of damping and tandem spacing on the RMS lift coefficient

The root-mean-square (RMS) lift coefficient, $C_{L_{RMS}}$, is the ratio of the combined RMS lift force of two cylinders to the total fluid force at a velocity U through an area projected by two cylinders, i.e, $C_{L_{RMS}} = F_{L_{RMS}}/0.5\rho U^2 D$, where $F_{L_{RMS}}$ is the combined RMS lift force of two cylinders. The lift coefficients for various ζ values are plotted against U^* for different L in Figure 4.3. The RMS lift coefficient of the stationary tandem cylinders is denoted as C_{L_S}. Peak $C_{L_{\mathrm{RMS}}}$ occurs at different U^*, depending on ζ and L. After reaching a minimum point, $C_{L_{\mathrm{RMS}}}$ recovers in the lower branch. The transition from one branch to another is observed when the lift coefficient approaches the lowest value. In the initial branch, $C_{L_{\mathrm{RMS}}}$ increases and then decreases. The jump and fall of $C_{L_{\mathrm{RMS}}}$ are prominent for lower ζ values, but with the increase in ζ, the jump is smeared out except for $L = 3.0$ and 4.0. Therefore, the initial to lower branch transition for $L = 2.0$, 3.0, 4.0, 5.0, and 6.0 happens at $U^* = 5.5$, 6.0, 6.5, 6.5 and 7.0, respectively (Figure 4.3). For all tandem gaps, peak $C_{L_{\mathrm{RMS}}}$ of all ζ converges beyond $U^* \geqslant 9.0$ except at $L = 3.0$. In the transition region, the minimum $C_{L_{\mathrm{RMS}}}$ varies with different values of ζ. With the increase in gaping, the transition shifts to a higher U^* value. In the initial branch, the force and displacement are in phase, which corresponds to high $C_{L_{\mathrm{RMS}}}$. However, in the transition region, the phase reversal leads to a reduction in $C_{L_{\mathrm{RMS}}}$, and the lift coefficient is observed to decrease beyond C_{L_S}. In the lower branch, $C_{L_{\mathrm{RMS}}}$ either remains constant or increase slightly depending on ζ and L. Also, at minimum $C_{L_{\mathrm{RMS}}}$, the maximum oscillation amplitude is observed except for $L = 2.0$. At lower L, due to the proximity interference, the vortices from the upstream cylinder roll up into the downstream cylinder, making a single wake that suppresses the total lift. At higher L, the wake of the cylinders has little effect on each other. This should results in a weak lift force as seen from the observation of stationary tandem cylinders (Alam et al., 2003). However, an increase in C_L at $L = 6.0$ contradicts the observation. This indicates a highly non-linear effect of oscillation on fluid force due to complex wake-interference pattern.

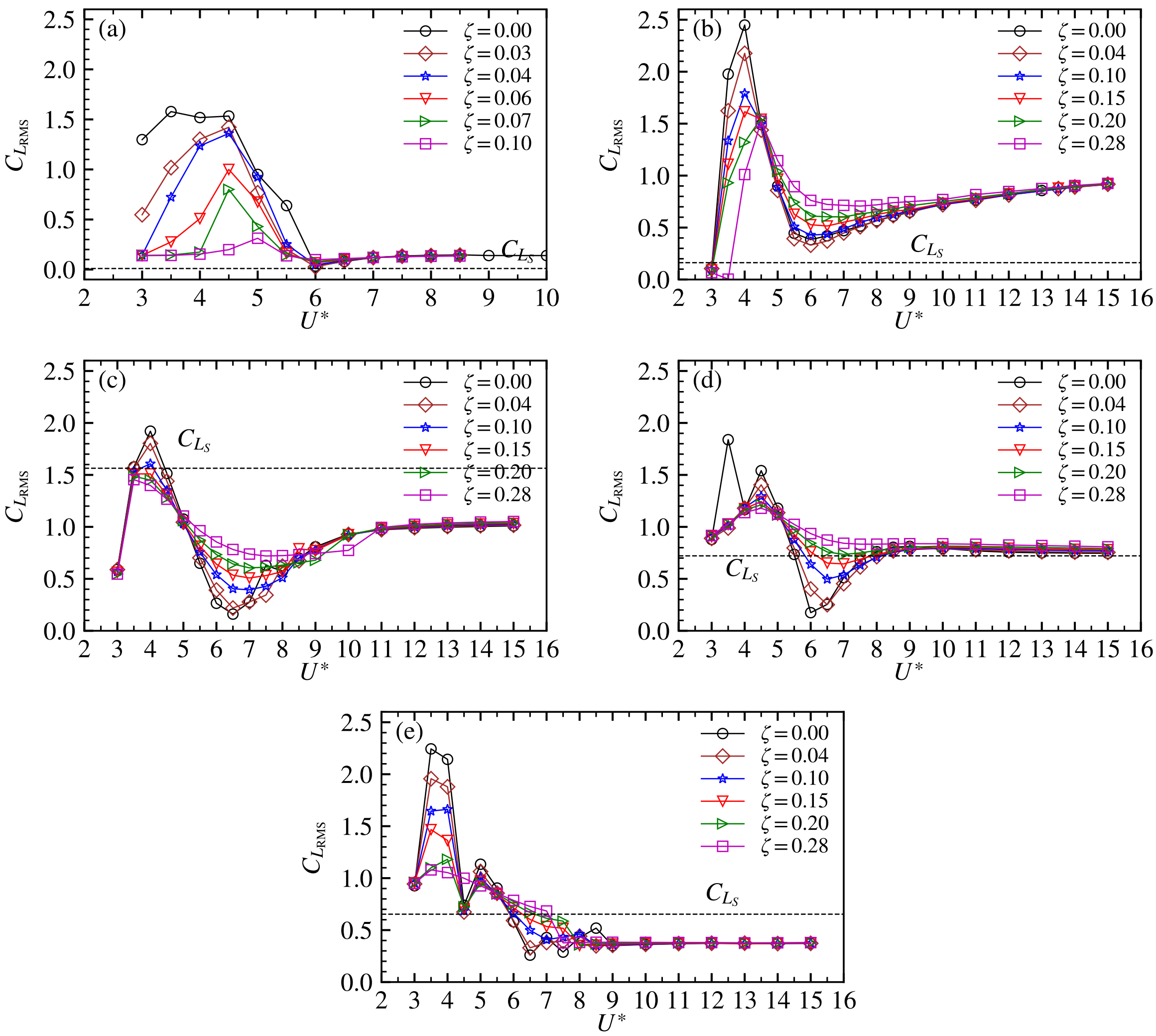

Fig. 4.3 Variation of RMS lift coefficient with U^* for (a) $L = 2.0$, (b) $L = 3.0$, (c) $L = 4.0$, (d) $L = 5.0$, and (e) $L = 6.0$ across different ζ, - - - - -denotes RMS lift coefficient of stationary tandem cylinders, C_{L_S}

4.3.4 The effect of damping and tandem spacing on power extraction

The oscillatory motion of the cylinders arises from the energy transferred by the fluid through hydrodynamic forces. The fluctuating lift forces predominantly govern this energy transfer. In this study, the cylinder motion is constrained in the y-direction. The power can be modeled as the power dissipated by the damper. The non-dimensional average extracted power, $P(t)$, is calculated as the ratio of power dissipated by the damper to the power available with the free stream that crosses the cylinder frontal area.

$$P(t) = \frac{c\dot{y}^{*^2}}{\frac{1}{2}\rho U^3 D} \tag{4.2}$$

The above expression in Equation 4.2 can be written in terms of dimensionless parameters as,

$$P(t) = \frac{4\pi^2 m^* \zeta}{U^*}\dot{y}^2 \tag{4.3}$$

Therefore, the average power for a time-period of oscillation (T_{total}) can be evaluated as,

$$\bar{P} = \frac{1}{T_{total}}\int_0^{T_{total}} P(t)dt = \frac{4\pi^2 m^* \zeta}{U^*}\dot{y}^2_{\mathrm{RMS}} \tag{4.4}$$

where, $\dot{y}_{\mathrm{RMS}} = \sqrt{\frac{1}{T_{total}}\int_0^{T_{total}} \dot{y}^2 dt}$. Peak in power is observed during the transition from the initial to the lower branch. When the lower branch transitions to the desynchronization regime, the power almost drops to zero as the vibration amplitude becomes negligible. The average power follows the same trend as vibration amplitude response with U^*. The damping ratio and reduced velocity are varied over ranges that capture significant changes in vibration amplitude and power extraction. For instance, for $L = 2.0$, the damping ratio is restricted to $\zeta \leq 0.1$, since at higher damping values the vibration amplitude, and consequently the harvested power, became negligibly small. A similar rationale is adopted for the choice of reduced velocity (U^*); only the range of U^* values that exhibited meaningful vibration response and energy harvesting is considered. Figure 4.4 depicts that the U^*, corresponding to the peak mean power, lags behind the U^* at which the maximum amplitude response occurs. This lag arises due to the phase difference between velocity and displacement, as power is proportional to velocity. Noticeably, for every ζ, there is a particular U^* where the power is maximum. The mean power output remains low for $L = 2.0$. The highest power of 0.245 is observed at $L = 5.0$ and $\zeta = 0.20$. Further increasing L to 6.0 reduces maximum average power, as the peak of maximum average power is observed to be 0.175 at $\zeta = 0.15$. There is a monotonic increase of maximum amplitude with L, but maximum power is a non-monotonic function of L. Moreover, as the range of U^* for significant amplitude increases for $L = 3.0$, 4.0, and 5.0, the range of significant power widens, consistent with the widening of the synchronization region discussed in Section 4.3.1. When the displacement and force are in phase, the power increases with U^*; when out of phase, the power starts decreasing. In the transition regime of the initial and lower branch, maximum power is observed.

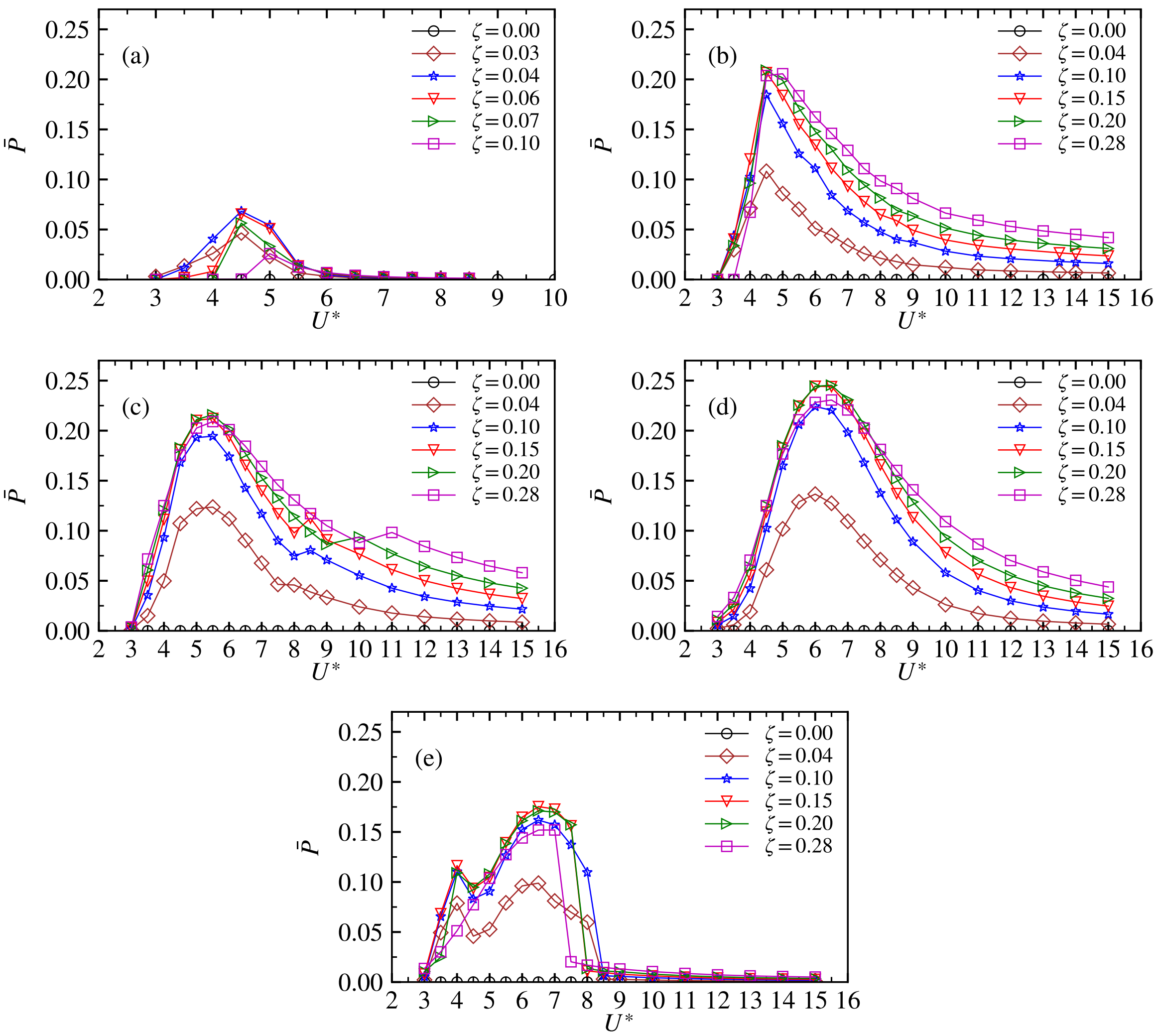

Fig. 4.4 Variation of average power, $\bar{P}$ with varying U^* at (a) $L = 2.0$, (b) $L = 3.0$, (c) $L = 4.0$, (d) $L = 5.0$ and (e) $L = 6.0$ across different ζ.

The relations of $C_{L_{\mathrm{RMS}}}$ and RMS value of cylinder velocity ($\dot{y}_{\mathrm{RMS}}$) with U^* are responsible for the variation of $\bar{P}$ with U^*, as power is a product of fluid force and cylinder velocity. The trend of $\dot{y}_{\mathrm{RMS}}$ with U^* resembles the variation of amplitude with U^* (Figure 4.5). However, the trends of the maximum vibration amplitude and the maximum $\dot{y}_{\mathrm{RMS}}$ with respect to L do not align. The $\dot{y}_{\mathrm{RMS}}$ value peaks at $L = 5.0$ and then decreases at $L = 6.0$, contrary to the variation of maximum amplitude with L. Though the $C_{L_{\mathrm{RMS}}}$ values are higher at $L = 3.0$, due to lower $\dot{y}_{\mathrm{RMS}}$, the average power is relatively low. At higher U^*, all $C_{L_{\mathrm{RMS}}}$ converge to relatively higher values for $L = 3.0$, 4.0, and 5.0, but at lower values at 2.0 and 6.0. The same trend is observed for $\dot{y}_{\mathrm{RMS}}$, leading to high power even at high U^* for $L = 3.0$, 4.0, and 5.0. Since ζ

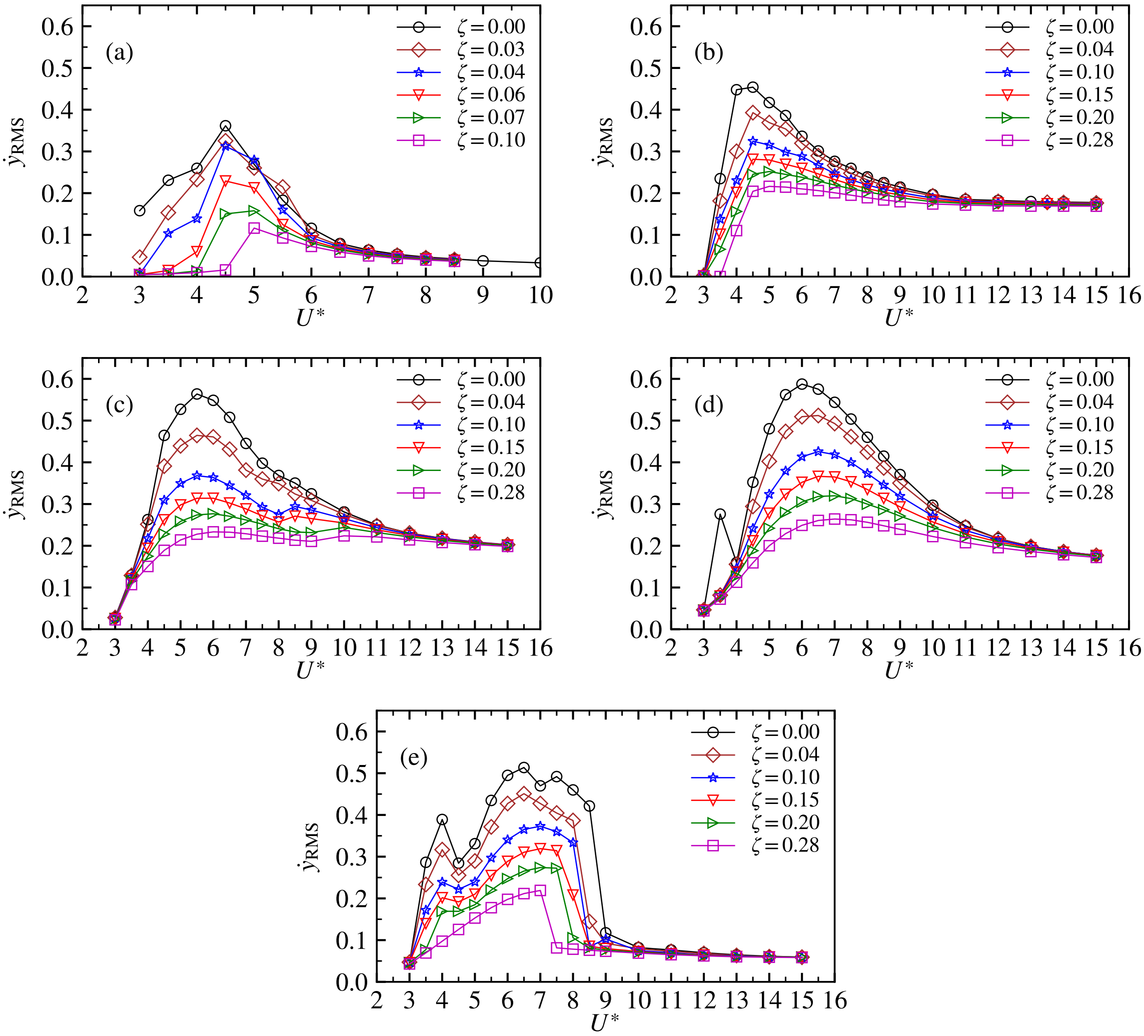

Fig. 4.5 Variation of $\dot{y}_{\mathrm{RMS}}$ with varying U^* at (a) $L = 2.0$, (b) $L = 3.0$, (c) $L = 4.0$, (d) $L = 5.0$ and (e) $L = 6.0$ across different ζ.

directly influences power extraction, the collapse of $C_{L_{\mathrm{RMS}}}$ and $\dot{y}_{\mathrm{RMS}}$ values across all ζ at high U^* implies that power increases with ζ in this regime.

At the lowest ζ, despite significant vibration amplitude, the extracted power is minimal since power extraction is proportional to the damping coefficient (Equation 4.4), which approaches zero. As ζ increases, the power increases, but at the same time, the oscillation amplitude decreases. When ζ approaches ∞, the amplitude ceases to exist, and no power generation is observed. Therefore, in between there should be a ζ where power is maximum, and this ζ is called the optimum ζ. Hence, for a constant L, with an increase in ζ, the maximum average power increases to a certain ζ value, beyond which it starts to decline. Maximum average power at every mass-damping

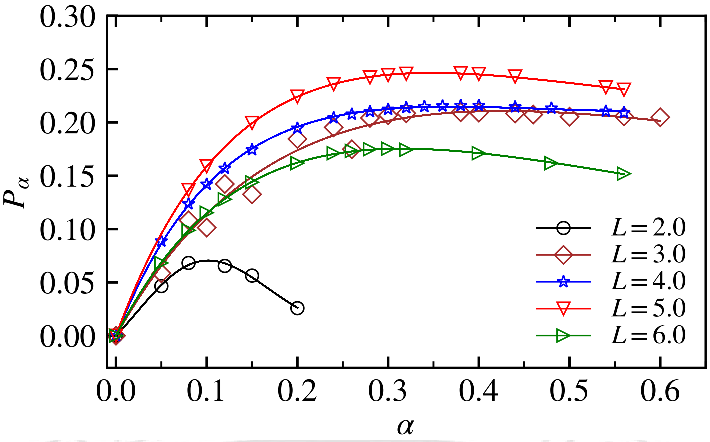

Fig. 4.6 Variation of maximum average power with α for different L

parameter, $\alpha = m^*\zeta$, is plotted in Figure 4.6 for different L values. As m^* is constant, the variation of α denotes the variation of ζ. The optimum α for $L = 2.0$, 3.0, 4.0, 5.0, and 6.0 is observed at 0.08, 0.38, 0.40, 0.38, and 0.30, respectively. Therefore, the optimum damping for maximum power is a non-monotonic function of L, as optimum damping peaks at $L = 4.0$ before dropping at higher L. It is also noted that the maximum average power for $L = 3.0$ and 4.0 is comparable. At Re = 150, the maximum attainable power for the tandem configuration is nearly twice that of a single circular cylinder, for which the reported maximum is ≈ 0.13 (Soti et al., 2017), except at $L = 2.0$, where the enhancement is not observed.

The maximum vibration amplitude for a single circular cylinder is an exponentially decaying function of α(Soti and De, 2020; Soti et al., 2018). The maximum vibration amplitude and cylinder velocity for a single circular cylinder is observed at the upper branch, and the U^*, where maximum amplitude and maximum power are observed, only differ by 0.5 (Soti et al., 2018). Therefore, it is safe to assume that maximum average power is also an exponentially decaying function of α. Soti and De (2020) proposed that maximum average power can be expressed as, $\bar{P}_\alpha = C_0\alpha(A^*_\alpha)^2$, where C_0 is a constant and A^*_α is the peak vibration amplitude. Considering $\bar{P}_\alpha$ for tandem cylinders, the same function of α as that of a single circular cylinder (Soti et al., 2018), then $\bar{P}_\alpha$ can be expressed as,

$$\bar{P}_\alpha = C_3\alpha \exp\Big(C_1\alpha + C_2\alpha^2\Big) \tag{4.5}$$

where, $C_3 = C_0(A^*_0)^2$, A^*_0 is the peak vibration amplitude at zero damping. It is observed from Figure 4.6 that the highest power of 2 of α is sufficient to fit the $\bar{P}_\alpha$

Table 4.1 Coefficients of the exponential fit, obtained by least-squares fitting method, for the maximum average power.

L	C_3	C_1	C_2
2.0	0.891	4.898	-72.361
3.0	1.516	-2.917	0.675
4.0	2.134	-4.337	2.208
5.0	2.317	-3.939	1.531
6.0	1.653	-3.741	0.909

curve. Similar findings were reported by Soti et al. (2018). Except for $L = 3.0$ at low damping, all $\bar{P}_\alpha$ values fit the curve, as observed from Figure 4.6. The data is fitted to Equation 4.5 using the least-squares method of Levenberg-Marquardt (LM) algorithm Kenneth Levenberg (1944); Marquardt (1963). The constants of Equation 4.5 obtained by the least-squares fit are listed in Table 4.1.

4.3.5 The effect of damping on power extraction efficiency and power density

The power extraction efficiency (η) is the ratio of the extracted power to the maximum power that can be obtained from the flow. The maximum energy from the flow is achieved when the total kinetic energy of the flow is converted into harnessed energy. The maximum energy per unit area that can be extracted from a flow of free-stream velocity, U, and density, ρ, can be written as $\frac{1}{2}\rho U^3$. As the cylinder is of unit length, the total area covered by the cylinder in one oscillation cycle is $(D + 2A)$, where A is the dimensional amplitude of vibration. Therefore, the expression of power extraction efficiency as follows,

$$\eta = \frac{\bar{P}}{1 + 2A^*} \tag{4.6}$$

Figure 4.7(a) shows the variation of maximum power extraction efficiency (η_α) with mass-damping parameter α. The peak of maximum η_α is found to be 0.131 at $L = 3.0$ (Figure 4.7(a)), which is almost twice the maximum efficiency of a single cylinder (0.0744 at Re = 150) as reported by Soti et al. (2017). However, the maximum non-dimensional average power is observed to be 0.245 at $L = 5.0$. Therefore, maximum power does not translate to maximum efficiency as efficiency depends not only on average power but also on the vibration amplitude. As the gap increases, the amplitude increases as observed from Figure 4.1 but average power decreases after $L = 5.0$. For instance, while $L = 6.0$ yields considerable vibration amplitude, its extracted power is lower than that at $L = 3.0$, 4.0, and 5.0, resulting in a dip in efficiency. The lowest efficiency is reported in the case of $L = 2.0$, where both average power and oscillation amplitude are relatively low. The maximum efficiency for $L = 3.0$, 4.0, and 5.0 is comparable, as seen from Figure 4.7(a). Moreover, the maximum α at which the maximum efficiency occurs is noticed to be greater than or equal to the α for maximum average power. The optimum α for η_α is at 0.12, 0.56, 0.54, 0.54, and 0.40 for $L = 2.0$, 3.0, 4.0, 5.0, and 6.0, respectively.

From the cost stand of point, higher L should be avoided as it would increase the size of the setup. Therefore, a parameter has been introduced, power density (χ), that takes into account the total available energy in the volume of fluid influenced by the cylinders. The power density thus is the ratio of the extracted power to the total power available in the fluid volume influenced by tandem cylinders. For simplicity, the flow between the cylinders is considered uniform. Therefore, χ can be expressed as,

$$\chi = \frac{\bar{P}}{(1 + 2A^*)(D + L)} = \frac{\eta}{1 + L} \tag{4.7}$$

as D is unit. Figure 4.7(b) shows the variation of maximum power density, χ_α with the mass-damping parameter, α. The peak of maximum χ_α of 0.032 is observed at $L = 3.0$. The maximum χ_α at $L = 2.0$ is found to be 0.013 at $\alpha = 0.12$, which is identical to that at $L = 6.0$, but observed at $\alpha = 0.40$. This is due to the low volume of influence at $L = 2.0$ despite lower power generation at smaller α. Moreover, at $\alpha \leq 0.10$, except for $L = 3.0$, the χ_α is superior at $L = 2.0$ than the other arrangements. The maximum χ_α is observed to decrease with L beyond $L = 3.0$. The optimal α for χ_α is found to be less than or equal to the optimal α for η_α, but higher than or equal to the optimal α for power.

Since power density is one of the benchmarks for comparing different energy sources, it gives an insight into a cost-effective and energy-efficient arrangement. It is seen that the net power extraction and efficiency is greater for the case of $L = 5.0$. However, in terms of power extraction per unit volume, $L = 3.0$ is found to be best among all the tandem lengths.

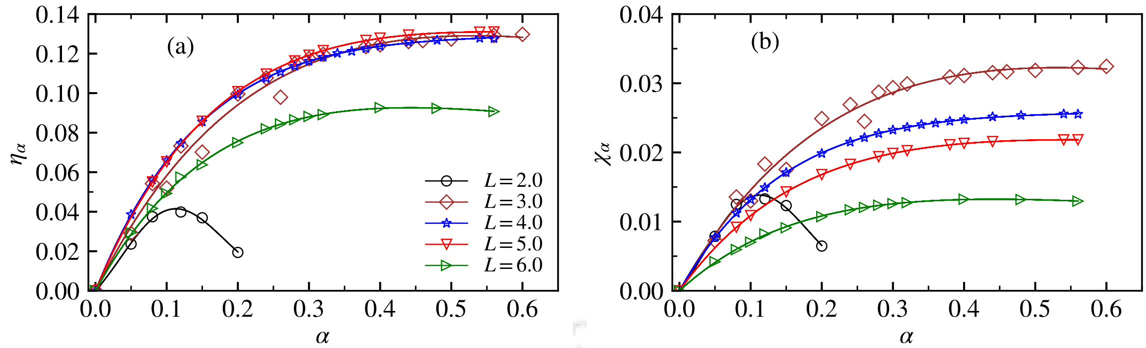

Fig. 4.7 Variation of (a) η_α and (b) χ_α with α for different spacing ratios L. The legends for Figure 10(b) are the same as those shown in Figure 10(a).

4.4 Summary

This study investigates the VIV of two rigidly coupled circular cylinders in tandem arrangement at a Reynolds number (Re) of 150. The effects of damping ratio (ζ) and gap (L) between two cylinders on their VIV characteristics, namely vibration amplitude, phase difference, and lift coefficient, as well as their flow power extraction capability, are presented. The tandem gap (L) is varied between 2.0 and 6.0, and the ζ between 0 and 0.30.

The amplitude response with U^* remains similar under damping, though the maximum amplitude is reduced compared to the undamped case. The highest non-dimensional amplitude of 0.842 occurs at $L = 6.0$, exceeding that of a single cylinder at zero damping (≈ 0.57). At zero damping, the amplitude for $L = 2.0$ is comparable to that of a single cylinder (Zhao, 2013). For $L = 3.0 - 5.0$, the amplitude decays gradually with U^* and converges beyond $U^* = 11.0$. The amplitude peak shifts to higher U^* and the maximum amplitude increases with L, except at $L = 6.0$.

With increasing ζ, the phase-difference jump diminishes as the structural response slows, and the maximum amplitude no longer occurs at $\phi = 90°$. In the initial branch, force and displacement are in phase, resulting in a high $C_{L_{\text{RMS}}}$ value. In the transition region, phase reversal lowers $C_{L_{\text{RMS}}}$, which decreases further beyond C_{L_S}. In the lower branch, $C_{L_{\text{RMS}}}$ remains nearly constant or slightly increases depending on ζ and L. Except at $L = 2.0$, the maximum amplitude coincides with minimum $C_{L_{\text{RMS}}}$.

At small L, proximity effects cause the upstream vortices to roll into the downstream cylinder, forming a single wake that suppresses lift. At larger L, weak wake interaction yields low lift (Alam et al., 2003). The trends of $\dot{y}_{\text{RMS}}$ and $C_{L_{\text{RMS}}}$ with L govern the variation in maximum power, which peaks at 0.245 for $L = 5.0$, nearly twice that of a single cylinder at Re $= 150$ (≈ 0.13). Both maximum power and amplitude decay exponentially with the mass–damping parameter α. The maximum average power and optimum α are non-monotonic functions of L. Moreover, the region of significant power increases up to $L = 5.0$. The optimal α for maximum power is lower than that for efficiency and power density (χ) for all L. The lowest power is harvested at $L = 2.0$, while higher vibration amplitude and lower power are achieved at $L = 6.0$ compared to $L = 3.0$, 4.0, and 5.0. The maximum efficiency (0.131) is found at $L = 3.0$, twice that of a single cylinder (Soti et al., 2017). The power density provides a more meaningful performance metric for multi-cylinder harvesters. Its peak value, $\chi_\alpha = 0.032$, occurs at $L = 3.0$, making this configuration the most favorable when considering both energy yield and installation cost. Therefore, for multi-cylinder energy harvesters, power density—not efficiency—should be used as the benchmark for comparison.

Chapter 5

Power extraction from vortex-induced vibration of two rigidly coupled cylinders in staggered arrangement

This chapter discusses on the effect of damping in various staggered distances of two rigidly coupled cylinders undergoing VIV. This is an extension to the work of previous chapter 4. All the other parameters remains same including m^* and Re, except the range of ζ and U^*. The Chapter starts with a brief overview of past literature (§ 5.1). The numerical methodology, mesh independence and validation is already discussed in Chapter 4. The effects of damping and staggered gaping on power extraction is discussed in § 5.3. The chapter then concludes with a summary of the outcomes (§ 5.4).

5.1 Introduction

The mass-damping parameter ($m^*\zeta$) is one of the controlling parameters in energy extraction (Barrero-Gil et al., 2012). Barrero-Gil et al. (2012) showed that there is an optimum $m^*\zeta$, where the power extraction efficiency (η) is maximum. For high mass ratios ($m^* \gg 1$), a decrease in $m^*\zeta$ results in a broader region of significant efficiency. This observation deviates from the results reported by Narendran et al. (2016) and Sun et al. (2016), wherein η was found to increase with $m^*\zeta$ as $m^* \sim 1$. Past investigations indicate that the maximum efficiency is positively influenced by the

Reynolds number (Re) (Barrero-Gil et al., 2012; Raghavan and Bernitsas, 2011). For staggered arrangements, Zhang et al. (2018a) showed that the power increases with increase in T at smaller L values but converges for all T at larger L. Alias et al. (2025, 2024) further revealed that decreasing mass ratio and increasing U^* can enhance power generation, with the optimal arrangement depending on the U^* range. However, the effect of gaping on power extraction from two rigidly coupled cylinders in a staggered configuration remains unexplored.

The purpose of this study is to examine how gaping affects power extraction from two rigidly coupled cylinders arranged in a staggered configuration at Re $= 150$ and whether this arrangement can generate greater power compared to a single cylinder. Staggered cases have variable spacing in the tandem direction, with L ranging from 2.0 to 4.0, while T ranges from 2.0 to 4.0 in the side-by-side direction. The cylinders are only allowed to move in the transverse direction to the flow, resulting in a one-degree-of-freedom (1-DOF) system. The reduced velocity (U^*) is varied in the range of 3.0–8.5. The damping ratio (ζ) also varied from 0.04 to 0.28 and the mass ratio, $m^* = 2.0$, is kept constant for all cases.

5.2 Formulation

5.2.1 Problem definition

The present numerical study involves VIV of two rigidly coupled cylinders at staggered arrangements. The non-dimensional tandem spacing, L, is varied from 2.0 to 4.0, while the side-by-side spacing, T, is simultaneously varied over the same range. The cylinders are idealized as being mounted on frictionless bearings constrained to move along two parallel rails, ensuring motion is restricted to the direction perpendicular to the incoming flow. The cylinders are attached to linear springs to impart structural stiffness. Constant mass ratio ($m^* = 2.0$) is used for a circular cylinder, as the maximum amplitude (Govardhan and Williamson, 2006) and maximum power (Soti et al., 2017) do not depend on m^*.

Schematic of the rectangular numerical domain is shown in Figure 3.2 in Chapter 3. The domain and temporal independence study is shown in Chapter 3 and Appendix B, respectively. The numerical methodology and boundary conditions are mentioned in details in Chapters 2 and 3.

The mesh independence and validation are shown in Tables 3.6 and 3.3, respectively. The detailed computational mesh around the cylinders are shown in Appendix A.

5.3 Results and discussion

In this numerical study, nine arrangements of staggered cylinders are demonstrated to enhance power output as the lift coefficient of the stationary cylinder increases with increasing T (Griffith et al., 2017). Among several key parameters for power generation, the lift coefficient is one of the important parameters along with cylinder velocity and damping. Additionally, Zhao (2013) demonstrated that the vibration amplitude of rigidly coupled cylinders for $T \geq 2.0$ is the same as that of a single cylinder. Nevertheless, power does not exclusively depend on oscillation amplitude. Therefore, nine possible arrangements have been chosen that may exhibit different flow characteristics, enhanced lift over a single cylinder, and increased amplitude, which could augment power extraction.

5.3.1 Effect on flow parameters with the variation in T at $L = 2.0$

The tandem (L) and side-by-side (T) distances are altered from 2.0 to 4.0. The non-dimensional vibration amplitude (A^*) for each configuration is investigated against U^* in the range of 3.0 to 8.5. Furthermore, the effect of damping on A^* is also discussed, where damping, ζ, varies between $0.04 \leqslant \zeta \leqslant 0.28$.

The vibration amplitude responses at $L = 2.0$ with varying vertical spacing (T) between 2.0 and 4.0 are shown in Figure 5.1. At the lowest damping, the maximum A^* increases with the increase in T from 2.0 to 3.0. However, between $T = 3.0$ and 4.0, the maximum A^* is almost the same, as is the range of U^* where the significant oscillation amplitude is observed. One key difference between $T = 2.0$ and other T values at low damping values is that at $T = 2.0$, the vibration amplitude does not drop to a low value even at $U^* = 8.5$. Each T case exhibits a distinct jump in vibration amplitude at a specific U^*, consistent across ζ values but varying between T values. However, at $T = 2.0$, the oscillation amplitude does not follow a smooth path with the progression of U^*, unlike the other T. A smooth decrease in A^* value is followed by a dip in amplitude at $U^* = 7.0$, as seen for $T = 3.0$ and 4.0. The oscillation amplitude in the range of $3.5 \leqslant U^* \leqslant 7.0$ decreases as ζ increases. Moreover, at higher ζ, the jump and drop in oscillation amplitude disappear.

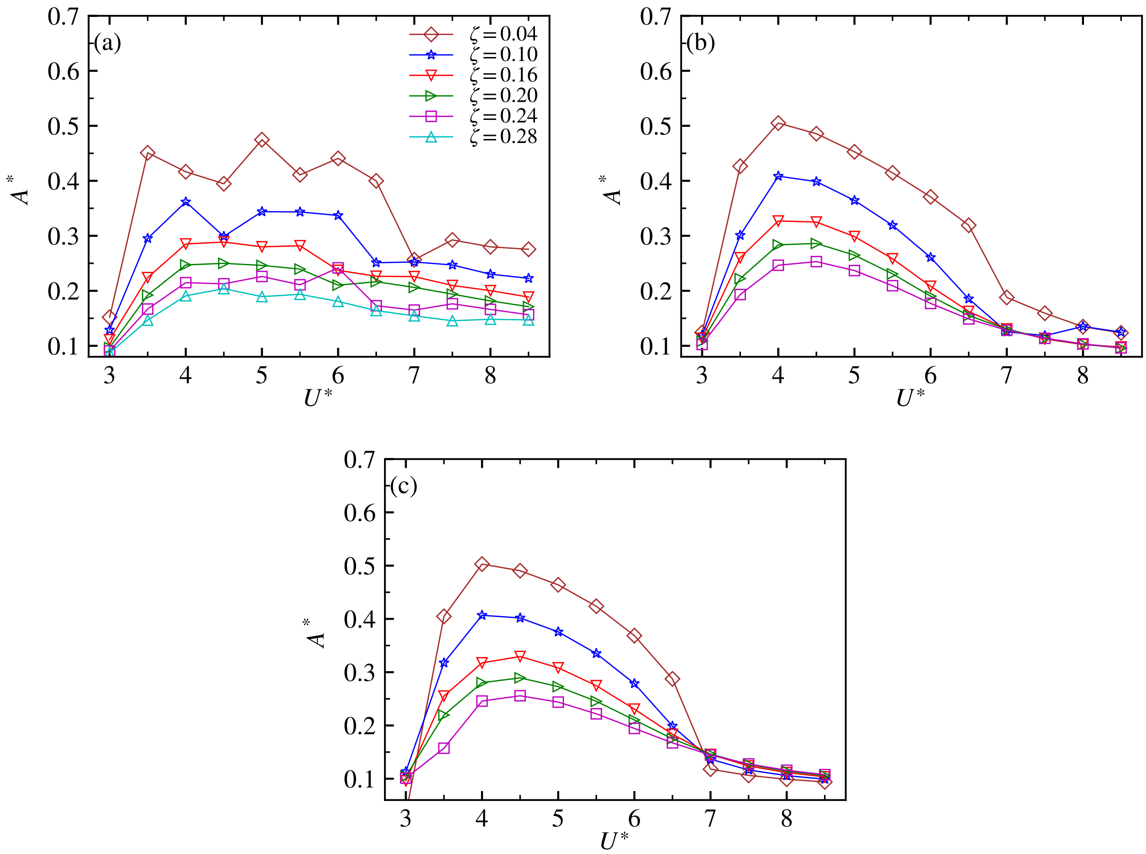

Fig. 5.1 Variation of amplitude response with U^* for $L = 2.0$ at (a) $T = 2.0$, (b) $T = 3.0$, and (c) $T = 4.0$ for $0.04 \leqslant \zeta \leqslant 0.28$.

The non-dimensional frequency response $f^* = f/f_n$ shows an increase in value with U^*, where f is the frequency of cylinder oscillation. The black dotted line represents the vortex-shedding frequency of corresponding stationary staggered cylinders. It is also called the Strouhal frequency, $f_{\mathrm{St}} = \mathrm{St}U/D$, where St represents the Strouhal number. The oscillation frequency up to $U^* = 4.0$ is observed to be close to the Strouhal frequency in Figure 5.2(a-i). Beyond $U^* = 4.0$, oscillation frequency departs from Strouhal frequency, and in the range of $U^* = 5.0 - 7.0$, f is close to f_n. The increased vibration amplitude in this U^* range is a consequence of the resonance phenomenon, and this region is called the synchronization region. In the synchronization region, vortex-shedding frequency of the oscillating cylinders $f_s \approx f \approx f_n$ (Khalak and Williamson, 1999). However, at low m^*, $f \approx f_n$ does not strictly imply lock-in region (Khalak and Williamson, 1999). The jump in phase difference (ϕ) at $U^* = 7.0$ corresponds to the

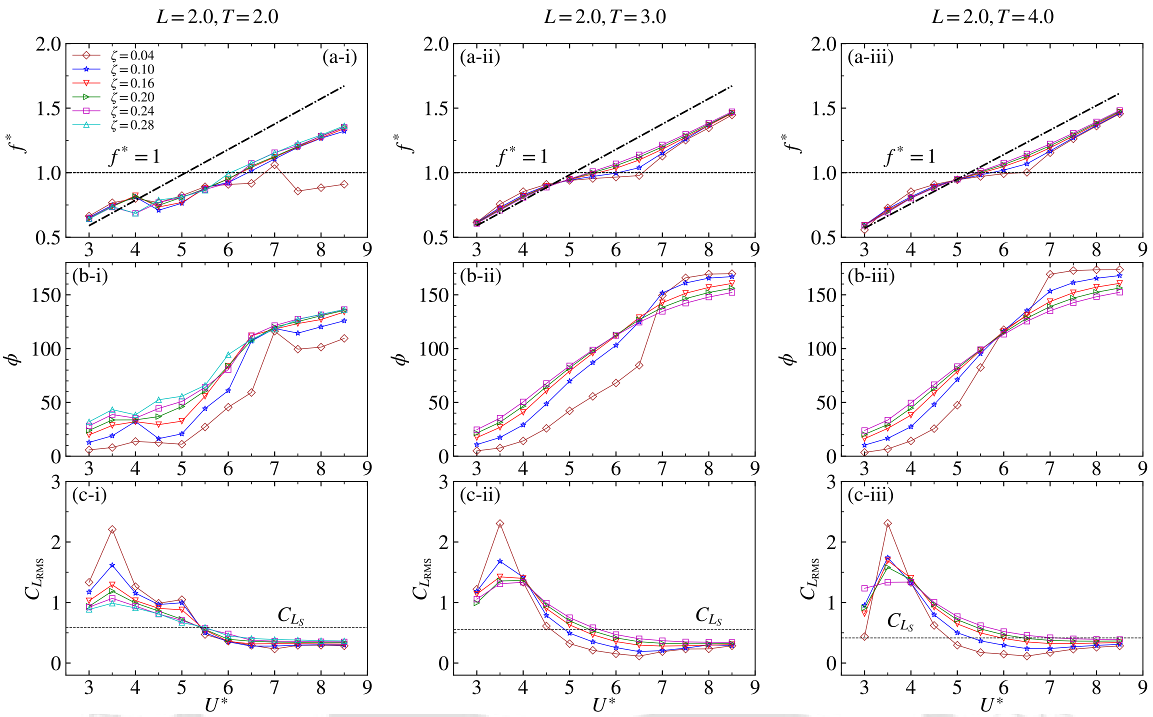

Fig. 5.2 Non-dimensional frequency response (f^*), phase difference (ϕ) and $C_{L_{\mathrm{RMS}}}$ as a function of U^* for (a) $T = 2.0$ and (b) $T = 3.0$, and (c) $T = 4.0$ at fixed $L = 2.0$ for $0.04 \leqslant \zeta \leqslant 0.28$.

jump in frequency at that U^* (Figures 5.2b-i). For all other ζ cases, the ϕ starts above $0°$ and stays below $150°$. Also, as damping increases, the jump in ϕ gradually decreases. The damped cases cross $\phi = 90°$ at $U^* = 6.0$ and a drop in amplitude after that U^* is observed. The regime $3.0 \leqslant U^* \leqslant 5.5$ is identified as the initial branch, beyond which the response transitions to the lower branch. The combined root-mean-square (RMS) of lift coefficient of two cylinders are denoted as $C_{L_{\mathrm{RMS}}}$. The combined $C_{L_{RMS}}$ is calculated by combining the transient fluid forces of the cylinders, and computing the RMS value. For the sake of simple nomenclature, the $C_{L_{\mathrm{RMS}}}$ of individual cylinders are denoted by C_{L_i}, where $i = 1, 2$ is the upstream and downstream cylinder, respectively. Hence, $C_{L_{\mathrm{RMS}}}$ can be calculated as,

$$C_{L_{\mathrm{RMS}}} = \sqrt{\frac{1}{T_{total}} \int_0^{T_{total}} \left(C_{L_1}(t) + C_{L_2}(t)\right)^2 dt} \tag{5.1}$$

where, $C_{L_i}(t)$ are the transient lift coefficients of the cylinders. The RMS is taken over 50 cycles of oscillation. Therefore, $T_{total} = 50 \times T_e$, where T_e is the time period of a single oscillation. The U^* corresponding to the peak $C_{L_{\mathrm{RMS}}}$ coincides with the onset of the initial jump in A^*. A constant dip in the $C_{L_{\mathrm{RMS}}}$ value is followed in the range $3.0 \leqslant U^* \leqslant 6.5$ (Figures 5.2c-i). The C_L value drops below the stationary cylinder $C_{L_{\mathrm{RMS}}}$, i.e., C_{L_S}, in the range of $5.5 \leqslant U^* \leqslant 8.5$. The frequency responses from Figures 5.2(a-ii) and 5.2(a-iii) show similar types of variation with U^* with increasing T. The width of the $f \approx f_n$ region is the same for both arrangements ($4.5 \leqslant U^* \leqslant 6.5$) at the lowest damping. However, the $f \approx f_n$ region gets smaller with an increase in ζ for all T cases of L. The ϕ shows a similar trend for $T = 3.0$ and 4.0, which is consistent with the frequency response (Figures 5.2b-ii and 5.2b-iii). The $C_{L_{\mathrm{RMS}}}$ for both arrangements cross the C_{L_S} value for different ζ at different U^* (Figures 5.2c-ii and 5.2c-iii). However, all the $C_{L_{\mathrm{RMS}}}$ collapse at $U^* = 4.0$, and at that U^*, the maximum vibration amplitude is recorded for both the arrangements, which is not observed for the $L = 2.0$, $T = 2.0$ case.

5.3.2 Effect on flow parameters with the variation in T at $L = 3.0$

The oscillation amplitude curve for $L = 3.0$ in Figure 5.3 shows that the maximum A^* decreases with an increase in T from 2.0 to 4.0. The decrease in maximum amplitude with increasing vertical distance between cylinders is due to the weakening of interaction between the cylinders (Zhao, 2013). For $T = 2.0$, the maximum amplitude is observed between $4.5 \leqslant U^* \leqslant 5.0$ (Figure 5.3a), whereas the maximum vibration amplitude for $T = 3.0$ and 4.0 is between $4.0 \leqslant U^* \leqslant 4.5$ (Figures 5.3b and 5.3c). The amplitude curve at all ζ converges at $U^* = 7.0$. The vibration amplitude for $T = 2.0$ drops suddenly from $U^* = 5.5$ to 6.0 at $\zeta = 0$. However, at $U^* = 6.5$, the slope of decreasing amplitude is observed to be less before plunging to a lower amplitude at $U^* = 7.0$.

The frequency plot in Figure 5.4(a-i) indicates that the $f \approx f_n$ region lies within $5.0 \leqslant U^* \leqslant 6.5$ for $L = 3.0$, $T = 2.0$ at $\zeta = 0.04$. In contrast, for $L = 3.0$, $T = 3.0$ and 4.0, $f \approx f_n$ occurs over the range $4.5 \leqslant U^* \leqslant 6.5$ (Figures 5.4a-ii and 5.4a-iii). At the end of the synchronization region, the phase increases to almost 180° (Figures 5.4bi–iii). As damping increases, instead of a jump, a gradual rise in phase is observed with U^*. The jump in oscillation amplitude at $U^* = 3.5$ matches the jump in $C_{L_{\mathrm{RMS}}}$ at the same U^*. The lowest $C_{L_{\mathrm{RMS}}}$ is observed over the range of $5.5 \leqslant U^* \leqslant 6.0$. However, this range of U^* is not associated with the maximum A^*; instead, it marks the region where the $C_{L_{\mathrm{RMS}}}$ values for all ζ intersect. The maximum $C_{L_{\mathrm{RMS}}}$ corresponds to the jump in vibration amplitude, and after the minimum $C_{L_{\mathrm{RMS}}}$, a drop in A^* is observed.

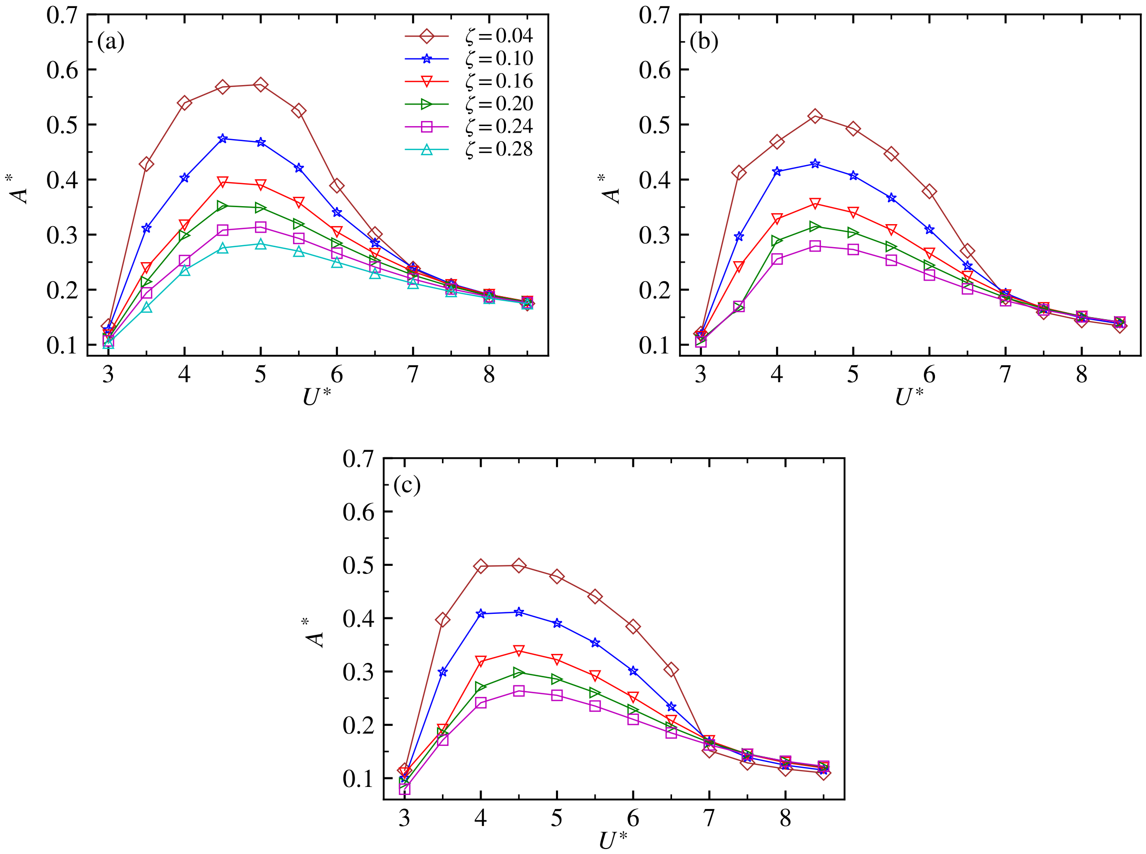

Fig. 5.3 Variation of amplitude response with U^* for $L = 3.0$ at (a) $T = 2.0$, (b) $T = 3.0$, and (c) $T = 4.0$ for $0.04 \leqslant \zeta \leqslant 0.28$.

5.3.3 Effect on flow parameters with the variation in T at $L = 4.0$

Figure 5.5 illustrates the variation in vibration amplitude with U^* for $L = 4.0$ across T from 2.0 to 4.0. As with other L cases, with increasing T, A^* decreases, and the peak A^* shifts to lower U^* values. The values of oscillation amplitude at zero damping are very close to the single cylinder value (Soti et al., 2018). Nevertheless, one noticeable thing is that A^* at the highest reported U^* exceeds that of the single cylinder. It incites a broader region of synchronization. Compared to other L cases, A^* at maximum U^* is higher for $L = 4.0$ at the corresponding T.

The frequency response from Figure 5.6(a-i) shows an early detachment from the Strouhal frequency at $U^* = 4.0$. At this U^*, a significant vibration amplitude is noticed. The $f \approx f_n$ region is observed within $6.0 \leqslant U^* \leqslant 7.0$ for all ζ at $L = 4.0$, $T = 2.0$. The $f \approx f_n$ region for $L = 4.0$, $T = 3.0$ and 4.0 is observed in the range of $5.0 \leqslant U^* \leqslant 7.0$.

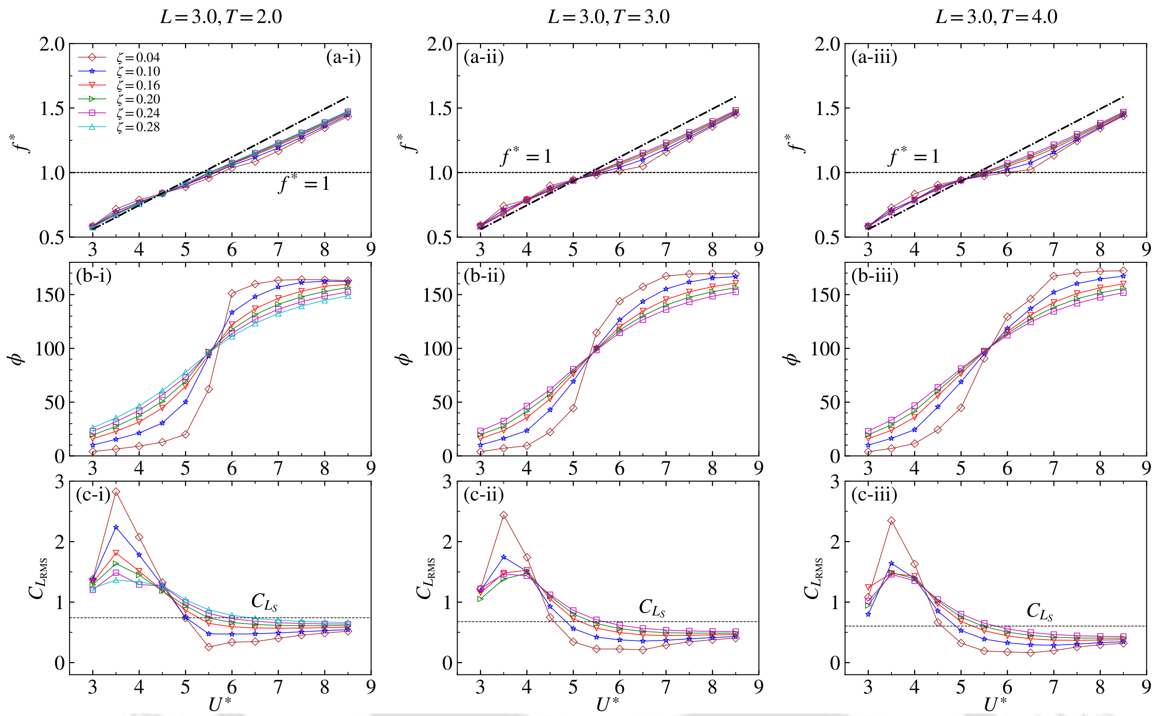

Fig. 5.4 Variation of f^*, ϕ and $C_{L_{\mathrm{RMS}}}$ as a function of U^* for (a) $T = 2.0$ and (b) $T = 3.0$, and (c) $T = 4.0$ at fixed $L = 3.0$ for $0.04 \leqslant \zeta \leqslant 0.28$.

The ϕ plot is the same for all arrangements, but the jump position shifts according to the synchronization region. The maximum $C_{L_{\mathrm{RMS}}}$ is observed to decrease with an increase in T up to 3.0, then increases again at $T = 4.0$. Though the amplitude is higher at lower T. Unlike the case for $L = 3.0$, the U^* at which $C_{L_{\mathrm{RMS}}}$ for all ζ converge does not coincide with the U^* at which the maximum oscillation amplitude is observed. However, a phase change is observed at the U^* where minimum $C_{L_{\mathrm{RMS}}}$ occurs. The peak $C_{L_{\mathrm{RMS}}}$ of a constant T is increasing up to $L = 3.0$ and then decreases at $L = 4.0$.

5.3.4 Effect of damping on the average power

The non-dimensional instantaneous extracted power is calculated as the ratio of the power dissipated by the damper to the power available from the displacement of the cylinders.

$$P(t) = \frac{c\dot{y}^{*2}}{\frac{1}{2}\rho U^3 D} \tag{5.2}$$

where c is the damping coefficient and $\dot{y}$ defines the instantaneous velocity of the cylinders. Therefore, the instantaneous power can be expressed as the product of the unsteady fluid force $F(t)$ and $\dot{y}^*$, $P(t) = F(t)\dot{y}^*$. The dimensionalization process is

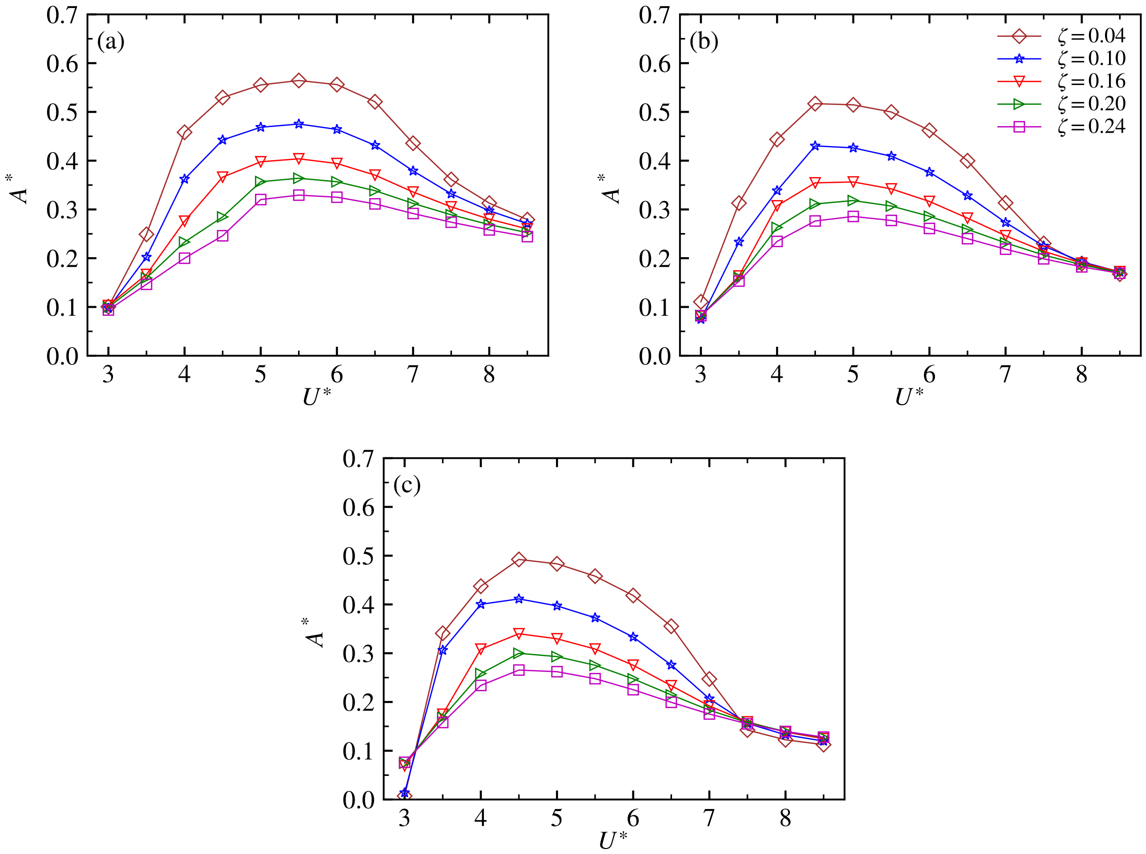

Fig. 5.5 Variation of amplitude response with U^* for $L = 4.0$ at (a) $T = 2.0$, (b) $T = 3.0$, and (c) $T = 4.0$ for $0.04 \leqslant \zeta \leqslant 0.28$.

given below,

$$P(t) = \frac{c\,\dot{y}^{*2}}{\frac{1}{2}\rho U^3 D}, \qquad y^* = D\,y,\ t^* = \frac{D}{U}t,$$

$$\dot{y}^* = U\frac{dy}{dt} \;\Rightarrow\; P(t) = \frac{2c}{\rho U D}\left(\frac{dy}{dt}\right)^2,$$

$$c = 4\pi m\zeta\frac{U}{U^* D} \;\Rightarrow\; P(t) = \frac{8\pi m\zeta}{\rho D^2 U^*}\left(\frac{dy}{dt}\right)^2,$$

$$m = m^* m_d, \quad m_d = \frac{\pi}{2}\rho D^2$$

Therefore, the instantaneous power can be non-dimensionalized as,

$$P(t) = \frac{4\pi^2 m^*\zeta}{U^*}\dot{y}^2 \tag{5.3}$$

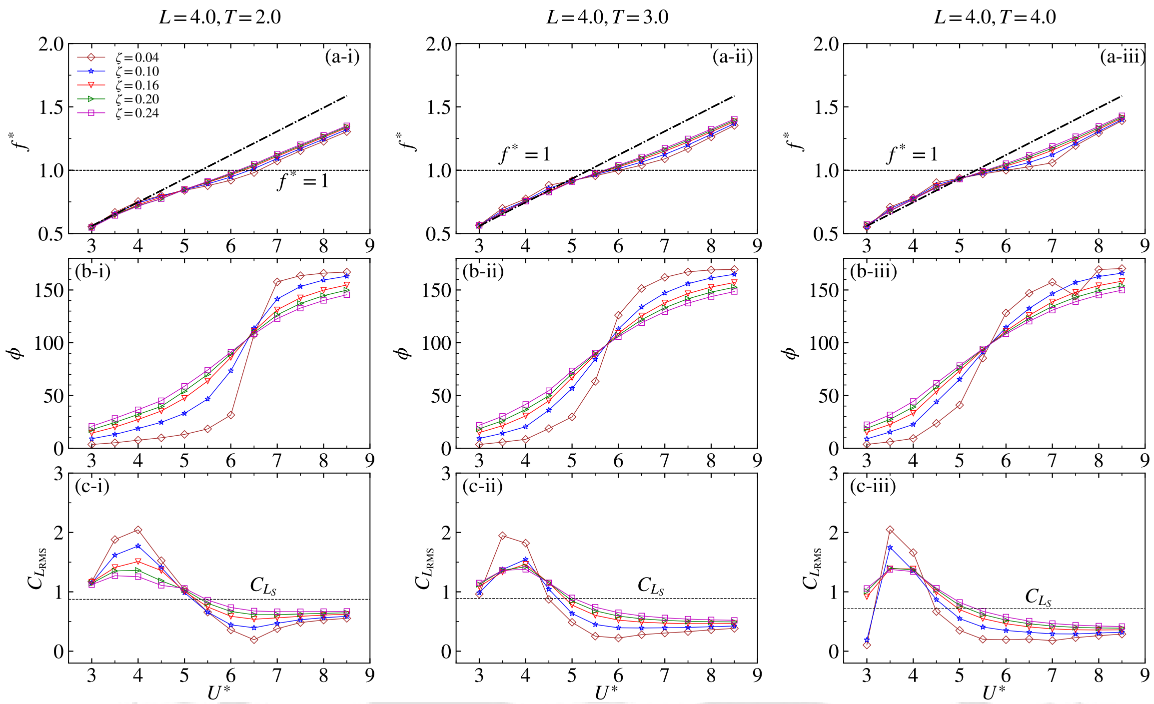

Fig. 5.6 Variation of f^*, ϕ and $C_{L_{\mathrm{RMS}}}$ as a function of U^* for (a) $T = 2.0$ and (b) $T = 3.0$ and (c) $T = 4.0$ at fixed $L = 4.0$ for $0.04 \leqslant \zeta \leqslant 0.28$.

The average power for a period of oscillation (T_{total}) can be evaluated as,

$$\bar{P} = \frac{1}{T_{total}} \int_{T_{total}} P(t)dt \tag{5.4}$$

So the average power, $\bar{P}$, can be expressed in non-dimensional terms as,

$$\bar{P} = \frac{4\pi^2\alpha}{U^*} \dot{y}^2_{\mathrm{RMS}} \tag{5.5}$$

where, α is the mass-damping parameter expressed as $\alpha = m^*\zeta$ and $\dot{y}_{\mathrm{RMS}} = \sqrt{\frac{1}{T_{total}} \int_0^{T_{total}} \dot{y}^2 dt}$. From Equation 5.5, the average power depends on several parameters, namely U^*, m^*, ζ, and $\dot{y}_{\mathrm{RMS}}$. However, Soti et al. (2017) reported that the peak of average power does not depend on m^*. Govardhan and Williamson (2000) found that as m^* decreases, the average power curve becomes flatter, inciting an extended synchronization region at lower m^*. Figure 5.7 shows the variation of average power as a function of reduced velocity at different ζ for different T at $L = 2.0$. It is observed that $\bar{P}$ is a non-monotonic function of U^*. For every ζ value, a peak in average power is observed at a particular U^*. No power is generated at zero damping, as the

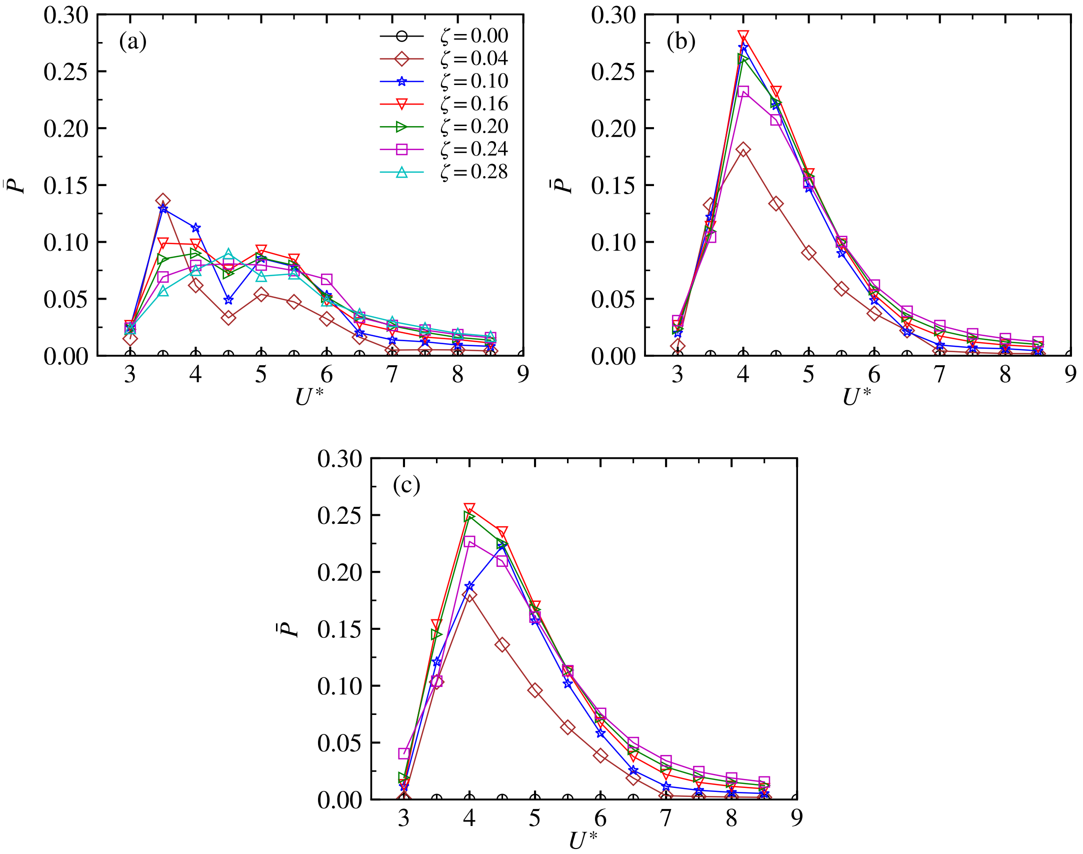

Fig. 5.7 Variation of average power, $\bar{P}$ with U^* for $L = 2.0$ at (a) $T = 2.0$, (b) $T = 3.0$, and (c) $T = 4.0$ for $0 \leqslant \zeta \leqslant 0.28$.

power is defined as the energy dissipated by the damper (Equation 5.2). Although the amplitude of vibration is highest at zero damping, as no resistance acts against the motion, kinetic energy can not be converted into any useful form of energy (e.g., electrical energy). As damping increases, the maximum vibration amplitude decreases. Conversely, the average power initially increases with ζ, but beyond a particular value, it starts to decline (Figure 5.7). It is because the vibration almost ceases as $\zeta \to \infty$. Therefore, there is an optimum ζ or mass-damping parameter ($\alpha = m^*\zeta$) where the maximum average power, $\bar{P}_\alpha$, can be obtained. The maximum average power for $L = 2.0, T = 2.0$, is observed at $\zeta = 0.04$ and 0.10, as $\bar{P}_\alpha$ for both ζ are almost the same. At $U^* = 3.5$, $\bar{P}_\alpha$ is recorded, and it is also consistent with the jump in oscillation amplitude at this U^* for previously discussed ζ values. For other ζ also, a jump in power is observed at $U^* = 3.5$, consistent with a jump in oscillation amplitude. It is evident from Equation 5.5 that $\dot{y}_{\mathrm{RMS}}$ has a greater influence on average power than U^* and α. For every ζ, several peaks in average power are observed, which is due to

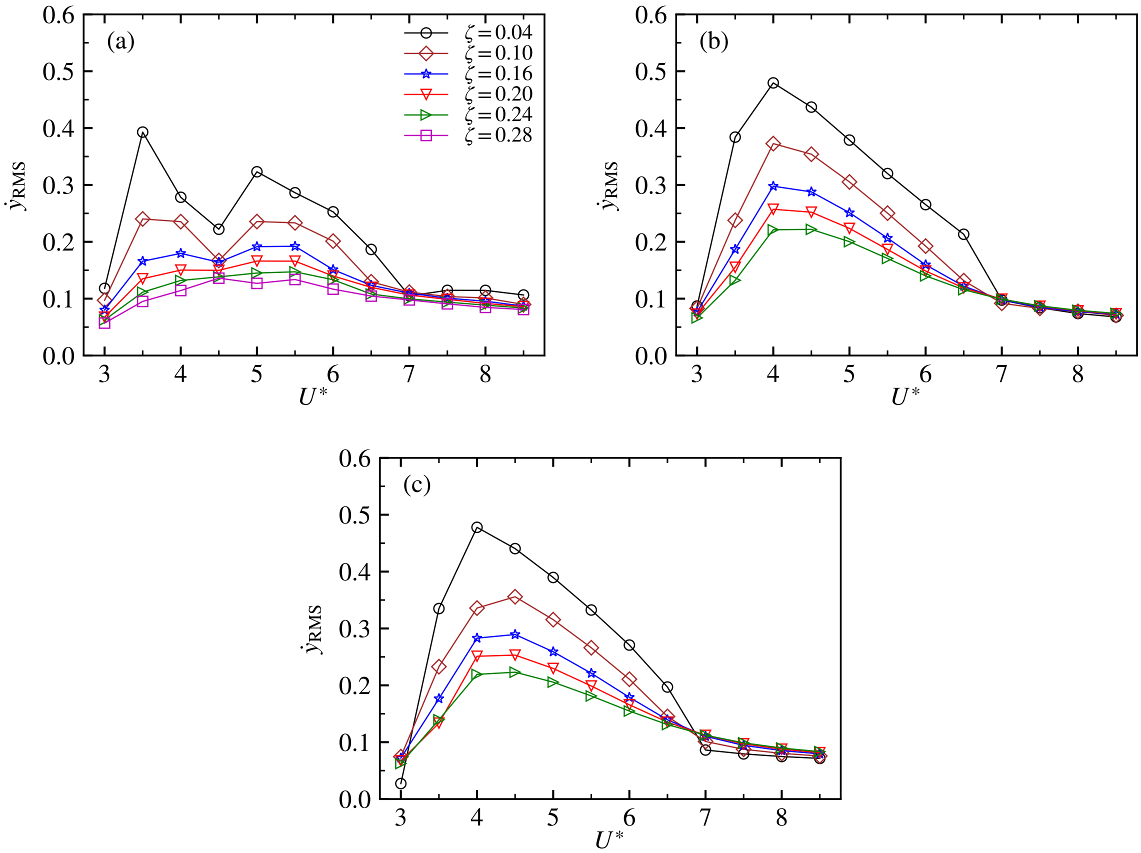

Fig. 5.8 Variation of RMS of cylinder velocity, $\dot{y}_{\mathrm{RMS}}$ with U^* for $L = 2.0$ at (a) $T = 2.0$, (b) $T = 3.0$, and (c) $T = 4.0$ for $0 \leqslant \zeta \leqslant 0.28$.

the peaks in $\dot{y}_{\mathrm{RMS}}$ values (Figure 5.8). Although A^* and $\dot{y}_{\mathrm{RMS}}$ show the same trend, the power is controlled directly by $\dot{y}_{\mathrm{RMS}}$ rather than A^*, because the cylinder motion is not a pure sinusoid and therefore amplitude does not map uniquely to velocity. Figure 5.2 shows that the peak $C_{L_{\mathrm{RMS}}}$ increases with the increase in T at $L = 2.0$. However, peak $\dot{y}_{\mathrm{RMS}}$ maxed at $T = 3.0$. For this reason $\bar{P}_{\alpha}$ increases up to $T = 3.0$ before decreasing at $T = 4.0$. A sudden increase in $\dot{y}_{\mathrm{RMS}}$ at $U^* = 3.5$ corresponds to a similar rise in the average power (Figure 5.8a). At $U^* = 4.5$, there is a significant drop in both $\dot{y}_{\mathrm{RMS}}$ and the average power. However, for $\zeta = 0.20$ and 0.24, $\dot{y}_{\mathrm{RMS}}$ rises till $U^* = 5.0$ and 5.5, respectively. It is also observed that the U^* corresponding to $\bar{P}_{\alpha}$ differs from that of the maximum $\dot{y}_{\mathrm{RMS}}$ at higher ζ. Therefore, at higher damping, the maximum average power is optimized at a slightly lower reduced velocity than the point of maximum oscillation amplitude. For $L = 2.0, T = 3.0$ and $L = 2.0, T = 4.0$, a single peak of average power is noticed for every ζ value. The optimum ζ values where the maximum average power is achieved are 0.16 for both cases. Beyond the optimum

ζ, the maximum power output starts to decrease as ζ increases. The power curve is observed to be consistent with the behaviour of $\dot{y}_{\text{RMS}}$ with U^* as seen from Figures 5.8(b) and (c). It is also observed that the maximum power peaks at $T = 3.0$ and then decreases at $T = 4.0$. The $\dot{y}_{\text{RMS}}$ also peaked at $T = 3.0$. A single circular cylinder can generate a maximum power of 0.13 at $\text{Re} = 150$ (Soti et al., 2017). Therefore, at $T = 2.0$, only $\zeta = 0.04$, 0.10, and 0.16 can achieve more power than a single cylinder, whereas the other two arrangements yield greater power for all considered ζ values. For the case of $L = 2.0, T = 3.0$, the maximum power reported is 0.28, while that for $L = 2.0, T = 4.0$, it is 0.25. Both values are almost two times the power achieved from a single-cylinder VIV case. Therefore, $L = 2.0, T = 3.0$, and $L = 2.0, T = 4.0$ are better in terms of power generation than a single cylinder.

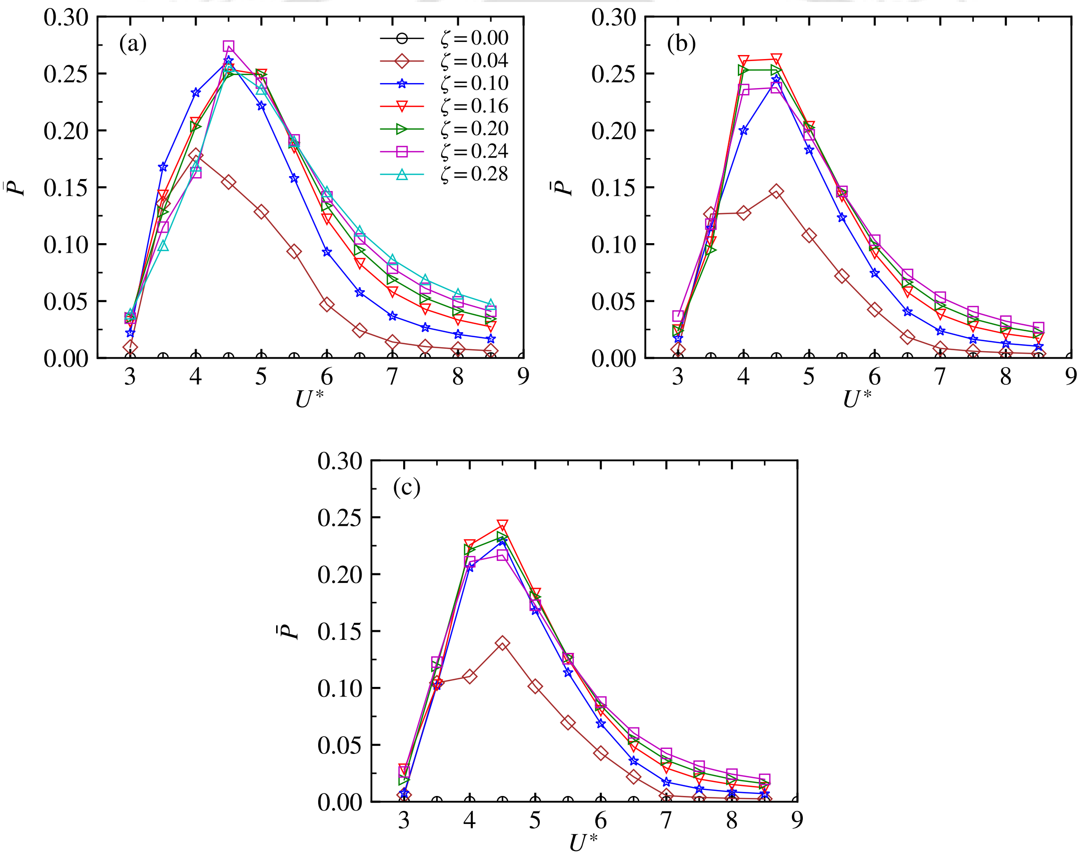

Fig. 5.9 Variation of $\bar{P}$ with U^* for $L = 3.0$ at (a) $T = 2.0$, (b) $T = 3.0$, and (c) $T = 4.0$ for $0 \leqslant \zeta \leqslant 0.28$.

The average power for the case with $L = 3.0$ is shown in Figure 5.9. In the case where $T = 2.0$, the maximum power of 0.28 is observed at optimum $\zeta = 0.24$. The maximum power is observed at $U^* = 4.5$ for all values of ζ, while the lowest peak

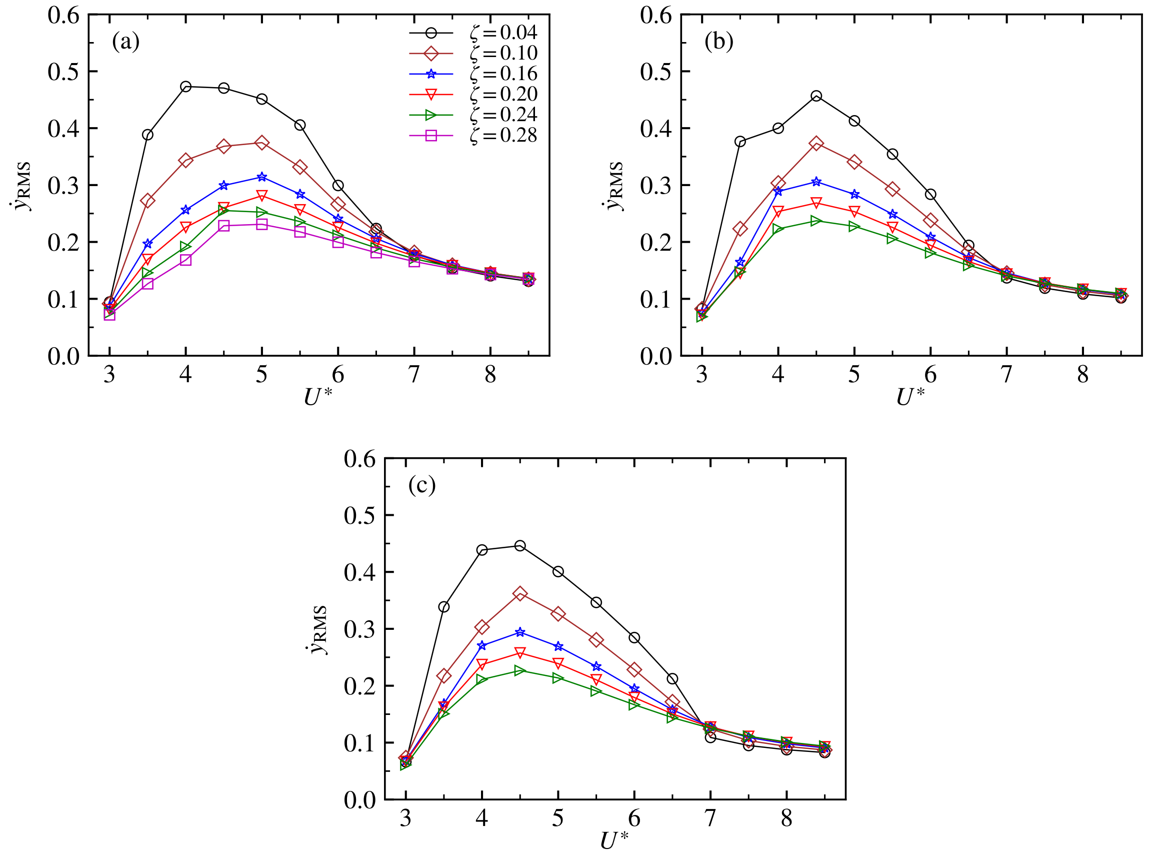

Fig. 5.10 Variation of $\dot{y}_{\mathrm{RMS}}$ with U^* for $L = 3.0$ at (a) $T = 2.0$, (b) $T = 3.0$, and (c) $T = 4.0$ for $0 \leqslant \zeta \leqslant 0.28$.

occurs at $\zeta = 0.04$. For $\zeta = 0.10$, 0.16, and 0.20, the U^* at which $\bar{P}_\alpha$ is observed also corresponds to the peak A^* (Figures 5.3 and 5.9). At $\zeta = 0.28$, the maximum power decreases to 0.25. The maximum $\dot{y}_{\mathrm{RMS}}$ for $\zeta = 0.04$ occurs at $U^* = 4.0$, which also corresponds to the peak average power, $\bar{P}_{\max}$, for the same damping ratio. However, for $0.10 \leqslant \zeta \leqslant 0.20$, peak $\dot{y}_{\mathrm{RMS}}$ is observed at $U^* = 5.0$, where $\bar{P}_\alpha$ is recorded at $U^* = 4.5$. The average power depends on the ratio of $\dot{y}^2_{\mathrm{RMS}}/U^*$, which is higher at $U^* = 4.5$ than at $U^* = 5.0$ (Figure 5.10). For $L = 3.0, T = 3.0$, the maximum power at $\zeta = 0.16$ coincides with the peak vibration amplitude. The corresponding peak power, 0.26, is lower than the maximum power attained for $L = 3.0$, $T = 2.0$. It raises the question of why the $\bar{P}_\alpha$ is observed at $\zeta = 0.24$ for $L = 3.0$, $T = 2.0$, while the corresponding $\bar{P}_\alpha$ at the same ζ for $T = 3.0$ is comparatively lower. It is quite obvious from Figures 5.10(a) and (b) that the $\dot{y}_{\mathrm{RMS}}$ value at $\zeta = 0.24$ for $L = 3.0, T = 2.0$ is higher than that of $\zeta = 0.24$ for $L = 3.0, T = 3.0$. Since the average non-dimensional power is the product of $C_{L_{\mathrm{RMS}}}$ and $\dot{y}_{\mathrm{RMS}}$, the power transmitted from the fluid to the structure is equal to the power dissipated. From Figures 5.4(a) and (b), it is observed that the $C_{L_{\mathrm{RMS}}}$ at $\zeta = 0.24$ for $L = 3.0, T = 2.0$ is higher than that for $L = 3.0, T = 3.0$. It leads to an increased power output at $\zeta = 0.24$ for the $L = 3.0$, $T = 2.0$ arrangement. At fixed $L = 3.0$, the maximum power is achieved at $U^* = 5.0$ and 4.5 for $T = 3.0$ and 4.0, respectively. The optimum ζ for $L = 3.0, T = 3.0$ and 4.0 is found to be 0.16. Also, the $\bar{P}_\alpha$ decreases with T. With the increase in damping, the power curve at higher U^* becomes flatter, which indicates that at higher U^*, power does not die down quickly with increasing damping. The reason is a higher $C_{L_{\mathrm{RMS}}}$ value at higher damping values at higher U^*.

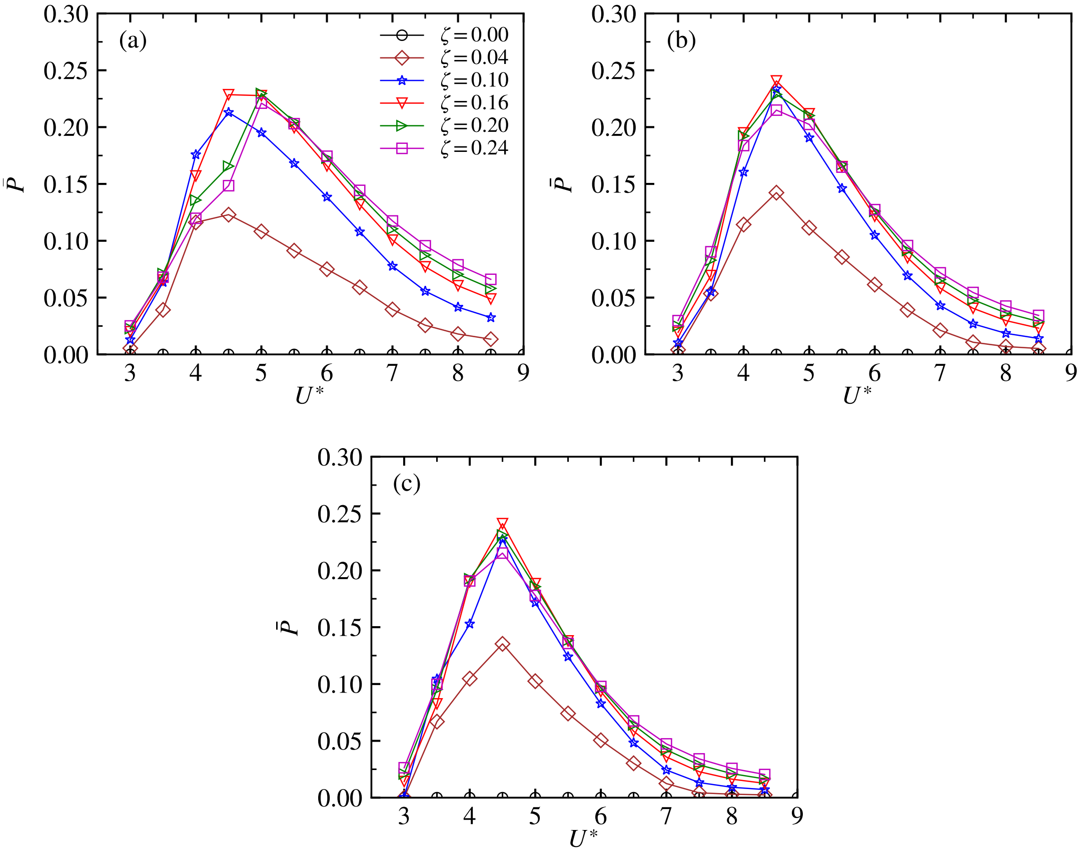

Fig. 5.11 Variation of $\bar{P}$ with U^* for $L = 4.0$ at (a) $T = 2.0$, (b) $T = 3.0$, and (c) $T = 4.0$ for $0 \leqslant \zeta \leqslant 0.28$.

Figure 5.11 represents the average power for the $L = 4.0$ configuration at different T. The $\bar{P}_\alpha$ observed for $L = 4.0, T = 2.0$ is 0.23. For $T = 3.0$ and 4.0, the maximum power is 0.24 for both cases. Therefore, based on the previous L cases, it is evident that $\bar{P}_\alpha$ increases with increasing T. However, with an increase in T for a particular L, a decline in oscillation amplitude is observed. So, the results are counterintuitive. For all $L = 4.0$ cases, the optimum ζ is observed to be 0.16. The U^* for $\bar{P}_\alpha$ at $T = 3.0$ and 4.0 coincides with that where maximum A^* is observed. Nevertheless, for $T = 2.0$, the U^* for maximum amplitude and the maximum average power are different. The U^* for peak amplitude is found to be higher than that for maximum power output at this T.

The relation between the maximum average power, $\bar{P}_\alpha$, and mass-damping, α, is illustrated in Figure 5.12. As observed earlier, the average power is maximized at a specific value of α for a given staggered arrangement. Except for a few cases ($L = 2.0, T = 2.0$ and $L = 3.0, T = 2.0$), the optimum α where maximum power is obtained is 0.32. However, from Figure 5.12, no apparent relation of maximum power with L and T is observed. The reason lies with the gap flow characteristics. Except for $L = 2.0$, a decrease in maximum power with increasing L is found at a particular T. But for fixed L, the peak of $\bar{P}_\alpha$ occurs at $T = 3.0$ before decreasing at $T = 4.0$. From the above discussions, it is evident that A^* influences power implicitly, while $\dot{y}_{\mathrm{RMS}}$, $C_{L_{\mathrm{RMS}}}$, and α explicitly do. The influence of ϕ on the harvested power is minimal. The trend of ϕ reveals that maximum power appears in the initial branch, and does not correspond to any specific value of ϕ. For example, even at $\phi = 90°$, the power is not maximized. As ϕ increases, the fluid–structure interaction becomes progressively desynchronized, which reduces the motion amplitude and weakens the force–velocity alignment. This loss of synchronization leads to a monotonic decrease in harvested power at higher U^*.

Maximum power extraction efficiency, η_α, is plotted against α in Figure 5.13(a). The power extraction efficiency (η) is the ratio between the extracted power and the maximum power extracted from the flow. The maximum power from the flow is achieved when the entire kinetic energy from the flow is harnessed. The maximum power per unit area, extracted from a flow of free-stream velocity U and density ρ, can be written as $\frac{1}{2}\rho U^3$. As the cylinders are of unit length, the total area covered by the two cylinders in one oscillation cycle is $(D + 2A + T)$. Therefore, η can be calculated as shown in Equation 5.6,

$$\eta = \frac{\bar{P}}{1 + 2A^* + T} \tag{5.6}$$

Maximum efficiency (η_α) is reported as 0.075 for $L = 3.0, T = 2.0$ at $\alpha = 0.48$, though the maximum power is observed at $L = 2.0, T = 3.0$. The reason is higher T and lower amplitude at optimum damping for $\bar{P}_\alpha$. The maximum efficiency is observed within the minimum and maximum α range. As this efficiency is the maximum power non-dimensionalized by the gaping and vibration amplitude, the total swept area

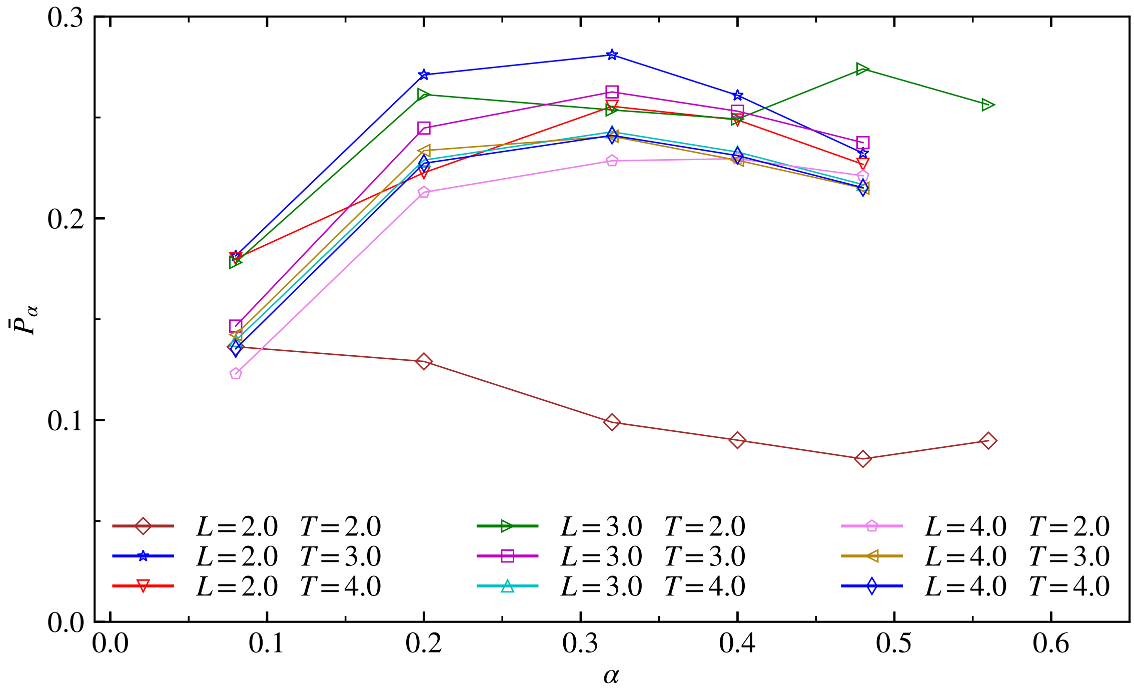

Fig. 5.12 Variation of maximum average power, $\bar{P}_\alpha$ with mass-damping parameter, α for all the staggered arrangements.

increases with an increase in amplitude or vertical gaping. The η_α follows almost the same trend as the maximum power versus ζ. However, at lower T values, higher efficiency is observed despite the lower $\bar{P}_\alpha$ compared to other configurations. It is also observed from the amplitude response and average power curve that the effect of T in amplitude and power is more than the effect of L. Nevertheless, it is advisable to avoid using higher L and T from a cost standpoint. In this regard, the $L = 2.0, T = 3.0$ and $L = 3.0, T = 2.0$ cases are the best as they represent a cost-effective arrangement in terms of total volume swept. Also, the $L = 4.0, T = 2.0$ arrangement boasts the second-highest efficiency.

Another way to describe the effectiveness of harnessed power is power density, χ. The power density is defined as the ratio of the average power to the volume of fluid displaced in a cycle of oscillation. The total volume of fluid displaced in a staggered arrangement is $(D + L)(D + T + 2A)$. For simplicity, it is assumed that the flow is uniform between the cylinders. Therefore, χ is defined as follows,

$$\chi = \frac{\eta}{1 + L} \tag{5.7}$$

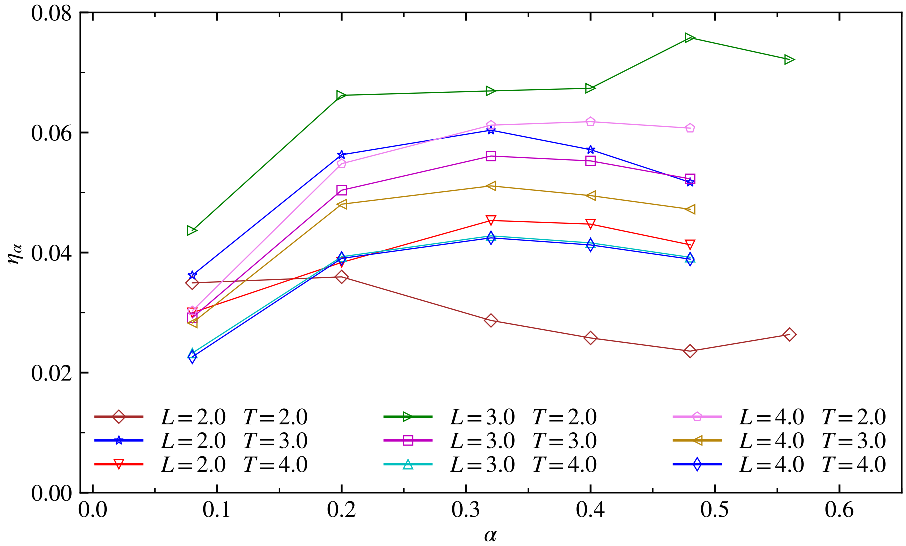

(a)

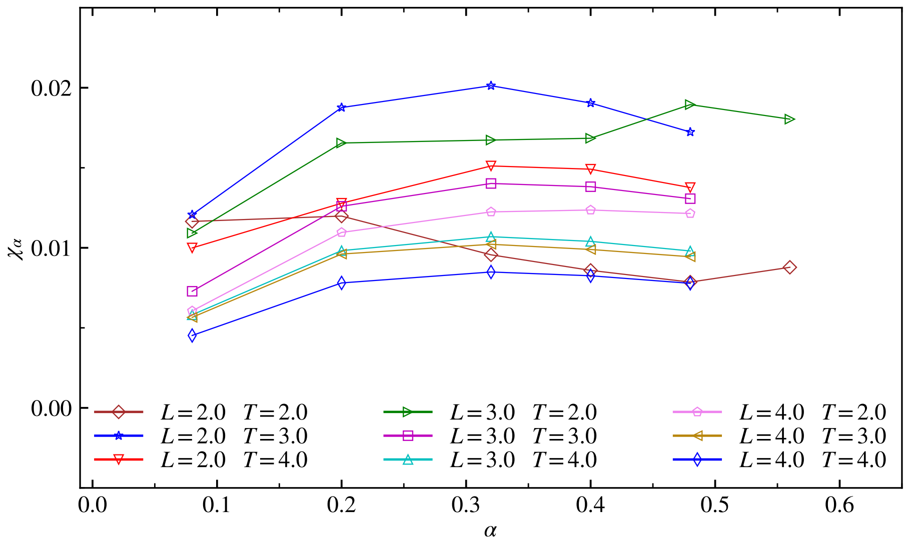

(b)

Fig. 5.13 Variation of maximum power extraction efficiency (a) η_α and maximum power density (b) χ_α with α with different L and T.

Figure 5.13(b) shows the maximum power density χ_α of 0.02 for the case of $L = 2.0, T = 3.0$, while for $L = 3.0, T = 2.0$, $\chi_\alpha = 0.018$. As L increases from 2.0 to 3.0, the swept volume increases, resulting in a decrease in power density, though the η_α is highest in $L = 3.0, T = 2.0$. The χ_α curves are flatter than the efficiency curve. However, the maximum χ_α is observed at $\alpha = 0.32$ except for the $L = 3.0, T = 2.0$ arrangement. Although the efficiency at $L = 2.0, T = 4.0$ is very low, the power density is found to be much higher than other T cases due to the lower swept volume. The lowest χ_α is observed at $L = 4.0, T = 4.0$ and $L = 2.0, T = 2.0$, due to the highest gaping and lowest peak power, respectively.

The minimum η_α and χ_α is recorded at $L = 2.0, T = 2.0$. The configurations $L = 3.0, T = 2.0$ and $L = 2.0, T = 3.0$ are comparable, as both exhibit relatively higher η_α and χ_α compared to other arrangements. Also, from the cost perspective, $L = 3.0, T = 2.0$, and $L = 2.0, T = 3.0$ are favorable options. In contrast, $L = 4.0, T = 4.0$ is the least favourable choice, as the increase in gaping does not correspond with a proportional increase in power. Increased gaping raises the cost because the cylinders are to be mounted on a single shaft, resulting in a longer shaft length. Additionally, $L = 2.0, T = 2.0$ is not a viable option, as the maximum power generated is less than that of a single cylinder. Comparing the power density χ_α with that of the tandem arrangement (Figure 4.7b), the staggered configuration consistently yields lower values across all L and T combinations. This is attributable to the larger total area swept by the staggered arrangement, which includes both the streamwise spacing L and the cross-stream width T in the denominator of χ, resulting in a greater area penalty relative to the tandem case.

5.3.5 Vorticity contours

The z-vorticity contours at $L = 2.0, T = 2.0$ shown in Figure 5.14 represented at the maximum power at two representative ζ values. The small black lines represent the maximum displacement position of the center of the cylinder, and the pink line represents the current displacement. The blue arrow illustrates the magnitude and direction of cylinder velocity. The time-averaged skin-friction coefficient ($\bar{C_f}$) and pressure coefficient ($\bar{C_p}$) of individual cylinders are calculated around the surface of the cylinders at varying θ. The angle θ is measured from the front stagnation point in the clockwise direction. The fluctuating components are represented by the filled shaded region within $\bar{C_f} \pm C_f{}'$ and $\bar{C_p} \pm C_p{}'$. The localized gap flow velocity, c_g, is the flow velocity normal to the line joining the cylinder centers, and shown by black arrows (Sharma and Bhardwaj, 2023). The The length of the arrow is proportional to the magnitude of c_g. The damping ratio has a significant influence on the wake behaviour. At lower damping ($\zeta = 0.04$), both cylinders undergo large-amplitude VIV, producing more irregular vortex structures in the near-wake compared to $\zeta = 0.16$ (Figure 5.14). The fluctuations of pressure and wall shear stress diminish as ζ increases (Figure 5.15), with the downstream cylinder consistently showing greater sensitivity to wake disturbances than the upstream cylinder. The subscripts 1 and 2 in the coefficients denote the upstream and downstream cylinders, respectively. The spread of the maximum and minimum pressure and shear stress is more at the downstream cylinder than in the upstream cylinder, irrespective of ζ. At $\zeta = 0.04$, both cylinders, particularly the downstream one, show strong fluctuations in $\bar{C_p}$ and $\bar{C_f}$, as reflected by the larger amplitudes and wider fluctuation bands. Both the mean upper separation (around 133°–135°) and lower separation (around 226°–230°) points remain consistent for both cylinders; however, the larger temporal fluctuation indicates wake instability. When the damping is increased ($\zeta = 0.16$), both $\bar{C_p}$ and $\bar{C_f}$ become smoother and more symmetric, especially in the range of 90° and 270°. The suction peak weakens and the zero-crossing of $\bar{C_f}$ shifts downstream, indicating early lower separation points for both cylinders. This demonstrates that larger damping suppresses the vortex-induced motion, and consequently reduces unsteadiness in the wake. The downstream cylinder is consistently more sensitive to wake disturbances, showing greater variation than the upstream cylinder. The lower variation in pressure and shear stress is a direct indication of lower lift. Therefore, the lift generated at $\zeta = 0.04$ is more than that of $\zeta = 0.16$.

The effects of L and T can both be visible for the vorticity contours of $L = 4.0, T = 4.0$ in Figure 5.16. As L and T both increase, the gap flow is reduced, and the wake characteristics show two independent vortex streets with negligible interaction between them. The wake is more organized at $\zeta = 0.16$, and the upstream cylinder exhibits C(2S) vortex shedding instead of two 2S vortex streets at $\zeta = 0.04$. The vortices at $\zeta = 0.04$ are more pronounced than at $\zeta = 0.16$, and increased damping leads to earlier diffusion of the wake, consistent with the reduced oscillation amplitude at higher damping. At maximum power, both $\bar{C_p}$ and $\bar{C_f}$ show similar shapes for the upstream cylinder for the two damping ratios. The fluctuations are reduced at higher damping. At $\zeta = 0.04$, the downstream cylinder shows more pressure asymmetry with larger peaks, while at $\zeta = 0.16$, the upstream and downstream curves look similar, indicating weaker wake interaction (Figure 5.17). The separation points remain unchanged for

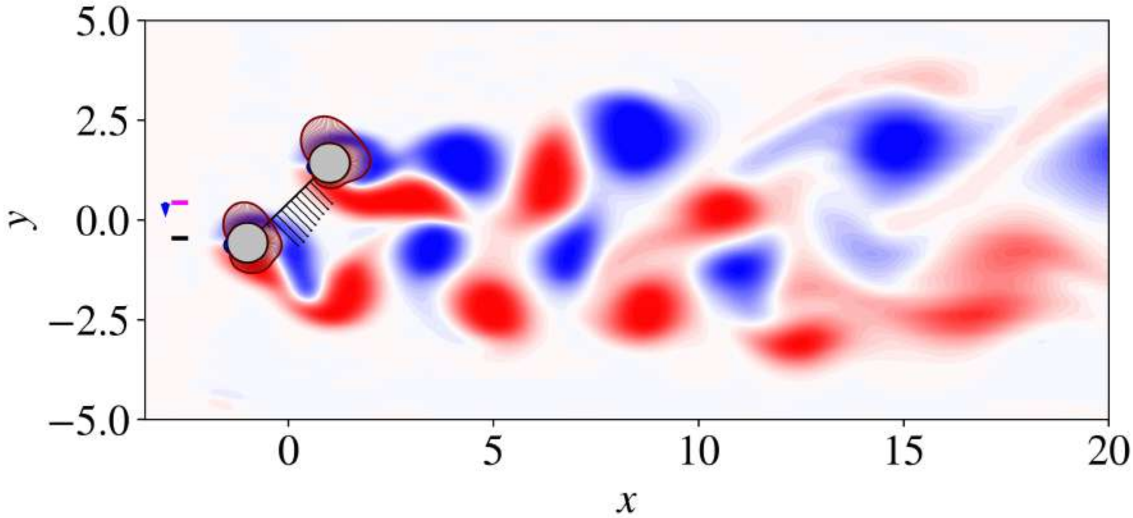

(a)

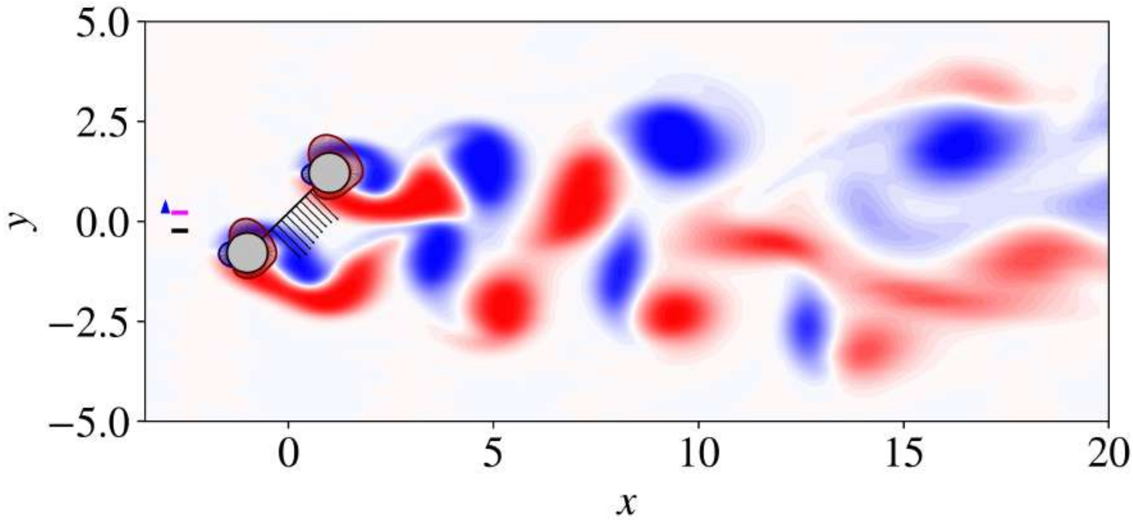

(b)

Fig. 5.14 Vorticity contours for $L = 2.0, T = 2.0$ at maximum power at (a) $\zeta = 0.04$ and (b) 0.16. The vorticity is captured when the cylinder is at maximum displacement and ranged between -1 (blue, clockwise) to 1 (red, anticlockwise).

both the cylinders and dampings. Although the amplitude and fluctuation of $\bar{C}_p$ and $\bar{C}_f$ decrease at $\zeta = 0.16$, the combined lift is seen to be higher for $\zeta = 0.16$ at maximum power. To analyze the combined lift response of the two cylinders, the instantaneous lift coefficients are decomposed as

$$C_{Li}(t) = \overline{C}_{Li} + C'_{Li}(t),$$

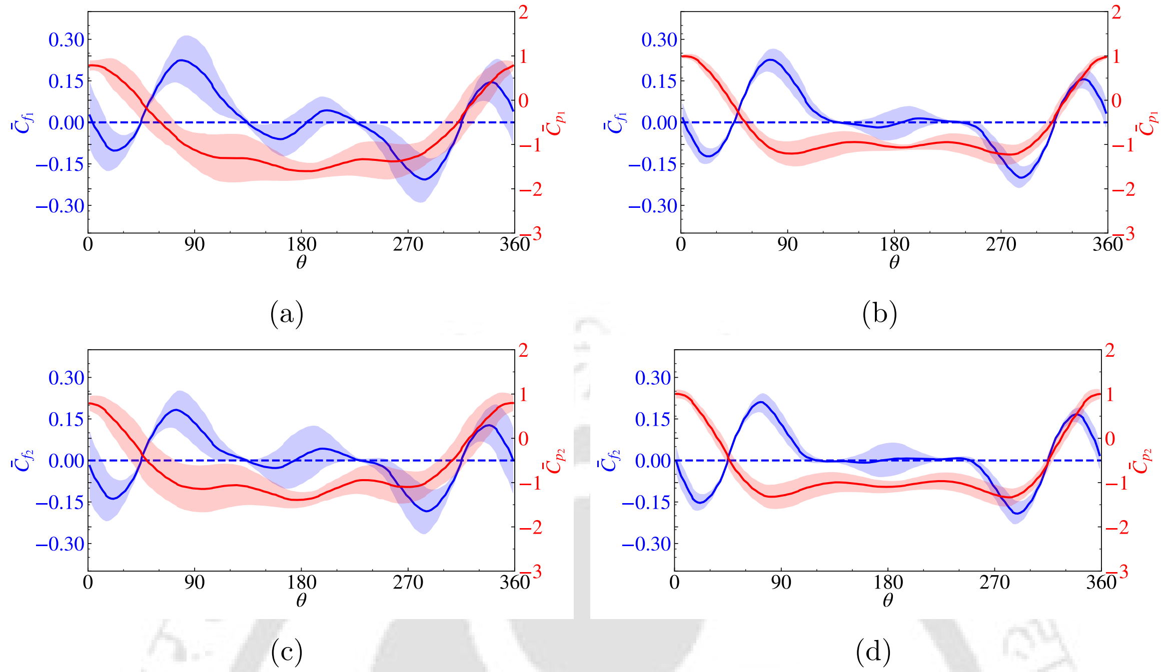

Fig. 5.15 Time-averaged skin-friction coefficient ($\bar{C}_f$) and pressure coefficient ($\bar{C}_p$) with the variation of θ at maximum power at (a,c) $\zeta = 0.04$ and (b,d) 0.16 for $L = 2.0, T = 2.0$. The first column of figures denotes the $\zeta = 0.04$ and second column for $\zeta = 0.16$.

where $\overline{C}_{Li}$ is the time-averaged lift coefficient and $C'_{Li}(t)$ denotes the fluctuating component. The root-mean-square (RMS) of the lift fluctuations is defined as

$$\sigma_{Li} = \sqrt{\left\langle \left(C'_{Li}(t)\right)^2 \right\rangle},$$

which quantifies the strength of the unsteady lift acting on each cylinder.

The degree of temporal alignment between the lift fluctuations of the two cylinders is measured using the correlation coefficient

$$\rho_{12} = \frac{\langle C'_{L1}(t)\, C'_{L2}(t)\rangle}{\sigma_{L1}\, \sigma_{L2}}.$$

A value of $\rho_{12} = 1$ indicates perfectly in-phase (fully constructive) lift oscillations, $\rho_{12} = 0$ corresponds to uncorrelated behaviour, and $\rho_{12} = -1$ represents perfectly out-of-phase (destructive) oscillations. These quantities are introduced because the RMS of the combined lift coefficient, defined as

$$C_{L_{\mathrm{RMS}}} = \left\langle \left(C_{L1}(t) + C_{L2}(t)\right)^2 \right\rangle^{1/2},$$

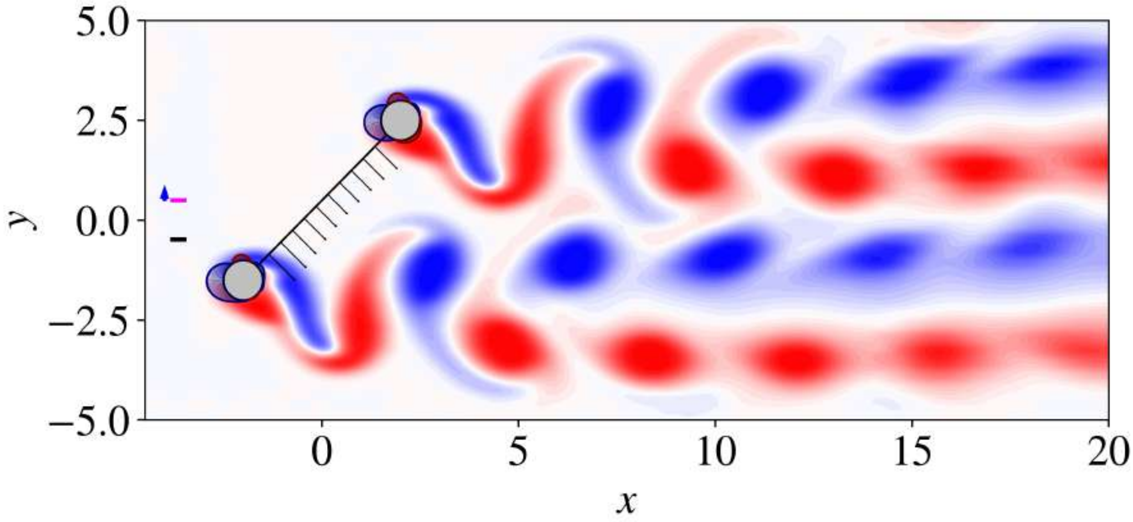

(a)

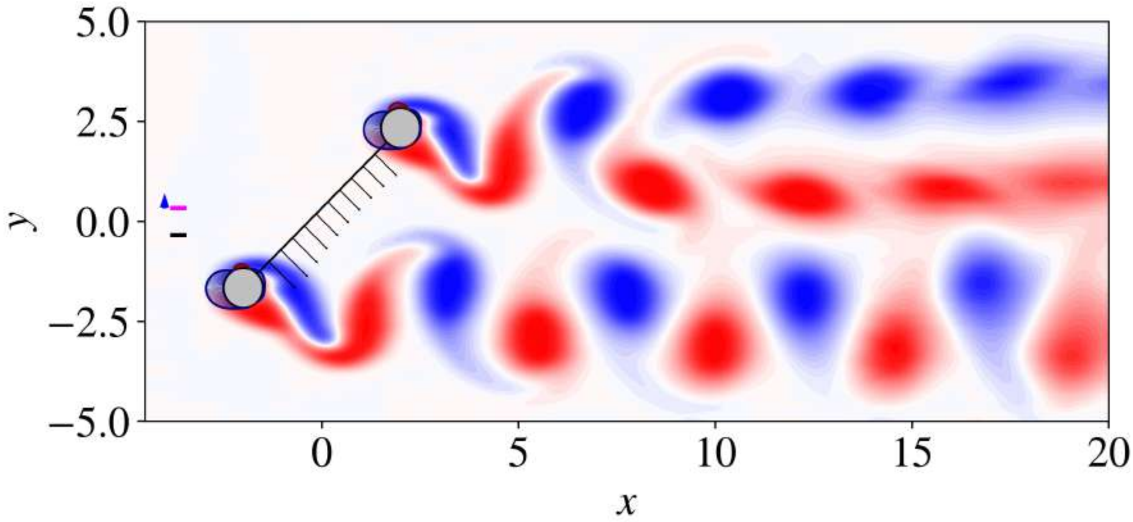

(b)

Fig. 5.16 Vorticity contours for $L = 4.0, T = 4.0$ at maximum power at (a) $\zeta = 0.04$ and (b) 0.16.

can be written in terms of the individual RMS values and their correlation as

$$C_{L_{\mathrm{RMS}}}^2 = \sigma_{L1}^2 + \sigma_{L2}^2 + 2\,\sigma_{L1}\sigma_{L2}\rho_{12}.$$

This expression shows that the combined lift depends not only on the magnitude of the individual lift fluctuations (σ_{L1} and σ_{L2}), but also on their phase relationship through ρ_{12}. Consequently, even if the individual lift amplitudes decrease with increasing

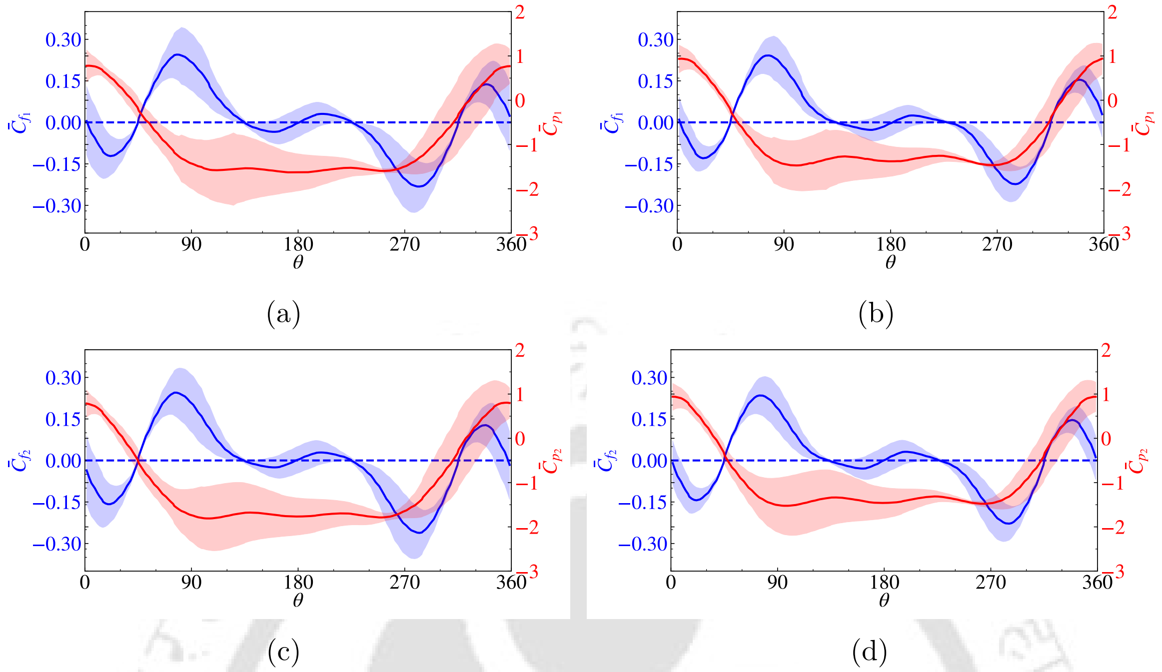

Fig. 5.17 Time-averaged skin-friction coefficient ($\bar{C_f}$) and pressure coefficient ($\bar{C_p}$) with the variation of θ at maximum power at (a,c) $\zeta = 0.04$ and (b,d) 0.16 for $L = 4.0, T = 4.0$. The first column of figures denotes the $\zeta = 0.04$ and second column for $\zeta = 0.16$.

damping, a higher value of ρ_{12} leads to a stronger constructive interaction and thus a larger combined RMS lift can be observed. For this case, the lift fluctuations of the two cylinders become highly synchronized at $\zeta = 0.16$: the correlation coefficient increases from $\rho_{12} \approx 0.93$ ($\zeta = 0.04$) to $\rho_{12} \approx 0.99$ ($\zeta = 0.16$). Since the much larger covariance term at $\zeta = 0.16$ leads to constructive addition of the instantaneous lifts, the combined $C_{L_{\mathrm{RMS}}}$ increases despite the reduction in the individual σ_{L_i}. Physically, higher damping suppresses broadband phase jitter and promotes phase-locked vortex shedding, resulting in nearly in-phase forcing on both cylinders and, consequently, a stronger combined lift response.

For $L = 2.0$ and $T = 3.0$, the upstream and downstream cylinders interact noticeably through the near wake (Figure 5.18). At the lower damping ($\zeta = 0.04$), the larger structural oscillations generate strong, orderly vortices, which extend to the far wake. When the damping is increased to $\zeta = 0.16$, the large-amplitude oscillations are suppressed, resulting in a less energetic wake. Moreover, the 2S vortex streets at $\zeta = 0.04$ are replaced by C(2S) from the downstream cylinder and a more diffused 2S pattern from the upstream cylinder at $\zeta = 0.16$. For the upstream and downstream

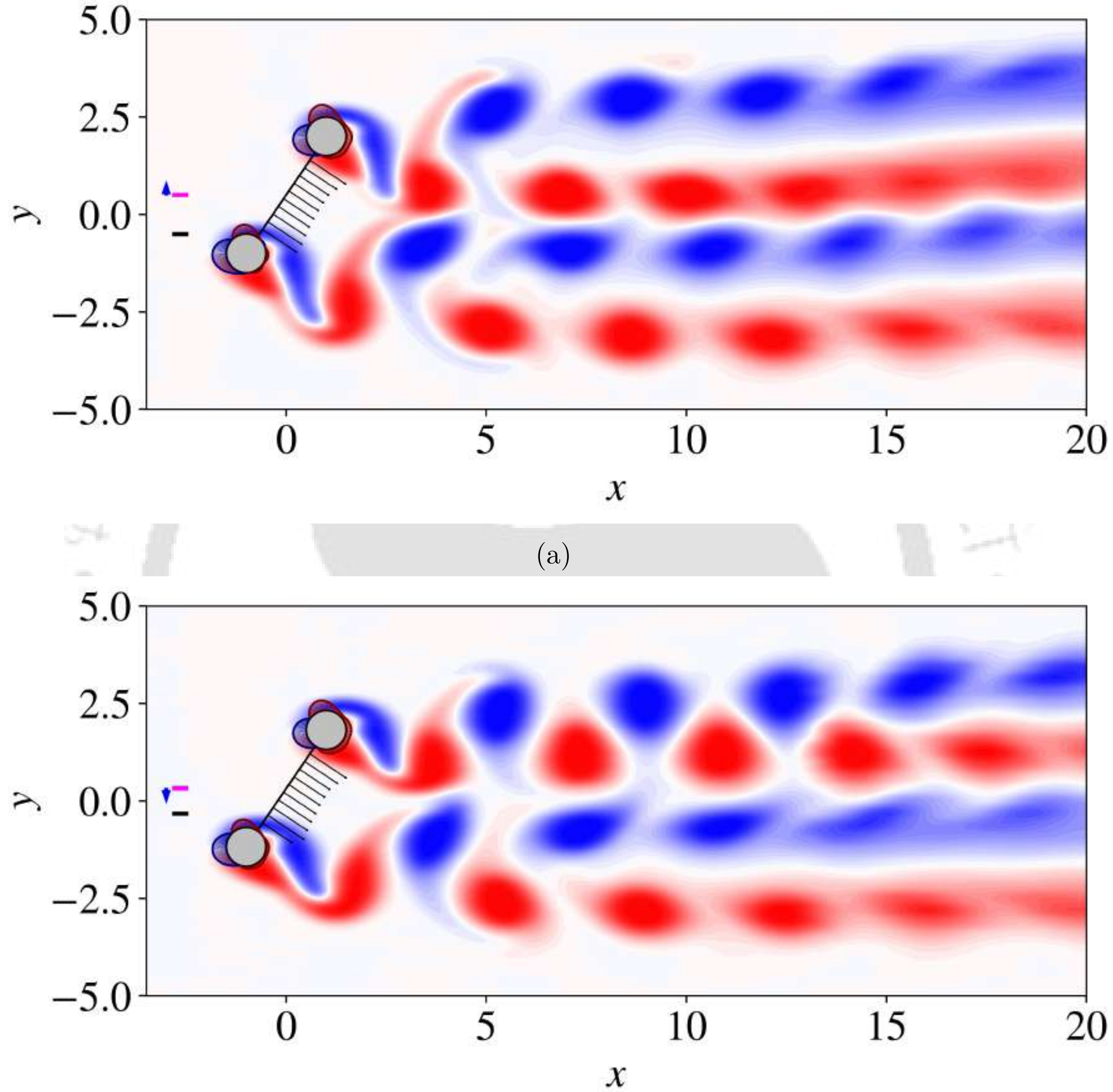

(a)

(b)

Fig. 5.18 Vorticity contours for $L = 2.0, T = 3.0$ at maximum power at (a) $\zeta = 0.04$ and (b) 0.16.

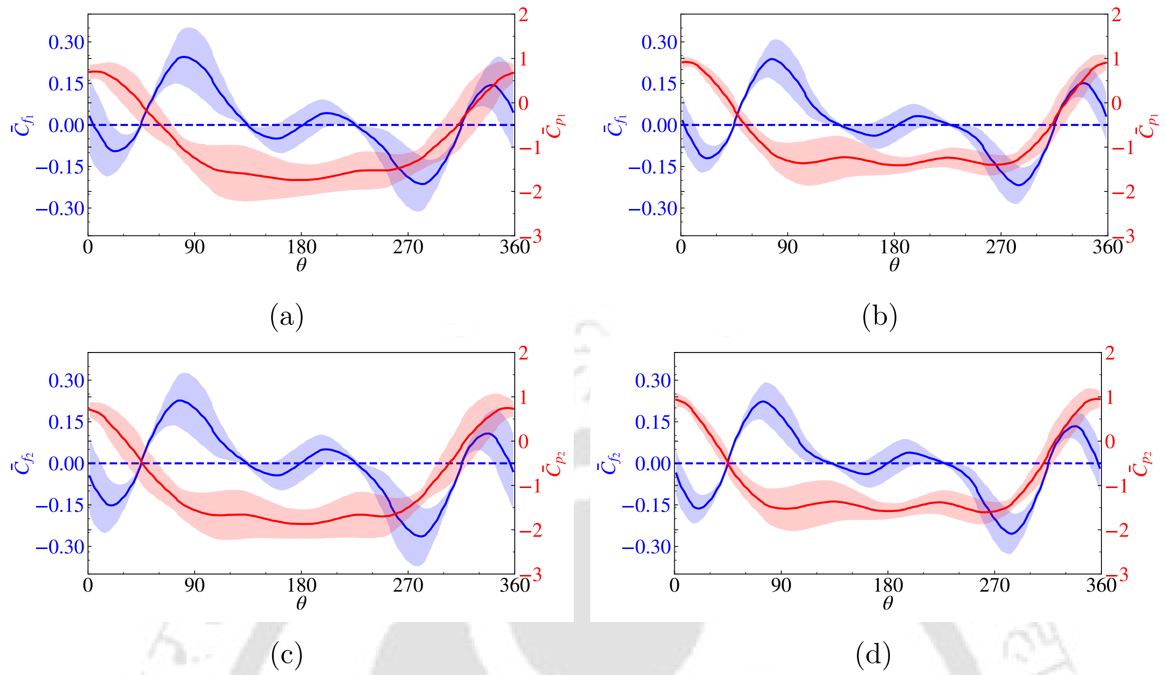

(a) (b) (c) (d)

Fig. 5.19 Time-averaged skin-friction coefficient ($\bar{C}_f$) and pressure coefficient ($\bar{C}_p$) with the variation of θ at maximum power at (a,c) $\zeta = 0.04$ and (b,d) 0.16 for $L = 2.0, T = 3.0$. The first column of figures denotes the $\zeta = 0.04$ and second column for $\zeta = 0.16$.

cylinders at $L = 2.0, T = 3.0$, the $\bar{C}_p$ and $\bar{C}_f$ distributions exhibit broadly similar behavior for both damping levels (Figure 5.19). At $\zeta = 0.04$, $\bar{C}_p$ shows slightly deeper suction in the upper separation region, and the $\bar{C}_f$ displays marginally stronger variations near the onset of separation for both the cylinders, consistent with the more energetic vortex shedding at lower damping. At $\zeta = 0.16$, the $\bar{C}_p$ and $\bar{C}_f$ curves become smoother with narrower fluctuations, indicating reduced unsteadiness. Although the overall magnitude and spatial distribution of the surface loading are higher in the case of $\zeta = 0.04$, the combined lift coefficient is slightly lower at that ζ compared to $\zeta = 0.16$. The reason is that the cross-cylinder correlation coefficient for $\zeta = 0.16$ ($\rho_{12} \approx 0.97$) is higher than that of $\zeta = 0.04$ ($\rho_{12} \approx 0.92$), leading to more constructive interference in the lift fluctuations at higher damping.

5.4 Summary

This study focuses on the effect of damping and gaping between the rigidly coupled staggered cylinders on the power generation from VIV at Re = 150. The vibration amplitude response, frequency response, phase difference, and lift coefficient are also investigated for different arrangements. The mass ratio is kept constant at 2.0. L and T are varied between 2.0 and 4.0, while ζ is varied between 0.04 and 0.28.

The vibration amplitude response at $L = 2.0, T = 2.0$ exhibits multiple peaks at lower damping values ($\zeta = 0.04$ and 0.10), resulting from stronger wake interaction. With the increase in damping, the peaks and valleys become smoother. This type of non-monotonic behavior is not observed at $T = 3.0$ and 4.0 for $L = 2.0$. At $T = 2.0$, the peak amplitude has a non-monotonic relation with L, while for a particular L it decreases monotonically with T.

The synchronization region decreases with an increase in damping and T for a particular L. However, with an increase in L, there is no change in the width of the synchronization—only the onset of desynchronization changes. At the end of the synchronization, a phase jump occurs, which is the onset of the lower branch. The maximum $C_{L_{\text{RMS}}}$ corresponds to a jump in vibration amplitude in the initial branch. In the transition region between the initial and lower branches, the location of minimum $C_{L_{\text{RMS}}}$ coincides with the point of maximum vibration amplitude.

At $L = 2.0, T = 2.0$, peak power corresponds to a jump in amplitude, and the U^* for maximum power is shifted to lower U^* values than that of the maximum vibration amplitude. With the increase in T, maximum amplitude and power are recorded at the same U^*, which also corresponds to maximum $\dot{y}_{\text{RMS}}$. The maximum power at $\zeta = 0.04 - 0.16$ for $L = 2.0, T = 2.0$ is comparable to single cylinder power (Soti et al., 2017), whereas for all ζ, the maximum power is almost twice that of the single cylinder for $T = 3.0$ and 4.0. The maximum power of 0.28 is recorded at $L = 2.0, T = 3.0$ with optimum $\zeta = 0.16$. The optimum ζ for $L = 2.0, T = 2.0$ is at the lowest damping. However, for $L = 3.0, T = 2.0$, a similar maximum power (0.28) is observed at optimum $\zeta = 0.24$. The maximum power peaks at $T = 3.0$ before decreasing at $T = 4.0$ for a particular L. Moreover, the power is higher for $L = 3.0$ cases compared to other L cases. The optimum ζ for the rest of the L cases and for all $L = 4.0$ cases is observed at $\zeta = 0.16$. Therefore, the optimum mass-damping parameter ($m^*\zeta = \alpha$) for maximum power is 0.32. There is no concrete relation found between the maximum power and L and T. Maximum power extraction efficiency (η_α) is though observed at $L = 3.0, T = 2.0$, not at maximum power ($L = 2.0, T = 3.0$). The trend of η_α resembles the maximum power trend ($\bar{P}_\alpha$). However, at lower T, higher η_α is recorded despite lower $\bar{P}_\alpha$ values. The maximum power density (χ_α) is observed at $L = 2.0, T = 3.0$, followed by $L = 3.0, T = 2.0$. Therefore, from a cost standpoint and due to higher power, efficiency, and power density, $L = 2.0, T = 3.0$ and $L = 3.0, T = 2.0$ are the most favorable options. $L = 4.0, T = 4.0$ and $L = 2.0, T = 2.0$ should be avoided due to the lower power-to-swept volume ratio.

Chapter 6

The effect of damping and aspect ratio on power extraction from vortex-induced vibration of elliptical cylinder

The bluff body dynamics of a cylindrical body and an elliptical body undergoing VIV are different. The optimum damping parameter and aspect ratio for power harvesting is investigated at a constant m^* and Re. A single elliptical cylinder constrained to vibrate only in the transverse direction is considered. The chapter starts by outlining the previous investigations on VIV and power extraction from different cross-section bluff bodies and motivation of this study (§ 6.1). Then, the computational model is discussed (§ 6.2). Validation of the numerical model with earlier studies is also laid out in that section. The effects of damping and aspect ratio on power extraction are explored (§ 6.3). The chapter then concludes with a summary of the outcomes (§ 6.4).

6.1 Introduction

As discussed in Chapter 1, the geometry of a bluff body significantly influences its VIV response. Unlike sharp-edged bodies, elliptic cylinders lack edges that can trip the flow from VIV to galloping, making their response characteristics distinct. When constrained to move in the cross-flow direction at $\mathrm{Re} = 100$, Vijay et al. (2020) observed only two response branches, with amplitude approximately twice that of a circular cylinder at $\epsilon = 0.1$ and an earlier onset of the initial branch. Kim and Park (2006) found that lift force increases with angle of attack (AOA) or by reducing cylinder thickness, while drag decreases with increasing Re. Zhao et al. (2019) showed that the lock-in region changes with $\epsilon = 0.67$ to 1.5. At lower ϵ, lock-in spans two amplitude regimes over $4.0 \leqslant U^* \leqslant 12.0$, with the major axis perpendicular to the flow producing amplitudes of around 1.05 and 1.56 at $\epsilon = 1.25$ and 1.50, respectively.

Apart from $m^*\zeta$ and Re, geometry affects the power extraction. Bhattacharya and Shahajhan (2016) numerically simulated flow past an elliptic cylinder and modeled power extraction as the power dissipated by the torsional spring only. They have attached the spring such that the ellipse is making $\pi/4$ angle to the incoming flow to generate a large unsteady rotational moment. They have varied density ratios similar to m^* from 0.1 to 25.0 and found power output increases up to a certain density ratio and decreases again for a particular damping coefficient. At Re = 100, power output is the highest for damping coefficient = 400 and then decreases for higher damping coefficient. While at Re = 200, power output increases with increasing damping coefficient.

Prior research has focused on examining the vibration response of undamped elliptical cylinders undergoing vortex-induced vibration (VIV). To the best of our knowledge, the effect of damping and its implication on flow power extraction from elliptical cylinder has not been reported in the literature. In this paper, power extraction from elliptical cylinders of different aspect ratios will be numerically investigated. Apart from this, the effect of frequency ratio, lift coefficient, and other parameters related to the VIV of the ellipse will also be highlighted.

6.2 Formulation

6.2.1 Governing Equations and Computational Methods

A 2-D incompressible Newtonian fluid flow model is considered to simulate the VIV response of the present study (§ 3). The Arbitrary Lagrangian-Eulerian (ALE) scheme is applied to deal with the moving boundary problem. The flow around long elliptical cylinders at Re = 100 has been shown to be two-dimensional (Thompson et al., 2014). Furthermore, as shown in Zhao et al. (2014), there are no differences in the vibration response predicted by 2D and 3D ($L/D = 9.6$) simulations at such low Re. Therefore, 2D simulations were performed to save computational time.

The general equation of motion of the elastically mounted elliptical solid body is given by the spring-mass-damper system in non-dimensional form as:

$$\ddot{y} + \frac{4\pi\zeta}{U^*}\dot{y} + \frac{4\pi^2}{U^{*2}}y = \frac{2}{\pi}\frac{C_L}{m^*}\frac{1}{\epsilon} \tag{6.1}$$

where $C_L = 2F(t)/\rho U^2 D$ is the lift force coefficient, where $F(t)$ denotes the lift force on the body. The extracted power is non-dimensionalized by the power available over the fluid region occupied by the body $(1/2\rho U^3 D)$. The average non-dimensional instantaneous power can be expressed as follows.

$$\bar{P} = \frac{2\pi^2\alpha}{U^*}(\epsilon)\dot{y}^2_{\mathrm{RMS}} \tag{6.2}$$

where $\alpha = m^*\zeta$ is the mass-damping parameter. The aspect ratio (ϵ) is defined as the ratio of the minor diameter (b) to the major diameter D $(\epsilon = b/D)$. The temporal term is discretized by the first-order implicit Euler method. The gradient (∇) and divergence $(\nabla\cdot)$ terms in the governing equation are discretized using second-order accurate schemes. The surface integral at each face of the finite volume and the volume integral of the source term are computed through Gauss quadrature. The interpolation method used is linear interpolation for both gradient and divergence terms. The Laplacian term is also integrated with the Gauss method with second-order accurate linear interpolation. The surface-normal gradients are corrected with explicit non-orthogonal correction.

6.2.2 Problem description

An elliptical cylinder of major diameter D and minor diameter b is placed in a flowing fluid with uniform velocity U where the major diameter is normal to the direction of flow. The center of the cylinder is taken as the origin. The blockage ratio is kept at 2.5% to eliminate the effect of top and bottom boundaries on the flow characteristics. The Reynolds number (Re) is kept constant at 100. The peak vibration amplitude of the elliptical and circular cylinders had been shown to be independent of the mass ratio (Soti et al., 2017; Vijay et al., 2020). Soti et al. (2017) showed that peak power extracted by the circular cylinder is also independent of the mass ratio. Therefore, the effect of mass ratio (m^*) is not explored in the present work; instead, it is kept fixed at $m^* = 10$. This value is close to the m^* values of other experimental studies done in water (Ding et al., 2015a; Govardhan and Williamson, 2006; Khalak and Williamson,

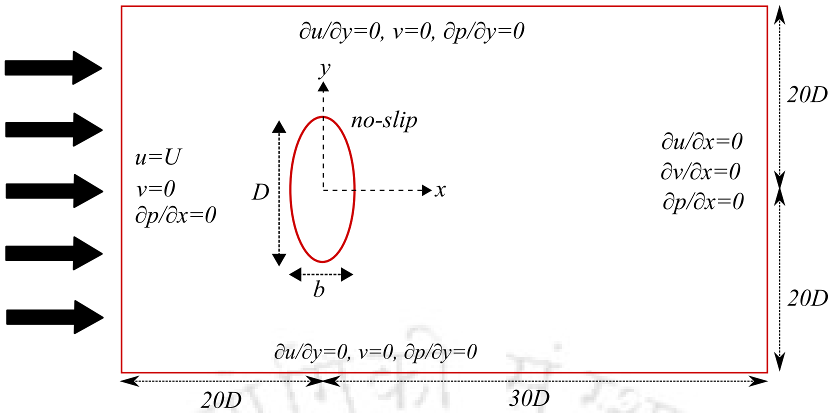

Fig. 6.1 Schematic of computational domain of the 1-DOF vortex-induced vibration of the elliptical cylinder

1999; Soti et al., 2018). The Reynolds number Re $= 100$ and mass ratio $m^* = 10$ are selected to match the parameters of Vijay et al. (2020), enabling direct comparison and validation of the present results against their study. The cylinder is elastically mounted on a spring of stiffness k and a linear damper with damping constant c that emulates the structural damping. In order to quantify power extraction, simulations are performed by varying reduced velocity (U^*) from 2.0–9.0 and damping parameter (ζ) in between 0.1 and 1.0.

6.2.3 Computational domain and boundary condition

The computational domain shown in Figure 6.1 is defined as $\Omega = [-20D, 30D] \times [-20D, 20D]$. At the inlet, the velocity is specified as $(u, v) = (U, 0)$. No-slip boundary condition ($u_{wall} = v_{wall} = 0$) is used at the surface of the elliptical body. At the lateral boundaries, symmetry boundary condition ($\partial u/\partial y = 0$, $v = 0$) is used to maintain shear stress and zero flux at these boundaries. Neumann boundary condition ($\partial u/\partial x = 0$, $\partial v/\partial x = 0$) is used at the outlet for the flow velocity. Neumann boundary condition is used for pressure ($\partial p/\partial x = 0$) at all the boundaries. The computation is initialized with constant velocity ($u = U$, $v = 0$) and pressure $p = 0$.

6.2.4 Mesh Independence and Model validation

The mesh used for the current problem is presented in the Figure 6.2 (a). Zoomed-in view of mesh around elliptical cylinder is shown in Figure 6.2 (b). Mesh independence study are performed to obtain the accurate result at low computational cost. In this

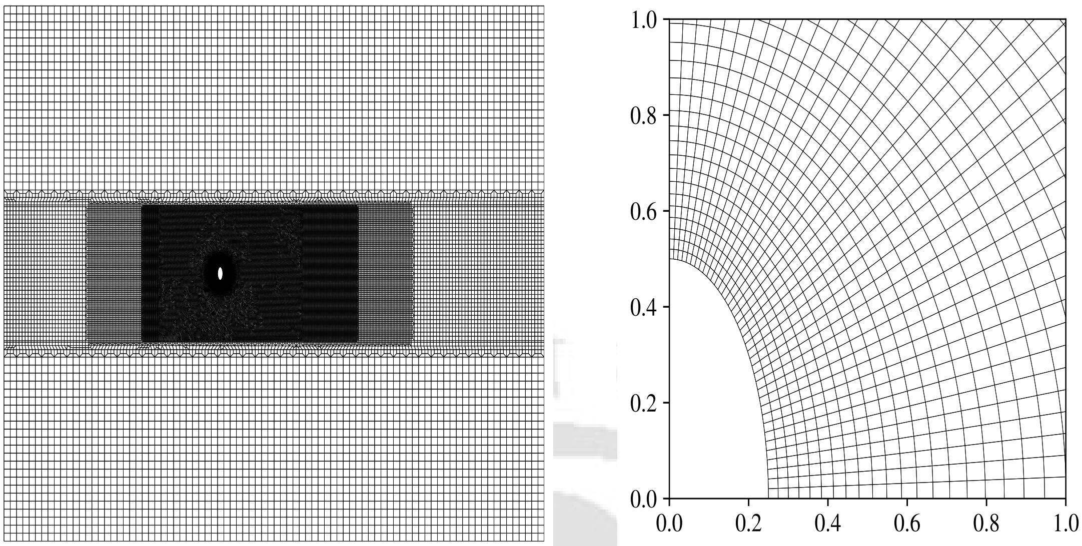

(a) (b)

Fig. 6.2 (a) Mesh of the total domain and (b) the mesh around the cylinder at $\epsilon = 0.50$

study, the amplitude of vibration is taken for validation by using four different mesh for aspect ratios 0.1, 0.25, 0.4, and 0.5. Table 6.1 shows the mesh independence data for $\epsilon = 0.10$. The mesh independence test for $\epsilon = 0.50$ (not shown here) is similar to Table 6.3. In this study, the amplitude of vibration is taken for validation by

Table 6.1 Mesh independence study on VIV of elliptical cylinder with $\epsilon = 0.10$ at $U^* = 4.7$.

Mesh	No of Cells	A^*	%Difference wrt M1
M1	45377	1.1857	0
M2	26437	1.1613	2.057
M3	24319	1.1168	5.810
M4	15684	1.009	14.90

Table 6.2 Mesh independence study on VIV of elliptical cylinder with $\epsilon = 0.25$ at $U^* = 4.0$.

Mesh	No of Cells	A^*	%Difference wrt M1
M1	105952	0.8724	0
M2	92016	0.8683	0.470
M3	54907	0.8639	0.974
M4	24602	0.9071	3.977

using four different mesh for aspect ratios 0.1, 0.25, and 0.4. Table 6.1 shows the mesh

Table 6.3 Mesh independence study on VIV of elliptical cylinder with $\epsilon = 0.40$ at $U^* = 4.5$.

Mesh	No of Cells	A^*	%Difference wrt M1
M1	56803	0.9711	0
M2	55574	0.9647	0.662
M3	43427	0.9555	1.609
M4	35023	0.9440	2.796

independence data for the present simulation. In order to validate the accuracy of the simulation, results are compared with that of Vijay et al. (2020) for the non-dimensional amplitude A^*. An elastically mounted elliptical cylinder, which is restricted to move in only transverse (y direction), is considered for validation. Table 6.4 compares the amplitude of vibration, A^* with Vijay et al. (2020). Results show good agreement with the results of Vijay et al. (2020). Furthermore, the maximum vibration amplitude of circular cylinder ($\epsilon = 1.00$) is tabulated for the present case and other literature (Shiels et al., 2001; Soti and De, 2020; Zhao, 2013) in Table 6.5. The present data shows good agreement with previous numerical studies. The temporal independence is shown in Appendix B.

Table 6.4 Comparison of vibration amplitude, A^* with Vijay et al. (2020)

ϵ	U^*	Present Study	Vijay et al. (2020)	%Difference in A^*
0.10	4.70	1.1613	1.175	1.165
0.25	4.00	0.8639	0.866	0.242
0.50	4.50	0.8625	0.850	1.470
1.00	5.00	0.5749	0.574	0.156

Table 6.5 Comparison of maximum amplitude with previous numerical investigations at $\epsilon = 1.00$

Investigation	Maximum amplitude
Present	0.5749
Shiels et al. (2001)	0.5800
Zhao (2013)	0.5759
Soti and De (2020)	0.5847

6.3 Results and discussion

6.3.1 Amplitude response and flow pattern for undamped system

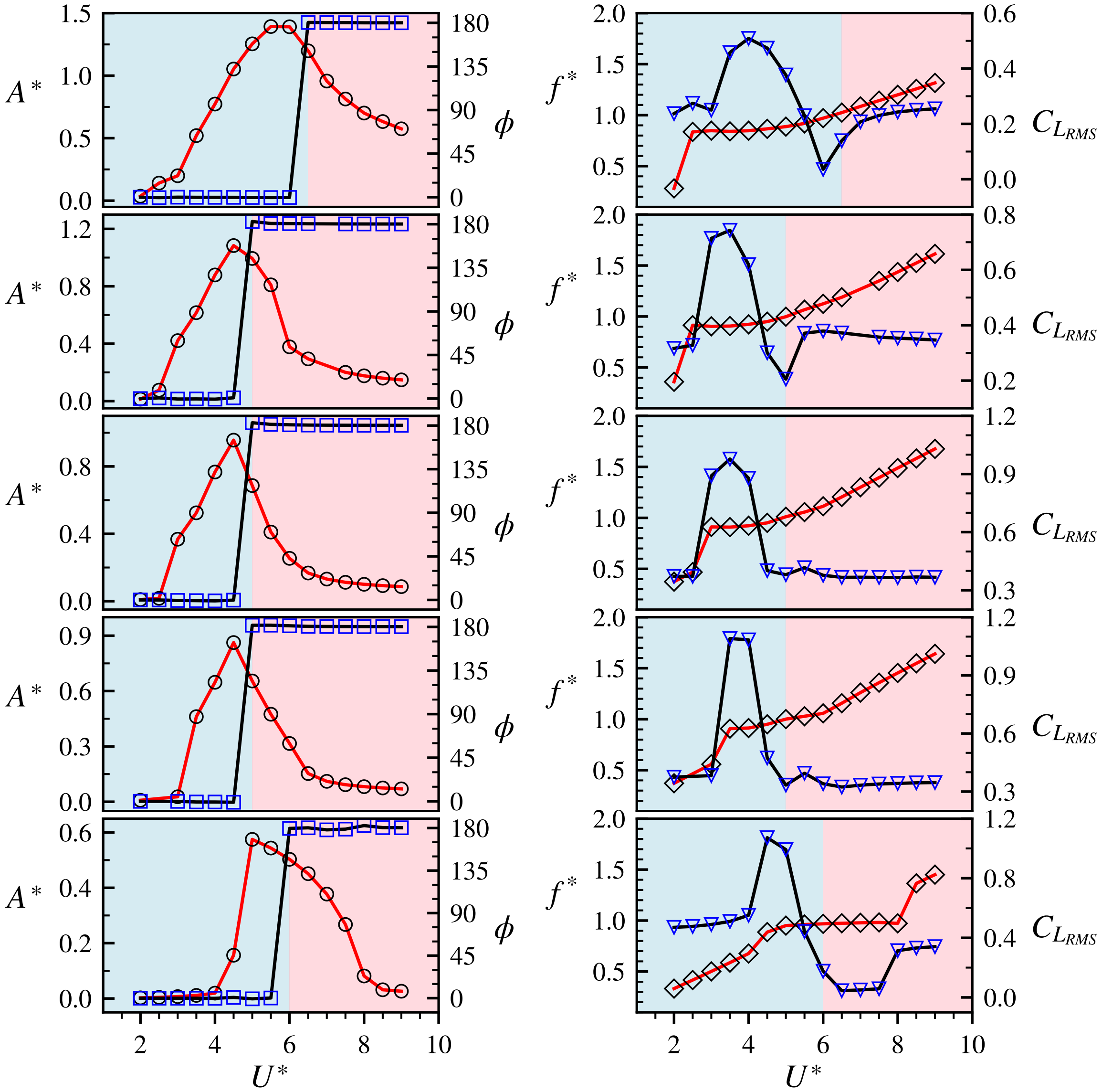

Fig. 6.3 Undamped response of amplitude (A^*), phase (ϕ), frequency (f^*) and lift coefficient $C_{L_{\mathrm{RMS}}}$ with U^* at (a) $\epsilon = 0.10$, (b) $\epsilon = 0.25$, (c) $\epsilon = 0.40$, (d) $\epsilon = 0.50$ and (e) $\epsilon = 1.00$. 'lightblue' denotes 'initial' branch and 'lightpink' denotes 'lower' branch.

The vibration amplitude response (A^*) along with phase angle (ϕ) of lift force is plotted against reduced velocity (U^*) plotted in Figure 6.3 for all the aspect ratios considered. A^* is defined as half the peak-to-peak displacement of the cylinder, normalized by the cylinder's major axis (D) as shown in Chapter 3. At zero damping, the amplitude is always greater than that of a damped system (Soti and De, 2020). Cylinder amplitude is seen close to zero for $\epsilon = 0.10$ and 0.50 at $U^* \leq 3.0$. However, at $\epsilon = 0.25$ and 0.40, the amplitude jumps to 0.40 at $U^* = 3.0$. The onset of that jump shifts to higher U^* ($U^* = 4.5$) at $\epsilon = 1.00$. Similar trend in variation of A^* is seen for all aspect ratio cylinders. Specifically, the cylinders are desynchronized with the flow at lower values of U^* and, therefore, A^* values are negligible. As U^* is increased, A^* jumps to a peak value due to synchronization of cylinder motion with the vortex shedding. The jump is steeper at higher ϵ. The onset of synchronization shifts to higher U^* with increase in ϵ. The peak vibration amplitude of the cylinders (A_0^*) is seen to increase with decreasing ϵ. The values of A_0^* are 1.412, 1.0837, 0.956, 0.8623, and 0.5728 for $\epsilon = 0.10$, 0.25, 0.40, 0.50, and 1.00, respectively. The peak vibration amplitudes are found in the range $4.5 \leqslant U^* \leqslant 5.5$. With further increase in U^*, vibrations of the cylinders tend to desynchronize, and A^* values drop. Except for $\epsilon = 0.10$, all other cylinders vibrate with much smaller amplitudes as compared to their A_0^* values in the desynchronized region. An illustration of the phase angle plot with U^* is also designated in Figure 6.3. The phase angle (ϕ) in Figure 6.3 represents the phase of the lift force with respect to the cylinder displacement. The method for finding phase angle is described in Soti and De (2020). Again, the trend of ϕ is similar for all cylinders. At lower U^*, the lift is in phase with cylinder displacement (phase angle is zero), and as U^* increases, the phase jumps to 180° implying that the lift became out of phase with phase with cylinder displacement. The jump in phase from 0° to 180° occurs when the vibration frequency of cylinder (f) goes from being smaller to higher than its natural frequency (f_n) (Soti and De, 2020). Non-dimensional frequency f/f_n or f^* and root mean square (RMS) lift coefficient $C_{L_{\mathrm{RMS}}}$ are also shown in Figure 6.3. The $\epsilon = 1.00$ case corresponds to a circular cylinder for which the amplitude response is categorized into two regions: initial branch ($4.0 \leqslant U^* \leqslant 6.5$) and lower branch ($6.5 \leqslant U^* \leqslant 8$) (Soti and De, 2020). The phase jump also coincides with the onset of the lower branch. The onset of the lower branch is seen to shift to lower U^* with increasing ϵ, except at $\epsilon = 1.0$. The onset of the initial branch is associated with a jump in vibration frequency value from close to vortex shedding frequency (f_s) to f_n. Some signs of the upper branch (usually associated with high Reynolds number cases) are also found in low Reynolds number vibration response of the circular cylinder (Leontini et al., 2006). Similar vibration response regions can be defined for other aspect ratio cylinders as shown in Figure 6.3. $C_{L_{\mathrm{RMS}}}$ touches lowest value when A^* is the highest except $\epsilon = 1.00$. Therefore, the lowest points of $C_{L_{\mathrm{RMS}}}$ mark the boundary between the initial and lower branches.

The instantaneous vortex shedding patterns at dynamically steady-state for all aspect ratios are shown in Figure 6.4 for two reduced velocities. The contour plots of Figure 6.4 show the z-component of vorticity ranging from -1 to 1. In Figure 6.4, the direction of the 'red' coloured arrow indicates the direction of cylinder motion, and the length of the arrow shows the magnitude of cylinder velocity in the y-direction. The small black lines indicate the maximum and minimum position of the cylinder in cross-flow direction for particular cases, and the magenta line informs the instantaneous position of the cylinder. The vortex shedding pattern for aspect ratios 0.10 and 0.25, as well as 0.40, is found to be similar at initial branch of oscillation. At $U^* = 9.0$, the vortex shedding pattern is identical to the pattern observed when flow occurs past a stationary cylinder, as the amplitude response is significantly less at the desynchronization region. At lower U^*, the two opposite sign vortices shed prominently from the two edges of the ellipse. They form a vortex street with two pairs of vortices shed in a single cycle of oscillation leading to 2S type vortex-shedding mode. However, after a certain wake distance, the vortex street merges to form a single von-Kármán-type street. At higher U^*, the width of the vortex street (the vertical separation between the vortices shedding from two ends of a cylinder) increases at $\epsilon = 0.10$ and 0.25. At $\epsilon = 0.25$ at $U^* = 4.5$, the width of the vortex street becomes the highest. However, with the increase in ϵ, the vortex street width gets shorter. At lower branch, 2S type vortices are observed, as two single vortices of the opposite shed from the body in a single cycle of oscillation. Additionally, pressure distribution around the cylinders is also represented in Figure 6.4 using 'navy' and 'maroon' colors to represent the negative (suction) and positive (blow) gauge pressure, respectively. The magnitude of the pressure distribution corresponds to the length of the lines spread out in the normal direction from the cylinder surface. In Figure 6.4(a), the cylinder oscillation is in an upward direction from the mid position. The pressure at the top edge of the cylinder is higher compared to the bottom due to the cylinder's upward motion. Flow separates from the back of the bottom end. The amplitude increases with U^* is clearly interpreted from Figure 6.4(b). Though the direction of velocity is upward, the magnitude is small compared to velocity in Figure 6.4(a) as the cylinder is in the bottom position. Increased magnitude of pressure is

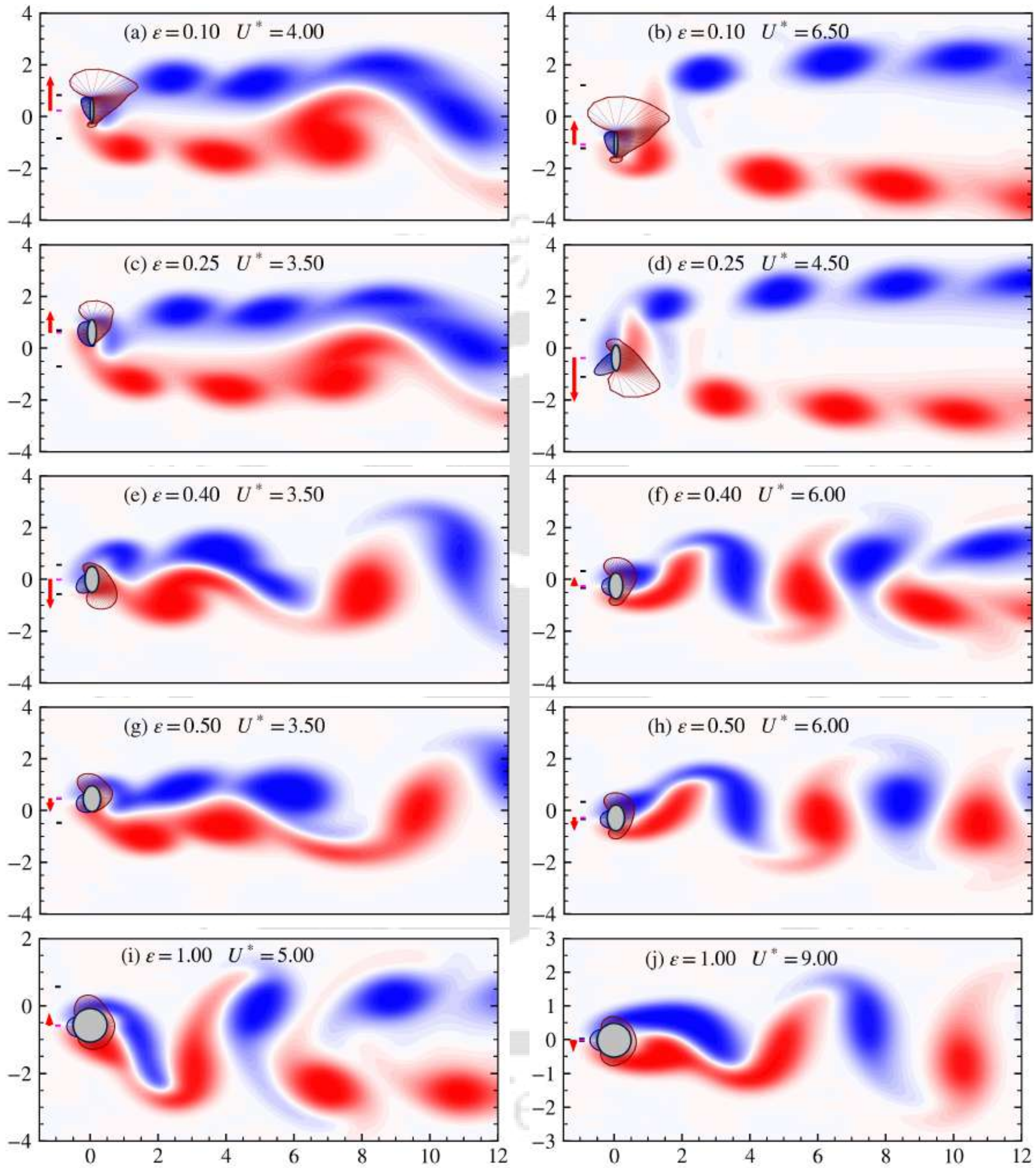

Fig. 6.4 Instantaneous z-vorticity contours and pressure distribution of VIV of elliptical cylinder for different aspect ratio at zero damping. For each ϵ, the two U^* values are selected to illustrate the change in vorticity shedding pattern observed across the response. 'red' and 'blue' represent counterclockwise and clockwise vortices respectively; 'navy'and 'maroon' represent negative and positive pressure respectively.

observed compared to the $U^* = 4.0$ case. At $\epsilon = 0.25$, when the cylinder is almost at the top end of the amplitude, as shown in Figure 6.4(c), the magnitude of positive pressure gets smaller, and negative pressure stretches to the aft end of the cylinder. The pressure profile reverses, i.e., increased pressure at the top and decreased pressure at the bottom is observed when the cylinder motion is in a downward direction, shown in Figure 6.4(d). The vorticity patterns are similar in the case of $\epsilon = 0.10$ and $\epsilon = 0.25$ for both the U^* cases. Also, as ϵ increases, the width of the vortex street decreases, and vortices are stretched in the flow direction.

6.3.2 VIV characteristics for damped system

Effect of damping at aspect ratio $\epsilon = 0.10$

The damping in the system affects not only the amplitude at different U^* but also other parameters like phase difference and frequency response. Damping does affect the flow-structure interaction due to the change in vortex-shedding patterns. Under dynamic steady-state condition of an undamped system, the net work done by the structure on the fluid matches with the net work done by the fluid on the structure. Therefore, no net energy is extracted from the flow. The damping in the system is introduced in the form of friction or additional structural damping. For a damped system, there is a net energy extracted from the flow in each cycle of cylinder oscillation. This extracted energy is dissipated by the damper. The vibration amplitude response in the damped case follows a similar trend as observed in the undamped case. The amplitude increases with U^*, attains a maximum value, and decreases with a further increase in U^* as shown in Figure 6.5. The vibration amplitude response for all ζ collapses to a single curve from $U^* = 8.0$ onwards. The amplitude of vibration is significant at $U^* = 9.0$, indicating no desynchronization at the highest reported U^*. With the increase in damping, the maximum A^* for specific U^* gradually declines. Maximum A^* for a particular ζ shifts towards higher U^* as ζ increases because the damped natural frequency is always less than the undamped natural frequency. The variation of the RMS value of body velocity $\dot{y}_{\mathrm{RMS}}$ is also shown for each ζ with the variation of U^*. However, the same trend for $\dot{y}_{\mathrm{RMS}}$ vs U^* is observed, as seen in the variation of A^* vs U^*. At every U^*, the standard deviation (σ) of transient amplitude response is also plotted. Standard deviation, σ is calculated as $\sigma = \sqrt{\frac{1}{M-1}\sum_{i=1}^{M}(p_i - \bar{p})^2}$. The peak value of displacement signal, p_i calculated by identifying the threshold such that p_i is greater than $A^*/50$. Therefore, p_i is the individual peak values, M denotes number of peaks and $\bar{p}$ is the

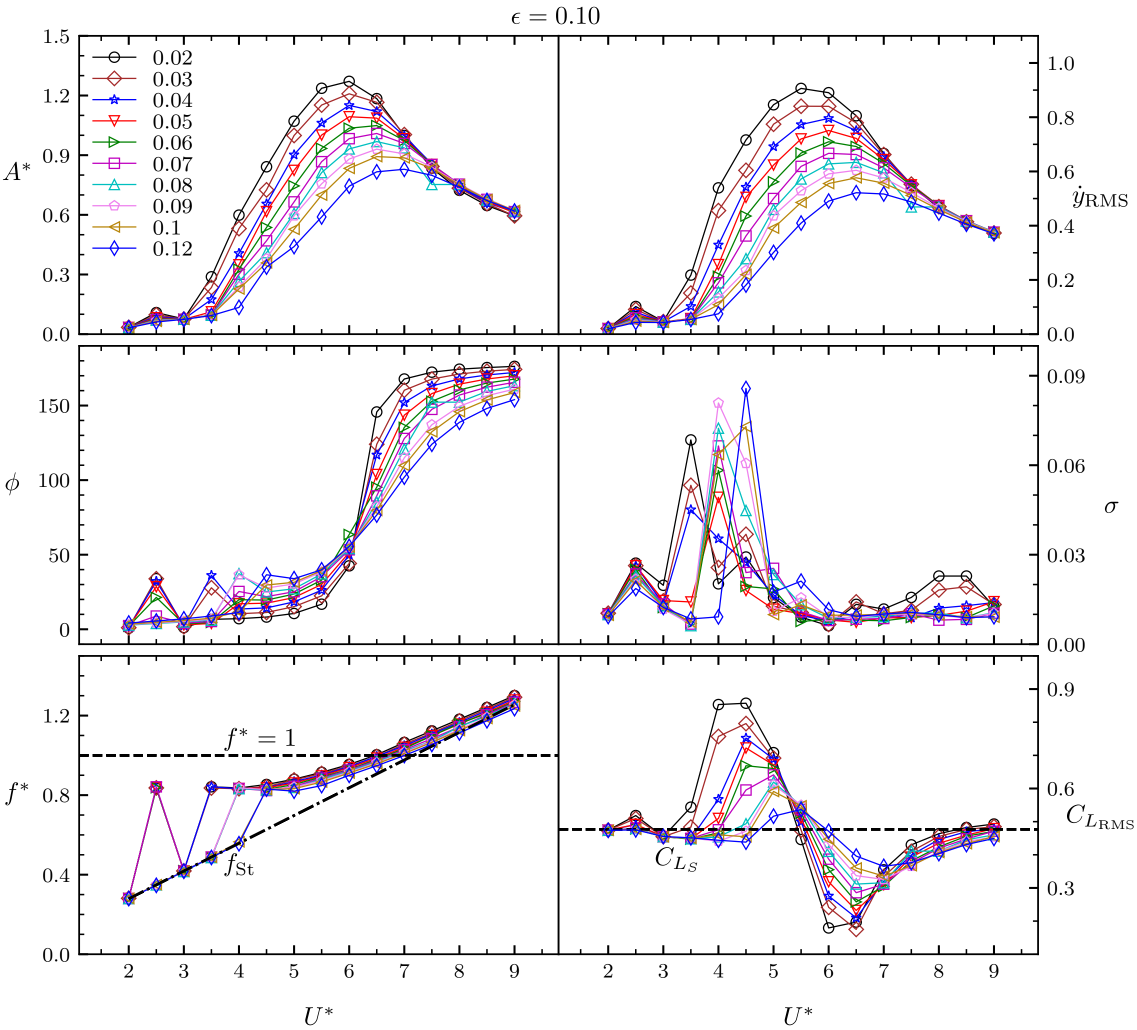

Fig. 6.5 Flow characteristics at $\epsilon = 0.10$ with varying ζ and U^*

mean of the peak values, $\frac{1}{M}\sum_{i=1}^{M} p_i$. Multiple peaks have been observed for σ plot. At $2.0 \leqslant U^* \leqslant 3.0$, A^* momentary increases and then decreases at $0.02 \leqslant \zeta \leqslant 0.07$ before attaining the highest value. However, σ shows the same variation for all ζ between the aforementioned U^*. The σ increases in the U^* range between 2.0 and 2.5 for all ζ before decreasing at $U^* = 3.0$. It is also observed that σ is higher at lower ζ, indicating a more stable amplitude response. At $U^* = 3.5$, σ becomes the lowest for $0.06 \leqslant \zeta \leqslant 0.10$. From the context of A^* and $\dot{y}_{\mathrm{RMS}}$, no sudden increase is observed at $U^* = 3.5$ for $0.06 \leqslant \zeta \leqslant 0.10$. Higher σ value for $0.02 \leqslant \zeta \leqslant 0.04$ at $U^* = 3.5$ indicates displacement has a more chaotic nature. This non-monotonic nature in standard deviation represents the chaotic nature in the initial branch and the transition between the initial and lower branches. At $U^* = 4.0$, σ for $0.02 \leqslant \zeta \leqslant 0.04$ decreases, while for other ζ a jump in value is observed. Therefore, the onset of the initial branch at $0.02 \leqslant \zeta \leqslant 0.04$ is earlier than other ζ cases. The dispersion of displacement from the mean is higher at higher ζ $(0.04 \leqslant \zeta \leqslant 0.10)$ at $4.0 \leqslant U^* \leqslant 5.0$. On closely examining only $\zeta = 0.02$ and 0.03, σ is found to increase again at $7.5 \leqslant U^* \leqslant 8.5$. The phase plot reveals the feature observed for σ at $2.0 \leqslant U^* \leqslant 4.5$. However, for $\zeta = 0.02$, there is no sudden increase in ϕ as anticipated at $U^* = 3.5$. The highest amplitude occurs when ϕ crosses 90°. The initial to lower-branch transition is apparent, as ϕ changes from nearly 0° to close to 180°. However, unlike the undamped case, the phase does not jump directly from 0° to 180°. With the increase in ζ, the difference in phase decreases, which means it strolls further away from 180° at higher U^*. It means the jump in ϕ gets smoother as damping increases. At $U^* \geqslant 5.0$, σ value is lower, which corresponds to periodicity in displacement. The periodicity in displacement can be captured from the σ plot, which also corresponds to ϕ reaching a higher value at higher U^*. However, the loss of periodicity is not observed for $\zeta = 0.02$ and 0.03 in ϕ response at higher U^*, as reported in σ plot. Non-dimensional frequency response, $f^* = f/f_n$ can be correlated to both ϕ and σ at $2.0 \leqslant U^* \leqslant 4.5$. The rapid rise and fall between $2.0 \leqslant U^* \leqslant 3.0$ are observed for $0.02 \leqslant \zeta \leqslant 0.07$, which correspond to ϕ response. The sudden increase in σ at $U^* = 3.5$ for $0.02 \leqslant \zeta \leqslant 0.04$ is clearly captured in frequency response as well. This marks the onset of the initial branch. The onset of the initial breach is delayed for higher ζ. Therefore, the synchronization regime decreases as ζ increases. With the increase in U^* from 5.0 onwards, f increases to almost f_n. The f^* reaches the vortex-shedding frequency of stationary cylinder, f_{St}. At this U^*, A^* is very low and almost approaching the stationary case. Soti et al. (2017) showed that at lower U^*, $C_{L_{\mathrm{RMS}}}$ increases and then decreases below the value of the stationary cylinder, C_{L_S}.

However, $C_{L_{\mathrm{RMS}}}$ increases close to the value of a stationary cylinder. A similar trend in $C_{L_{\mathrm{RMS}}}$ is also observed in the present case. The highest $C_{L_{\mathrm{RMS}}}$ reported in the range of $4.0 \leqslant U^* \leqslant 5.0$ corresponds to the onset of the initial branch. When $C_{L_{\mathrm{RMS}}}$ crosses C_{L_S}, ϕ crosses 90° and synchronization regime starts. At lowest $C_{L_{\mathrm{RMS}}}$, maximum A^* is recorded.

Time history of displacement (y) and lift coefficient (C_L) is shown in the Figure 6.7, where t defines non-dimensional time ($t = t^* f_n$). At $U^* = 2.5$, the variation of displacement and C_L over time cycles are almost the same for $\zeta = 0.03$ and 0.10, with values of y and C_L being slightly higher for $\zeta = 0.03$. The maximum C_L is much higher than the maximum displacement at this low U^*. The displacement is not periodic from one cycle to the next, as the values do not repeat immediately in the next cycle. Instead, after several t, peak repeats and the repetition are not regular. This chaotic nature of amplitude is observed till $U^* = 4.0$. At $U^* = 2.50$ and $\zeta = 0.03$, y and C_L are not always in-phase. This out-of-phase phenomenon results in a bump in ϕ at $U^* = 2.50$. This aperiodicity in displacement is correlated to high σ values for different ζ. Also, from the vorticity contours seen in Figure 6.6, shed vortices adhere to the cylinder surface at low U^* ($U^* = 2.50$). The upper vortex engulfs the back end of the cylinder and cuts off the supply to the lower vortex. The shed lower vortex creates an undulated long structure behind the cylinder up to $x = 3.0$. At this low amplitude, no change in the vorticity pattern with ζ is observed. At $U^* = 3.5$, the flow characteristics vary between $\zeta = 0.03$ and 0.10. The variation of displacement over the time period is more prominent for $\zeta = 0.03$ than $\zeta = 0.10$, as seen from the standard deviation plot. The variation in displacement is very chaotic at $\zeta = 0.03$, as the displacement has quasi-periodicity with more than two periods present in the temporal history. Though the variation is higher at lower ζ, the frequency of oscillation is higher owing to a lower time period between major frequencies. However, the frequency is lower at higher ζ, although the periodicity is re-established. As U^* increases to 4.0, the amplitude for $\zeta = 0.03$ increases, and the amplitudes of displacement and C_L become comparable. Also, the phase between lift and displacement is almost zero for both ζ. However, unlike the $U^* = 3.5$ case, an opposite of temporal variation of y is observed between two ζ values. There is aperiodicity for both cases, but irregular variation of displacement is more in the case of $\zeta = 0.10$, causing a higher time period of oscillation and deviation from the mean value. There is no significant change in the vorticity contours, as observed for the lower U^*, from 2.5 to 4.0. As U^* reaches the highest-amplitude points for $\zeta = 0.03$ and 0.10 at $U^* = 6.0$ and 7.0, respectively, a significant decrease in C_L

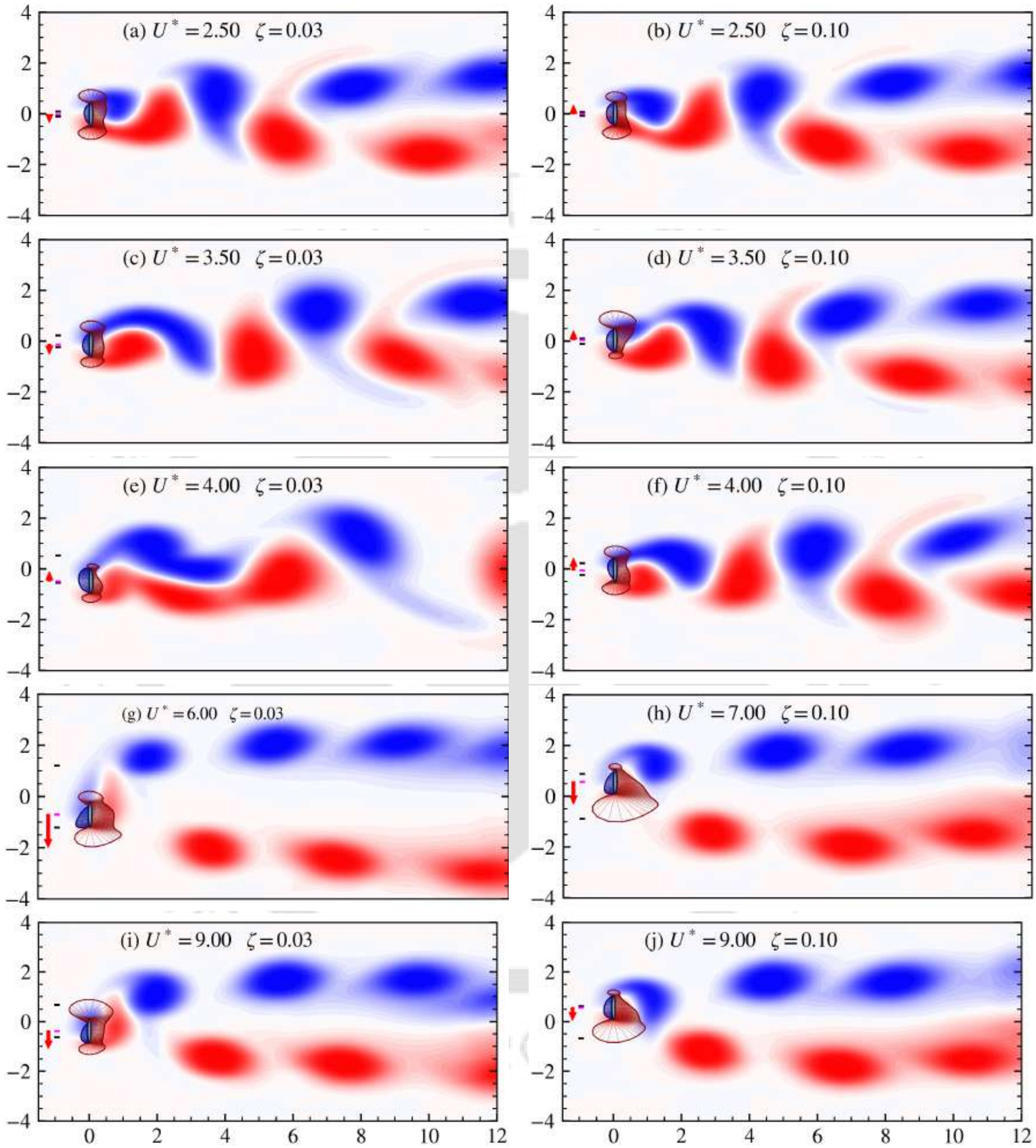

Fig. 6.6 Instantaneous vorticity contours and pressure distribution of VIV of elliptical cylinder for $\epsilon = 0.10$ with varying U^* and ζ

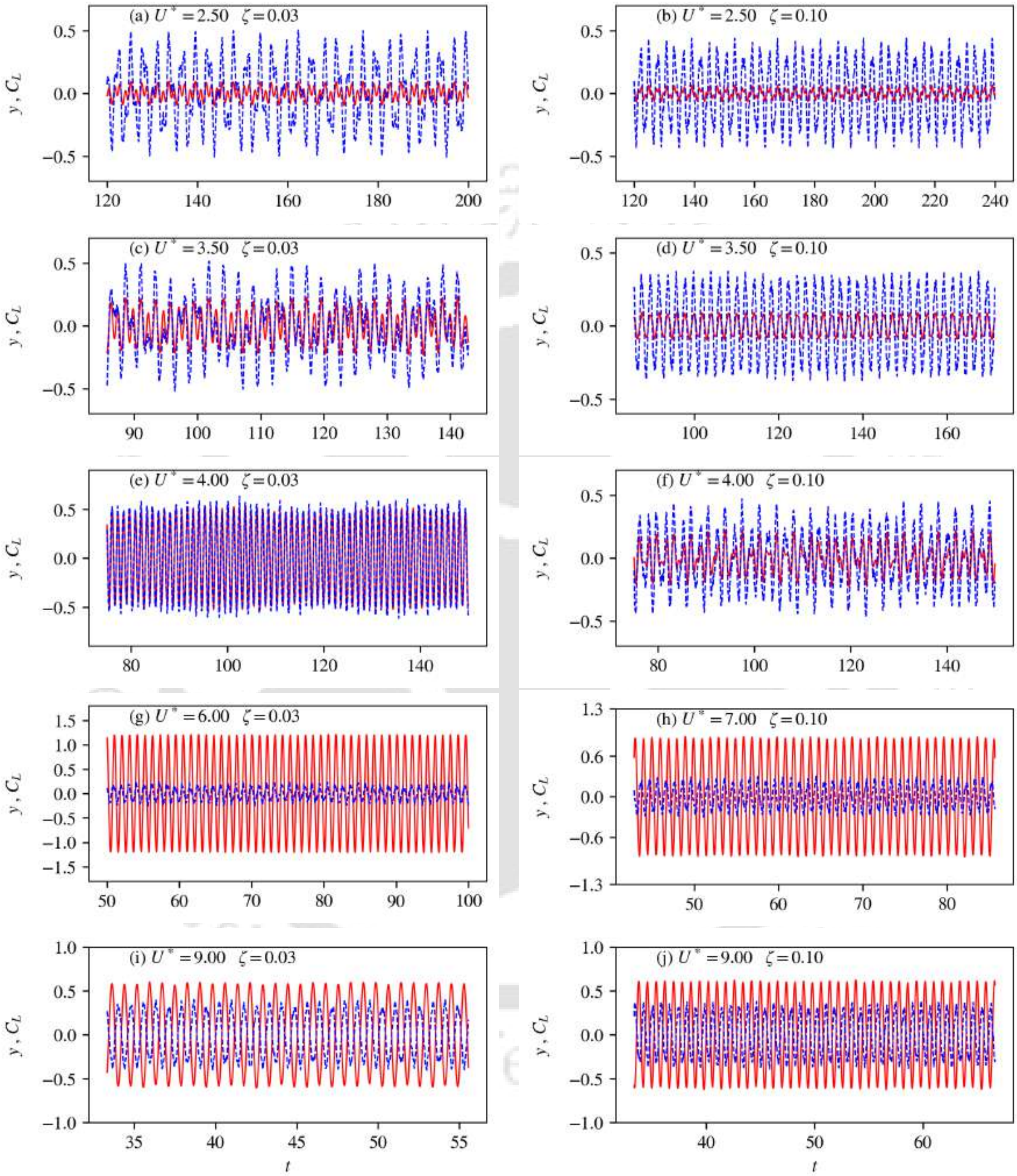

Fig. 6.7 Time history of displacement and lift coefficient of elliptical cylinder for $\epsilon = 0.10$ with varying U^* and ζ. The —— denotes displacement, y and - - - denotes C_L.

relative to the displacement amplitude is observed. Periodicity is observed for both ζ values, and the oscillation frequency also increases. A decrease in amplitude and an increase in C_L is observed at $U^* = 9.0$. The deviation from the mean value decreases, and the periodic nature of displacement is also maintained. This infers the initialization of the lower branch from $U^* = 6.0$. The vorticity contour shows that the width of the vortex street increases with amplitude, as the cylinder drags the fluid mass along with it. Also, the time history shows that up to $U^* = 4.0$, y and C_L are in phase. However, when $U^* \geqslant 6.0$, they are out of phase.

Effect of damping at aspect ratio ϵ = 0.25

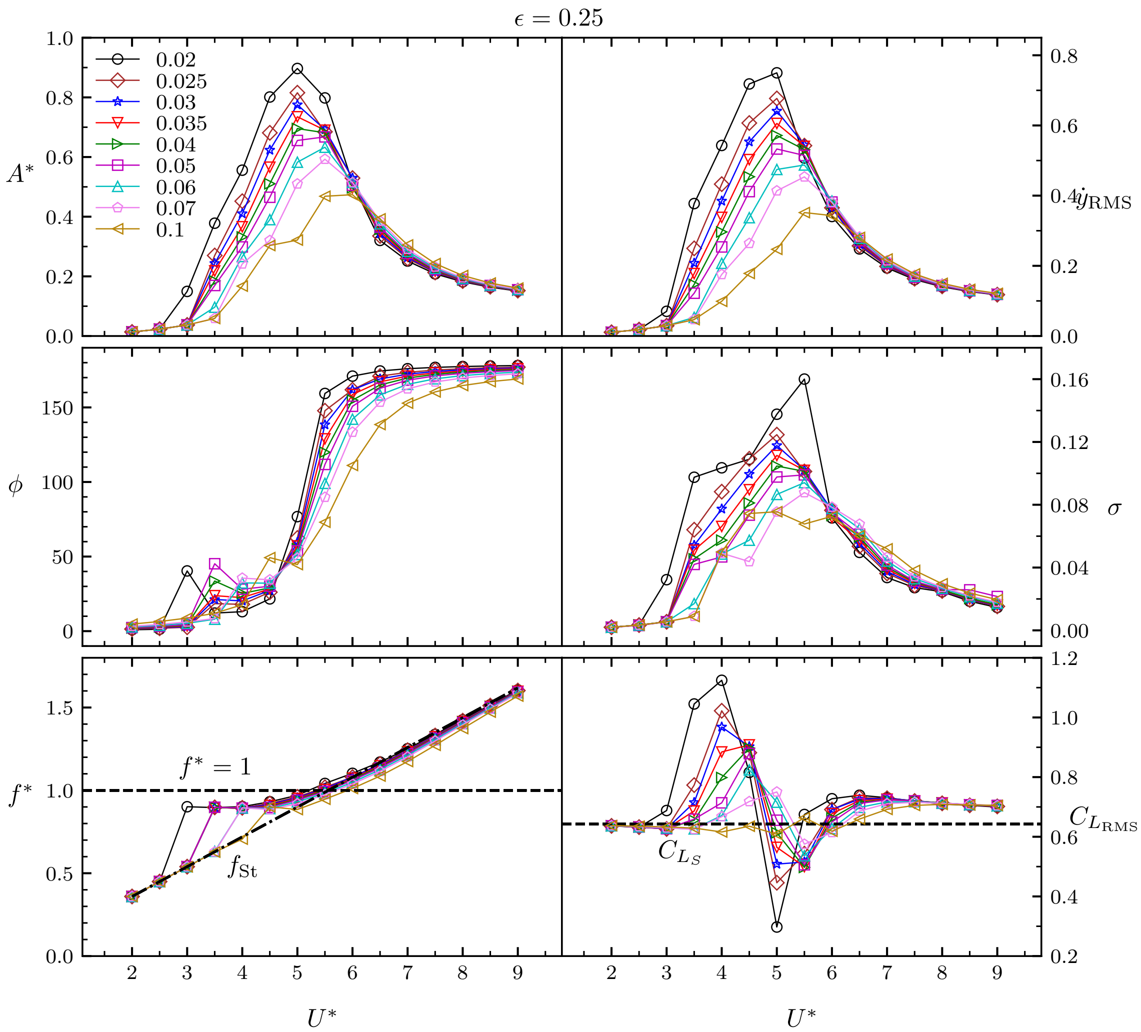

Fig. 6.8 Flow characteristics at $\epsilon = 0.25$ with varying damping ratio ζ and U^*

The nature of the amplitude variation with U^* for $\epsilon = 0.25$ is the same as of $\epsilon = 0.10$, as seen in Figure 6.8. The highest A^* is observed at U^* around 5.0 and 6.0. The U^* where the highest A^* is observed shifted towards higher U^* as ζ increases. As obvious from the plot, the highest amplitude decreases with the increase in damping. Also, the highest A^* recorded for $\epsilon = 0.25$ is lower than that of $\epsilon = 0.10$. The RMS value of $\dot{y}$ does not add any value to the existing amplitude plot, as it follows the same trend as the A^* plot. The ϕ jumps at $U^* = 3.0$ at lowest ζ, which corresponds to jump in σ at that U^*. This can be seen as the onset of the initial branch, as f^* also jumps close to 1.0. The sudden increase in the parameters at $\zeta = 0.02$ and $U^* = 3.0$ discussed earlier is also observed for A^* and $\dot{y}_{\mathrm{RMS}}$. Onset of initial branch happens at higher U^* with increasing ζ. The jump in f^* for $0.02 \leqslant \zeta \leqslant 0.07$ corresponds to the respective jump in value in σ, except for $\zeta = 0.10$. While the onset of the initial branch can be predicted from σ values only, the jump in σ for $\zeta = 0.10$ does not match with the jump in f^*. It can only be seen from the jump in ϕ for all ζ values, as the jump in ϕ correlates to the jump in f^*. The σ is observed to be the highest at the lowest ζ, as the displacement is more spread about the mean, indicating a chaotic nature. Standard deviation (σ) does not match with the chaotic behavior of $\epsilon = 0.10$. However, compared to $\epsilon = 0.10$, σ value is significant in the range $5.0 \leqslant U^* \leqslant 9.0$. In the range of $U^* = 5.0$ to 6.0, the phase, $C_{L_{\mathrm{RMS}}}$, and f^* see a change in trend; this points to a transition from initial to lower branch. At maximum A^* and transition between initial and lower branch, the temporal deviation in amplitude in time history is very significant. Also, σ seems to decrease with the increase in damping. Hence, damping leads to a smoother variation in displacement. There is a distinct feature for $\zeta = 0.07$ and 0.10 in phase difference at $U^* = 4.5$ and 5.0. This peculiarity is reflected in the σ plot, as an increase and decrease in ϕ correlated with an increase and then a decrease in σ. As discussed earlier, the jump points in frequency gradually shifted to higher U^* with increasing damping. However, it meets with the vortex shedding frequency of stationary cylinder at $U^* = 7.0$. This implies a decrease in the synchronization region with increasing damping. It is also clear in the amplitude plot that at around $U^* = 7.0$, all the amplitude collapse to the same value. Lift coefficient $C_{L_{\mathrm{RMS}}}$, for $\epsilon = 0.25$, has the same trend as $\epsilon = 0.10$. It increases to a high value and then continuously decreases to a meager value at U^*, where the maximum A^* is spotted. After that, it maintains a constant value above the C_{L_S}.

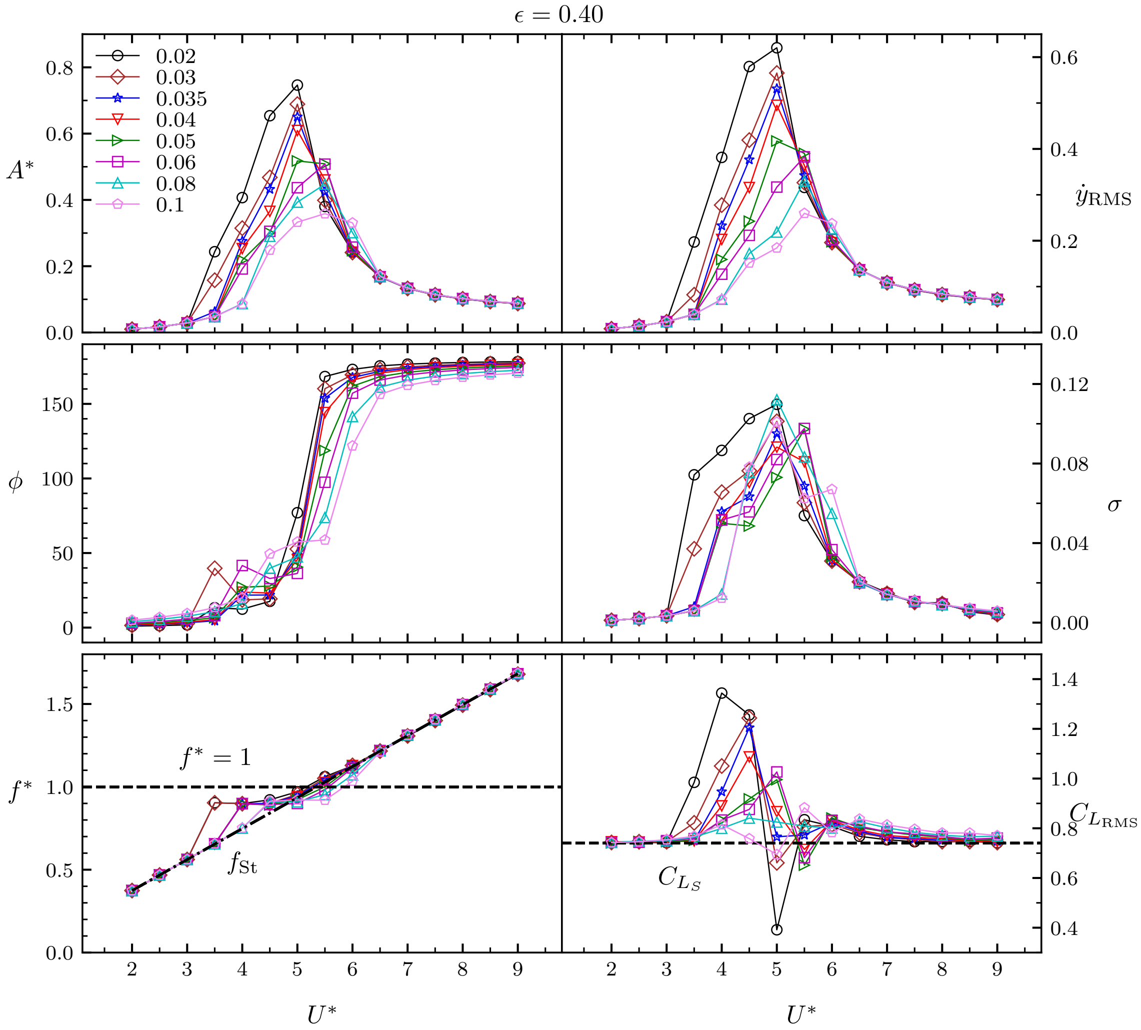

Fig. 6.9 Flow characteristics at $\epsilon = 0.40$ with varying damping ratio ζ and U^*

Effect of damping at aspect ratio ϵ = 0.40 and 0.50

The characteristics of different parameters for aspect ratios 0.40 and 0.50 are aligned with the results of $\epsilon = 0.25$, as seen in Figure 6.9 and Figure 6.10. With the increase in ϵ, the peak amplitude for different ζ sees a decline in their values as well as in the RMS value of $\dot{y}$. The peaks and valleys in phase difference at lower U^* are consistent with the results of $\epsilon = 0.25$. Moreover, the peaks in ϕ at lower U^* correlated to the onset of the initial branch pertinent to each ζ for both the ϵ values. Surprisingly enough, the peak amplitude is observed between $U^* = 5.0$ and 6.0, as seen in $\epsilon = 0.25$. Maximum σ at each ζ is the lowest at $\epsilon = 0.10$, peaks at $\epsilon = 0.25$, and then decreases. Therefore, with the increase in ϵ, the temporal fluctuation of amplitude seems to first increase and

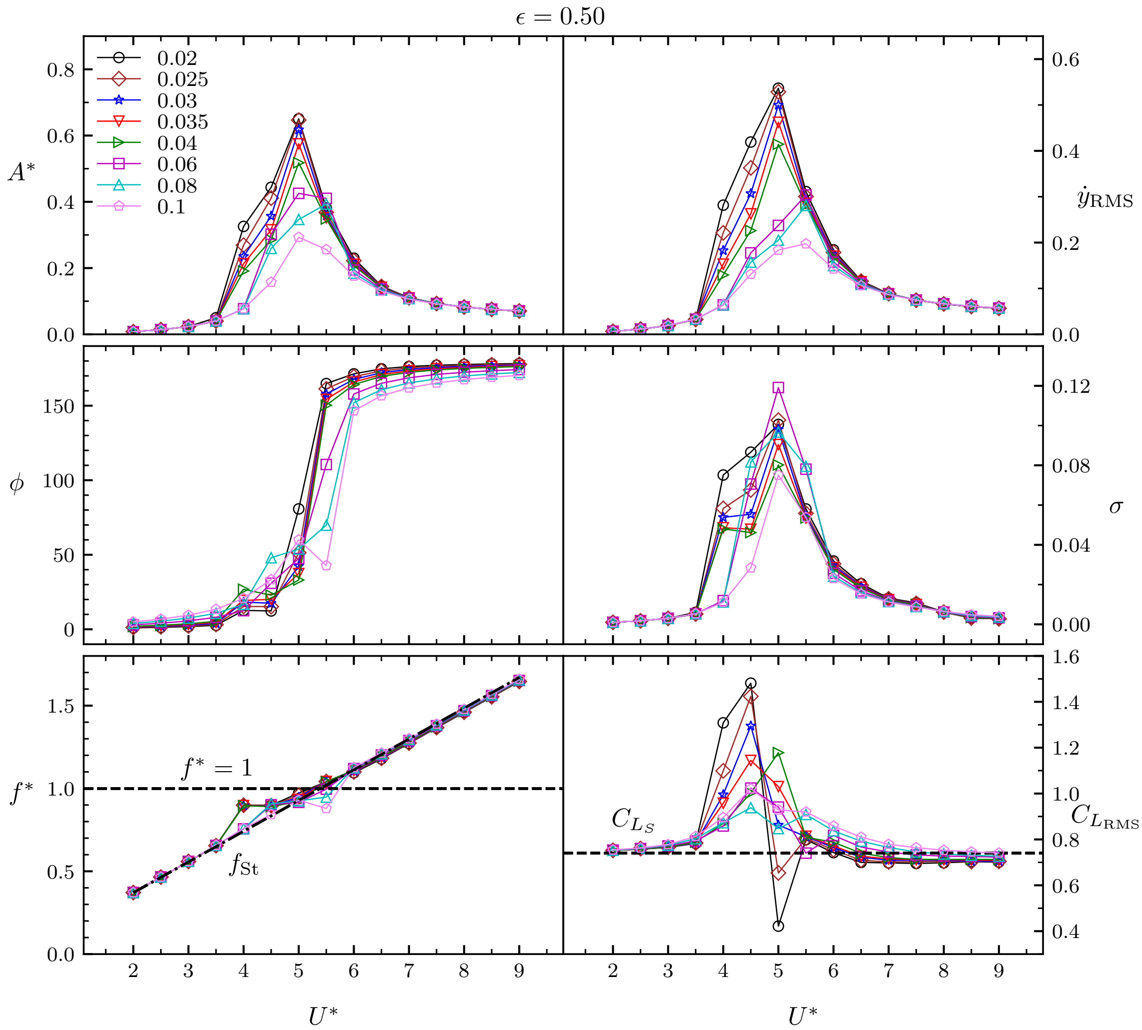

Fig. 6.10 Flow characteristics at $\epsilon = 0.50$ with varying damping ratio ζ and U^*

then diminish. Also, the U^* range exhibiting significant σ decreases with increasing ϵ. However, the region of significant σ ($3.5 \leqslant U^* \leqslant 6.0$) is almost the same for both ϵ. As for the frequency response values, the sharp change in f^* over a smaller region of U^* indicates the shrinking of the synchronization regime. The shrinkage in the synchronization region with increasing ϵ is also observed from A^*. The jump in A^* is correlated to jump in σ, f^*, and ϕ for all ζ. At $\epsilon = 0.40$, $C_{L_{\mathrm{RMS}}}$ does not follow the previously observed trend, as the $\zeta = 0.035$ and 0.08 cases do not exceed the C_{L_S} value. Besides that, the maximum A^* does not correspond to the lowest $C_{L_{\mathrm{RMS}}}$ in the range of $0.04 \leqslant \zeta \leqslant 0.10$. The $C_{L_{\mathrm{RMS}}}$ for $\epsilon = 0.50$ also exhibits same variation with U^*. In general, A^*, $\dot{y}_{\mathrm{RMS}}$, and the synchronization region where $f^* = 1.0$ decrease when

ϵ increases from 0.10 to 0.50. However, the maximum value of $C_{L_{\mathrm{RMS}}}$ increases as ϵ increases from 0.10 to 0.50.

Effect of damping at aspect ratio ϵ = 1.00 (circular cylinder)

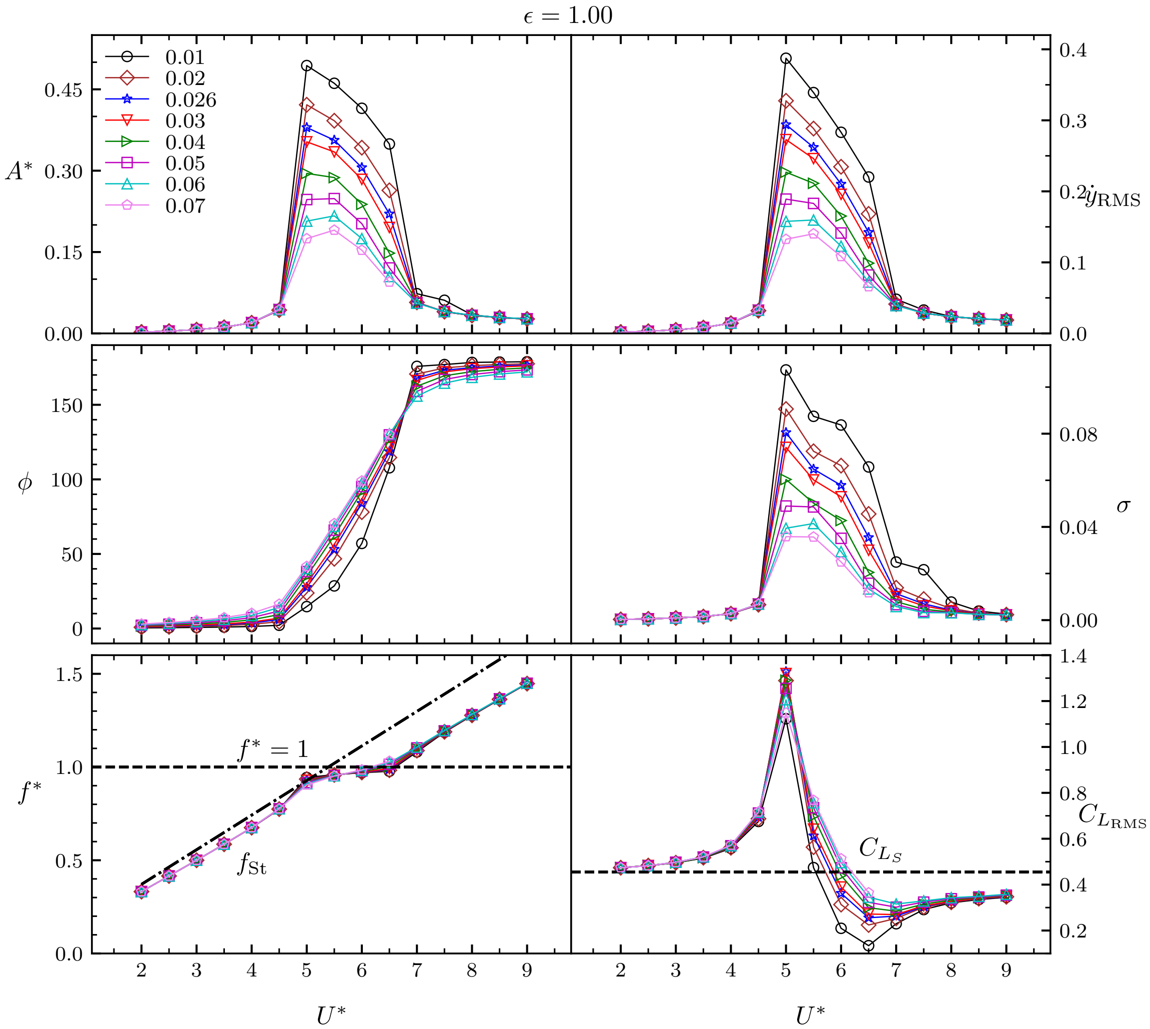

Fig. 6.11 Flow characteristics at ϵ = 1.00 (circular cylinder) with varying damping ratio ζ and U^*

The flow characteristics of ϵ = 1.00 (circular cylinder) are shown in Figure 6.11. A sharp rise in amplitude is observed, but all cases collapse to a single U^* value, U^* = 5.0. The RMS values of velocity also follow the same trend as A^*. The jump means onset of the initial branch since it drops to the negligible amplitude at U^* = 7.0 and maintains a low amplitude. The jump in σ at U^* = 5.0 indicates the initiation of chaotic nature in displacement. However, with the increase in U^* and ζ, periodicity in displacement is gradually regained. Hence, a high σ value between $U^* = 5.0$ and 7.0 points towards loss of periodicity at high amplitude. The phase difference of different ζ collapses to the same values since there is no significant change in phase difference with ζ. The transition region between the initial and the lower branches is prominent compared to other ϵ cases. Frequency response also shows lock-in or synchronization between $U^* = 5.0$ and 7.0, where f is close to f_n. Then, with the increase in U^*, the f^* value deviates from f_{St}. The maximum value of $C_{L_{\mathrm{RMS}}}$ decreases from $\epsilon = 0.50$ to $\epsilon = 1.00$. Also, the stationary lift coefficient, C_{L_S} decreases to the value of $\epsilon = 0.10$.

6.3.3 Effect of damping on power extraction

The damping coefficient is considered constant for power extraction. Soti et al. (2017) considered a realistic electromagnetic device used for variable damping and a constant damping ratio model and found that both models predict the same average power. Therefore, the constant damping model can accurately predict the power extraction. The non-dimensional instantaneous power is defined as the ratio of the power dissipated by the damper to the power available over the fluid region occupied by the body, and is given by Equation 4.2. In order to get average power, Equation 4.2 is integrated over a number of oscillation cycles. The number of oscillation cycles for averaging is taken as 50. Equation 6.2 represents average power extraction from VIV of the elliptical cylinder, and this shows dependency on flow power extraction is not only limited to the mass-damping parameter ($m^*\zeta$) but also depends on the aspect ratio (ϵ) and root-mean-square velocity, $\dot{y}_{\mathrm{RMS}}$ of the elliptical cylinder. The average power extraction with respect to reduced velocity for all the aspect ratios (ϵ) is shown in Figure 6.12. The average power, $\bar{P}$, varies from one cycle to another cycle because of the variation in the amplitude response.

$\bar{P}$ increases with the increase of reduced velocity (U^*) in the initial branch, reaches a peak, and decreases again with U^* in the lower branch. It is noticed that the peak of the average power is obtained at a particular value of the damping ratio, and it is not the same damping ratio where the A^* is maximum. The U^* at which maximum power is obtained is lower than the U^* at which maximum amplitude is obtained. Also, with increasing damping, the region of higher power decreases, resulting in a smaller operating region. For $\epsilon = 0.10$, the maximum power is attained at $\zeta = 0.08$, beyond which it decreases with increasing ζ. The maximum power is at peak in between the ζ range ($0.02 \leqslant \zeta \leqslant 0.10$) for all ϵ cylinders. Therefore, an optimal ζ exists at which

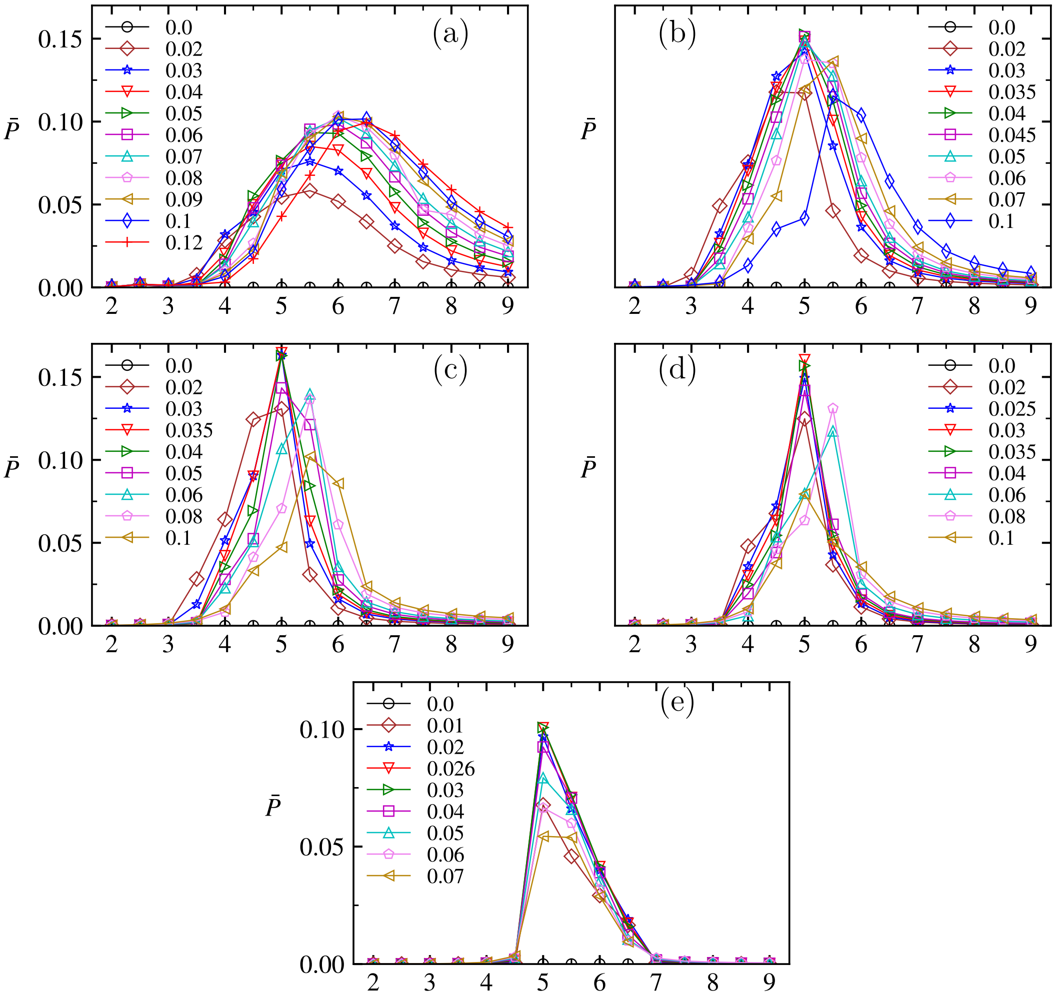

Fig. 6.12 Effect of damping on power extraction at different ϵ = (a) 0.10 (b) 0.25 (c) 0.40 (d) 0.50, and (e) 1.00 (circular cylinder)

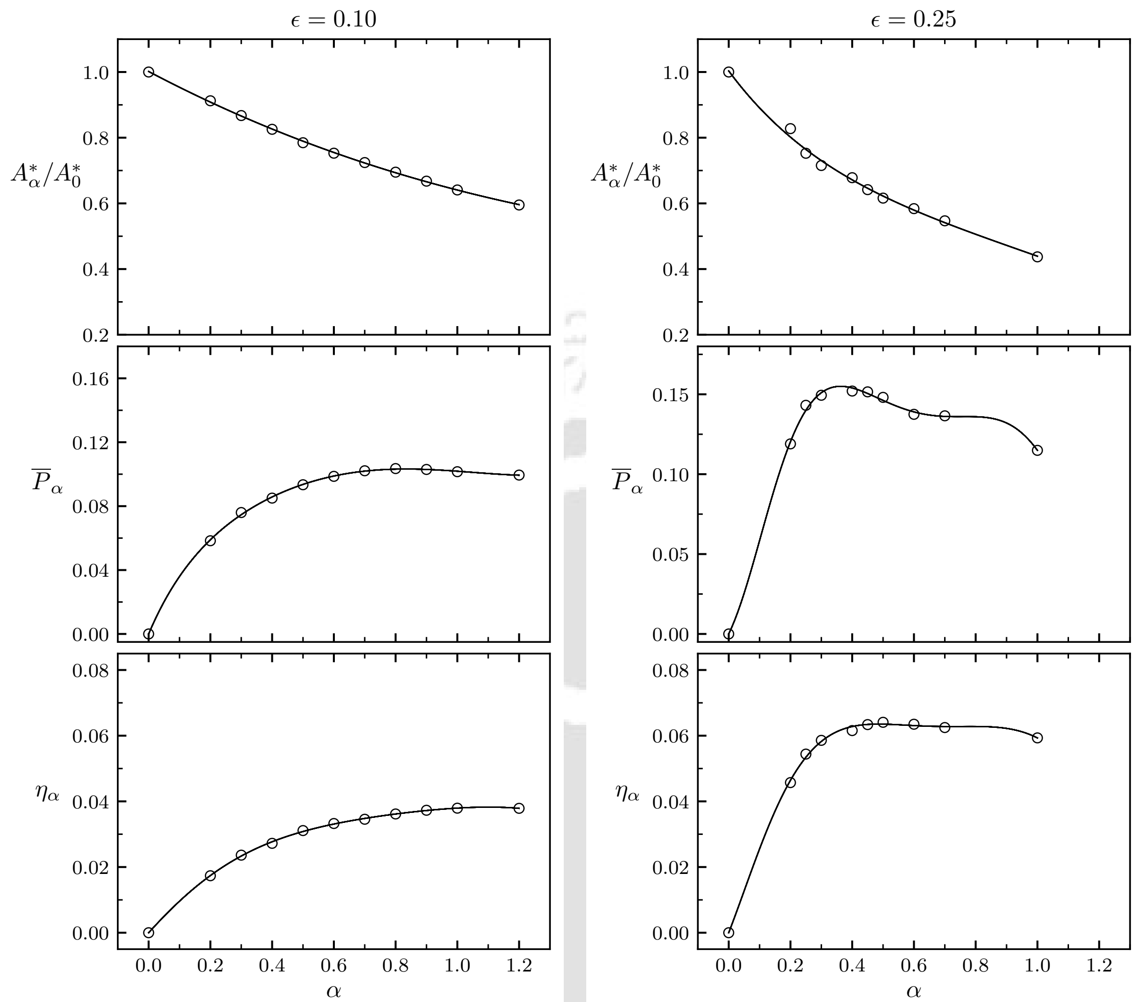

Fig. 6.13 Effect of α on A^*_α, $\bar{P}_\alpha$ and η_α at $\epsilon = 0.10$ and 0.25. $A^*_0 = 1.39$ for $\epsilon = 0.10$ and 1.08 for $\epsilon = 0.25$. Peak of $\bar{P}_\alpha$ does not coincides with peak of η_α. Two local $\bar{P}_\alpha$ peaks at $\epsilon = 0.25$ and one peak at $\epsilon = 0.10$ at $\alpha = 1.0$.

the maximum average power is obtained. Also, with the increase in ϵ, the maximum obtainable average power increases. The operating range of power becomes smaller when ϵ increases from 0.10 to 0.25. At higher ζ, maximum $\bar{P}$ shifts to higher U^*. There exists an optimum ζ at which the maximum power is obtained for a given ϵ. The optimum ζ also decreases with increasing ϵ, from 0.07 at $\epsilon = 0.10$, and gradually decreases in the subsequent ϵ cases.

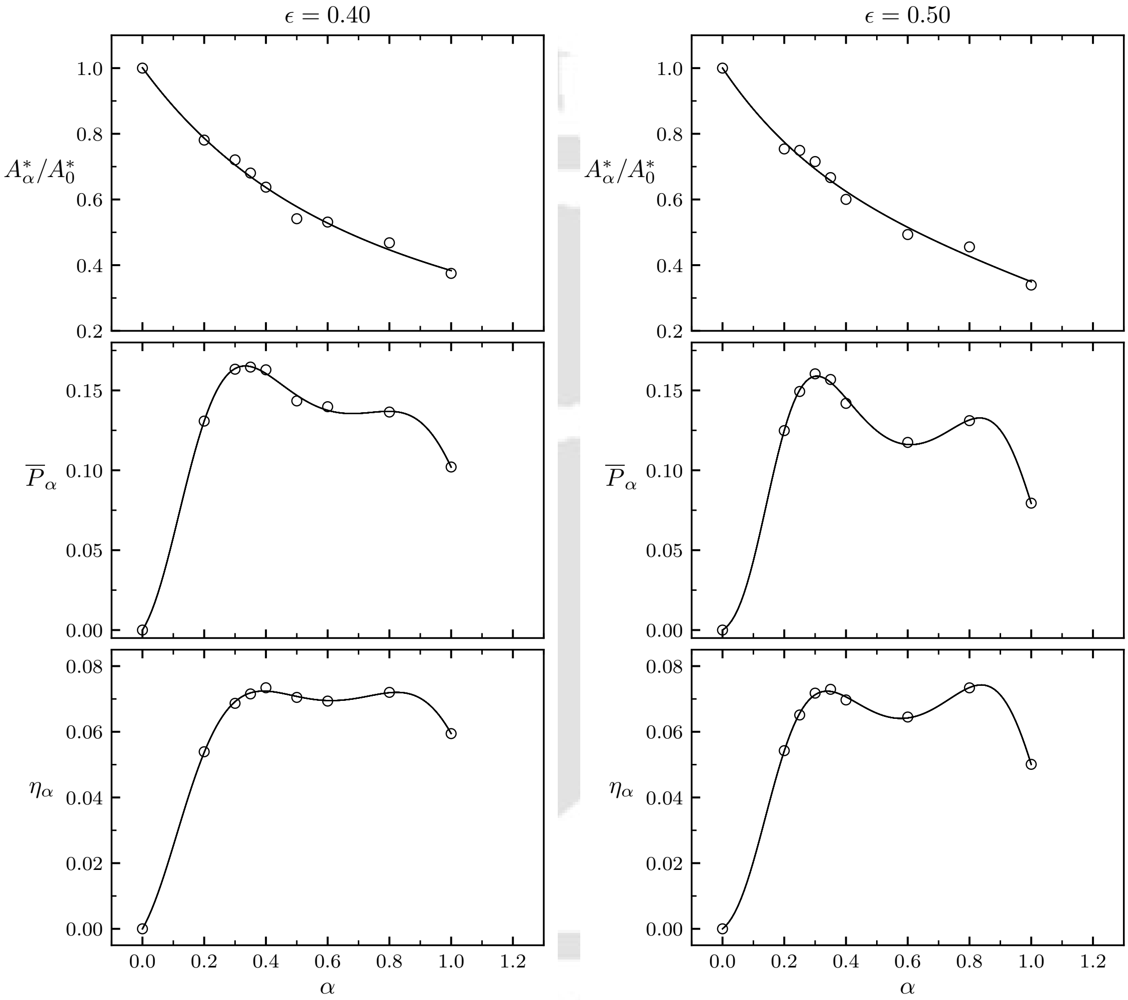

Fig. 6.14 Effect of α on A^*_α, $\bar{P}_\alpha$ and η_α at $\epsilon = 0.40$ and 0.50. $A^*_0 = 0.96$ for $\epsilon = 0.40$ and 0.86 for $\epsilon = 0.50$. Two local peaks of $\bar{P}_\alpha$ and η_α at $\epsilon = 0.40$ and 0.50.

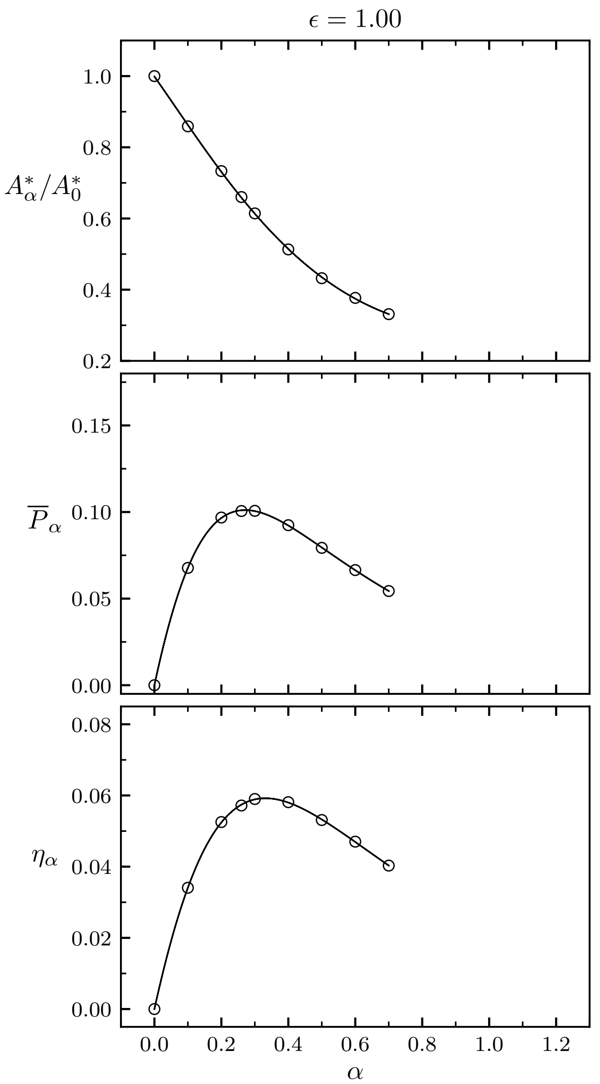

Fig. 6.15 Effect of α on A^*_α, $\bar{P}_\alpha$ and η_α at $\epsilon = 1.00$. $A^*_0 = 0.57$ for $\epsilon = 1.00$. Peak of $\bar{P}_\alpha$ coincides with peak of η_α.

6.3.4 Maximum average extracted power

The maximum vibration amplitude A^*_α at a particular mass-damping (α) is shown in Figures 6.13, 6.14, and 6.15 for different ϵ values. For each ϵ, A^*_α has been normalized by corresponding A^*_0 which represent the value of A^*_α at $\alpha = 0$. A^*_α is decreasing with increasing ζ. The results are plotted against mass-damping parameter $\alpha = m^*\zeta$. The scatter plot shows that A^*_α almost follows an exponentially decreasing pattern with α. At certain α values, peak amplitude A^*_α stray from the negative exponent path if the term inside the exponent is linear. Therefore, it is better to express the amplitude as the exponent of higher-order polynomials. The following exponential fit has been used to fit the data (Soti and De, 2020).

$$A^*_\alpha = A^*_0 \exp\left(\sum_{i=1}^{n} K_i \alpha^i\right) \tag{6.3}$$

A third-order fit is found to fit the data with an acceptable accuracy, as shown in Figures 6.13, 6.14, and 6.15. Maximum average extracted power, $\bar{P}_\alpha$ at a particular mass damping parameter is plotted similarly to A^*_α. It is clear that the maximum average power depends on the damping ratio (ζ) and mass ratio (m^*). Thus, from plots, the maximum average power first increases with increasing mass-damping parameter ($m^*\zeta$), reaching a peak and after a further increase in α, $\bar{P}_\alpha$ decreases. The reason for this trend can be understood as follows: at a very low damping ratio, power is nearly zero because power extraction is modeled as power dissipated by the damping of the system. Therefore, if there is no damping, then there is no power. For the higher side of damping, the maximum average power drops to lower values. This happens because higher damping to the system suppresses the oscillation of the cylinder, and hence harnessed power diminishes. Therefore, if the damping ratio is increased from zero, the extracted power should increase with damping before reaching a maximum at optimal damping and then decreasing to zero. The average power is modeled as the function of α and U^*, but not constrained within the two parameters. It is also found to vary with ϵ. However, for a given ϵ, assuming that the cylinder displacement with time is fairly periodic, the displacement can be represented as $y = A^* \sin(2\pi f^* t/U^*)$. Therefore, with the help of Equation 6.2 the average extracted power can be approximated as,

$$\bar{P} = 4\pi^4 \frac{(f^*A^*)^2}{(U^*)^3}\alpha(\epsilon) \tag{6.4}$$

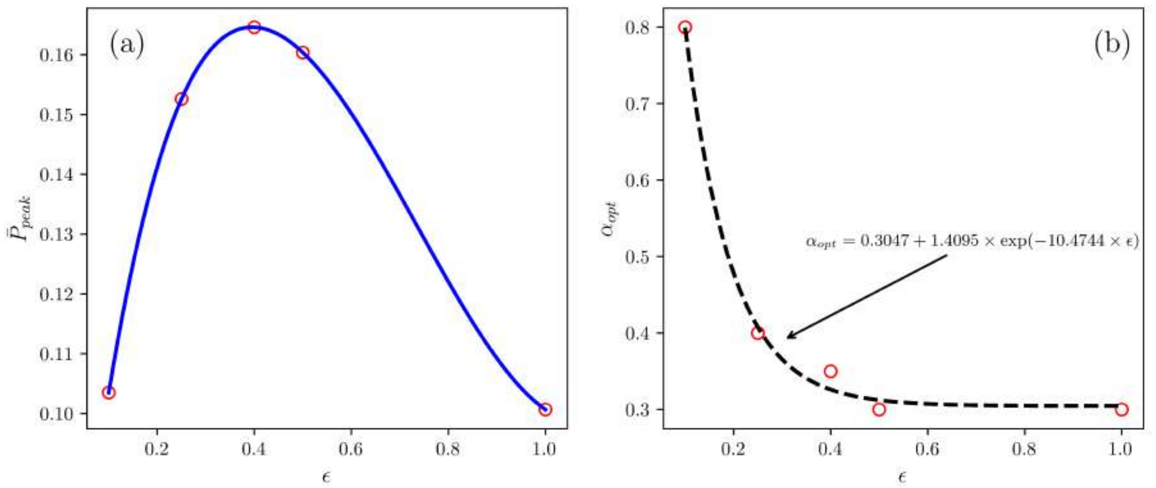

Fig. 6.16 (a) Variation of peak of maximum power, $\bar{P}_{peak}$ at different ϵ (b) Variation of optimum mass-damping parameter, α_{opt} at different ϵ. Exponential variation of α_{opt} with ϵ is shown.

Therefore, the average power varies with the second power of A^*, and the maximum average power is approximately given by $\bar{P}_\alpha \propto \alpha A^{*2}$, where A^* is the peak vibration amplitude (Soti et al., 2018). This relation can be inferred, since the highest powers are attained in the higher-amplitude region. However, the U^* where maximum amplitude is recorded is not the same where maximum power is recorded and differs by 0.5. Following the approximation of A^*_α using the mass–damping parameter, the maximum average power can also be approximated and represented as,

$$\bar{P}_\alpha = K_4 \alpha \exp\Big(K_1\alpha + K_2\alpha^2 + K_3\alpha^3\Big) \tag{6.5}$$

where $K_4 = K_0 A_0^{*2}$, K_0 is a constant and A^*_0 is the peak mean amplitude at zero damping. However, another local maximum of peak power is observed in the plotted data for higher ϵ, i.e., $\epsilon \geqslant 0.10$. This fit behaves poorly with the data. If the order is increased to 4, the fit shows good agreement with the data. Therefore, $\bar{P}_\alpha$ can be written as $\bar{P}_\alpha = K_5 \alpha \exp(K_1\alpha ... K_4\alpha^4)$. The maximum energy is extracted when the flow is brought to complete rest, and all its kinetic energy is harnessed. In a uniform flow, ρU mass of fluid will cross a unit area per second with velocity U. Therefore, $\rho U^3/2$ is the maximum flow power per unit area that can be extracted. For an unconfined transversely vibrating cylinder, the maximum extractable power is equal to $(D + 2A)\rho U^3/2$ (assuming unit length of the cylinder), where A is dimensional vibration amplitude. Therefore, the mathematical expression of power extraction efficiency is as follows:

$$\eta = \frac{\bar{P}}{1 + 2A^*} \tag{6.6}$$

The efficiency is a function of the reduced velocity and mass-damping. It has a peak value for any mass-damping at an optimal reduced velocity. The peak of the efficiency, η_α is shown against α in the previous figures alongside A^*_α and $\bar{P}_\alpha$. The η_α curve follows the $\bar{P}_\alpha$ curve since the peaks and valleys are the same in both curves at the corresponding α values. The optimal α or α_{opt} for power extraction is not the same as efficiency. In the case of $\epsilon = 0.10$, α_{opt} for $\bar{P}_\alpha$ is 0.80 and η is 1.00. The α_{opt} for power coincides with efficiency at $\epsilon = 0.40$ and $\epsilon = 1.00$. However, for $\epsilon = 0.25$ and 0.50, optimal mass-damping for maximum η is greater than for maximum $\bar{P}$. Therefore, in general, the optimal mass–damping for maximum efficiency is greater than or equal to that for maximum power extraction. In Figure 6.16 (a), the value of maximum average power at each ϵ, which is designated as peak power ($\bar{P}_{peak}$), is plotted against each ϵ. With the increase of aspect ratio, the peak power increases up to $\epsilon = 0.40$, where maxima occurs, and then decreases. The peak power thus obtained is 0.103, 0.152, 0.164, 0.160, and 0.101 times the flow power contained in an area equal to the area of the flow blocked by the cylinder at aspect ratios of 0.10, 0.25, 0.40, 0.50, and 1.00 (circular cylinder), respectively. Therefore, the peak is observed at $\epsilon = 0.40$. From this, it is concluded that an elliptical cylinder with an aspect ratio less than one can extract up to 62.37% more power from the flowing fluid compared to a circular cylinder. Also, A^* values for which maximum $\bar{P}_\alpha$ is observed are 0.968, 0.735, 0.650, 0.617, and 0.353 for $\epsilon = 0.10$, 0.25, 0.40, 0.50, and 1.00, respectively. Hence with increasing ϵ, A^* for which maximum $\bar{P}_\alpha$ is obtained, decreases. The η_{opt} for $\epsilon = 0.10$, 0.25, 0.40, 0.50, and 1.00 are found to be 0.0379, 0.0641, 0.0734, 0.0729, and 0.0590. Therefore, η_{opt} also peaks at $\epsilon = 0.40$, similar to $\bar{P}_\alpha$. The $\bar{P}_{peak}$ is obtained at different values of α for each ϵ. The variation of optimum mass-damping parameter (α_{opt}) with respect to aspect ratio (ϵ) at Reynolds number, Re = 100 is shown in Figure 6.16 (b), and it follows an exponential curve of the form $\alpha_{opt} = C_0 + C_1 \exp(C_2 \times \epsilon)$. From the curve fit, the values of C_0, C_1, and C_2 are 0.30, 1.41, and -10.47, respectively. The optimum value of α at m^* of 10 is 0.30, 0.31, 0.33, 0.41, and 0.80 for aspect ratios 1.0, 0.50, 0.40, 0.25, and 0.10, respectively. Soti et al. (2017) found the optimum damping ratio to be 0.28 at the Reynolds number of 150 by considering mass ratio $m^* = 2$. However, peak power is independent of mass ratio (Soti et al., 2017). The above discussion suggests that α_{opt} may be a function of not only ϵ but also the Reynolds number.

The $\bar{P}_{peak}$ vs ϵ curve, shown in Figure 6.16 (a), has an inverted U shape. This relation is apparent from the Equation 6.4 which shows that $\bar{P}_{peak}$, the maximum value of $\bar{P}$, depends on f^*, A^*, U^*, and α for a particular aspect ratio. The values of these parameters when $\bar{P}_{peak}$ is obtained for different aspect ratio cylinders are tabulated below:

Table 6.6 Values of the various parameters when peak power is obtained for different aspect ratio cylinders

ϵ	f^*_{opt}	A^*_{opt}	U^*_{opt}	α_{opt}	C_L	$\dot{y}_{\mathrm{RMS}}$	$\bar{P}_{peak}$
0.10	0.921	0.931	6.0	0.80	0.410	0.628	0.103
0.25	0.951	0.735	5.0	0.40	0.564	0.606	0.152
0.40	0.947	0.650	5.0	0.35	0.765	0.531	0.164
0.50	0.945	0.617	5.0	0.30	0.862	0.499	0.160
1.00	0.928	0.353	5.0	0.30	1.319	0.273	0.101

From Table 6.6, it can be seen that the values of optimal vibration frequency (f^*_{opt}) and reduced velocity (U^*_{opt}), where peak power is obtained, show small variations with ϵ. Therefore, $\bar{P}_{peak}$ for a cylinder depends primarily on A^*_{opt} and α_{opt}. The mean extracted power is equal to the mean power transferred from the fluid to the cylinder. The power transmitted to the cylinder is equal to the product of lift force (C_L) and cylinder velocity ($\dot{y}$). Table 6.6 shows that C_L at peak power increases with increasing ϵ. This could be attributed to a larger project area in the direction of lift for larger aspect ratio cylinders. On the contrary, the vibration amplitude and velocity of cylinders decreases with increasing ϵ. For elliptical cylinders, the added mass coefficient for motion in the transverse direction is equal to ϵ (Patton, 1965). A cylinder having larger added mass would accelerate a larger mass of the neighboring fluid along with itself. This would require a significant portion of kinetic energy of the cylinder being transferred to the neighboring fluid causing its vibration amplitude to be smaller as compared to a cylinder having smaller ϵ. Therefore, the decrease in vibration amplitude, and thereby $\dot{y}$ could be attributed to the increase in added mass. Since C_L increased and $\dot{y}$ decreases with ϵ, their product i.e., the peak extracted power attains a maximum at certain ϵ that is found to be 0.4 at Re = 100.

6.4 Summary

This study examines the impact of damping and aspect ratio on the flow characteristics and power extraction from elliptical cylinders. The cylinders are elastically mounted with linear springs to allow movement in the transverse direction of flow. The vortex-induced vibration characteristics of elliptical cylinders with varying aspect ratios are numerically investigated at a Reynolds number of 100. The mass ratio (m^*) of the cylinders is fixed at 10, and the power extraction from the vibration of the cylinders is modeled as power dissipation from a linear damper attached to the cylinders. The flow characteristics and extracted power are investigated with varying reduced velocity, $2.0 \leqslant U^* \leqslant 9.0$. Additionally, the relationships between maximum average power and power extraction efficiency are explored in relation to mass-damping parameters.

For all aspect ratios, two branches of amplitude response are observed in the undamped case: the initial branch and the lower branch. The initial branch starts with a quasi-periodic vibration response. The standard deviation (σ) in the vibration amplitude has moderate values in this region. The vibration response becomes aperiodic towards the end of the branch with relatively higher values of σ. With a further increase in U^*, the lower branch is observed where the vibration response is periodic and thereby σ is small. The vibration amplitude, RMS velocity, width of the synchronization region, and the range of U^* where the cylinder vibrates with a significant amplitude, increase with decreasing aspect ratio. These vibration characteristics decrease monotonically with damping for all aspect ratios. However, σ decreases monotonically with damping for $\epsilon = 0.25$ and 1.0 only. For $\epsilon = 0.1$, 0.4, and 0.5, it sometimes increases with an increase in damping.

The variation of average power extraction with U^* is found to be similar to that of the amplitude response. For every ϵ, there is an optimum ζ where the peak of maximum average power, $\bar{P}_\alpha$, is attained. Also, with the increase in ϵ, the range of U^*, where a significant power generation is observed, shrinks. The A^*, where the maximum $\bar{P}_\alpha$ is observed, decreases with an increase in ϵ. The amplitude decay with α is found to be closely approximated by an exponential fit with a third-order polynomial as the exponent. Power extraction appears to be strongly dependent on α, as evidenced by the increase in mass-damping parameter, where two local maxima are observed, except at $\epsilon = 0.10$ and 1.00. Though power can be modeled as a function of amplitude, power exhibits a higher-order dependence on α, with a fourth-order polynomial inside the exponent. Compared to the circular cylinder ($\epsilon = 1.00$), all other ϵ cases show enhanced power extraction, with the minimum enhancement being 1.98% for $\epsilon = 0.10$. With further increase in ϵ, the enhancement in power extraction efficiency peaks at a particular ϵ and then falls. The maximum enhancement of 62.37% is observed for $\epsilon = 0.40$. A maximum enhancement of 24.40% in efficiency, defined as the ratio of power extracted by the cylinder to the maximum energy available in the flow, is observed at $\epsilon = 0.40$ in comparison to a circular cylinder. An exponential fit has been found for the optimal α corresponding to peak power extraction as a function of ϵ.

The vibration amplitude and power extraction at $\epsilon = 1.00$ are known to increase with Re (Govardhan and Williamson, 2006; Soti and De, 2020). Therefore, the low Re results can be seen as a lower bound of the performance characteristics of the circular cylinder at operational Re. Comparing our low Re results with those of the experimental work of Zhao et al. (2019) on VIV of elliptical cylinders at higher Re ($860 \leqslant \mathrm{Re} \leqslant 8050$) suggests that the vibration amplitude of elliptical cylinders also increases with Reynolds number.

Chapter 7

Effect of frequency and damping ratio on power extraction from flow-induced vibration of elliptical cylinder with passive heaving and pitching

The bluff body dynamics of a cylindrical body and an elliptical body undergoing VIV are different. The optimum damping parameter and aspect ratio for power harvesting is investigated at a constant m^* and Re. We consider a single elliptical cylinder performing transverse vibration only. The chapter starts by outlining the previous investigations on power extraction from heaving and pitching configurations and motivation of this study (§ 7.1). Then, the computational model is discussed (§ 7.2). The validation of the numerical model with previously reported studies is discussed in the same section. The effects of damping and aspect ratio on power extraction are explored (§ 7.3). The chapter then concludes with a summary of the outcomes (§ 7.4).

7.1 Introduction

Oscillating turbines offer an environment-friendly alternative for energy harvesting, as their blade tip speed is lower than that of conventional turbines. Power can be extracted from both airfoils and elliptical bodies through combined heaving and pitching motion, controlled actively, passively, or through a combination of both approaches (Griffith et al., 2016).

For passive heaving and pitching, Peng and Zhu (2009) demonstrated a 20% efficiency with an optimal pivot location, while Simpson et al. (2008) reported up to 50% efficiency. Wang et al. (2017) achieved 32% efficiency at Re = 400 with a fully passive flapping foil, showing that pivot location significantly affects heave and pitch amplitudes. Zhao et al. (2021) further improved this to 47% by optimizing the heaving limiter configuration. For elliptical cylinders specifically, Griffith et al. (2016) investigated active pitching with passive heaving at Re = 200, achieving 20% efficiency at $\epsilon = 0.167$. Pal and Soti (2025) investigated the effect of ϵ and damping ratio on power extraction of a 1-DOF elliptical cylinder at Re = 100, reporting a maximum efficiency of 16.4% at $\epsilon = 0.40$.

The above literature shows that flapping airfoils can achieve up to 50% efficiency with passive heaving and pitching. In contrast, the maximum efficiency reported for both active heaving and pitching is 40%, while a semi-active mechanism yields only 20% efficiency. These findings suggest that fully passive heaving and pitching offer certain advantages in terms of power generation. To the best of our knowledge, power extraction at low Re from an elliptical cylinder with passive heaving and pitching has not been investigated. This study presents a numerical investigation of power extraction from an elliptical cylinder with a fixed aspect ratio of 0.40 at Re = 100, undergoing two-degree-of-freedom motion in heaving and pitching.

7.2 Formulation

7.2.1 Governing Equations and Computational Methods

A 2-D incompressible Newtonian fluid flow model is considered to simulate the VIV response of the present study (§ 3). The Arbitrary Lagrangian-Eulerian (ALE) scheme is applied to deal with the moving boundary problem.

The general equation of motion of the elastically mounted elliptical solid body is given by the spring-mass-damper system in non-dimensional form as:

$$\ddot{y} + \frac{4\pi\zeta}{U^*}\dot{y} + \frac{4\pi^2}{U^{*2}}y = \frac{2}{\pi}\frac{C_L}{m^*}\frac{1}{\epsilon} \tag{7.1}$$

where $C_L = 2F(t)/\rho U^2 D$ is the lift force coefficient, and $F(t)$ denotes the lift force on the body. In addition to the Navier–Stokes equations and the spring–mass–damper equation, an additional equation is required to account for the moment acting on the body. To this end, the instantaneous rotational angle is denoted by θ and measured in the anticlockwise direction from the positive y-axis. The angular velocity and angular acceleration are represented by $\dot{\theta}$ and $\ddot{\theta}$, respectively. The pitching motion of the body, governed by a torsional spring and damper system, is described by the following equation:

$$I_\theta \ddot{\theta}^* + c_\theta \dot{\theta}^* + k_\theta \theta^* = M(t) \tag{7.2}$$

where I_θ is the moment of inertia of the ellipse in the direction perpendicular to both streamwise and cross-flow direction, and c_θ and k_θ are the damping coefficient and spring constant for the torsional spring, respectively. The time-dependent torque acting on the body is represented by $M(t)$. Above Equation 7.2 can be non-dimensionalized by introducing moment of inertia ratio $I_\theta^* = I_\theta/\rho D^4$ and reduced velocity of moment $U_\theta^* = U/f_\theta D$. Here, f_θ denotes the natural torsional frequency of the system in vacuum. Therefore, from the relation of I_θ and $I_\theta{}^*$, we can say $I_\theta{}^* = I_\theta$ since D is taken as unity. The non-dimensional form of Equation 7.2 can be written as mentioned below:

$$\ddot{\theta} + \frac{4\pi\zeta_\theta}{U_\theta^*}\dot{\theta} + \frac{4\pi^2}{U_\theta^*}\theta = \frac{C_M}{2I_\theta^*} \tag{7.3}$$

The moment of inertia (MOI), I_θ, is defined as $\pi ab(a^2 + d^2)/4$, where a and d are the semi-major and semi-minor axes of the ellipse, respectively, with the corresponding major and minor diameters defined as $D = 2a$ and $b = 2d$. Therefore, the MOI can be represented as $\pi Db(D^2 + b^2)/64$. MOI is fixed by the geometry of the cylinder, with a value of 0.0227. Therefore, apart from solving continuity, momentum, and 7.1 equations, we are also solving Equation 7.3. The Equations 7.1 and 7.3 are solved separately but are coupled with the continuity and momentum equations from Chapter 2. The ratio of the natural frequency of oscillation of the heaving to pitching is defined as $f_r = f_n/f_\theta$. So torsional spring stiffness, k_θ, is related to k_y of the linear spring by the following relation:

$$k_\theta = \frac{k_y}{f_r{}^2}\frac{I_\theta}{m} \tag{7.4}$$

The above Equation 7.4 can be non-dimensionalized as follows:

$$\begin{aligned} k_\theta &= \frac{k_y}{{f_r}^2}\frac{{I_\theta}^*}{m^*}\frac{4D^4}{\pi Db} \\ &= \frac{k_y}{{f_r}^2}\frac{{I_\theta}^*}{m^*}\frac{4}{\pi\epsilon} \end{aligned} \tag{7.5}$$

As the damping ratio for pitching and heaving is the same ($\zeta_y = \zeta_\theta = \zeta$), the damping constant for pitching c_θ can be written as $c_\theta = 2\zeta\sqrt{k_\theta I_\theta}$. Moreover, the relation between U^* and ${U_\theta}^*$ is ${U_\theta}^* = f_r U^*$.

The Newmark-β method is used to numerically integrate Equations 7.1 and 7.3 to get the transverse displacement and rotational angle of the cylinder. The coupled NS and two structural equations are solved using OpenFOAM, an open-source CFD tool based on the finite volume method. The temporal term is discretized using a first-order implicit scheme. The convection terms in the governing equation are discretized using second-order linear upwind schemes, while the second-order accurate central differencing is utilized for the diffusion part. The surface-normal gradients are corrected with explicit non-orthogonal correction.

7.2.2 Problem description

An elliptical cylinder of $\epsilon = 0.40$ of minor diameter b is placed in a free-stream with a uniform velocity of U. At a constant Re = 100, the cylinder with a fixed $m^* = 10$ is mounted on a spring and damper system. Two types of springs are used to allow passive heaving and pitching: a linear spring and a torsional spring with equal ζ. The damping ratio varies between $\zeta = 0.02$ and 0.30. In this problem, U^* varies from 3.0 to 21.0 and f_r from 0.25 to 3.0. The ϵ is chosen to be 0.40 for the present study, as maximum power is noticed at $\epsilon = 0.40$ for a 1-DOF elliptical cylinder at Re = 100 (Pal and Soti, 2025). At Re = 100, the flow is fairly two-dimensional as three-dimensionality is observed for Re $\geq$ 300 (Leontini et al., 2006). Also, for an oscillating cylinder, the onset of three-dimensionality is delayed up to Re = 280 when cylinder frequency is synchronized with the natural frequency (Leontini et al., 2007). Therefore, it is safe to assume that at Re = 100, the present study falls within the two-dimensional regime.

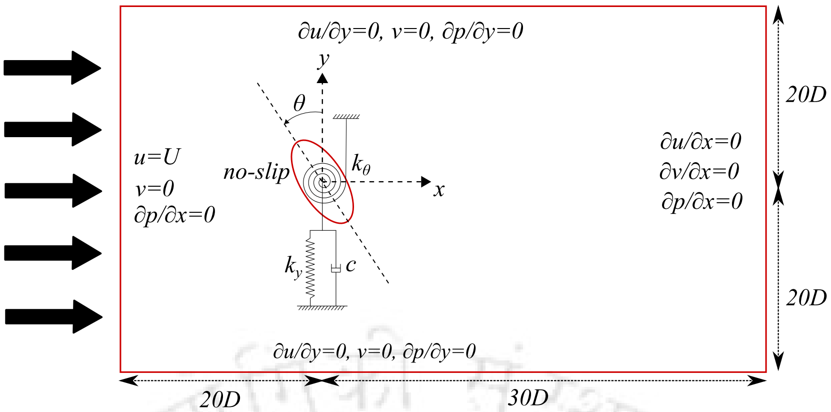

Fig. 7.1 Schematic of computational domain for 2-DOF motion of elliptical cylinder at $\epsilon = 0.40$

7.2.3 Computational domain and boundary condition

The computational domain shown in Figure 7.1 is defined as $\Omega = [-20D, 30D] \times [-20D, 20D]$. At the inlet, the velocity is $(u, v) = (U, 0)$. No-slip boundary condition ($u_{rel} = v_{rel} = 0$) is used at the surface of the elliptical body. At the lateral boundaries, a symmetry boundary condition ($\partial u/\partial y = 0$, $v = 0$) is used to maintain shear stress and zero flux at these boundaries. Neumann boundary condition ($\partial u/\partial x = 0$, $\partial v/\partial x = 0$) is used at the outlet for the flow velocity. The Neumann boundary condition is used for pressure ($\partial p/\partial x = 0$) at all the boundaries. The computation is initialized with a constant velocity ($u = U$, $v = 0$) and pressure $p = 0$.

7.2.4 Mesh Independence and model validation

The detailed mesh around the elliptical cylinder is shown in Figure 7.2. A mesh independence study is performed to obtain an accurate result at a low computational cost. In this study, the amplitude of vibration is used for validation. The grid size around the cylinder varies from 0.01 to 0.03. All the simulations are carried out at $U^* = 5.0$ and $\zeta = 0.003$. Table 7.1 shows the mesh independence data for the present simulation. From the Mesh independence test, we can see that mesh M4 is suitable, as the variation in A^* and θ^* is less than 1%. Therefore, we proceeded with our numerical study using that mesh. We validate our case with that of Wang et al. (2019). The validation is shown in Figure 7.3. We can observe that the pitching amplitude is almost in accordance with that of Wang et al. (2019). However, the transverse amplitude

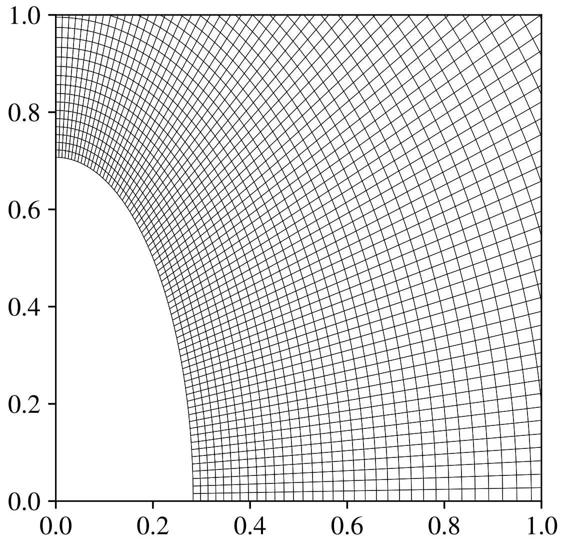

Fig. 7.2 The computational mesh around the cylinder at $\epsilon = 0.40$

has a maximum variation of 4%. The reason may be the use of different meshes and numerical schemes.

Table 7.1 Mesh independence study on VIV of elliptical cylinder with $\epsilon = 0.40$ at $U^* = 5.0$.

Mesh	**No of Cells**	$\boldsymbol{\Delta x_{cylinder}}$	$\boldsymbol{A^*}$	$\boldsymbol{\theta^*}$	**%Diff. wrt M6 of** A^*	**%Diff. wrt M6 of** θ^*
M1	15957	0.03	0.317331	0.378193	3.889	2.684
M2	19803	0.025	0.321541	0.381554	2.614	1.819
M3	28646	0.02	0.325110	0.384668	1.533	1.018
M4	**43512**	**0.015**	**0.326787**	**0.384869**	**1.025**	**0.966**
M5	63676	0.012	0.327391	0.385728	0.842	0.745
M6	89258	0.01	0.330172	0.388624	0	0

7.3 Results and discussion

This section examines the flow characteristics–non-dimensional amplitude response (A^*), angular amplitude (θ^*), phase difference for translation (ϕ_y), phase difference for rotation (ϕ_θ), lift coefficient (C_L), and moment coefficient (C_M)–as well as the average power ($\bar{P}$), with respect to the variation of U^*, f_r, and ζ. Results are presented for three representative damping ratios, $\zeta = 0.02$, 0.04, and 0.07.

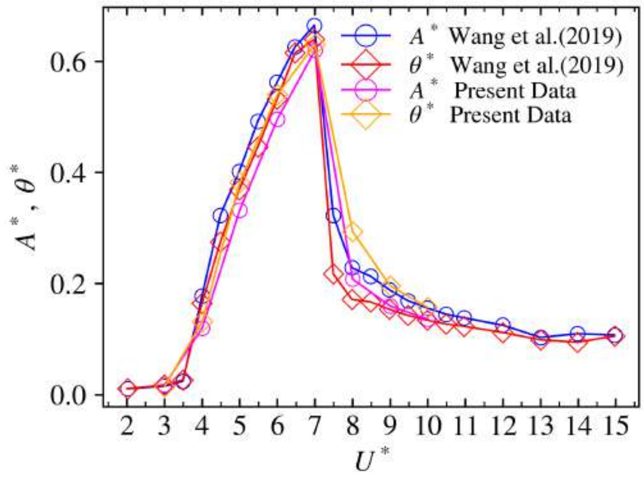

Fig. 7.3 Validation of transverse amplitude A^* and pitching amplitude θ^* with Wang et al. Wang et al. (2019)

7.3.1 Flow and average power characteristics at $\zeta = 0.02$

The non-dimensional vibration amplitude A^* is defined as, $A^* = \frac{1}{2}(y_{\max} - y_{\min})$, where $y_{\max}$ and $y_{\min}$ are the maximum and minimum displacement of the cylinder after reaching a quasi-periodic state. The vibration amplitude increases with U^* up to $U^* = 7.0$ for all f_r as seen from Figure 7.4(a). Maximum A^* is reported to be 0.56, which is very close to peak A^* for a circular cylinder for zero damping at Re $= 100$ Singh and Mittal (2005). The peak A^* does not follow a linear relation with f_r. After reaching its peak, A^* decreases monotonically with further increase in U^*. However, even at high U^*, A^* stabilizes at a value close to 0.2, and the response for all f_r converges in this regime. A sudden dip in A^* is observed for $f_r = 2.0$ at $U^* = 23.0$. Figure 7.4(b) shows that the trend of θ with U^* is also non-monotonic, with peak θ increases with f_r up to $f_r = 2.0$ before decreasing at $f_r = 3.0$. The little drop in θ at $U^* = 23.0$ for $f_r = 2.0$ is consistent with the drop in A^*. Figure 7.4(c) shows that the lift coefficient, C_L, at $f_r = 0.50$ exceeds that at $f_r = 0.25$ up to $U^* = 9.0$. After a sharp increase in C_L at $U^* = 9.0$ for $f_r = 0.25$, the C_L remains nearly constant with further rise in U^*. The same scenario is spotted for $f_r = 2.0$. The C_L value for $f_r = 0.50$ and 3.0 drops below the C_L of the stationary cylinder (C_{L_S}) at $U^* = 9.0$, and after that, C_L recovers to C_{L_S}. The C_L at $f_r = 0.50$ and 3.0 closely follow each other along the entire range of U^*. The jump in C_M is visible at $U^* = 9.0$ for $f_r = 0.25$ and 2.0 as seen from Figure 7.4(d). The C_M value for $f_r = 0.25$ and 2.0 remains almost constant for $U^* > 9.0$, like the C_L curve. For $f_r = 3.0$, C_M increases up to $U^* = 8.0$ and then decreases gradually. The C_M curve for $f_r = 0.50$ closely resembles the trend for $f_r = 3.0$. The phase difference between transverse force and displacement is denoted by ϕ_y, and between moment and angular displacement by ϕ_θ. Up to $U^* = 8.0$, ϕ_y and ϕ_θ curves show totally different variation with U^*. The jump in ϕ_y to 180° at $U^* = 9.0$ for $f_r = 0.50$ and 3.0 corresponds to the dip in the C_L curve, while the ϕ_y stays at 90° for $f_r = 0.25$ and 2.0 after $U^* = 9.0$. Therefore, it can be inferred that up to $U^* = 9.0$, the system follows one response branch, whereas beyond $U^* = 9.0$, it transitions to a different branch. In the range of $3.0 \leqslant U^* \leqslant 9.0$, ϕ_θ and ϕ_y are out of phase. For $U^* \geq 9.0$, the difference between ϕ_θ and ϕ_y is 90° for $f_r = 0.50$ and 3.0. In contrast, for $f_r = 0.25$ and 2.0 at $U^* \geq 9.0$, no noticeable variation is observed with U^*, as both phases remain at 90°.

In a cycle of oscillation, we can model the energy from the flow to the body as the energy dissipated by the damping from the linear and torsional dampers. The power is non-dimensionalized by the power available over the fluid region occupied by the body $(1/2\rho U^3 D)$. We have taken both the damping coefficients as equal, $c = c_y = c_\theta$. The power from the 2-DOF is only the algebraic summation of the power from the transverse $(P_y(t))$ and pitching motions $(P_\theta(t))$. So, the instantaneous power can be represented as,

$$P(t) = \frac{c_y \dot{y}^2 + c_\theta \dot{\theta}^2}{\frac{1}{2}\rho U^3 D} \tag{7.6}$$

After integrating over the cycle of oscillation and non-dimensionalizing Equation 7.6, we get:

$$\begin{aligned} \bar{P} &= \bar{P}_y + \bar{P}_\theta \\ \bar{P} &= \frac{2\pi^2 \alpha_y}{U^*}(\epsilon)\dot{y}^2_{\text{RMS}} + \frac{8\pi\alpha_\theta}{U^*_\theta}\dot{\theta}^2_{\text{RMS}} \end{aligned} \tag{7.7}$$

where $\alpha_y = m^*\zeta$ and $\alpha_\theta = I^*_\theta\zeta$ are the mass-damping parameters for heaving and pitching motion, respectively. The root-mean-square transverse and angular velocity of the cylinder are represented as $\dot{y}_{\text{RMS}}$ and $\dot{\theta}_{\text{RMS}}$ and can be calculated as,

$$\dot{y}_{\text{RMS}} = \sqrt{\frac{1}{T_{total}}\int_0^{T_{total}} \dot{y}^2 dt} \quad \text{and} \quad \dot{\theta}_{\text{RMS}} = \sqrt{\frac{1}{T_{total}}\int_0^{T_{total}} \dot{\theta}^2 dt} \tag{7.8}$$

After further manipulation, $\bar{P}$ can be represented as

$$\bar{P} = \frac{2\pi^2 \alpha_y(\epsilon)}{U^*}\left[\dot{y}^2_{\text{RMS}} + \frac{4}{\pi}\frac{I^*_\theta}{m^*}\frac{1}{\epsilon}\frac{1}{f_r}\dot{\theta}^2_{\text{RMS}}\right] \tag{7.9}$$

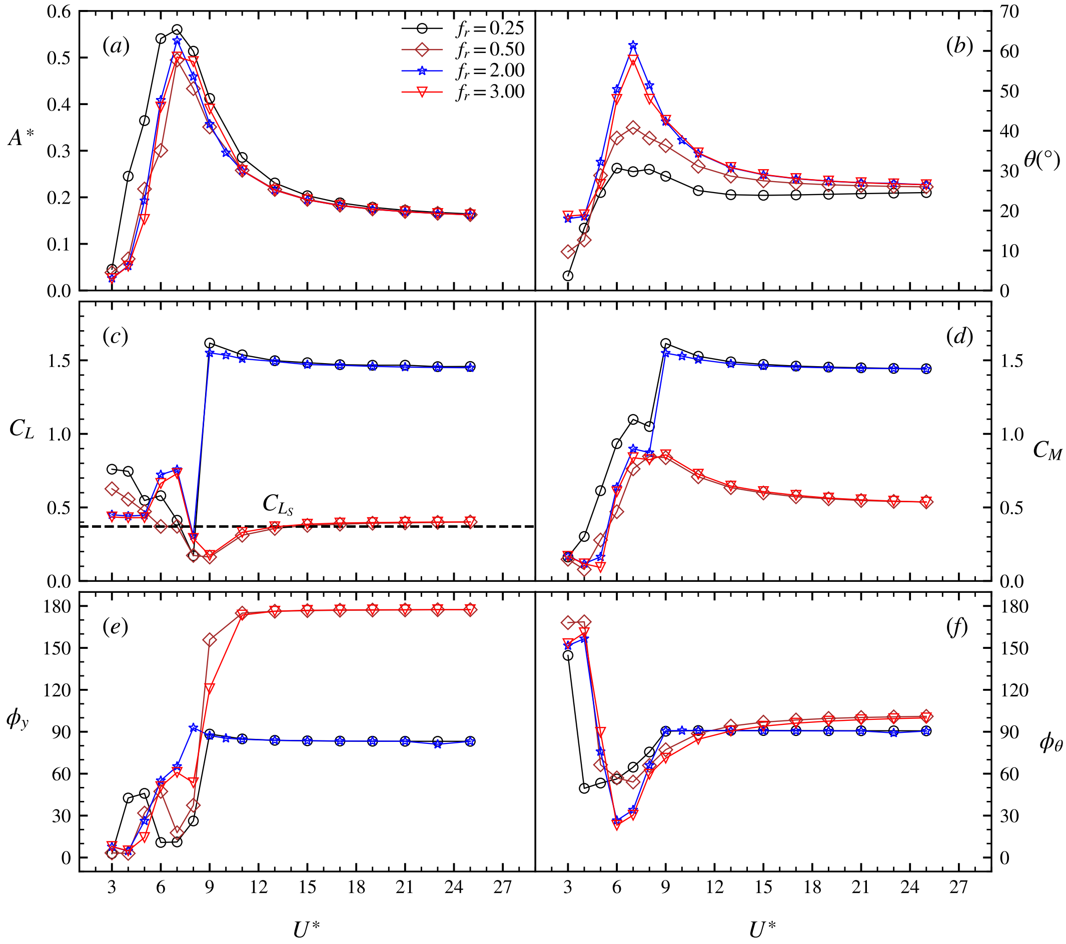

Fig. 7.4 Flow characteristics at $\zeta = 0.02$ at different f_r (a) non-dimensional amplitude (A^*), (b) angular displacement $\theta(°)$, (c) lift coefficient (C_L), (d) moment coefficient (C_M), (e) transverse phase difference (ϕ_y) and (f) phase difference in pitching (ϕ_θ)

The average power $\bar{P}$, as well as $\dot{y}_{\text{RMS}}$ and $\dot{\theta}_{\text{RMS}}$, are plotted with variation of U^* in Figure 7.5. The RMS of $\dot{y}$ follows a non-monotonic trend with U^*. The maximum $\dot{y}_{\text{RMS}}$ for all f_r is found at $U^* = 7.0$, and except for $f_r = 0.50$, values of the maximum $\dot{y}_{\text{RMS}}$ collapse for all f_r. Also at $U^* > 15.0$, $\dot{y}_{\text{RMS}}$ converges for all f_r. Peak $\dot{\theta}_{\text{RMS}}$ for all f_r is also observed at $U^* = 7.0$, and increases with f_r up to $f_r = 2.0$. After $U^* = 9.0$, values of $\dot{\theta}_{\text{RMS}}$ for $f_r = 2.0$ and 3.0 follow each other. As average power depends upon $\dot{y}_{\text{RMS}}$ and $\dot{\theta}_{\text{RMS}}$, we observe the same non-monotonic trend of $\bar{P}$ with U^*. The maximum $\bar{P}_y$ is found at $f_r = 0.25$, followed by $f_r = 2.0$ and 3.0. However, the maximum $\bar{P}_\theta$ is observed at $f_r = 2.0$. It is also noticed that $\bar{P}_\theta$ is almost one order of magnitude lower than $\bar{P}_y$. Therefore, the contribution of $\bar{P}_\theta$ to the total average power is negligible. The

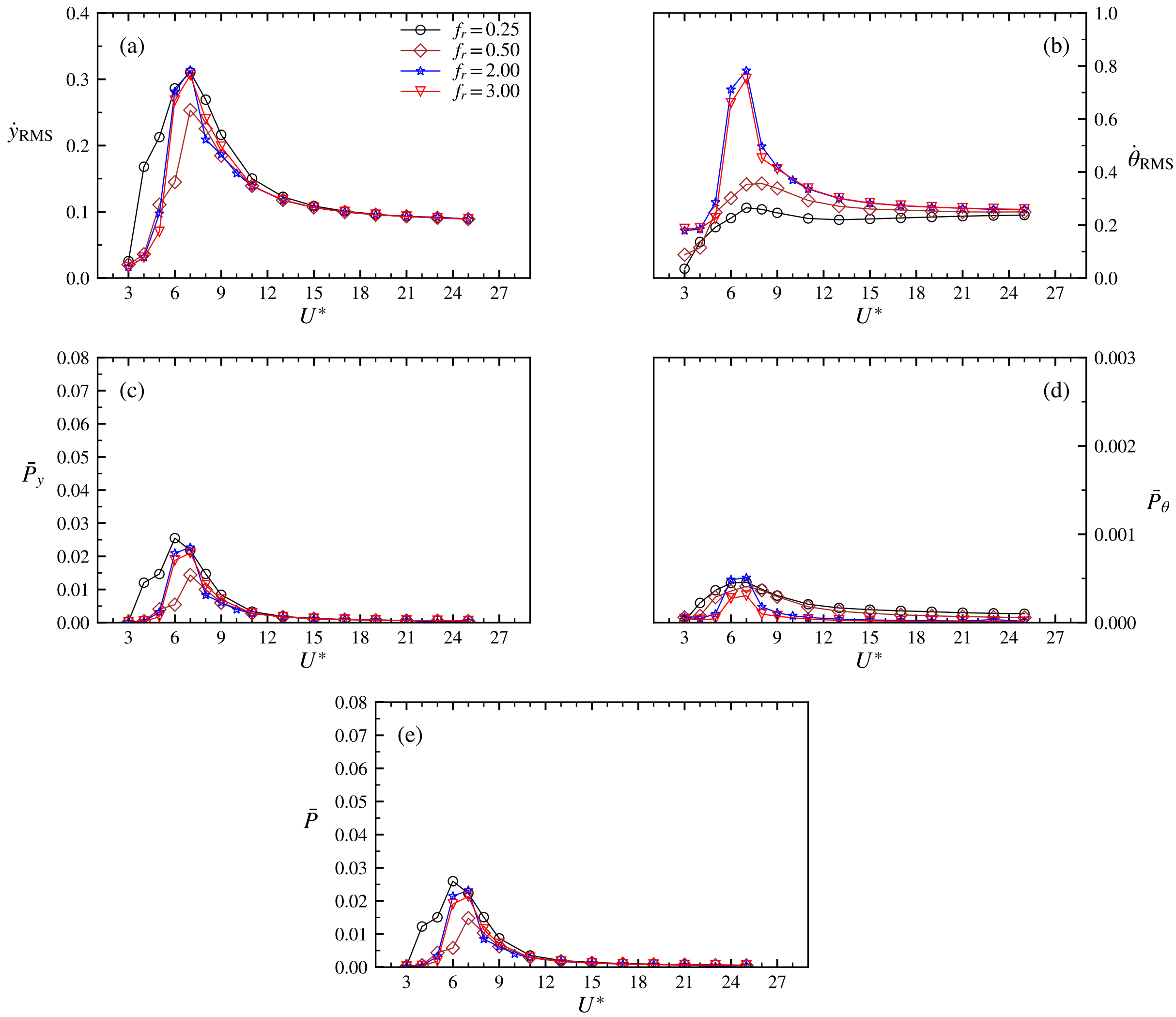

Fig. 7.5 (a) RMS velocity of cylinder $\dot{y}_{\mathrm{RMS}}$, (b) RMS of angular velocity $\dot{\theta}_{\mathrm{RMS}}$ and (c) average power for transverse motion $\bar{P}_y$, (d) average power for rotational motion $\bar{P}_\theta$ and (e) total average power $\bar{P}$ with the variation of f_r at $\zeta = 0.02$.

trend of $\bar{P}$ thus resembles the trend of $\bar{P}_y$. The maximum $\bar{P}$ does not follow a relation with f_r, as the maximum $\bar{P}$ and second maximum of $\bar{P}$ are observed at $f_r = 0.25$ and 2.0, respectively. The lowest peak is observed at $f_r = 0.50$, as $\dot{y}_{\mathrm{RMS}}$ is lowest at this f_r. Though $\dot{\theta}_{\mathrm{RMS}}$ is higher for $f_r = 2.0$ and 3.0, the maximum $\bar{P}_\theta$ for all f_r is very close. The reason is clear from the second term in Equation 7.9, as in the denominator there is f_r. Therefore, the higher the f_r, the lower the corresponding $\bar{P}_\theta$. Despite the lower values of $\dot{\theta}_{\text{RMS}}$ observed at $f_r = 0.25$ and 0.50, the decrease in f_r results in an increase in $\bar{P}_\theta$.

7.3.2 Flow and average power characteristics at $\zeta = 0.04$

Figure 7.6 shows the variation of heaving and pitching output parameters, A^*, θ, C_L, C_M, ϕ_y, and ϕ_θ with U^* at $\zeta = 0.04$. The vibration amplitude and angular displacement at $\zeta = 0.04$ exhibit a similar non-monotonic behavior with U^* as seen for $\zeta = 0.02$. The maximum oscillation amplitude is observed at $U^* = 7.0$ for all f_r, while it occurs at $U^* = 8.0$ for $f_r = 0.50$. The maximum amplitude decreases with f_r up to $f_r = 0.50$, followed by increases. However, the peak of maximum amplitude is observed at $f_r = 0.25$. Contrary to the oscillation amplitude response, θ increases with f_r, and the peak of maximum θ is found at $f_r = 2.0$ and 3.0. Lift coefficient shows a sharp drop at $U^* = 8.0$ for $f_r = 2.0$ and 3.0, while the lift coefficient gradually decreases for $f_r = 0.25$ and 0.50. After the plunge, C_L recovers and converges to C_{L_S}. Unlike at $\zeta = 0.02$, there is no sharp jump in C_L at $\zeta = 0.04$. The moment coefficient increases with increasing U^* and peaks at $U^* = 7.0$ before decreasing at higher U^* values. The peak of maximum C_M is observed for $f_r = 0.25$ at $U^* = 7.0$. A sharp drop from higher ϕ_θ values is observed at $U^* = 6.0$ and 7.0; beyond this point, ϕ_θ increases and stabilizes at approximately 100°. Within the range $3.0 \leqslant U^* \leqslant 7.0$, ϕ_θ shows a decreasing trend, while ϕ_y exhibits an increasing trend. At $U^* = 10.0$, a jump in ϕ_y is observed for all f_r.

The trend of $\dot{y}_{\text{RMS}}$ and $\dot{\theta}_{\text{RMS}}$ with U^* for $\zeta = 0.04$, as seen from Figure 7.7, is observed to be identical of results of $\zeta = 0.02$. The maximum $\dot{y}_{\text{RMS}}$ of $f_r = 0.25$ and 3.0 matches, while the maximum $\dot{y}_{\text{RMS}}$ drops at $f_r = 0.50$. A jump in $\dot{\theta}_{\text{RMS}}$ is observed for $f_r = 2.0$ and 3.0, which is consistent with the jump in θ value. The values of $\dot{\theta}_{\text{RMS}}$ for $f_r = 0.25$ and 0.50 are minimal compared to $f_r = 2.0$ and 3.0. The peak average power is observed at $U^* = 7.0$, as the maximum $\dot{y}_{\text{RMS}}$ and $\dot{\theta}_{\text{RMS}}$ are also observed at that U^*, except at $f_r = 0.50$. The peak of maximum $\bar{P}$ is observed again at $f_r = 2.0$, and the lowest peak is at $f_r = 3.0$. It stems from the increase in f_r from 2.0 to 3.0, although $\dot{y}_{\text{RMS}}$ and $\dot{\theta}_{\text{RMS}}$ remain identical for both f_r values. For the same reason, at high U^*, with increasing f_r, $\bar{P}$ decreases.

7.3.3 Flow and average power characteristics at $\zeta = 0.07$

Figure 7.8 shows that the maximum amplitude is higher for $f_r = 0.25$ than for $f_r = 2.0$, while θ is higher for $f_r = 2.0$. Moreover, A^* and θ decrease with an increase in damping.

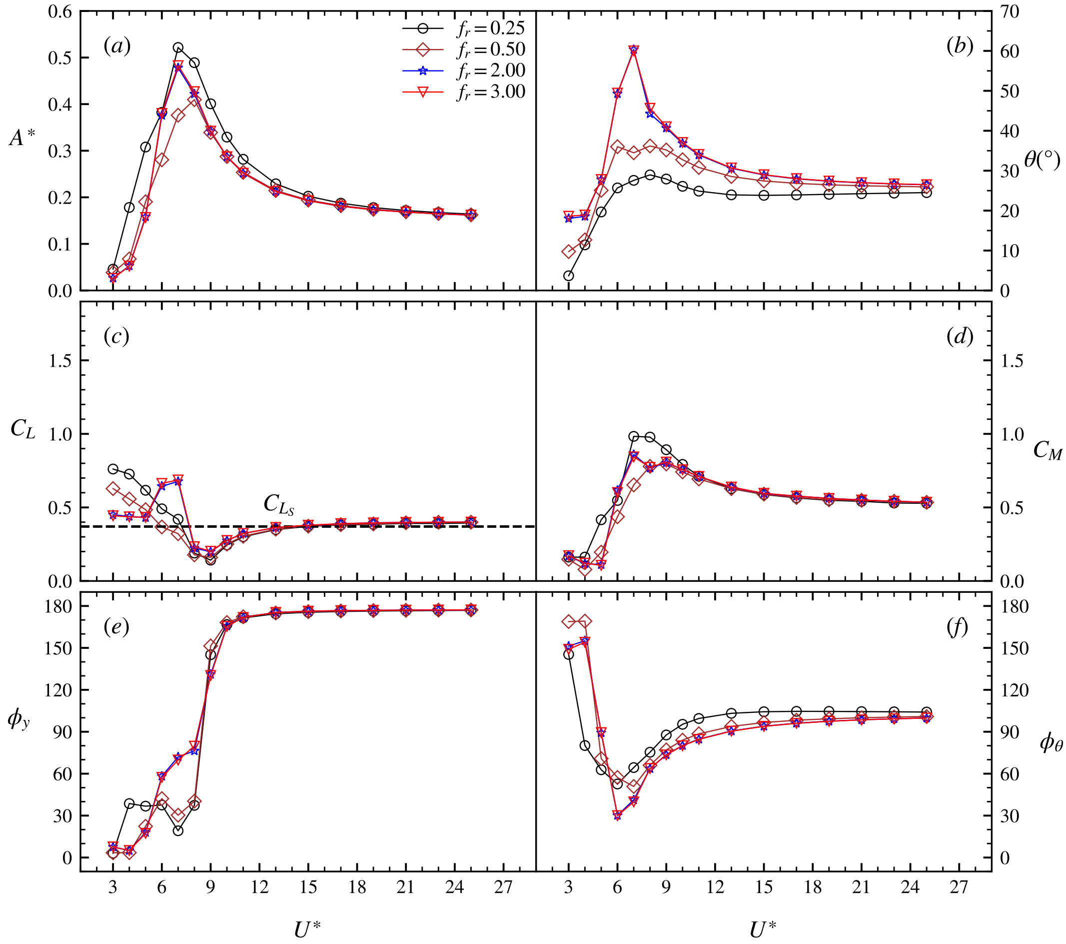

Fig. 7.6 Flow characteristics at $\zeta = 0.04$ at different f_r (a) non-dimensional amplitude (A^*), (b) angular displacement $\theta(°)$, (c) lift coefficient (C_L), (d) moment coefficient (C_M), (e) transverse phase difference (ϕ_y) and (f) phase difference in pitching (ϕ_θ)

Simultaneously, the values of C_L and C_M decrease as the damping increases. From the other two damping cases ($\zeta = 0.02$ and 0.04), the U^*, where maximum or minimum C_L is observed, does not always correspond to the U^* of maximum A^*; however, corresponding U^* for maximum θ and C_M matches. Additionally, at minimum C_L, ϕ_y increases to approximately 180°. The maximum C_M does not correspond to the minimum ϕ_θ, and there is a lag in U^* between the maximum C_M and the minimum ϕ_θ. However, for all ζ, ϕ_θ at high U^* ($U^* \geqslant 12.0$) almost remain constant.

Figure 7.9 shows the same trend of $\dot{y}_{\text{RMS}}$ and $\dot{\theta}_{\text{RMS}}$ with U^* as of A^* and θ. Thus, maximum $\dot{y}_{\text{RMS}}$ is observed at $f_r = 0.25$, and maximum $\dot{\theta}_{\text{RMS}}$ at $f_r = 2.0$. With an increase in damping, $\dot{y}_{\text{RMS}}$ and $\dot{\theta}_{\text{RMS}}$ both decrease. However, $\bar{P}_y$ and $\bar{P}_\theta$ increase with

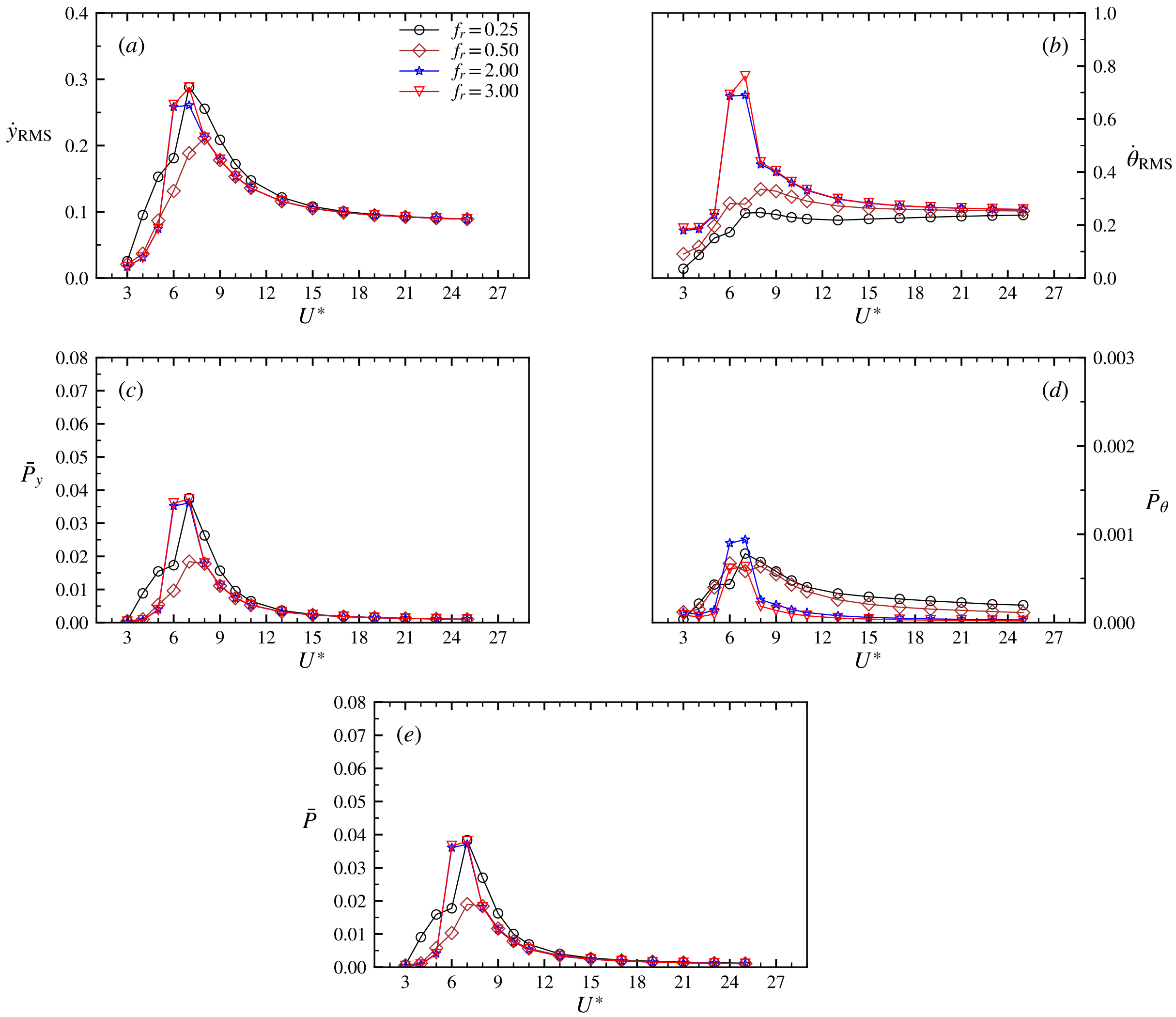

Fig. 7.7 (a) RMS velocity of cylinder $\dot{y}_{\mathrm{RMS}}$, (b) RMS of angular velocity $\dot{\theta}_{\mathrm{RMS}}$ and (c) average power for transverse motion $\bar{P}_y$, (d) average power for rotational motion $\bar{P}_\theta$ and (e) total average power $\bar{P}$ with the variation of f_r at $\zeta = 0.04$.

damping (as observed for three ζ), and maximum $\bar{P}_y$ and $\bar{P}_\theta$ are observed at maximum $\dot{y}_{\mathrm{RMS}}$ and $\dot{\theta}_{\mathrm{RMS}}$, respectively. Again, the influence of $\bar{P}_\theta$ on $\bar{P}$ is negligible compared to $\bar{P}_y$. As $\dot{y}_{\mathrm{RMS}}$ is higher at $f_r = 0.25$, $\bar{P}_y$ and hence $\bar{P}$ are higher at $f_r = 0.25$. In contrast, maximum $\bar{P}$ for $\zeta = 0.02$ and 0.04 is recorded at $f_r = 2.0$.

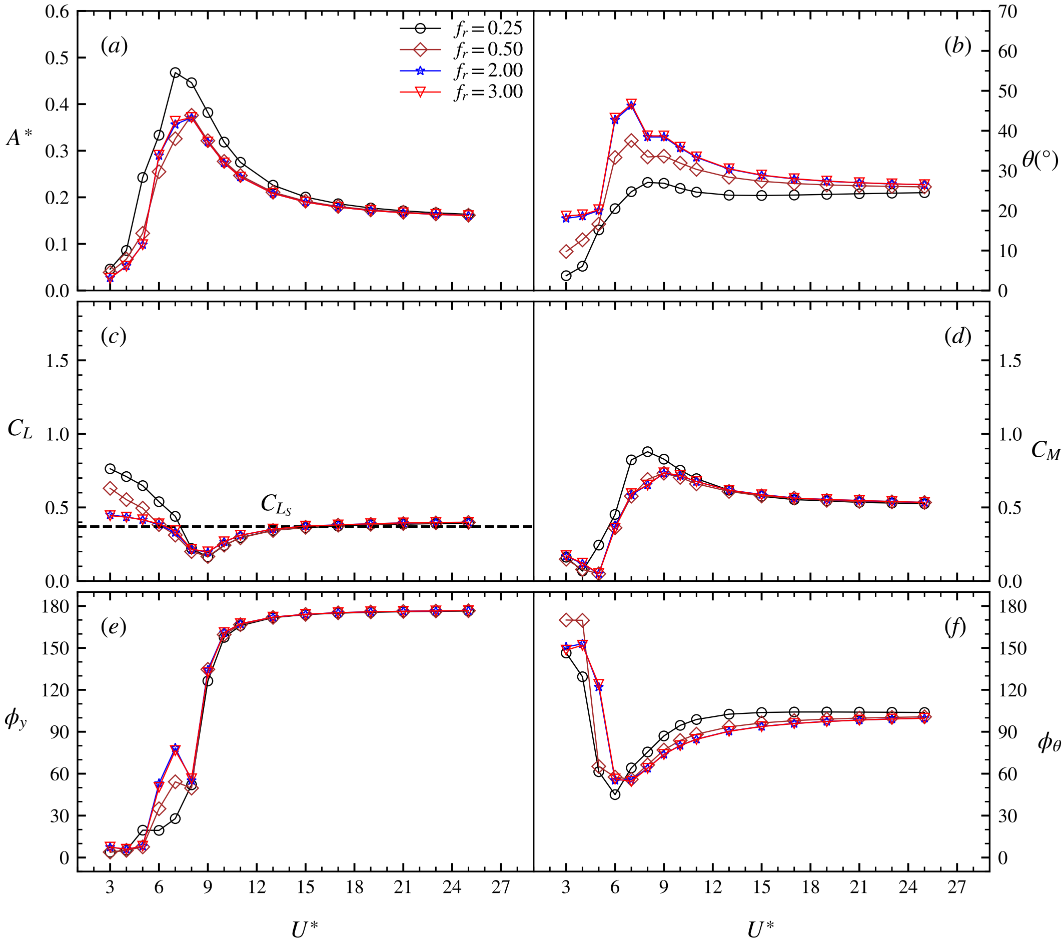

Fig. 7.8 Flow characteristics at $\zeta = 0.07$ at different f_r (a) non-dimensional amplitude (A^*), (b) angular displacement $\theta(°)$, (c) lift coefficient (C_L), (d) moment coefficient (C_M), (e) transverse phase difference (ϕ_y) and (f) phase difference in pitching (ϕ_θ)

7.3.4 Flow and average power characteristics at $\zeta = 0.30$

The flow characteristics at $\zeta = 0.30$ are shown in Figure 7.10. The maximum oscillation amplitude grows as f_r decreases, while θ exhibits an increasing trend with f_r. With the increase in damping from $\zeta = 0.02$ to 0.30, both oscillation amplitude and rotational amplitude decrease. Angular amplitudes for $f_r = 2.0$ and 3.0 closely follow each other. Moreover, beyond $U^* = 12.0$, A^* and θ stabilize and converge to a single value. The values of C_L and C_M also converge towards a particular value after $U^* \geq 12.0$. The values of ϕ_y are identical for all f_r and gradually increase to 180° in the range of $U^* = 6.0$–18.0. In contrast, ϕ_θ exhibits a drop at $U^* = 6.0$ before being constant for $U^* \geq 12.0$.

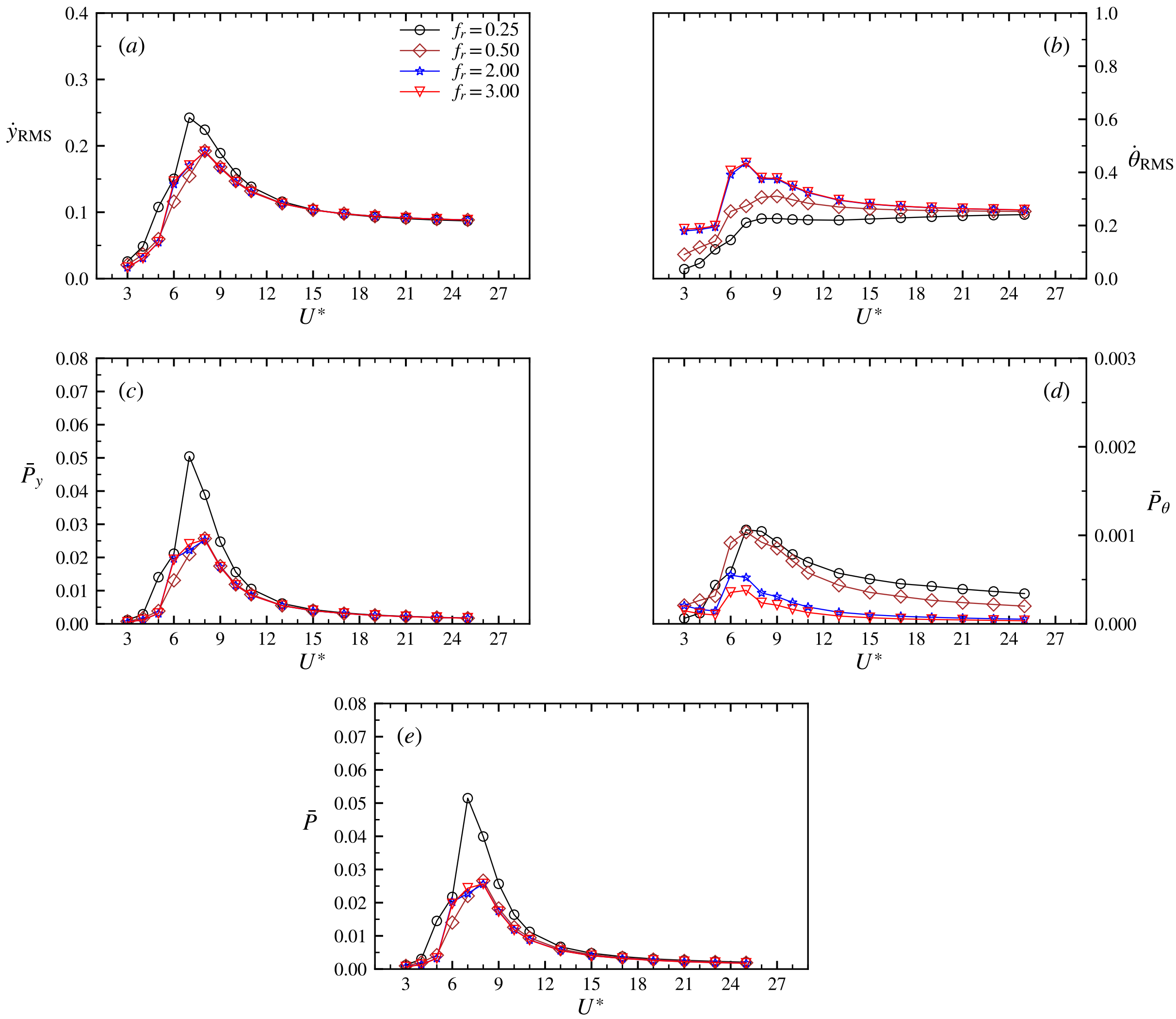

Fig. 7.9 (a) RMS velocity of cylinder $\dot{y}_{\mathrm{RMS}}$, (b) RMS of angular velocity $\dot{\theta}_{\mathrm{RMS}}$ and (c) average power for transverse motion $\bar{P}_y$, (d) average power for rotational motion $\bar{P}_\theta$ and (e) total average power $\bar{P}$ with the variation of f_r at $\zeta = 0.07$.

The $\dot{y}_{\mathrm{RMS}}$ and $\dot{\theta}_{\mathrm{RMS}}$ follow the same trend with U^* (Figure 7.11) as of A^* and θ. There is a noticeable reduction in $\bar{P}_y$ and $\bar{P}_\theta$ with an increase in f_r. The maximum $\bar{P}_y$ and $\bar{P}_\theta$ are observed at $f_r = 0.25$. Additionally, as damping increases, while $\bar{P}_y$ decreases, $\bar{P}_\theta$ increases with damping from $\zeta = 0.02$ to 0.30. However, as the contribution of $\bar{P}_\theta$ in $\bar{P}$ is negligible, overall $\bar{P}$ decreases between $\zeta = 0.07$ and 0.30. Therefore, there must be an optimal ζ between 0.07 and 0.30 with the highest extracted power.

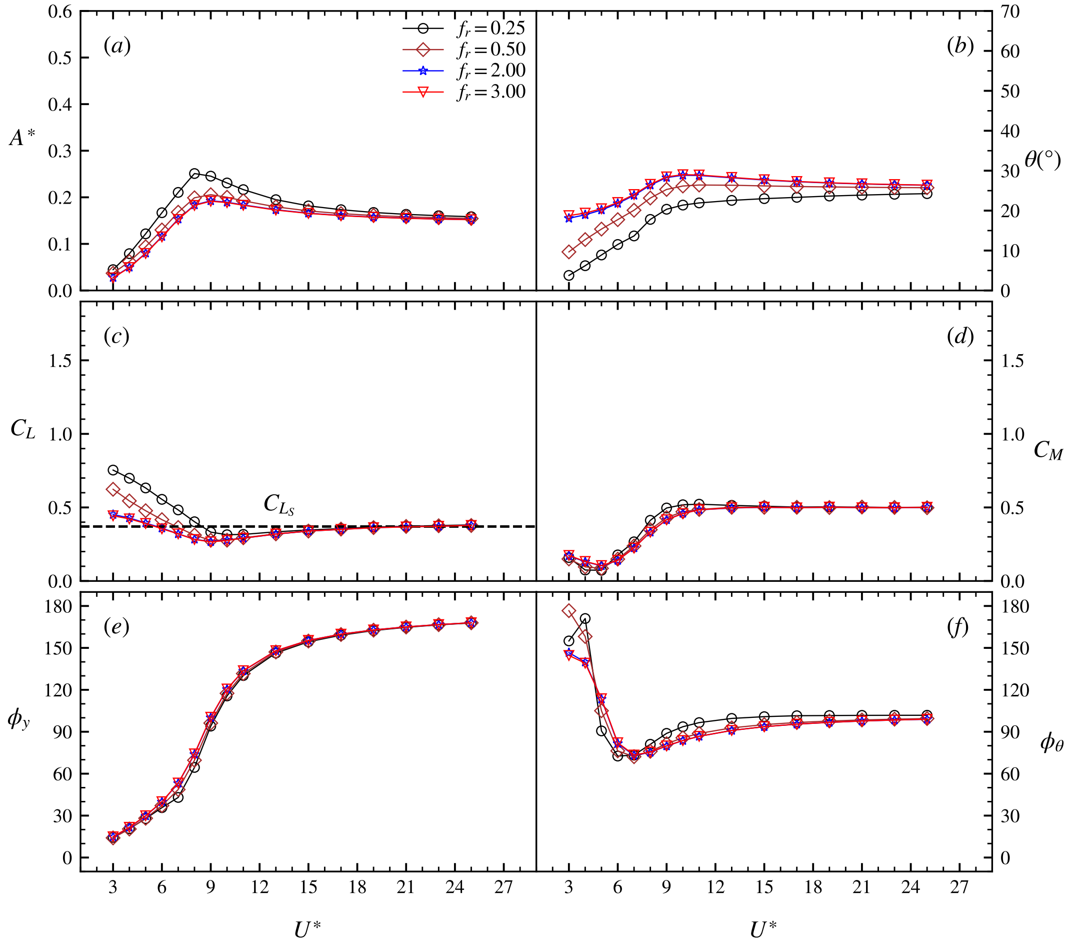

Fig. 7.10 Flow characteristics at $\zeta = 0.30$ at different f_r (a) non-dimensional amplitude (A^*), (b) angular displacement $\theta(°)$, (c) lift coefficient (C_L), (d) moment coefficient (C_M), (e) transverse phase difference (ϕ_y) and (f) phase difference in pitching (ϕ_θ)

7.3.5 Variation of maximum extracted power and efficiency with damping

The relations of maximum average power for transverse motion, $\bar{P}_{y_\alpha}$, and rotational motion, $\bar{P}_{\theta_\alpha}$, with variation of mass-damping parameter $\alpha = m^*\zeta$ are shown in Figures 7.12(a) and (b), respectively. As seen in the figures, $\bar{P}_{y_\alpha}$ for $f_r = 0.25$ increases with α up to 0.70, but then $\bar{P}_{y_\alpha}$ starts to decline. However, for $f_r = 2.0$ and 3.0, $\bar{P}_{y_\alpha}$ drops down to a lower value at $\alpha = 0.50$ and 0.60, respectively. In contrast, for $f_r = 0.50$, although $\bar{P}_{y_\alpha}$ is lower, it exhibits a steady increase with α up to $\alpha = 1.5$. Similar drops in $\bar{P}_{\theta_\alpha}$ are observed at $f_r = 2.0$ and 3.0, consistent with the trend in $\bar{P}_{y_\alpha}$. An increasing

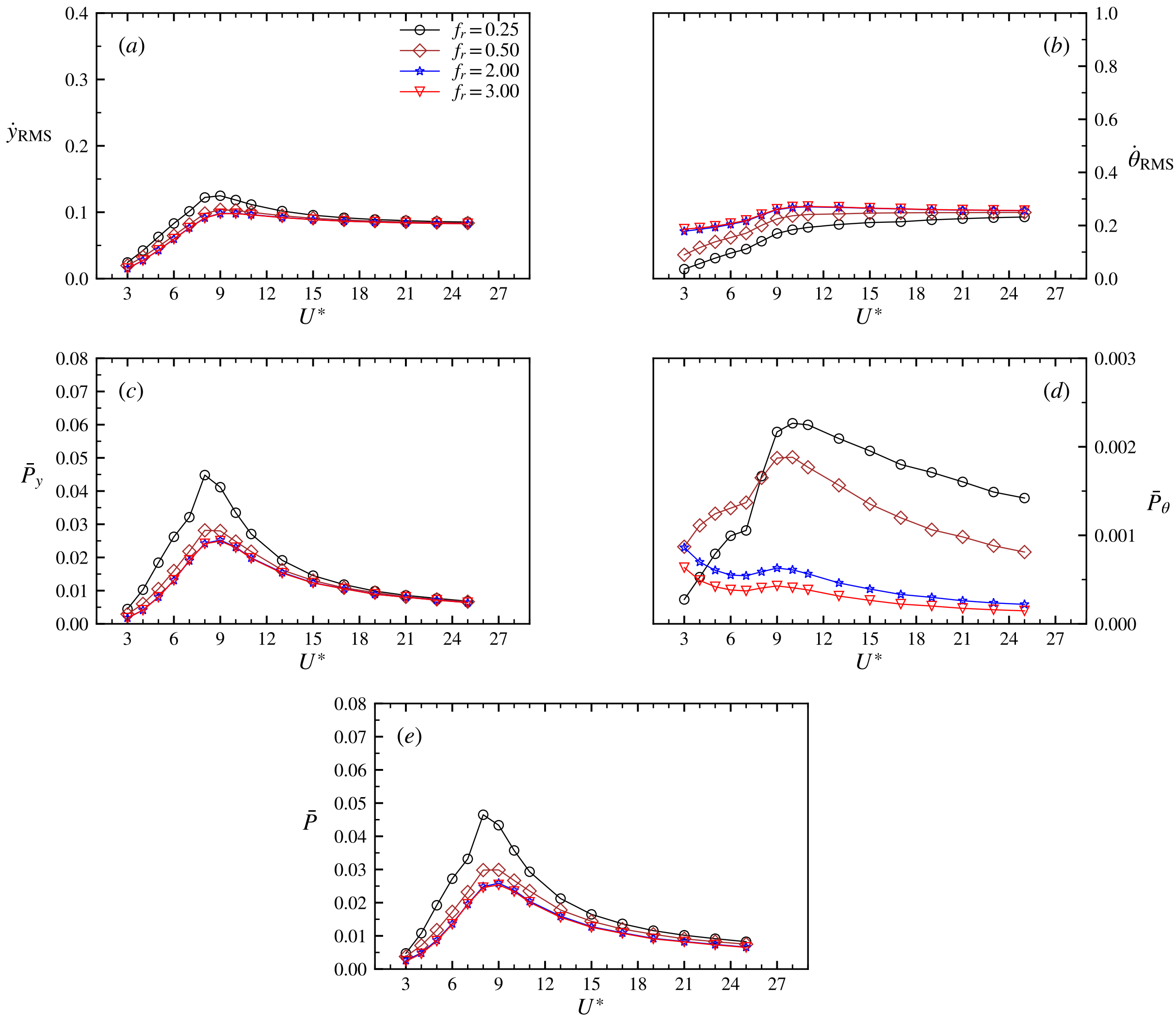

Fig. 7.11 (a) RMS velocity of cylinder $\dot{y}_{\mathrm{RMS}}$, (b) RMS of angular velocity $\dot{\theta}_{\mathrm{RMS}}$ and (c) average power for transverse motion $\bar{P}_y$, (d) average power for rotational motion $\bar{P}_\theta$ and (e) total average power $\bar{P}$ with the variation of f_r at $\zeta = 0.30$.

trend is noticed for $\bar{P}_{\theta_\alpha}$ with the increase in α. For $\alpha \leq 0.40$, $\bar{P}_{\theta_\alpha}$ is highest at $f_r = 2.0$, whereas for $\alpha > 0.40$, the maximum occurs at $f_r = 0.25$. Surprisingly, the $\bar{P}_{\theta_\alpha}$ at $f_r = 0.50$ has comparable values to those of $f_r = 0.25$. However, beyond $\alpha = 1.4$, $\bar{P}_{\theta_\alpha}$ for $f_r = 0.25$ outgrows $f_r = 0.50$. As the values of $\bar{P}_{\theta_\alpha}$ is one order of magnitude lower than $\bar{P}_{y_\alpha}$, the contribution of $\bar{P}_{\theta_\alpha}$ to total power is insignificant. Therefore, we observe a similar curve of $\bar{P}_\alpha$ as that of $\bar{P}_{y_\alpha}$. The present 2-DOF $\bar{P}_\alpha$ is compared to the 1-DOF (transverse) data at $\epsilon = 0.40$ and Re $= 100$ (Pal and Soti, 2025). From Figure 7.12(c),

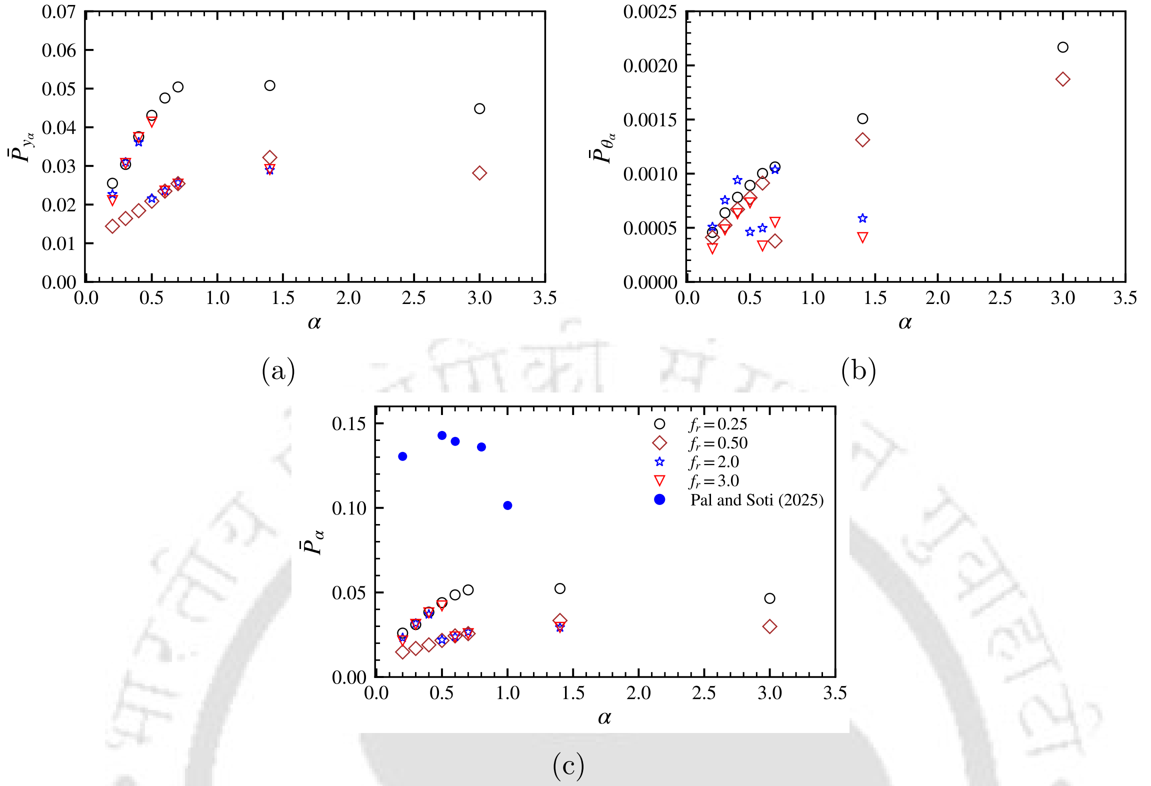

Fig. 7.12 Variation of (a) maximum average power for transverse motion $\bar{P}_{y_\alpha}$, (a) maximum average power for rotational motion $\bar{P}_{\theta_\alpha}$ and (c) total maximum average power $\bar{P}_\alpha$ with mass-damping parameter $\alpha = m^*\zeta$ at different f_r. Present 2-DOF data is compared with 1-DOF (transverse) data at $\epsilon = 0.40$ at Re = 100 Pal and Soti (2025).

it is observed that the maximum $\bar{P}_\alpha$ of 1-DOF is almost three times higher than that of 2-DOF. Therefore, this 2-DOF setup is not feasible for power generation as the maximum $\bar{P}_\alpha$ is also lower than that of a single circular cylinder (0.13) at Re = 150 (Soti et al., 2017).

Efficiency is the ratio of extracted power to the maximum power available at the fluid based on the swept area. If we consider uniform flow of U over the cylinder, the maximum power available in the fluid based on the swept area will be $1/2\rho U^3(D+2A)$, where A is the dimensional amplitude. Therefore, efficiency η can be expressed as,

$$\eta = \frac{\bar{P}}{1+2A^*} \tag{7.10}$$

Figure 7.13 shows the maximum power extraction efficiency η_α with α at different f_r. Efficiency follows the same trend as $\bar{P}_\alpha$ with α. The efficiency of the 1-DOF setup of Pal and Soti (2025) is more than three times higher than that of the present 2-DOF

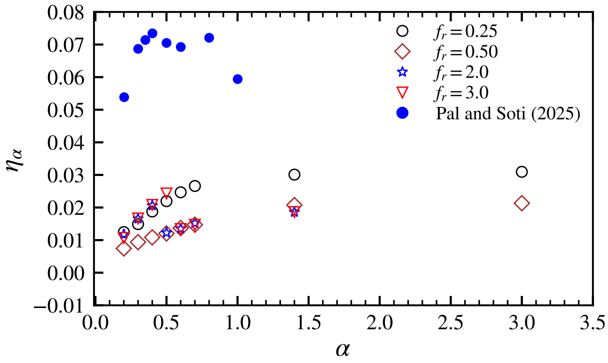

Fig. 7.13 Maximum efficiency with the variation of α at different f_r. Present 2-DOF efficiency data is compared with 1-DOF efficiency data at $\epsilon = 0.40$ at Re = 100 Pal and Soti (2025).

data. From Figure 7.13, $f_r = 0.25$ is preferable from an efficiency perspective, as it yields high efficiency across all α.

7.4 Summary

The present numerical study evaluates the effect of damping and frequency ratio (f_r) on flow characteristics and power extraction from an elliptical cylinder of constant $\epsilon = 0.40$. The f_r varies between 0.25 and 3.0, and the damping ratio between 0.02 and 0.30. The vibration amplitude and angular displacement decrease with damping. Maximum oscillation amplitudes are very close at $f_r = 0.25$, 2.0, and 3.0. However, angular displacement is higher for $f_r = 2.0$ and 3.0. Lower torsional spring frequencies (low stiffness) lead to higher rotational amplitudes, whereas variations in f_r do not significantly affect the transverse oscillation. The power from the transverse part is much higher (one order of magnitude) than the power from the rotational counterpart. It implies that power extraction from only transverse motion is enough, as power extraction arrangements from both motions are practically complex and, in this case, unnecessary. The drop in power at higher f_r suggests that higher stiffness is not practical for power generation across all damping levels. However, the maximum power and efficiency from the two-degree-of-freedom (2-DOF) arrangement is three times less than the power from a one-degree-of-freedom (1-DOF) arrangement of an elliptical cylinder. It means that the present 2-DOF arrangement is not feasible for power generation.

Chapter 8

Conclusions and scope for future work

This thesis investigates the flow characteristics and power extraction from multiple bluff bodies arranged in a rigidly coupled configuration under vortex-induced vibration (VIV). It also examines the power-generation potential of a single elliptical cylinder undergoing purely transverse motion as well as combined transverse and pitching motion. Based on the main findings of the study, the following conclusions are drawn (§ 8.1). In addition, key areas requiring further research to achieve a more complete understanding of the underlying interaction dynamics are outlined at the end of this chapter (§ 8.2).

8.1 Conclusions

We provided a detailed literature review of past work on wake-induced vibration, single-cylinder, and multiple-cylinder VIV to identify the research gap. We also demonstrated the effects of Reynolds number (Re), spacing, geometry, degree of freedom of the motion, and relative arrangements on VIV. The same parameters are also studied on power extraction from VIV. The studies in this thesis are solely based on numerical simulations at low Re. The details of the numerical framework in OpenFOAM are presented in great detail.

- The gap flow and shear layer interaction, not the location of mean separation points, influence the vibration amplitude and lift coefficient. The fluctuating pressure also influences the lift coefficient.

- Based on the phase difference three response branches (initial, upper, and lower) are observed even at low Re.
- The downstream cylinder primarily governs the wake characteristics.
- For the tandem configuration, three distinct wake regimes are identified at $L = 2.0$: overshoot mode (OS), alternate reattachment (AR), and continuous reattachment (CR). Increasing the spacing to $L = 3.0$ produces AR and co-shedding (CS), whereas at $L = 4.0$, the wake is dominated solely by the AR mode.
- In staggered cases, the wake exhibits an asymmetric shear layer at lower T and U^*, whereas a symmetric shear layer develops at higher T and U^*.
- For tandem cylinders, the extracted power increases with L, reaches a peak at an intermediate spacing, and decreases with further increase in L. The maximum extracted power is twice that of a single cylinder.
- If the cylinders are moving as a unit in tandem configuration, irrespective of the number of cylinders, the maximum power and amplitude can be expressed in terms of exponentially decaying functions of α.
- For multiple-cylinder power harvesters, power density, rather than efficiency, is the primary parameter for benchmarking.
- In the staggered case, for a fixed T, the maximum power varies inversely with L.
- Power generation correlates more strongly with the RMS of the cylinder velocity and total lift coefficient than with vibration amplitude for both arrangements (tandem and staggered).
- The optimal α for power generation for both arrangements lies within 0.2–0.48.
- Considering power output, efficiency, and cost, the most promising arrangement for the tandem case is $L = 3.0$, and for the staggered case, it is $L = 2.0, T = 3.0$, and $L = 3.0, T = 2.0$.
- The vibration amplitude increases significantly with decreasing aspect ratio (ϵ) of a one-degree-of-freedom (only transverse) elliptical cylinder.

- For both multiple circular (tandem) and single elliptical cylinders considered in the present study, the extracted power can be approximated using exponentially decaying functions of α. However, the maximum power $\bar{P}_\alpha$ differs with geometry.

- The maximum power has a non-monotonic relation with ϵ, with a peak at $\epsilon = 0.40$.

- For passive heaving and pitching of a single elliptical cylinder, we achieve a higher rotational amplitude at a lower frequency of the torsional spring (low stiffness), but changing the frequency ratio (transverse frequency/ torsional frequency) does not significantly affect the transverse oscillation.

- As the power from the transverse part is much higher (one order of magnitude) than the power from the rotational counterpart, only transverse motion is enough for power generation.

- The maximum power and efficiency from the two-degree-of-freedom (2-DOF) arrangement is three times less than that from a one-degree-of-freedom (1-DOF) arrangement of an elliptical cylinder. Therefore, the present 2-DOF arrangement is not feasible for power generation.

8.2 Scope of future work

This dissertation investigated the flow characteristics and power extraction performance of two rigidly coupled circular cylinders, as well as a transversely oscillating and 2-DOF single elliptic cylinder at low Reynolds numbers. These performance characteristics remain unexplored at high Reynolds numbers and in confined channels, which are essential for assessing their effectiveness in practical applications. Possible extensions of the present work are outlined below:

- The hysteresis analysis at low and high Re can be a good way to explain erratic behavior of some parameters at specific reduced velocities. Three-dimensional study should be invoked to investigate physical mechanism behind those behavior.

- The high Re simulation at confined channel can replicate practical situation in water tunnel. The experimental results can further verify simulation results. Moreover, the curve fit for power extraction proposed at low Re can also be extended to high Re situation.

- Highly turbulent flow can be used at inlet in numerical study to resemble the practical condition at rivers and oceans.

- Using numerical simulation and experimental data, mathematical model can be developed for multiple cylinder VIV. Moreover, machine learning techniques can be implemented to predict the amplitude response of multiple cylinder VIV.

- The flow dynamics in the combined heaving and pitching configuration of an elliptical cylinder may depend on the initial angular orientation of the ellipse. Investigating the effect of initial angular orientation on the VIV response and power extraction characteristics represents a valuable extension of the present work.

References

Alam, M. M., Moriya, M., Takai, K., and Sakamoto, H. (2003). Fluctuating fluid forces acting on two circular cylinders in a tandem arrangement at a subcritical Reynolds number. *Journal of Wind Engineering and Industrial Aerodynamics*, 91(1-2):139–154.

Alawadhi, E. M. (2015). Numerical simulation of flow past an elliptical cylinder undergoing rotationally oscillating motion. *Journal of Fluids Engineering, Transactions of the ASME*, 137(3):1–9.

Alias, F., Jusoh, M. A., Mohd, M. H., Kasiman, E. H., and Rahman, M. A. A. (2025). Investigation of Energy Harvesting from Vortex-Induced Vibrations : Numerical Study of Different Cylinder Arrangements. In *Proceedings of the Thirty-fifth (2025) International Ocean and Polar Engineering Conference*, pages 2942–2948.

Alias, F., Zailani, N., Mohd, M., Kasiman, E., and Rahman, M. (2024). Numerical Simulation on VIV Energy Harvesting of Four Cylinders in Close Staggered Formation with Different Mass Ratios. *Journal of Physics: Conference Series*, 2688(1):012007.

Alletto, M. (2022). Comparison of Overset Mesh with Morphing Mesh: Flow Over a Forced Oscillating and Freely Oscillating 2D Cylinder. *OpenFOAM® Journal*, 2(January):13–30.

Anagnostopoulos, P. and Bearman, P. W. (1992). Response characteristics of a vortex-excited cylinder at low reynolds numbers. *Journal of Fluids and Structures*, 6(1):39–50.

Assi, G. R., Meneghini, J. R., Aranha, J. A., Bearman, P. W., and Casaprima, E. (2006). Experimental investigation of flow-induced vibration interference between two circular cylinders. *Journal of Fluids and Structures*, 22(6-7):819–827.

Bao, Y., Huang, C., Zhou, D., Tu, J., and Han, Z. (2012). Two-degree-of-freedom flow-induced vibrations on isolated and tandem cylinders with varying natural frequency ratios. *Journal of Fluids and Structures*, 35(800):50–75.

Bao, Y., Zhou, D., and Tu, J. (2013). Flow characteristics of two in-phase oscillating cylinders in side-by-side arrangement. *Computers and Fluids*, 71:124–145.

Barrero-Gil, A., Pindado, S., and Avila, S. (2012). Extracting energy from Vortex-Induced Vibrations: A parametric study. *Applied Mathematical Modelling*, 36(7):3153–3160.

Bathe, K. (2014). *Finite Element Procedures*. Prentice Hall, Pearson Education, Inc., Watertown, MA, second edition.

Beal, D. N., Hover, F. S., Triantafyllou, M. S., Liao, J. C., and Lauder, G. V. (2006). Passive propulsion in vortex wakes. *Journal of Fluid Mechanics*, 549:385–402.

Bearman, P. W. (1984). Vortex shedding from oscillation bluff bodies. *Annual Review of Fluid Mechanics*, 16:195–222.

Bernitsas, M. M., Raghavan, K., Ben-Simon, Y., and Garcia, E. M. (2008). VIVACE (Vortex Induced Vibration Aquatic Clean Energy): A new concept in generation of clean and renewable energy from fluid flow. *Journal of Offshore Mechanics and Arctic Engineering*, 130(4):1–19.

Bhattacharya, A. and Shahajhan, S. S. (2016). Power extraction from vortex-induced angular oscillations of elliptical cylinder. *Journal of Fluids and Structures*, 63:140–154.

Bishop, R. E. D., Hassan, A. Y., and Saunders, O. A. (1964). The lift and drag forces on a circular cylinder oscillating in a flowing fluid. *Proceedings of the Royal Society of London. Series A. Mathematical and Physical Sciences*, 277(1368):51–75.

Blackburn, H. M. and Karniadakis, G. E. (1993). Two- and Three-dimensional simulations of vortex-induced vibration of a circular cylinder. In *Proceedings of the Third (1993) International Offshore and Polar Engineering Conference*, volume 3, pages 715–720.

Blevins, R. D. (1977). Flow-induced vibration. *New York*.

Bokaian, A. and Geoola, F. (1984). Proximity-induced galloping of two interfering circular cylinders. *Journal of Fluid Mechanics*, 146:417–449.

Borazjani, I. and Sotiropoulos, F. (2009). Vortex-induced vibrations of two cylinders in tandem arrangement in the proximity - Wake interference region. *Journal of Fluid Mechanics*, 621:321–364.

Boudreau, M., Gunther, K., and Dumas, G. (2019). Investigation of the energy-extraction regime of a novel semi-passive flapping-foil turbine concept with a prescribed heave motion and a passive pitch motion. *Journal of Fluids and Structures*, 84:368–390.

Brooks, P. N. H. (1960). *Experimental investigation of the aeroelastic instability of bluff two-dimensional cylinders*. PhD thesis, University of British Columbia.

Carmo, B. S., Sherwin, S. J., Bearman, P. W., and Willden, R. H. (2008). Wake transition in the flow around two circular cylinders in staggered arrangements. *Journal of Fluid Mechanics*, 597:1–29.

Celik, I. B., Ghia, U., Roache, P. J., Freitas, C. J., Coleman, H., and Raad, P. E. (2008). Procedure for estimation and reporting of uncertainty due to discretization in CFD applications. *Journal of Fluids Engineering, Transactions of the ASME*, 130(7):0780011–0780014.

Chang, C. C., Ajith Kumar, R., and Bernitsas, M. M. (2011). VIV and galloping of single circular cylinder with surface roughness at $3.0 \times 10^4 \leq \mathrm{Re} \leq 1.2 \times 10^5$. *Ocean Engineering*, 38(16):1713–1732.

Chen, W., Ji, C., Williams, J., Xu, D., Yang, L., and Cui, Y. (2018). Vortex-induced vibrations of three tandem cylinders in laminar cross-flow: Vibration response and galloping mechanism. *Journal of Fluids and Structures*, 78:215–238.

Chen, W., Ji, C., Xu, D., An, H., and Zhang, Z. (2020). Flow-induced vibrations of two side-by-side circular cylinders at low Reynolds numbers. *Physics of Fluids*, 32(2).

Chen, W., Ji, C., Xu, D., and Srinil, N. (2019). Wake patterns of freely vibrating side-by-side circular cylinders in laminar flows. *Journal of Fluids and Structures*, 89:82–95.

Chen, Z., Sun, Y., Liu, Q., Zhao, J., An, L., and Guo, P. (2024). Vortex-induced vibrations of three rigidly coupled circular cylinders in an equilateral-triangular arrangement. *Physics of Fluids*, 36(10).

Chen, Z., Sun, Y., Liu, Q., Zhao, J., An, L., and Guo, P. (2025). Effect of the spacing ratio on vortex-induced vibration of three rigidly coupled cylinders in an equilateral-triangular arrangement. *Physics of Fluids*, 37(10).

Dean, R., Milligan, R., and Wootton, L. (1977). An experimental study of flow-induced vibration. *EEC Report*, 4.

Ding, L., Bernitsas, M. M., and Kim, E. S. (2013). 2-D URANS vs. experiments of flow induced motions of two circular cylinders in tandem with passive turbulence control for $30{,}000 < \mathrm{Re} < 105{,}000$. *Ocean Engineering*, 72:429–440.

Ding, L., Zhang, L., Bernitsas, M. M., and Chang, C. C. (2016). Numerical simulation and experimental validation for energy harvesting of single-cylinder VIVACE converter with passive turbulence control. *Renewable Energy*, 85:1246–1259.

Ding, L., Zhang, L., Kim, E. S., and Bernitsas, M. M. (2015a). URANS vs. experiments of flow induced motions of multiple circular cylinders with passive turbulence control. *Journal of Fluids and Structures*, 54:612–628.

Ding, L., Zhang, L., Wu, C., Mao, X., and Jiang, D. (2015b). Flow induced motion and energy harvesting of bluff bodies with different cross sections. *Energy Conversion and Management*, 91:416–426.

Ding, L., Zou, Q., Zhang, L., and Wang, H. (2018). Research on Flow-Induced Vibration and Energy Harvesting of Three Circular Cylinders with Roughness Strips in Tandem. *Energies*, 11(11).

Ding, W., Sun, H., Xu, W., and Bernitsas, M. M. (2019). Numerical investigation on interactive FIO of two-tandem cylinders for hydrokinetic energy harnessing. *Ocean Engineering*, 187(May):106215.

Dowell, E. H. (2021). *A modern course in aeroelasticity*, volume 264. Springer Nature.

Dumas, G. and Kinsey, T. (2006). Eulerian simulations of oscillating airfoils in power extraction regime. *WIT Transactions on Engineering Sciences*, 52:245–254.

Feng, C. (1968). *The measurement of vortex induced effects in flow past stationary and oscillating circular and d-section cylinders*. PhD thesis, National Taiwan University.

Gabbai, R. D. and Benaroya, H. (2005). An overview of modeling and experiments of vortex-induced vibration of circular cylinders. *Journal of Sound and Vibration*, 282(3-5):575–616.

Gao, Y., Yang, B., Zhu, H., Peng, G., Zhang, Z., and Pan, G. (2022). Numerical simulation of flow induced vibration of two rigidly connected cylinders in different arrangements. *Ships and Offshore Structures*, 17(5):1142–1158.

Gao, Y., Yang, K., Zhang, B., Cheng, K., and Chen, X. (2019). Numerical investigation on vortex-induced vibrations of four circular cylinders in a square configuration. *Ocean Engineering*, 175(February):223–240.

Gao, Y., Zhang, Y., Zhao, M., and Wang, L. (2020). Numerical investigation on two degree-of-freedom flow-induced vibration of three tandem cylinders. *Ocean Engineering*, 201(May 2019):107059.

Gharib, M. R. (1999). *Vortex-induced vibration, absence of lock-in and fluid force deduction*. PhD thesis, California Institute of Technology.

Govardhan, R. and Williamson, C. H. (2000). Modes of vortex formation and frequency response of a freely vibrating cylinder. *Journal of Fluid Mechanics*, 420:85–130.

Govardhan, R. and Williamson, C. H. (2002). Resonance forever: Existence of a critical mass and an infinite regime of resonance in vortex-induced vibration. *Journal of Fluid Mechanics*, 473:147–166.

Govardhan, R. N. and Williamson, C. H. K. (2006). Defining the 'modified Griffin plot' in vortex-induced vibration: revealing the effect of Reynolds number using controlled damping. *Journal of Fluid Mechanics*, 561:147–180.

Griffin, O. M. and Ramberg, S. E. (1982). Some recent studies of vortex shedding with application to marine tubuiars and risers. *Journal of Energy Resources Technology, Transactions of the ASME*, 104(1):2–13.

Griffith, M. D., Jacono, D. L., Sheridan, J., and Leontini, J. S. (2017). Flow-induced vibration of two cylinders in tandem and staggered arrangements. *Journal of Fluid Mechanics*, 833:98–130.

Griffith, M. D., Lo Jacono, D., Sheridan, J., and Leontini, J. S. (2016). Passive heaving of elliptical cylinders with active pitching – From cylinders towards flapping foils. *Journal of Fluids and Structures*, 67:124–141.

Gu, M., Song, B., Zhang, B., Mao, Z., and Tian, W. (2020). The effects of submergence depth on Vortex-Induced Vibration (VIV) and energy harvesting of a circular cylinder. *Renewable Energy*, 151:931–945.

Hairer, E. (2006). *Geometric Numerical Integration*, volume 3 of *Springer Series in Computational Mathematics*. Springer-Verlag, Berlin/Heidelberg.

Han, P., De Langre, E., Thompson, M. C., Hourigan, K., and Zhao, J. (2023). Vortex-induced vibration forever even with high structural damping. *Journal of Fluid Mechanics*, 962:1–16.

Han, P., Pan, G., and Tian, W. (2018). Numerical simulation of flow-induced motion of three rigidly coupled cylinders in equilateral-triangle arrangement. *Physics of Fluids*, 30(12).

Han, P., Pan, G., Zhang, B., Wang, W., and Tian, W. (2020). Three-cylinder oscillator under flow: Flow induced vibration and energy harvesting. *Ocean Engineering*, 211(June):107619.

Han, X., Lin, W., Zhang, X., Tang, Y., and Zhao, C. (2016). Two degree of freedom flow-induced vibration of cylindrical structures in marine environments: frequency ratio effects. *Journal of Marine Science and Technology (Japan)*, 21(3):479–492.

Hodges, D. H. and Pierce, G. A. (2011). *Introduction to structural dynamics and aeroelasticity*, volume 15. cambridge university press.

Hover, F. and Triantafyllou, M. (2001). Galloping response of a cylinder with upstream wake interference. *Journal of Fluids and Structures*, 15(3):503–512.

Hover, F. S., Techet, A. H., and Triantafyllou, M. S. (1998). Forces on oscillating uniform and tapered cylinders in crossflow. *Journal of Fluid Mechanics*, 363:97–114.

Huera-Huarte, F. J. and Gharib, M. (2011). Flow-induced vibrations of a side-by-side arrangement of two flexible circular cylinders. *Journal of Fluids and Structures*, 27(3):354–366.

Huera-Huarte, F. J. and Jiménez-González, J. I. (2019). Effect of diameter ratio on the flow-induced vibrations of two rigidly coupled circular cylinders in tandem. *Journal of Fluids and Structures*, 89:96–107.

Hughes J R, T. (1987). The Finite Element Method: Linear Static and Dynamic Finite Element Analysis.

Ji, C., Xu, W., Sun, H., Wang, R., Ma, C., and Bernitsas, M. M. (2018). Interactive flow-induced vibrations of two staggered, low mass-ratio cylinders in the TrSL3 flow regime ($2.5\times10^4 < Re < 1.2 \times 10^5$): Smooth cylinders. *Journal of Offshore Mechanics and Arctic Engineering*, 140(4):1–9.

Johnson, A. A. and Tezduyar, T. E. (1994). Mesh update strategies in parallel finite element computations of flow problems with moving boundaries and interfaces. *Computer Methods in Applied Mechanics and Engineering*, 119(1-2):73–94.

Kang, Z. and Jia, L. (2013). An experiment study of a cylinder's two degree of freedom VIV trajectories. *Ocean Engineering*, 70:129–140.

Kenneth Levenberg (1944). a Method for the Solution of Certain Non-Linear Problems in Least Squares. *Quarterly of Applied Mathematics*, 2(2):164–168.

Khalak, A. and Williamson, C. H. (1996). Dynamics of a hydroelastic cylinder with very low mass and damping. *Journal of Fluids and Structures*, 10(5):455–472.

Khalak, A. and Williamson, C. H. (1999). Motions, Forces and Mode Transitions in Vortex-Induced Vibrations At Low Mass-Damping. *Journal of Fluids and Structures*, 13(7-8):813–851.

Kim, E. S. and Bernitsas, M. M. (2016). Performance prediction of horizontal hydrokinetic energy converter using multiple-cylinder synergy in flow induced motion. *Applied Energy*, 170:92–100.

Kim, E. S., Bernitsas, M. M., and Ajith Kumar, R. (2013). Multicylinder flow-induced motions: Enhancement by passive turbulence control at 28,000 $<$ Re $<$ 120,000. *Journal of Offshore Mechanics and Arctic Engineering*, 135(2).

Kim, E. S., Sun, H., Park, H., chul Shin, S., Chae, E. J., Ouderkirk, R., and Bernitsas, M. M. (2021). Development of an alternating lift converter utilizing flow-induced oscillations to harness horizontal hydrokinetic energy. *Renewable and Sustainable Energy Reviews*, 145(September 2020):111094.

Kim, M.-S. and Park, Y.-B. (2006). Unsteady lift and drag forces acting on the elliptic cylinder. *Journal of Mechanical Science and Technology*, 20(1):167–175.

Kim, S. and Alam, M. M. (2015). Characteristics and suppression of flow-induced vibrations of two side-by-side circular cylinders. *Journal of Fluids and Structures*, 54:629–642.

Kim, S., Alam, M. M., Sakamoto, H., and Zhou, Y. (2009). Flow-induced vibrations of two circular cylinders in tandem arrangement. Part 1: Characteristics of vibration. *Journal of Wind Engineering and Industrial Aerodynamics*, 97(5-6):304–311.

King, R. (1975). *Vortex excited structural oscillations of a circular cylinder in flowing water*. PhD thesis, Loughborough University.

King, R. and Johns, D. J. (1976). Wake interaction experiments with two flexible circular cylinders in flowing water. *Journal of Sound and Vibration*, 45(2):259–283.

Kinsey, T. and Dumas, G. (2008). Parametric study of an oscillating airfoil in a power-extraction regime. *AIAA Journal*, 46(6):1318–1330.

Kinsey, T. and Dumas, G. (2012). Optimal tandem configuration for oscillating-foils hydrokinetic turbine. *Journal of Fluids Engineering, Transactions of the ASME*, 134(3).

Klamo, J. T., Leonard, A., and Roshko, A. (2006). The effects of damping on the amplitude and frequency response of a freely vibrating cylinder in cross-flow. *Journal of Fluids and Structures*, 22(6-7):845–856.

Kumar, R. A., Sohn, C. H., and Gowda, B. H. (2009). Influence of corner radius on the near wake structure of a transversely oscillating square cylinder. *Journal of Mechanical Science and Technology*, 23(9):2390–2416.

Lam, K. M. and To, A. P. (2003). Interference effect of an upstream larger cylinder on the lock-in vibration of a flexibly mounted circular cylinder. *Journal of Fluids and Structures*, 17(8):1059–1078.

Lee, J. H. and Bernitsas, M. M. (2011). High-damping, high-Reynolds VIV tests for energy harnessing using the VIVACE converter. *Ocean Engineering*, 38(16):1697–1712.

Lelieveld, J., Klingmüller, K., Pozzer, A., Burnett, R., Haines, A., and Ramanathan, V. (2019). Effects of fossil fuel and total anthropogenic emission removal on public health and climate. *Proceedings of the National Academy of Sciences*, 116(15):7192–7197.

Leontini, J. S., Griffith, M. D., Lo Jacono, D., and Sheridan, J. (2018). The flow-induced vibration of an elliptical cross-section at varying angles of attack. *Journal of Fluids and Structures*, 78:356–373.

Leontini, J. S., Thompson, M. C., and Hourigan, K. (2006). The beginning of branching behaviour of vortex-induced vibration during two-dimensional flow. *Journal of Fluids and Structures*, 22(6-7):857–864.

Leontini, J. S., Thompson, M. C., and Hourigan, K. (2007). Three-dimensional transition in the wake of a transversely oscillating cylinder. *Journal of Fluid Mechanics*, 577:79–104.

Li, H., Bernitsas, C. C., Congpuong, N., Bernitsas, M. M., and Sun, H. (2024). Experimental investigation on synergistic flow-induced oscillation of three rough tandem-cylinders in hydrokinetic energy conversion. *Applied Energy*, 359(December 2023):122587.

Li, M., Bernitsas, C. C., Guo, J., and Sun, H. (2021). Synergistic flow-induced oscillation of multiple cylinders in harvesting marine hydrokinetic energy. *Journal of Offshore Mechanics and Arctic Engineering*, 143(3).

Liao, J. C., Beal, D. N., Lauder, G. V., and Triantafyllou, M. S. (2003). Fish Exploiting Vortices Decrease Muscle Activity. *Science*, 302(5650):1566–1569.

Liu, D., Sun, H., Lin, H., Miao, J., and Liu, H. (2025). Vortex-induced vibration and energy harvesting in tandem three cylinders with different spacing ratios. *Physics of Fluids*, 37(1).

Löhner, R. and Yang, C. (1996). Improved ALE mesh velocities for moving bodies. *Communications in Numerical Methods in Engineering*, 12(10):599–608.

Looney, B. (2020). Statistical review of world energy, 2020.

Lugt, H. J. (1983). Autorotation. *Annual Review of Fluid Mechanics*, 15:123–147.

Marquardt, D. W. (1963). An algorithm for least-squares estimation of nonlinear parameters. *Journal of the Society for Industrial and Applied Mathematics*, 11(2):431–441.

Moe, G. and Wu, Z. J. (1990). The lift force on a cylinder wibrating in a current. *Journal of Offshore Mechanics and Arctic Engineering*, 112(4):297–303.

Moukalled, F., Mangani, L., and Darwish, M. (2016). *The Finite Volume Method in Computational Fluid Dynamics*, volume 113 of *Fluid Mechanics and Its Applications*. Springer International Publishing.

Mumtaz Qadri, M. N., Zhao, F., and Tang, H. (2020). Fluid-structure interaction of a fully passive flapping foil for flow energy extraction. *International Journal of Mechanical Sciences*, 177(March):105587.

Munir, A., Zhao, M., Wu, H., and Lu, L. (2019). Effects of gap ratio on flow-induced vibration of two rigidly coupled side-by-side cylinders. *Journal of Fluids and Structures*, 91:102726.

Narendran, K., Murali, K., and Sundar, V. (2016). Investigations into efficiency of vortex induced vibration hydro-kinetic energy device. *Energy*, 109:224–235.

Naudascher, E. (2017). *Flow-induced vibrations: an engineering guide: IAHR hydraulic structures design manuals 7*. Routledge.

Navrose, Yogeswaran, V., Sen, S., and Mittal, S. (2014). Free vibrations of an elliptic cylinder at low Reynolds numbers. *Journal of Fluids and Structures*, 51:55–67.

Nepali, R., Han, Z., Zhou, D., and Kushwaha, V. (2020). 2-DOF vortex-induced vibration of two tandem square cylinders with varying natural frequency ratios. *IOP Conference Series: Earth and Environmental Science*, 446(5).

Newman, D. and Karniadakis, G. E. (1996). Simulations of flow over a flexible cable: A comparison of forced and flow-induced vibration. *Journal of Fluids and Structures*, 10(5):439–453.

Païdoussis, M. P., Price, S. J., and De Langre, E. (2010). *Fluid-structure interactions: cross-flow-induced instabilities*. Cambridge University Press.

Pal, A. and Soti, A. K. (2025). The effect of damping and aspect ratio on power extraction from vortex-induced vibration of elliptical cylinder. *Physics of Fluids*, 37(2).

Papaioannou, G. V., Yue, D. K., Triantafyllou, M. S., and Karniadakis, G. E. (2008). On the effect of spacing on the vortex-induced vibrations of two tandem cylinders. *Journal of Fluids and Structures*, 24(6):833–854.

Parkinson, G. V. (1971). Wind-induced instability of structures. *Philosophical Transactions of the Royal Society of London. Series A, Mathematical and Physical Sciences*, 269(1199):395–413.

Patton, K. T. (1965). *An experimental determination of hydrodynamic masses and mechanical impedances*. PhD thesis, University of Rhode Island.

Peng, Z. and Zhu, Q. (2009). Energy harvesting through flow-induced oscillations of a foil. *Physics of Fluids*, 21(12):1–9.

Pesce, C. and Fujarra, A. (2000). Vortex-induced vibrations and jump phenomenon: Experiments with a clamped flexible cylinder in water. *International Journal of Offshore and Polar Engineering*, 10(01).

Piperno, S., Farhat, C., and Larrouturou, B. (1995). Partitioned procedures for the transient solution of coupled aroelastic problems Part I: Model problem, theory and two-dimensional application. *Computer Methods in Applied Mechanics and Engineering*, 124(1-2):79–112.

Prasanth, T. K. and Mittal, S. (2009a). Flow-induced oscillation of two circular cylinders in tandem arrangement at low Re. *Journal of Fluids and Structures*, 25(6):1029–1048.

Prasanth, T. K. and Mittal, S. (2009b). Vortex-induced vibration of two circular cylinders at low Reynolds number. *Journal of Fluids and Structures*, 25(4):731–741.

Qin, B., Alam, M. M., and Zhou, Y. (2017). Two tandem cylinders of different diameters in cross-flow: Flow-induced vibration. *Journal of Fluid Mechanics*, 829:621–658.

Raghavan, K. and Bernitsas, M. M. (2011). Experimental investigation of Reynolds number effect on vortex induced vibration of rigid circular cylinder on elastic supports. *Ocean Engineering*, 38(5-6):719–731.

Rostami, A. B. and Armandei, M. (2017). Renewable energy harvesting by vortex-induced motions: Review and benchmarking of technologies. *Renewable and Sustainable Energy Reviews*, 70:193–214.

Ryzhakov, P. B., Rossi, R., Idelsohn, S. R., and Oñate, E. (2010). A monolithic Lagrangian approach for fluid-structure interaction problems. *Computational Mechanics*, 46(6):883–899.

Sanaati, B. and Kato, N. (2014). A study on the proximity interference and synchronization between two side-by-side flexible cylinders. *Ocean Engineering*, 85:65–79.

Sarpkaya, T. (1978). Fluid forces on oscillating cylinders. *Journal of the Waterway, Port, Coastal and Ocean Division*, 104(3):275–290.

Sarpkaya, T. (1995). Hydrodynamic damping, flow-induced oscillations, and biharmonic response. *Proceedings of the International Conference on Offshore Mechanics and Arctic Engineering - OMAE*, 1(Part A):433–441.

Sarpkaya, T. (2004). A critical review of the intrinsic nature of vortex-induced vibrations. *Journal of Fluids and Structures*, 19(4):389–447.

Scanlan, R. H. and Tomko, J. J. (1971). Airfoil and bridge deck flutter derivatives. *Journal of the Engineering Mechanics Division*, 97(6):1717–1737.

Scruton, C. (1970). Wind effects on structures. *Proceedings of the Institution of Mechanical Engineers*, 185(1):301–317.

Sen, S. and Mittal, S. (2011). Free vibration of a square cylinder at low Reynolds numbers. *Journal of Fluids and Structures*, 27(5-6):875–884.

Sharma, G. and Bhardwaj, R. (2023). Flow-induced vibrations of elastically coupled tandem cylinders. *Journal of Fluid Mechanics*, 976:1–51.

Shiels, D., Leonard, A., and Roshko, A. (2001). Flow-induced vibration of a circular cylinder at limiting structural parameters. *Journal of Fluids and Structures*, 15:575–585.

Simpson, B. J., Hover, F. S., and Triantafyllou, M. S. (2008). Experiments in direct energy extraction through flapping foils. In *ISOPE International Ocean and Polar Engineering Conference*, pages ISOPE–I. ISOPE.

Singh, S. and Mittal, S. (2005). Vortex-induced oscillations at low Reynolds numbers: Hysteresis and vortex-shedding modes. *Journal of Fluids and Structures*, 20(8):1085–1104.

Soti, A. K. and De, A. (2020). Vortex-induced vibrations of a confined circular cylinder for efficient flow power extraction. *Physics of Fluids*, 32(3).

Soti, A. K., Thompson, M. C., Sheridan, J., and Bhardwaj, R. (2017). Harnessing electrical power from vortex-induced vibration of a circular cylinder. *Journal of Fluids and Structures*, 70(February):360–373.

Soti, A. K., Zhao, J., Thompson, M. C., Sheridan, J., and Bhardwaj, R. (2018). Damping effects on vortex-induced vibration of a circular cylinder and implications for power extraction. *Journal of Fluids and Structures*, 81:289–308.

Sourav, K., Kumar, D., and Sen, S. (2020). Vortex-induced vibrations of an elliptic cylinder of low mass ratio: Identification of new response branches. *Physics of Fluids*, 32(2).

Sovacool, B. K., Andersen, R., Sorensen, S., Sorensen, K., Tienda, V., Vainorius, A., Schirach, O. M., and Bjørn-Thygesen, F. (2016). Balancing safety with sustainability: Assessing the risk of accidents for modern low-carbon energy systems. *Journal of Cleaner Production*, 112:3952–3965.

Su, Y., Di, J., Li, S., Jian, B., and Liu, J. (2022). Buffeting Response Prediction of Long-Span Bridges Based on Different Wind Tunnel Test Techniques. *Applied Sciences (Switzerland)*, 12(6).

Sumner, D., Price, S. J., and Païdoussis, M. P. (2000). Flow-pattern identification for two staggered circular cylinders in cross-flow. *Journal of Fluid Mechanics*, 411:263–303.

Sun, H., Bernitsas, M. M., and Turkol, M. (2020). Adaptive harnessing damping in hydrokinetic energy conversion by two rough tandem-cylinders using flow-induced vibrations. *Renewable Energy*, 149:828–860.

Sun, H., Kim, E. S., Nowakowski, G., Mauer, E., and Bernitsas, M. M. (2016). Effect of mass-ratio, damping, and stiffness on optimal hydrokinetic energy conversion of a single, rough cylinder in flow induced motions. *Renewable Energy*, 99:936–959.

Sun, H., Ma, C., Kim, E. S., Nowakowski, G., Mauer, E., and Bernitsas, M. M. (2017). Hydrokinetic energy conversion by two rough tandem-cylinders in flow induced motions: Effect of spacing and stiffness. *Renewable Energy*, 107:61–80.

Sun, H., Ma, C., Kim, E. S., Nowakowski, G., Mauer, E., and Bernitsas, M. M. (2019). Flow-induced vibration of tandem circular cylinders with selective roughness: Effect of spacing, damping and stiffness. *European Journal of Mechanics, B/Fluids*, 74:219–241.

Techet, A. H., Allen, J. J., and Smits, A. J. (2002). Piezoelectric Eels for Energy Harvesting in the Ocean. *Proceedings of the International Offshore and Polar Engineering Conference*, 12(October):713–718.

Teixeira, P. and Awruch, A. (2005). Numerical simulation of fluid–structure interaction using the finite element method. *Computers and Fluids*, 34(2):249–273.

Thompson, M. C., Radi, A., Rao, A., Sheridan, J., and Hourigan, K. (2014). Low-Reynolds-number wakes of elliptical cylinders: from the circular cylinder to the normal flat plate. *Journal of Fluid Mechanics*, 751:570–600.

Vickery, B. and Watkins, R. (1964). Flow-induced vibration of cylindrical structures. In SILVESTER, R., editor, *Hydraulics and Fluid Mechanics*, pages 213–241. Pergamon.

Vijay, K., Srinil, N., Zhu, H., Bao, Y., Zhou, D., and Han, Z. (2020). Flow-induced transverse vibration of an elliptical cylinder with different aspect ratios. *Ocean Engineering*, 214(January):107831.

Wang, H., Zhai, Q., and Chen, K. (2019). Vortex-induced vibrations of an elliptic cylinder with both transverse and rotational degrees of freedom. *Journal of Fluids and Structures*, 84:36–55.

Wang, J., Zhao, W., Su, Z., Zhang, G., Li, P., and Yurchenko, D. (2020). Enhancing vortex-induced vibrations of a cylinder with rod attachments for hydrokinetic power generation. *Mechanical Systems and Signal Processing*, 145:106912.

Wang, Y., Xu, F., and Zhang, Z. (2025). Flow-induced vibrations of staggered circular cylinders. *Physics of Fluids*, 37(1).

Wang, Z., Du, L., Zhao, J., and Sun, X. (2017). Structural response and energy extraction of a fully passive flapping foil. *Journal of Fluids and Structures*, 72:96–113.

Williamson, C. H. and Govardhan, R. (2004). Vortex-induced vibrations. *Annu. Rev. Fluid Mech.*, 36:413–455.

Williamson, C. H. and Roshko, A. (1988). Vortex formation in the wake of an oscillating cylinder. *Journal of Fluids and Structures*, 2(4):355–381.

Wu, Y., Cheng, Z., McConkey, R., Lien, F. S., and Yee, E. (2022). Modelling of Flow-Induced Vibration of Bluff Bodies: A Comprehensive Survey and Future Prospects. *Energies*, 15(22).

Xu, W., Cheng, A., Ma, Y., and Gao, X. (2018a). Multi-mode flow-induced vibrations of two side-by-side slender flexible cylinders in a uniform flow. *Marine Structures*, 57(November 2017):219–236.

Xu, W., Ji, C., Sun, H., Ding, W., and Bernitsas, M. M. (2018b). Flow-induced vibration and hydrokinetic power conversion of two staggered rough cylinders for 2.5 $\times$ 104 < Re < 1.2 $\times$ 105. *Journal of Offshore Mechanics and Arctic Engineering*, 140(2):1–8.

Xu, W., Ji, C., Sun, H., Ding, W., and Bernitsas, M. M. (2019). Flow-induced vibration of two elastically mounted tandem cylinders in cross-flow at subcritical Reynolds numbers. *Ocean Engineering*, 173(January 2018):375–387.

Xu, W., Zhang, Q., Lai, J., Wang, Q., and Yu, Y. (2020). Flow-induced vibration of two staggered flexible cylinders with unequal diameters. *Ocean Engineering*, 211:107523.

Young, J., Ashraf, M. A., Lai, J. C., and Platzer, M. F. (2013). Numerical simulation of fully passive flapping foil power generation. *AIAA Journal*, 51(11):2727–2739.

Zdravkovich, M. (1988). Review of interference-induced oscillations in flow past two parallel circular cylinders in various arrangements. *Journal of Wind Engineering and Industrial Aerodynamics*, 28(1-3):183–199.

Zdravkovich, M. M. and Medeiros, E. B. (1991). Effect of damping on interference-induced oscillations of two identical circular cylinders. *Journal of Wind Engineering and Industrial Aerodynamics*, 38(2-3):197–211.

Zeng, L., Zhao, F., Wang, H., Liu, Y., and Tang, H. (2023). Control of flow-induced vibration of a circular cylinder using a splitter plate. *Physics of Fluids*, 35(8).

Zhang, B., Mao, Z., Song, B., Ding, W., and Tian, W. (2018a). Numerical investigation on effect of damping-ratio and mass-ratio on energy harnessing of a square cylinder in FIM. *Energy*, 144:218–231.

Zhang, B., Mao, Z., Song, B., Tian, W., and Ding, W. (2018b). Numerical investigation on VIV energy harvesting of four cylinders in close staggered formation. *Ocean Engineering*, 165(January):55–68.

Zhang, B., Song, B., Mao, Z., Tian, W., and Li, B. (2017). Numerical investigation on VIV energy harvesting of bluff bodies with different cross sections in tandem arrangement. *Energy*, 133:723–736.

Zhang, J., Wang, F., Zhang, J., Chen, D., and Liu, Z. (2023). Vortex-induced vibration characteristics of three cylinders with isosceles-triangle arrangements at low Reynolds number. *Physics of Fluids*, 35(12).

Zhao, F., Mumtaz Qadri, M. N., Wang, Z., and Tang, H. (2021). Flow-energy harvesting using a fully passive flapping foil: A guideline on design and operation. *International Journal of Mechanical Sciences*, 197(November 2020):106323.

Zhao, J., Hourigan, K., and Thompson, M. C. (2018). Flow-induced vibration of D-section cylinders: An afterbody is not essential for vortex-induced vibration. *Journal of Fluid Mechanics*, 851:317–343.

Zhao, J., Hourigan, K., and Thompson, M. C. (2019). Dynamic response of elliptical cylinders undergoing transverse flow-induced vibration. *Journal of Fluids and Structures*, 89:123–131.

Zhao, M. (2013). Flow induced vibration of two rigidly coupled circular cylinders in tandem and side-by-side arrangements at a low reynolds number of 150. *Physics of Fluids*, 25(12).

Zhao, M., Cheng, L., An, H., and Lu, L. (2014). Three-dimensional numerical simulation of vortex-induced vibration of an elastically mounted rigid circular cylinder in steady current. *Journal of Fluids and Structures*, 50:292–311.

Zhao, M., Murphy, J. M., and Kwok, K. (2016). Numerical simulation of vortex-induced vibration of two rigidly connected cylinders in side-by-side and tandem arrangements using RANS model. *Journal of Fluids Engineering, Transactions of the ASME*, 138(2):1–13.

Zhao, M., Tong, F., and Cheng, L. (2012). Numerical Simulation of Two-Degree-of-Freedom Vortex-Induced Vibration of a Circular Cylinder Between Two Lateral Plane Walls in Steady Currents. *Journal of Fluids Engineering*, 134(10):1–5.

Zhu, H., Zhang, X., Gao, Y., Ding, L., and Zhou, T. (2025). Vortex-induced vibration and wake interference of two rigidly connected tandem cylinders. *Physics of Fluids*, 37(4).

Zhu, H., Zhong, J., Shao, Z., Zhou, T., and Alam, M. M. (2024). Fluid-structure interaction among three tandem circular cylinders oscillating transversely at a low Reynolds number of 150. *Journal of Fluids and Structures*, 130:104204.

Zhu, Q. (2012). Energy harvesting by a purely passive flapping foil from shear flows. *Journal of Fluids and Structures*, 34:157–169.

Zhu, Q., Wolfgang, M. J., Yue, D. K., and Triantafyllou, M. S. (2002). Three-dimensional flow structures and vorticity control in fish-like swimming. *Journal of Fluid Mechanics*, 468:1–28.

Appendix A

Detailed mesh view

Figure A.1 shows the computational mesh around the cylinder for a tandem case at $L = 2.0$. A radially structured mesh is used up to $0.9D$, followed by a uniform unstructured mesh with $\Delta x = 0.08$. Figure A.2 presents the mesh for the staggered case at $L = 2.0, T = 3.0$, where the near-wall region is similarly structured up to $0.9D$, beyond which a uniform unstructured mesh of $\Delta x = 0.16$ is applied.

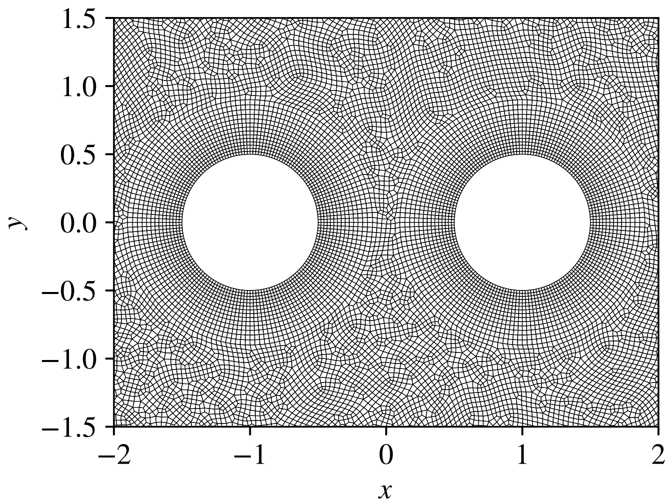

Fig. A.1 Zoomed-in view of the mesh around the cylinders at $L = 2.0$

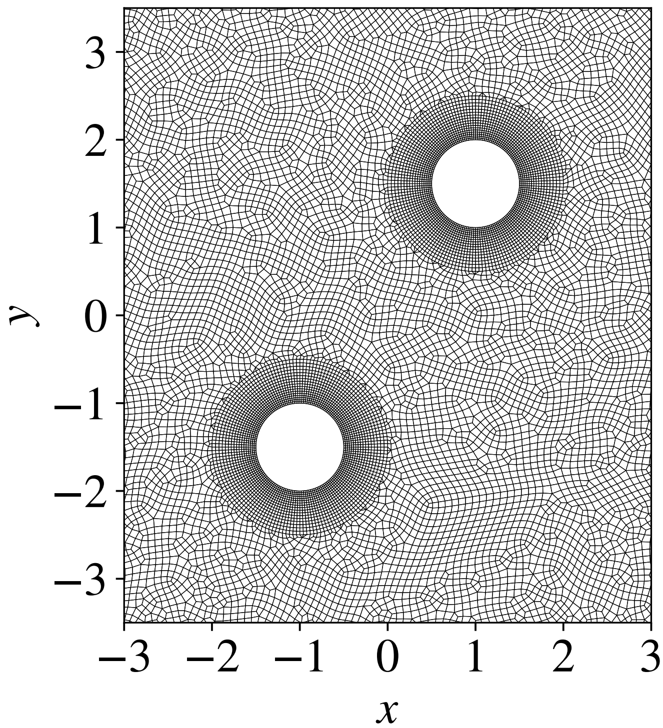

Fig. A.2 Detailed view of the computational mesh around the cylinders at $L = 2.0, T = 3.0$.

Appendix B

Temporal independence study

A temporal independence study is performed for a representative tandem case with $L = 6.0$ and $U^{=}7.5$ at $\zeta = 0$. The time step (Δt) is varied between 0.016 and 0.001. Table B.1 presents the temporal independence data of the vibration amplitude (A^*). The relative errors are computed with respect to $\Delta t = 0.001$. It is observed that the change in A^* between $\Delta t = 0.004$ and $\Delta t = 0.002$ is less than 0.5%. Therefore, $\Delta t = 0.002$ is adopted as the time step for the present study.

Table B.1 Temporal independence study at $U^* = 7.5$ for $L = 6.0$ under zero damping condition

Time-step (Δt)	**Vibration amplitude (A^*)**	**Error in A^*(%)**
0.016	0.828	1.595
0.008	0.823	0.981
0.004	0.819	0.491
0.002	0.817	0.245
0.001	0.815	0

A time step independence study is also performed for a representative staggered case with $L = 2.0, T = 3.0$ and $U^* = 4.0$ at $\zeta = 0.04$. The time step (Δt) is varied between 0.032 and 0.002. Table B.2 presents the time step independence data of the vibration amplitude (A^*). The relative errors are computed with respect to $\Delta t = 0.002$. It is observed that the change in A^* between $\Delta t = 0.008$ and $\Delta t = 0.004$ is 1.14% and beyond $\Delta t = 0.008$ the relative error is less than 2%. Therefore, $\Delta t = 0.008$ is adopted as the time step for the present study.

Time step independence study is performed for a representative case of 1-DOF ellipse at AR = 0.40 with zero damping at $U^* = 4.5$. The time step (Δt) is varied

Table B.2 Time step independence study at $U^* = 4.0$, $\zeta = 0.04$ for $L = 2.0, T = 3.0$

Time step (Δt)	**Vibration amplitude** (A^*)	**Error in** $\boldsymbol{A^*}$ **(%)**
0.032	0.51118	3.010
0.016	0.51185	3.145
0.008	0.50498	1.761
0.004	0.49928	0.612
0.002	0.49624	0

between 0.01 and 0.001. Table B.3 presents the time step independence data of the vibration amplitude (A^*). The relative errors are computed with respect to $\Delta t = 0.001$. It is observed beyond $\Delta t = 0.0025$ the relative error is less than 2%. Therefore, $\Delta t = 0.0025$ is adopted as the time step for the present study.

Table B.3 Time step independence study of 1-DOF elliptical cylinder at AR = 0.40 with zero damping at $U^* = 4.5$

Time step (Δt)	**Vibration amplitude** (A^*)	**Error in** $\boldsymbol{A^*}$ **(%)**
0.01	0.875512	4.0744
0.008	0.864935	2.817
0.004	0.859478	2.168
0.0025	0.853860	1.500
0.001	0.841236	0

Appendix C

Amplitude spectral density of lift and oscillation frequencies

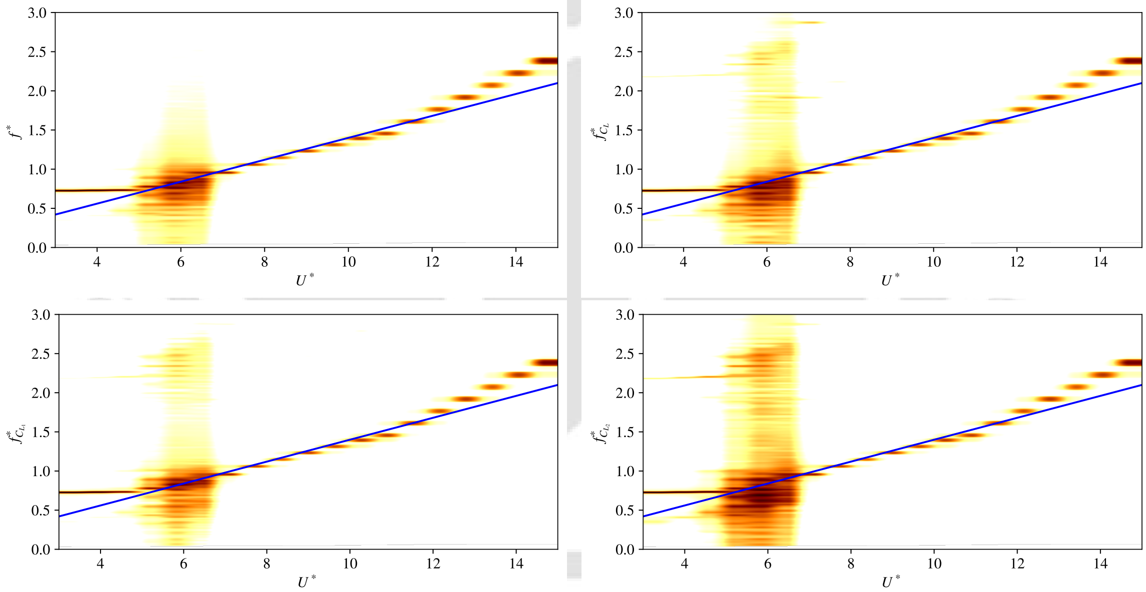

Fig. C.1 Contours of the amplitude spectral density (ASD) of normalized oscillation frequency (f^*) and lift frequencies ($f^*_{C_L}$,$f^*_{C_{L_1}}$,$f^*_{C_{L_2}}$) against U^* for $L = 2.0$, $T = 0.0$ at zero damping. Each power spectrum is plotted vertically and stacked horizontally for successive (U^*) to form the contour maps. The contours are presented on a ($\log_{10}$) scale of ASD, ranging from 0 (black) to (-3) (white). The solid line denotes the normalized stationary vortex-shedding frequency, ($f^*_{\mathrm{St}} = 0.1833$), corresponding to the Strouhal frequency of a stationary cylinder.

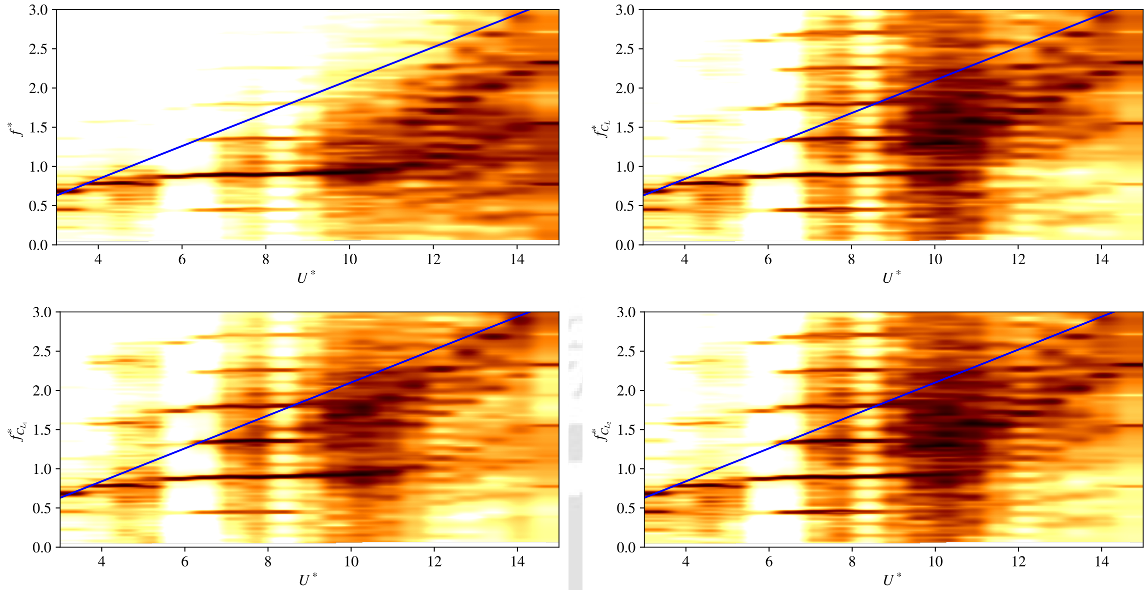

Fig. C.2 Contours of the amplitude spectral density (ASD) of normalized oscillation frequency (f^*) and lift frequencies ($f^*_{C_L}$,$f^*_{C_{L_1}}$,$f^*_{C_{L_2}}$) against U^* for $L = 2.0$, $T = 2.0$ at zero damping. The solid line denotes $f^*_{\text{St}} = 0.21$, corresponding to the Strouhal frequency of a stationary cylinder.

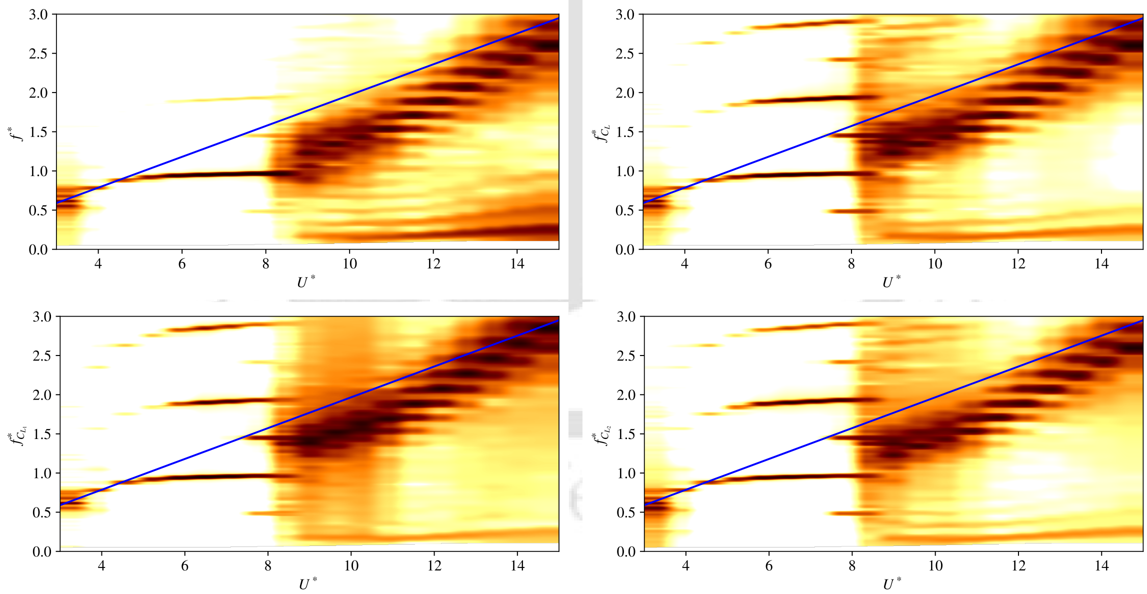

Fig. C.3 Contours of the amplitude spectral density (ASD) of normalized oscillation frequency (f^*) and lift frequencies ($f^*_{C_L}$,$f^*_{C_{L_1}}$,$f^*_{C_{L_2}}$) against U^* for $L = 2.0$, $T = 3.0$ at zero damping. The solid line denotes $f^*_{\text{St}} = 0.1967$, corresponding to the Strouhal frequency of a stationary cylinder.

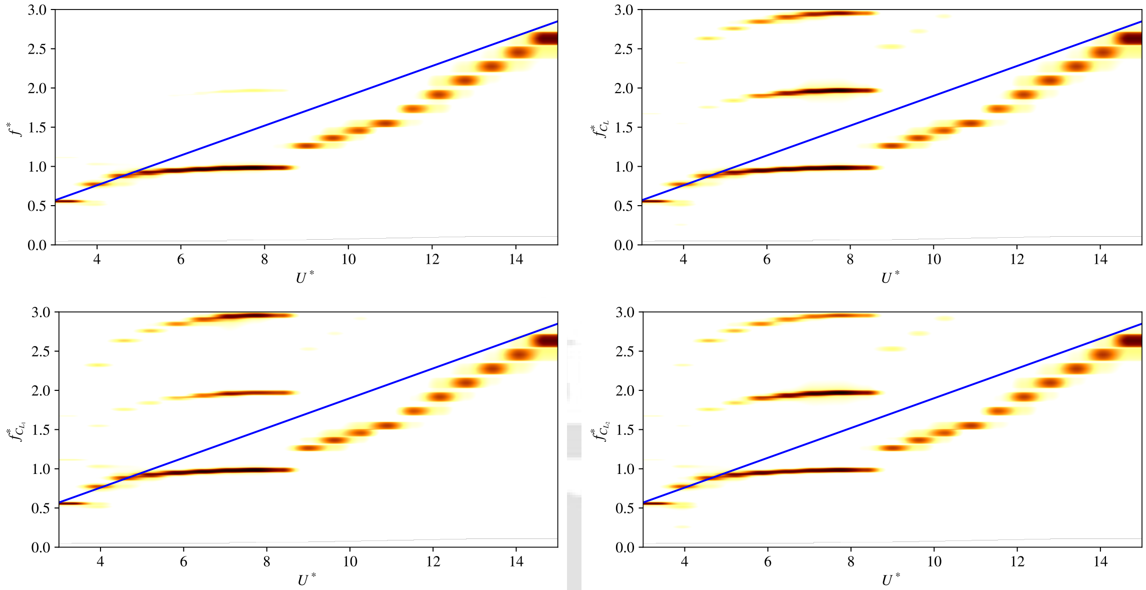

Fig. C.4 Contours of the amplitude spectral density (ASD) of normalized oscillation frequency (f^*) and lift frequencies ($f^*_{C_L}$,$f^*_{C_{L_1}}$,$f^*_{C_{L_2}}$) against U^* for L = 2.0, T = 4.0 at zero damping. The solid line denotes f^*_{St} = 0.19, corresponding to the Strouhal frequency of a stationary cylinder.

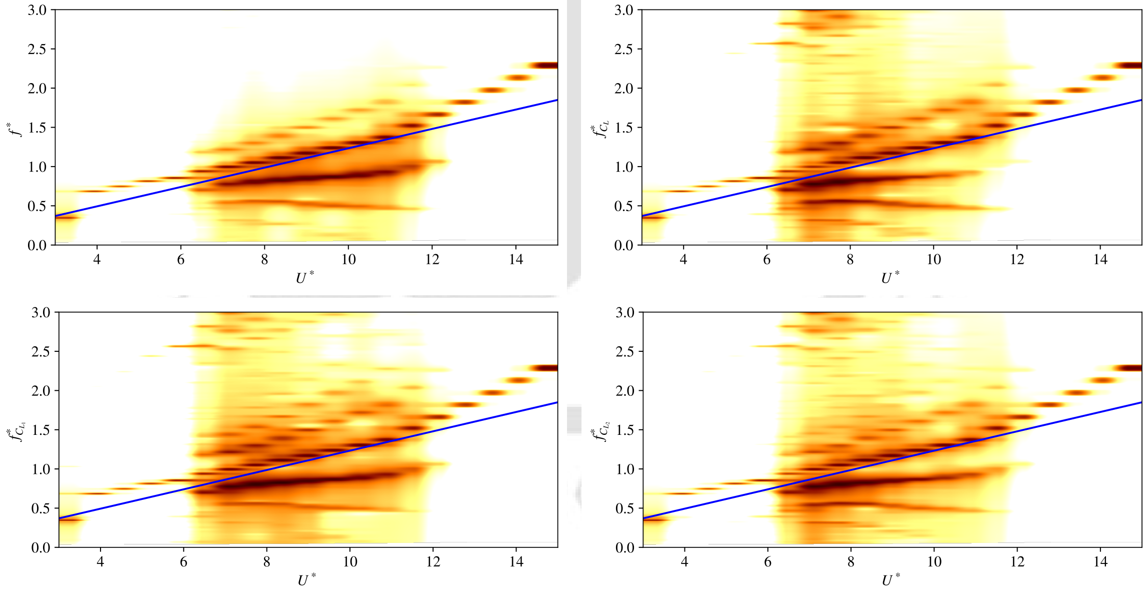

Fig. C.5 Contours of the amplitude spectral density (ASD) of normalized oscillation frequency (f^*) and lift frequencies ($f^*_{C_L}$,$f^*_{C_{L_1}}$,$f^*_{C_{L_2}}$) against U^* for L = 3.0, T = 0.0 at zero damping. The solid line denotes f^*_{St} = 0.1233, corresponding to the Strouhal frequency of a stationary cylinder.

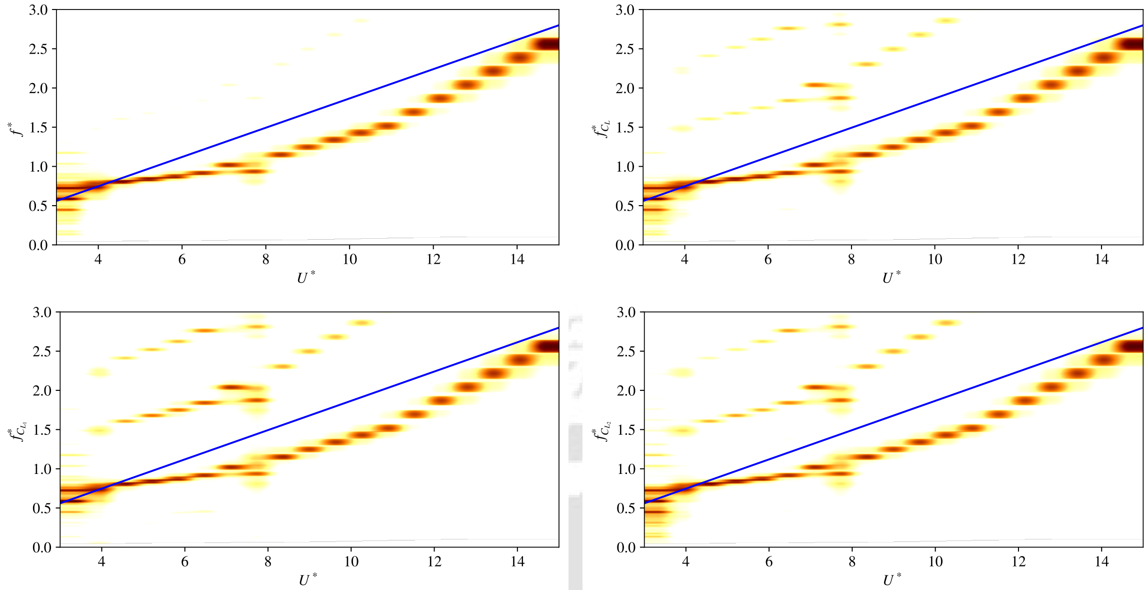

Fig. C.6 Contours of the amplitude spectral density (ASD) of normalized oscillation frequency (f^*) and lift frequencies ($f^*_{C_L}$,$f^*_{C_{L_1}}$,$f^*_{C_{L_2}}$) against U^* for $L = 3.0$, $T = 2.0$ at zero damping. The solid line denotes $f^*_{\mathrm{St}} = 0.1867$, corresponding to the Strouhal frequency of a stationary cylinder.

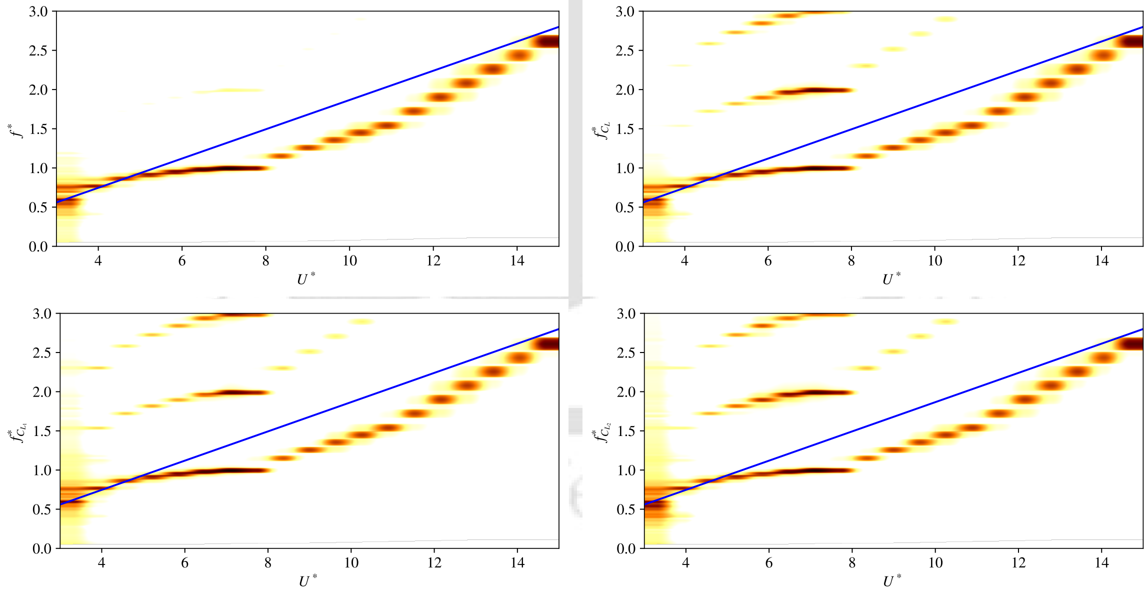

Fig. C.7 Contours of the amplitude spectral density (ASD) of normalized oscillation frequency (f^*) and lift frequencies ($f^*_{C_L}$,$f^*_{C_{L_1}}$,$f^*_{C_{L_2}}$) against U^* for $L = 3.0$, $T = 3.0$ at zero damping. The solid line denotes $f^*_{\mathrm{St}} = 0.1867$, corresponding to the Strouhal frequency of a stationary cylinder.

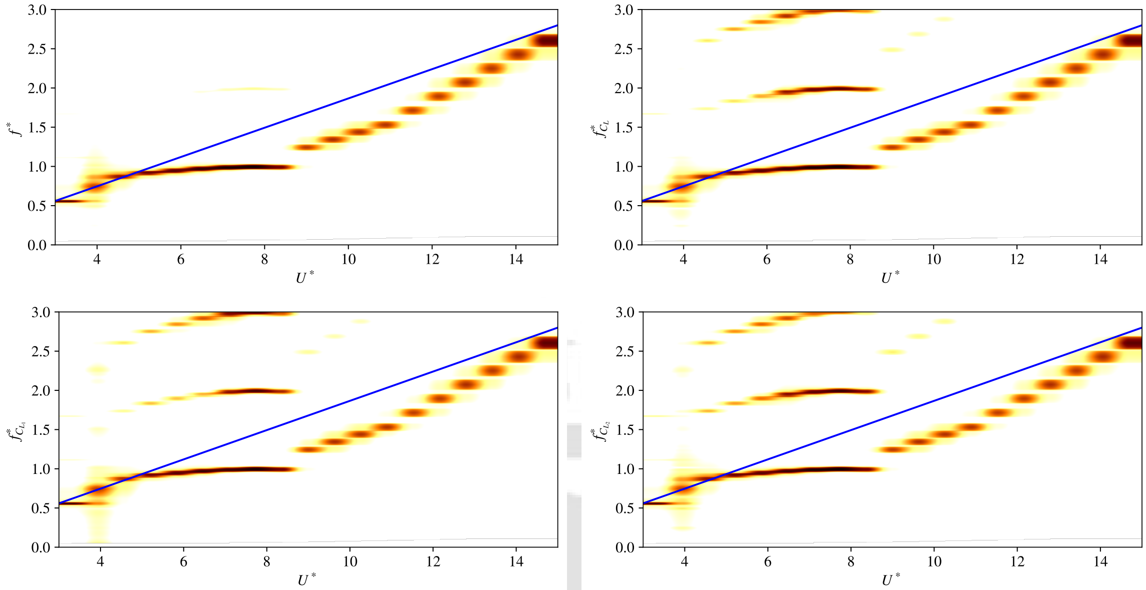

Fig. C.8 Contours of the amplitude spectral density (ASD) of normalized oscillation frequency (f^*) and lift frequencies ($f^*_{C_L}$,$f^*_{C_{L_1}}$,$f^*_{C_{L_2}}$) against U^* for L = 3.0, T = 4.0 at zero damping. The solid line denotes $f^*_{\mathrm{St}} = 0.1867$, corresponding to the Strouhal frequency of a stationary cylinder.

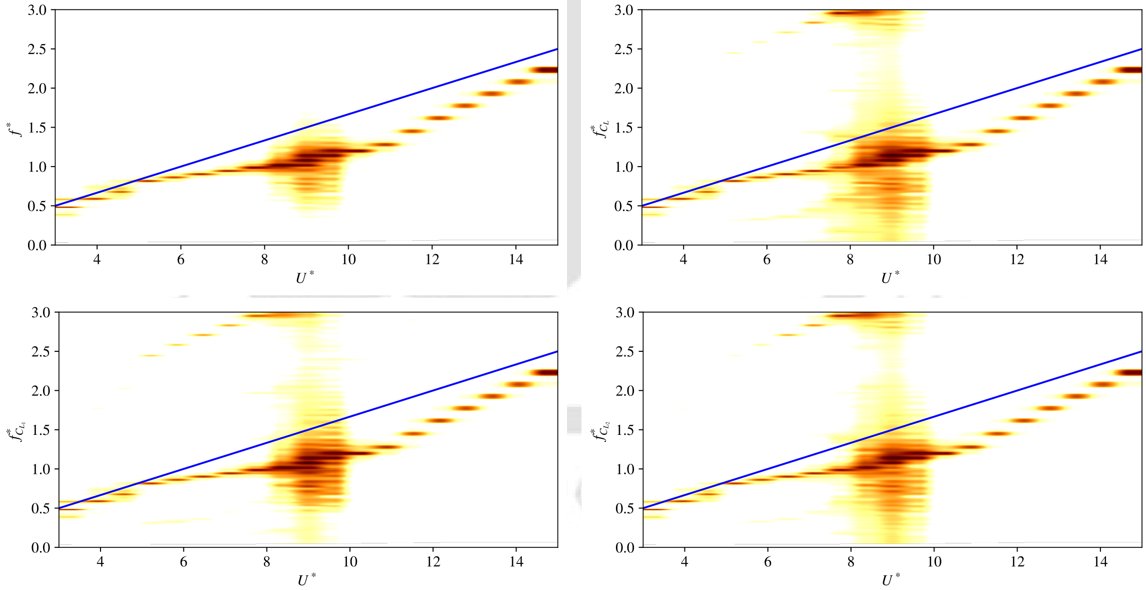

Fig. C.9 Contours of the amplitude spectral density (ASD) of normalized oscillation frequency (f^*) and lift frequencies ($f^*_{C_L}$,$f^*_{C_{L_1}}$,$f^*_{C_{L_2}}$) against U^* for L = 4.0, T = 0.0 at zero damping. The solid line denotes $f^*_{\mathrm{St}} = 0.1667$, corresponding to the Strouhal frequency of a stationary cylinder.

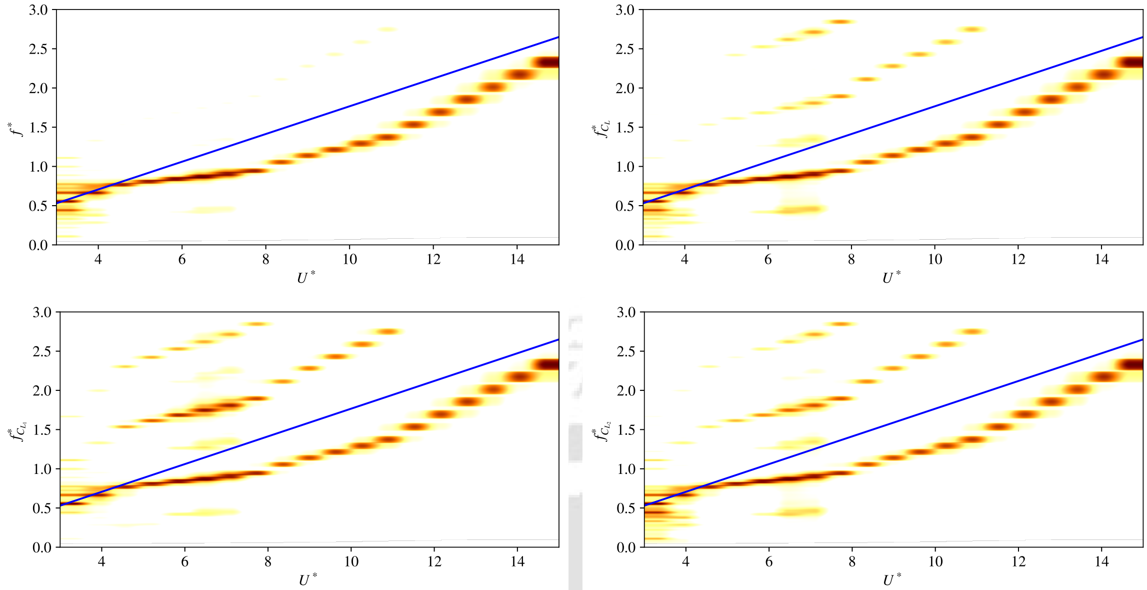

Fig. C.10 Contours of the amplitude spectral density (ASD) of normalized oscillation frequency (f^*) and lift frequencies ($f^*_{C_L}$,$f^*_{C_{L_1}}$,$f^*_{C_{L_2}}$) against U^* for $L = 4.0$, $T = 2.0$ at zero damping. The solid line denotes $f^*_{\mathrm{St}} = 0.1767$, corresponding to the Strouhal frequency of a stationary cylinder.

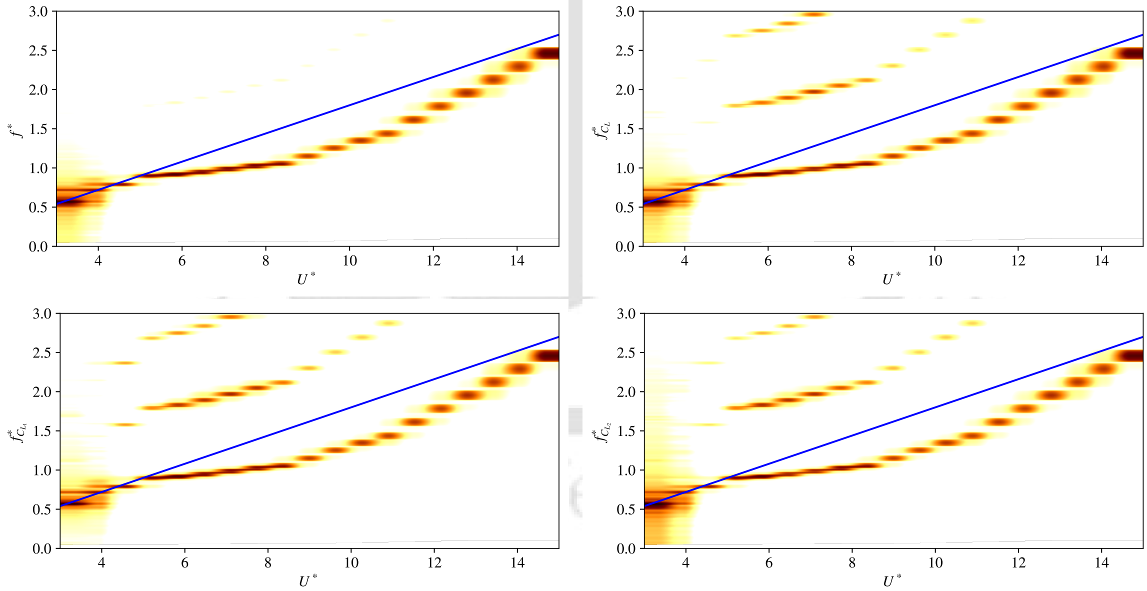

Fig. C.11 Contours of the amplitude spectral density (ASD) of normalized oscillation frequency (f^*) and lift frequencies ($f^*_{C_L}$,$f^*_{C_{L_1}}$,$f^*_{C_{L_2}}$) against U^* for $L = 4.0$, $T = 3.0$ at zero damping. The solid line denotes $f^*_{\mathrm{St}} = 0.18$, corresponding to the Strouhal frequency of a stationary cylinder.

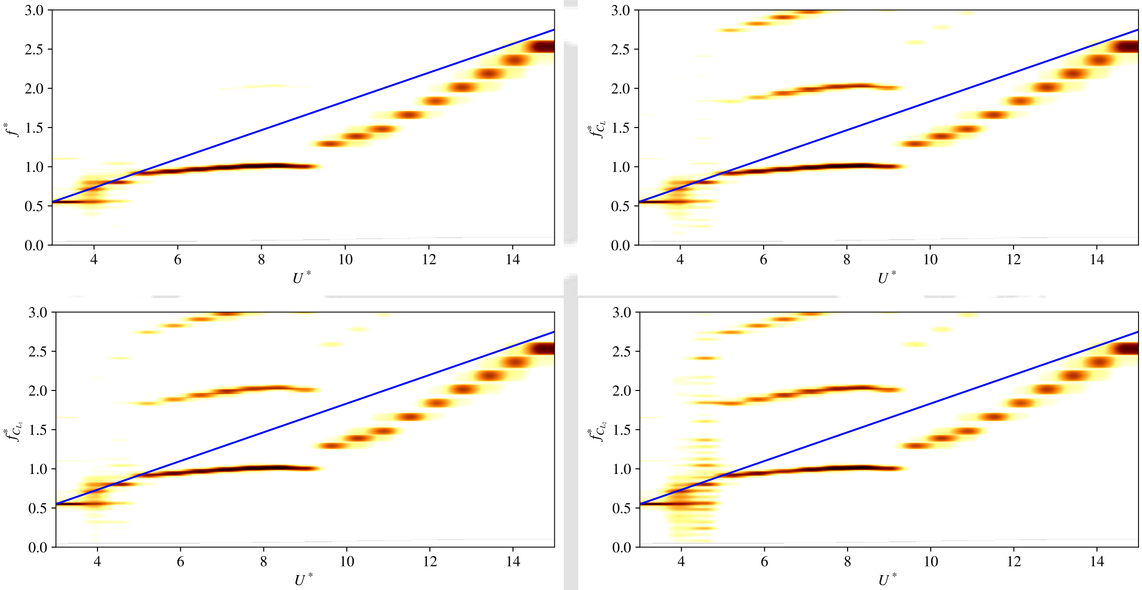

Fig. C.12 Contours of the amplitude spectral density (ASD) of normalized oscillation frequency (f^*) and lift frequencies ($f^*_{C_L}$,$f^*_{C_{L_1}}$,$f^*_{C_{L_2}}$) against U^* for L = 4.0, T = 4.0 at zero damping. The solid line denotes $f^*_{\mathrm{St}} = 0.1833$, corresponding to the Strouhal frequency of a stationary cylinder.

List of publications

1. **Abhijit Pal**, Atul Kumar Soti, The effect of damping and aspect ratio on power extraction from vortex-induced vibration of elliptical cylinder, *Physics of Fluids*, vol. 37, no. 2, p. 027162, 2025. https://doi.org/10.1063/5.0245013

2. **Abhijit Pal**, Atul Kumar Soti, The effects of spacing and damping on vortex-induced vibration of two rigidly coupled circular cylinders in tandem arrangement, *Physics of Fluids*, vol. 37, no. 10, p. 103623, 2025. https://doi.org/10.1063/5.0295924

3. **Abhijit Pal**, Atul Kumar Soti, Power extraction from vortex-induced vibration of two cylinders in staggered arrangement. *Physics of Fluids*, vol. 37, no. 12, p. 123617, 2025. https://doi.org/10.1063/5.0307191

4. **Abhijit Pal**, Atul Kumar Soti, Vortex-induced vibration of two rigidly coupled cylinders in staggered arrangement at low Reynolds number, *Physics of Fluids*, vol. 38, no. 5 p. 053606, 2026. https://doi.org/10.1063/5.0320772.

5. **Abhijit Pal**, Atul Kumar Soti, Effect of frequency and damping ratio on power extraction from flow-induced vibration of elliptical cylinder with passive heaving and pitching, (Under Preparation).

Conferences

1. **Abhijit Pal**, Atul Kumar Soti, Power Harvesting from VIV of Rigidly-Coupled Cylinders in Tandem Arrangement, *Fluid Mechanics and Fluid Power* (FMFP), BITS Pilani, 27th - 29th December, 2021. https://doi.org/10.1007/978-981-19-7055-9_53

2. **Abhijit Pal**, Atul Kumar Soti, Power Extraction from VIV of Rigidly-coupled Cylinders in Staggered arrangement, *International Conference in Fluid, Thermal and Energy Systems* (ICFTES), NIT Calicut, 9th - 11th June, 2022.

3. **Abhijit Pal**, Atul Kumar Soti, Extraction of Flow-Power from VIV of Two Cylinders in Diagonal Arrangement at Low Reynolds Number, *Research & Industrial Conclave-Integration* (RIC), IIT Guwahati, 9th - 11th August, 2024. https://doi.org/10.1007/978-981-96-8753-4_5

4. **Abhijit Pal**, Atul Kumar Soti, Power Harnessing from Flow-Induced Vibration of Five Cylinders in Sinusoidal Arrangement at Re = 150, *Proceedings of the 11th International Conference on Mechanical, Automotive and Materials Engineering* (CMAME), Bangkok, Thailand, 18th - 20th December, 2024. https://doi.org/10.1007/978-981-96-5622-6_11

Thesis_Abhijit_196103101.pdf

ORIGINALITY REPORT

13%	8%	10%	1%
SIMILARITY INDEX	INTERNET SOURCES	PUBLICATIONS	STUDENT PAPERS

PRIMARY SOURCES

1	Abhijit Pal, Atul K. Soti. "The effects of spacing and damping on vortex-induced vibration of two rigidly coupled circular cylinders in tandem arrangement", Physics of Fluids, 2025 Publication	1%
2	aip.scitation.org Internet Source	1%
3	Abhijit Pal, Atul K. Soti. "Power extraction from vortex-induced vibration of two rigidly coupled cylinders in staggered arrangement", Physics of Fluids, 2025 Publication	1%
4	flair.monash.edu Internet Source	1%
5	coek.info Internet Source	1%
6	"Fluid Mechanics and Fluid Power (Vol. 1)", Springer Science and Business Media LLC, 2023 Publication	1%

7	hdl.handle.net Internet Source	1%
8	www.researchgate.net Internet Source	1%
9	ppgen.poli.usp.br Internet Source	<1%
10	"Current Progress in Engineering Sciences", Springer Science and Business Media LLC, 2025 Publication	<1%
11	api.research-repository.uwa.edu.au Internet Source	<1%
12	stax.strath.ac.uk Internet Source	<1%
13	researchdirect.westernsydney.edu.au Internet Source	<1%
14	Zhipeng Yu, Huan Ping, Enhao Wang, Yan Bao, Hongteng Xu, Yang Huang, Qing Xiao. "Missing critical mass ratio in VIV of rigidly connected cylinders", International Journal of Mechanical Sciences, 2025 Publication	<1%
15	ses.library.usyd.edu.au Internet Source	<1%

16	Park, Hon. "Mapping of passive turbulence control to flow induced motions of circular cylinders", Proquest, 2014. Publication	<1 %
17	Gaurav Sharma, Rajneesh Bhardwaj. "Flow-induced vibrations of elastically coupled tandem cylinders", Journal of Fluid Mechanics, 2023 Publication	<1 %
18	Maojin Gong, Bassam Dally. "Numerical study on flow-induced vibration of an oscillating cylinder with an unattached downstream square plate at a low Reynolds number", Ocean Engineering, 2023 Publication	<1 %
19	Rahul Mishra, Rajneesh Bhardwaj, Salil S. Kulkarni, Mark C. Thompson. "Vortex-induced vibration of a circular cylinder on a nonlinear viscoelastic support", Journal of Fluids and Structures, 2021 Publication	<1 %
20	Hongjun Zhu, Xiaonian Tan, Yun Gao, Tongming Zhou, Wenli Liu. "Two-degree-of-freedom flow-induced vibration of two rigidly coupled tandem cylinders of unequal diameters", Ocean Engineering, 2020 Publication	<1 %

21	Rahul Mishra, Atul Soti, Rajneesh Bhardwaj, Salil S. Kulkarni, Mark C. Thompson. "Transverse vortex-induced vibration of a circular cylinder on a viscoelastic support at low Reynolds number", Journal of Fluids and Structures, 2020 Publication	<1 %
22	eprints.ncl.ac.uk Internet Source	<1 %
23	Deepak Kumar, Kumar Sourav. "Vortex-induced vibrations of tandem diamond cylinders: A novel lock-in behavior", International Journal of Mechanical Sciences, 2023 Publication	<1 %
24	ntnuopen.ntnu.no Internet Source	<1 %
25	Kaja, Kalyani. "Vortex-induced vibrations of circular cylinders in steady and oscillatory flow.", Western Sydney University (Australia), 2017 Publication	<1 %
26	Submitted to University of Aberdeen Student Paper	<1 %
27	Wanhai Xu, Shuhai Zhang, Yexuan Ma, Bin Liu, Junlei Wang. "A study on the FIV	<1 %

hydrodynamic force coefficients of two staggered flexible cylinders via an inverse method", Ocean Engineering, 2020
Publication

28	publications.polymtl.ca Internet Source	<1 %
29	Zhenhua Song, Yijun Shen, Menglan Duan, Jijun Gu. "Numerical investigation on the effect of diameter ratio on wake induced vibrations of tandem cylinders", Ocean Engineering, 2022 Publication	<1 %
30	Hongyu Zhu, Yan Zhao, Tao Qiu, Weiqun Lin, Xiaoqing Du, Haotian Dong. "Vortex-induced vibrations of two tandem rigidly coupled circular cylinders with streamwise, transverse, and rotational degrees of freedom", Physics of Fluids, 2023 Publication	<1 %
31	espace.curtin.edu.au Internet Source	<1 %
32	Ken, Chin Wei. "Computational Study of Vortex Induced Vibration Performance with Coupled Bluff Splitter Body and Elastic Plate Model", University of Malaya (Malaysia), 2023 Publication	<1 %

33	Yanfang Lv, Liping Sun, Michael M. Bernitsas, Hai Sun. "A comprehensive review of nonlinear oscillators in hydrokinetic energy harnessing using flow-induced vibrations", Renewable and Sustainable Energy Reviews, 2021 Publication	<1%
34	Hamid Hassan Khan, Md. Islam, Yap Yit Fatt, Isam Janajreh, Md. Mahbub Alam. "Effect of three tandem cylinder diameter difference on flow-induced vibrations and heat transfer", International Journal of Mechanical Sciences, 2022 Publication	<1%
35	Lee, Jonghun. "Hydrokinetic power harnessing utilizing vortex induced vibrations through a virtual c-k VIVACE model", Proquest, 20111003 Publication	<1%
36	Wanhai Xu, Haokai Wu, Kun Jia, Enhao Wang. "Numerical investigation into the effect of spacing on the flow-induced vibrations of two tandem circular cylinders at subcritical Reynolds numbers", Ocean Engineering, 2021 Publication	<1%
37	Hong Song, Weiping Huang, Xuepeng Fu, Haoran Yan, Shuang Chang. "Empirical model	<1%

of the wake-induced lift force on a cylinder with low mass ratio", Marine Structures, 2021
Publication

38	Wenjun Ding, Hai Sun, Wanhai Xu, Michael M. Bernitsas. "Experimental and computational investigation of interactive flow induced oscillations of two tandem rough cylinders at 3×104≤Re≤1.2×105", Ocean Engineering, 2021 Publication	<1 %
39	Sanjeev Kumar, Md Islam, Yap Yit Fatt, Isam Janajreh. "Flow-induced vibration and heat transfer in a cluster of three staggered cylinders with different angles of incidence", Ocean Engineering, 2023 Publication	<1 %
40	www.scholarmate.com Internet Source	<1 %
41	Submitted to Indian Institute of Technology, Madras Student Paper	<1 %
42	Abhishek, Atul Sharma, Sandip Kumar Saha. "Flow-induced vibration of a cylinder subjected to proximity interference by a downstream-cylinder", Journal of Fluid Mechanics, 2025 Publication	<1 %

43	Yosua Heru Irawan, Syed Ahmad Raza, Ming-Jyh Chern. "Numerical predictions of vibration responses and flow energy conversion efficiency of side-by-side cylinders at moderate Reynolds number", Applied Ocean Research, 2022 Publication	<1 %
44	Mehdi Badri Ghomizad, Hosnieh Kor, Minh Doan, Masashi Yamakawa. "Vortex-induced vibration and wake interference of two-degree-of-freedom elastically mounted elliptical cylinders in tandem at various spacing", Ocean Engineering, 2024 Publication	<1 %
45	Maojin Gong, Bassam Dally. "A review of flow-induced vibration in wind and oceanic flow: Mechanisms, applications, optimizations, and challenges", Ocean Engineering, 2025 Publication	<1 %
46	www.mdpi.com Internet Source	<1 %
47	Mohamed O. Awadallah, Changqing Jiang, Ould el Moctar, Amr Ali Hassan. "Boosting energy harvesting efficiency from wake-induced vibration using a multi-cylinder configuration", Applied Energy, 2025 Publication	<1 %

48 Adnan Munir, Ming Zhao, Helen Wu, Lin Lu. "Effects of gap ratio on flow-induced vibration of two rigidly coupled side-by-side cylinders", Journal of Fluids and Structures, 2019 <1%
Publication

49 Eduard Naudascher, Donald Rockwell. "Flow-Induced Vibrations - An Engineering Guide", CRC Press, 2017 <1%
Publication

50 Jiahuang Tu, Zhancheng He, Xiaoling Tan, Guanyu Wang, Jixiang Xu, Yuwang Xu. "Study for the cross-flow coupling mechanism of tandem cylinder groups at low Reynolds number", Ocean Engineering, 2022 <1%
Publication

51 Bin Qin, Md. Mahbub Alam, Yu Zhou. "Free vibrations of two tandem elastically mounted cylinders in crossflow", Journal of Fluid Mechanics, 2018 <1%
Publication

52 Wenyin Gu, Xu Xu, Mingjing Jiang, Wenjuan Yao. "Effects of spacing ratio on vortex-induced vibration of twin tandem diamond cylinders in a steady flow", Physics of Fluids, 2023 <1%
Publication

53 Mohamed O. Awadallah, Changqing Jiang, Ould el Moctar, Amr Ali Hassan. "Improving energy harvesting in flow-induced vibrations of multi-cylinder square arrays with vortex generators", Ocean Engineering, 2025 <1 %
Publication

---

54 Kumar, Mukesh. "Development and Validation of Stroke Risk Score in Symptomatic Carotid Stenosis Patients: Clinical and Multimodal Imaging Based Risk Modelling", Postgraduate Institute of Medical Education and Research, Chandigarh (India) <1 %
Publication

---

55 Khan, Niaz Bahadur. "Numerical Modeling and Analysis of Flow Around Stationary and Oscillating Circular Cylinder", University of Malaya (Malaysia), 2023 <1 %
Publication

---

56 Ming Zhao. "Flow induced vibration of two rigidly coupled circular cylinders in tandem and side-by-side arrangements at a low Reynolds number of 150", Physics of Fluids, 2013 <1 %
Publication

---

57 Kara, Mustafa Can. "Fluid-Structure Interaction (FSI) of Flow Past Elastically <1 %

Supported Rigid Structures.", Georgia Institute of Technology
Publication

58	Mohammadreza Rashki, Alireza Mojtahedi, Mohammad Ali Lotfollahi-Yaghin, Vahid Tamimi et al. "A review of two-degree-of-freedom vortex-induced vibrations with hydrokinetic energy harvesting applications", Ocean Engineering, 2025 Publication	<1 %
59	Ussama Ali, Md. Islam, Isam Janajreh, Yap Fatt, Md. Mahbub Alam. "Flow-Induced Vibrations of Single and Multiple Heated Circular Cylinders: A Review", Energies, 2021 Publication	<1 %
60	Zhancheng He, Hongsheng Yuan, Guanyu Wang, Jiahuang Tu. "Effect of spacing ratios on coupling mechanism of three tandem cylinders in planar shear flow", Ocean Engineering, 2024 Publication	<1 %
61	deepblue.lib.umich.edu Internet Source	<1 %
62	Peng Han, Guang Pan, Baoshou Zhang, Wei Wang, Wenlong Tian. "Three-cylinder oscillator under flow: Flow induced vibration	<1 %

and energy harvesting", Ocean Engineering, 2020
Publication

63	Deepak Kumar, Subhankar Sen. "Flow-induced vibrations of a pair of in-line square cylinders", Physics of Fluids, 2021 Publication	<1%
64	Yun Gao, Bin Yang, Hongjun Zhu, Geng Peng, Zhuangzhuang Zhang, Ganghui Pan. "Flow induced vibration of two rigidly connected circular cylinders in different arrangements at a low Reynolds number", Ocean Engineering, 2020 Publication	<1%
65	www.cambridge.org Internet Source	<1%
66	Ying Wu, Zhi Cheng, Ryley McConkey, Fue-Sang Lien, Eugene Yee. "Modelling of Flow-Induced Vibration of Bluff Bodies: A Comprehensive Survey and Future Prospects", Energies, 2022 Publication	<1%
67	Sigil Francis, Ashirbad Swain. "Modelling and harnessing energy from flow-induced vibration, particularly VIV and galloping: An explicit review", Ocean Engineering, 2024 Publication	<1%

68	Bowen Tang, Rui Bai, Hewei Yang, Jiawei Wang, Moxiao Liu, Xiaoyang Yu, Wei Tan. "Improving FIV Energy Harvesting Characteristics Using Rigidly Coupled Cylinders", Renewable Energy, 2025 Publication	<1 %
69	Submitted to IIT Delhi Student Paper	<1 %
70	Padrao, Daniel. "Thermofluid Optimisation of Additive Manufacturing High Heat Flux Components for Fusion", University of Nottingham (United Kingdom) Publication	<1 %
71	Zhao, Tianyang. "Numerical Simulation of Flow-Induced Vibration of Rigid and Flexible Structures: Using Overset Mesh Technique", The University of Manchester (United Kingdom), 2025 Publication	<1 %
72	Submitted to Khalifa University of Science Technology and Research Student Paper	<1 %
73	Pregent, Stive. "Polyelectrolyte Complexes for Encapsulation.", The University of Manchester (United Kingdom) Publication	<1 %

74	Peng Han, Qiaogao Huang, Guang Pan, Denghui Qin, Wei Wang, Rodolfo T. Gonçalves, Jisheng Zhao. "Optimal energy harvesting efficiency from vortex-induced vibration of a circular cylinder", Ocean Engineering, 2023 Publication	<1%
75	Submitted to Queen Mary and Westfield College Student Paper	<1%
76	Gomes, Jorge Miguel Pereira. "Fluid-Structure Interaction-Induced Oscillation of Flexible Structures in Uniform Flows.", Friedrich-alexander-Universitaet Erlangen-Nuernberg (Germany), 2021 Publication	<1%
77	Reza Abedi, Ming Zhao, Helen Wu, Adnan Munir. "Numerical simulation of vortex-induced vibration of tandem circular cylinders near a plane boundary", Ocean Engineering, 2025 Publication	<1%
78	Gadelhak, Ibrahim Ahmed Ibrahim. "Fluidelastic Excitation of a Fuel Rod Bundle Subjected to Combined Axial-Flow and Jet Cross-Flow", Ecole Polytechnique, Montreal (Canada), 2024 Publication	<1%

79	Klamo, Joseph Th. "Effects of Damping and Reynolds Number on Vortex-Induced Vibrations", Proquest, 2014. Publication	<1 %
80	Okuducu, Mahmut Burak. "Design of Passive Micromixers in Microfluidic Systems: A Computational Study.", Georgia Institute of Technology Publication	<1 %
81	Pires Vieira Serta, Clarissa. "Computational Fluid Dynamics (CFD) Investigations of Flow-Induced Vibrations of Two Rigidly Coupled Cylinders at High Reynolds Number", University of Stavanger (Norway) Publication	<1 %
82	Submitted to University of Western Sydney Student Paper	<1 %
83	Yan Bao, Dai Zhou, Jiahuang Tu. "Flow interference between a stationary cylinder and an elastically mounted cylinder arranged in proximity", Journal of Fluids and Structures, 2011 Publication	<1 %
84	Jia-song Wang, Dixia Fan, Ke Lin. "A review on flow-induced vibration of offshore circular cylinders", Journal of Hydrodynamics, 2020 Publication	<1 %

85	Ofuegbe, James Kayode. "Relation at the Fluid-Structure Interface and Residuary Force in Flow Induced Oscillations with Experimental Validation (Viv & Galloping)", University of Michigan, 2021 Publication	<1%
86	Submitted to University of Newcastle upon Tyne Student Paper	<1%
87	F. R. Menter. "Two-equation eddy-viscosity turbulence models for engineering applications", AIAA Journal, 1994 Publication	<1%
88	Mahat, Nabin Raj. "Numerical Study of Effect of Wall Thermal Boundary Conditions in Non-Premixed Flame Dynamics in a Confined Channel", Idaho State University, 2023 Publication	<1%
89	Maojin Gong, Bassam Dally. "Dynamic response of a cylinder-plate-cylinder system coupling wake-induced and interference effects", Physics of Fluids, 2025 Publication	<1%
90	documentsdelivered.com Internet Source	<1%

91	Tran, Huong. "Si-Based Germanium Tin Photodetectors for Infrared Imaging and High-Speed Detection", University of Arkansas, 2021 Publication	<1 %
92	Yosua Heru Irawan, Syed Ahmad Raza, Ming-Jyh Chern. "Passively enhanced VIV responses of side-by-side cylinders at moderate Reynolds number", Applied Ocean Research, 2023 Publication	<1 %
93	Submitted to Monash University Student Paper	<1 %
94	Submitted to Universiti Teknologi Malaysia Student Paper	<1 %
95	Submitted to Aligarh Muslim University, Aligarh Student Paper	<1 %
96	Huan Ping, Yong Cao, Kai Zhang, Zhaolong Han, Dai Zhou, Hongbo Zhu, Yan Bao. "Vortex-induced vibrations of two rigidly coupled circular cylinders in tandem arrangement", Ocean Engineering, 2022 Publication	<1 %
97	Submitted to University of Sheffield Student Paper	<1 %

98 Wolf, Ki Tae. "Computational Investigation of Lymphatic Valves and Vessels.", Georgia Institute of Technology <1 %
Publication

---

99 Mohamed O. Awadallah, Changqing Jiang, Ould el Moctar. "Numerical study into the impact of fixed upstream cylinder diameter ratios on vibration of leeward tandem cylinders", Ocean Engineering, 2023 <1 %
Publication

---

100 Oladipo, Olalaken Ayoola. "Encapsulation of Waste in Cementitious Systems for use in Civil Engineering Applications", University of South Wales (United Kingdom), 2020 <1 %
Publication

---

101 Multidiscipline Modeling in Materials and Structures, Volume 7, Issue 4 (2013-05-27) <1 %
Publication

---

102 Panagiotis Kaklamanos, Emily Buttler, Yatin Darbar, Andrew Lacey et al. ""Whatever Input to Torsion Transfer": Harvesting energy from a WITT gearbox device", Cambridge University Press (CUP), 2024 <1 %
Publication

---

103 Abstract not available. <1 %

. "M.E.Sc.", Proquest, .

Publication

104	Birudala Venkatesh Reddy, Y V Krishna Reddy, Md. Abdur Razzak, Surender Reddy Salkuti. "Sustainable Electrical Engineering and Intelligent Systems", CRC Press, 2025 Publication	<1 %
105	Guangjun Liu, Zhiyou Song, Wanhai Xu, Mu Sha. "Numerical study on the VIVs of two side-by-side elastically coupled cylinders under different Re and natural frequencies", Ocean Engineering, 2023 Publication	<1 %
106	Mitrovic, Ana. "Design Methodologies for High Density Superconducting Circuits and Systems", University of Rochester, 2025 Publication	<1 %
107	Muhamad Pauzi, Anas. "Axial Flow-Induced Vibrations Over a Blunt-Ended Cantilevered Rod for Nuclear Applications", The University of Manchester (United Kingdom), 2025 Publication	<1 %
108	Scheu, Kara R.. "Sediment Transport Due to River Plumes in Stratified, Rotationally-Influenced Lakes.", Stanford University, 2020 Publication	<1 %
109	Thoms, Alexander Douglas. "Resilient and Reliable SLAM for Autonomous Robotic	<1 %

Inspection", University of California, Los Angeles, 2025

Publication

110	sportdocbox.com Internet Source	<1 %
111	Pawelczak, Jakub M.. "Essays on Macroeconomics and Housing", University of Minnesota Publication	<1 %
112	Taiwo, Grace Oluwakemisola. "Evaluation of Hydrogen Storage Potential in Depleted Hydrocarbon Formations: A Case Study of the Middle Bakken Member in the Antelope Field, Williston Basin, North Dakota", The University of North Dakota, 2025 Publication	<1 %
113	"Wake-induced vibration of a circular cylinder at a low Reynolds number of 100", Physics of Fluids, 2019 Publication	<1 %

Exclude quotes	On	Exclude matches	Off
Exclude bibliography	On		